Airborne Multi-Axis and Direct Sun DOAS: Development and Urban Air Quality Applications

by

Sunil Baidar

B.S., Dickinson College, 2009

A thesis submitted to the

Faculty of the Graduate School of the

University of Colorado in partial fulfillment

of the requirements for the degree of

Doctor of Philosophy

Department of Chemistry and Biochemistry

2015

This thesis entitled:
Airborne Multi-Axis and Direct Sun DOAS: Development and Urban Air Quality Applications
written by Sunil Baidar
has been approved for the Department of Chemistry and Biochemistry

Rainer M. Volkamer

Dr. R. Michael Hardesty

Date

The final copy of this thesis has been examined by the signatories, and we find that both the content and the form meet acceptable presentation standards of scholarly work in the above mentioned discipline.

Baidar, Sunil (Ph.D., Chemistry)

Airborne Multi-Axis and Direct Sun DOAS: Development and Urban Air Quality Applications

Thesis directed by Prof. Rainer M. Volkamer

Tropospheric ozone (O_3) is one of the most prevalent air pollutants affecting human health and environment. It is also a greenhouse gas. O_3 is a secondary pollutant formed in the atmosphere by the chemical reaction between nitrogen oxides (NO_x) and volatile organic compounds (VOC) in the presence of sunlight, and a major constituent of photochemical smog. The O_3 formation is a complex non-linear process which depends on NO_x and VOC reactivity. As a result, reduction in emissions of precursor molecules do not always result in decrease in O_3 levels. Occurrence of higher O_3 on weekends in an urban environment as a response to reductions in NO_x emissions is commonly referred as weekend O_3 effect.

The Airborne Multi-Axis Differential Optical Absorption Spectroscopy (AMAX-DOAS) was deployed aboard the NOAA Twin Otter during the California Research at the Nexus of Air Quality and Climate Change (CalNex) and Carbonaceous Aerosols and Radiative Effects Study (CARES) field campaigns in summer 2010 in California to measure vertical profiles and columns of O_3 precursor molecules nitrogen dioxide (NO_2), formaldehyde (HCHO) and glyoxal (CHOCHO). Measurements from the two campaigns have been used extensively for evaluation of satellite measurements and atmospheric models over California. This work describes the instrument, retrievals of NO_2, HCHO and CHOCHO vertical profiles and columns from the measurements and the validation of NO_2 columns. In addition, application of three remote sensing instruments (AMAX-DOAS, NOAA TOPAZ O_3 and Doppler wind lidars) to constrain NO_2 and O_x (O_3 + NO_2) production rates from source regions in Bakersfield, CA is presented. I also present analysis of the aircraft and long term surface network measurements of NO_2 and O_3 showing recent weakening of the weekend O_3 effect in California's South Coast Air Basin. AMAX-DOAS measurements were also used to confirm the sand signal observed by satellite-borne instruments over deserts.

A mobile solar tracker was developed for direct sun DOAS measurements of NO_2 and other trace gases. It features an integrated motion compensation system and an imaging feedback loop allowing for autonomous sun tracking at very high precision from a mobile laboratory. Advantages of direct sun measurements over scattered sunlight include high photon flux, simple conversion of slant columns to vertical columns, and no Ring effect, all of which results in the improvement in measurement precision. This allows for mapping of temporal and spatial variability in NO_2 columns with unprecedented detail. The tracker can be simultaneously coupled with UV-vis and infrared spectrometers. Results from its first deployment during Front Range Air Pollution and Photochemistry Experiment (FRAPPE) in Colorado are presented.

Dedication

To my wife, Joy.

Acknowledgements

First and most importantly, I thank my advisor Rainer Volkamer for all his advice, guidance and support. I have enjoyed the opportunity to work on many exciting research projects beyond what is part of this thesis and travel around the world. I would also like to thank Mike Hardesty for providing the opportunity to spend time at NOAA and collaborate with researchers there. I truly appreciate his support and guidance.

I thank Hilke Oetjen and Barbara Dix for teaching me about instrumentation, DOAS, radiative transfer model, data analysis and many other topics. Sean Coburn and Ivan Ortega have been very helpful with instrumentation and data analysis. I acknowledge Christoph Senff, Alan Brewer, Andy Langford, Si-Wan Kim, Michael Trainer, Stu McKean from NOAA, Chenxia Cai from CARB, Andreas Richter from University of Bremen for sharing data and/or for many helpful discussions. Thanks to David Thomson, Philip Handley and Jim Kastengren for their help getting the mobile solar tracker ready and functional.

Thank you to everyone in the Volkamer Group and Atmospheric Remote Sensing Group at NOAA for all their help throughout the years. I would particularly like to thank Christoph Senff for his advice and guidance. Eleanor Waxman has been a great friend and I thank her for guiding me through the maze i.e. graduate school for the last six years and putting up with me constantly bothering her. I will miss my discussions with Ted Koening about anything and everything as well as his Conch Shell reminding the day's end.

Contents

Chapter

Tables

Table

Figures

Figure

Chapter 1

Introduction

1.1 Urban Air Pollution

Air pollution is one of the major problems in urban areas around the world. It adversely affects human health as well as having environmental concerns such as causing acid rain, degrading visibility, and damaging vegetation and materials. Major health issues related to air pollution include lung cancer, respiratory infection, and cardiopulmonary diseases. About 5% of the trachea, bronchus, and lung cancer in the world annually are caused by ambient air pollution (World Health Organisation, 2002). According to WHO assessment of burden of disease due to air pollution, about 1 million premature deaths each year can be attributed to the effects of urban outdoor air pollution (World Health Organisation, 2002). With more than half of the world population now living in urban areas and increasing by day, more people in the world are directly affected by urban outdoor air pollution today than at any time in the past. Further, long-range transport of these pollutants can affect areas far away from sources (e.g., Langford et al., 2010, 2012). Global air quality is predicted to worsen in the future with increase in background concentration of pollutants (Monks et al., 2009).

Urban air pollution is largely a consequence of human activities such as combustion of fossil fuels for transportation, power generation, and other activities. These human activities emit a large number of chemical compounds into the atmosphere and are the main source for air pollution. Emission of nitrogen oxides (NO_x) and volatile organic compounds (VOC) are particularly important because of their ability to form tropospheric ozone (O_3). NO_x and VOCs can react in the

presence of sunlight to produce tropospheric O_3. NO_x also forms nitrate aerosols, which is one of the major component of particulate matter (PM) (Finlayson-Pitts and Pitts Jr, 2000; Seinfeld and Pandis, 2006). NO_x, O_3, and PM are recognized by regulating agencies like the United States Environmental Protection Agency (EPA) as criteria pollutants due to their health and environmental concerns. These criteria pollutants are regulated by air quality regulating agencies throughout the world by setting health based standards. The National Ambient Air Quality Standard (NAAQS) set by the EPA are 75 ppb for O_3 (8 hour maximum), 53 ppb for NO_2 (annual mean), and 12 $\mu g\ m^{-3}$ and 15 $\mu g\ m^{-3}$ for primary and secondary $PM_{2.5}$, respectively (annual mean) (U.S. Environmental Protection Agency, 2012). The standards set by the World Health Organization (WHO) are even more stringent. The WHO air quality guideline recommends the standard to be set at 100 $\mu g\ m^{-3}$ ($\sim$51 ppb) for O_3 (8 hour mean), 40 $\mu g\ m^{-3}$ ($\sim$21 ppb) for NO_2 (annual mean), and 10 $\mu g\ m^{-3}$ for $PM_{2.5}$ (annual mean) (World Health Organisation, 2011). Further, O_3 and PM are relevant for climate discussions due to their radiative forcing properties (Intergovernmental Panel on Climate Change, 2013).

1.1.1 Nitrogen dioxide and its role in O_3 formation

Ozone formation chemistry in the troposphere has been widely studied. The following section is in large part based on two textbooks: Finlayson-Pitts and Pitts Jr (2000) and Seinfeld and Pandis (2006).

The only way to form O_3 in the atmosphere is by the combination of a free oxygen atom (O) and an oxygen molecule (O_2) (reaction R1)

$$O(^3P) + O_2 + M \longrightarrow O_3 + M \tag{R1}$$

Free O atoms are formed in the stratosphere from the photolysis of O_2 molecule (wl $<$ 242 nm). Light of wavelengths below 290 nm is not available in the troposphere due to the absorption by O_3 molecules in the stratosphere. In the troposphere, O atom is produced by NO_2 photolysis (wl $<$ 424 nm) (reaction R2). This O atom then reacts with O_2 molecule to produce O_3. Once

formed, O_3 is rapidly consumed in the subsequent reaction with NO to regenerate NO_2.

$$NO_2 + h\nu \longrightarrow NO + O(^3P) \quad (280 < \lambda < 430nm) \tag{R2}$$

$$NO + O_3 \longrightarrow NO_2 + O_2 \tag{R3}$$

Due to their rapid conversion, NO and NO_2 together are commonly referred to as NO_x and O_3 and NO_2 as O_x. The reactions R1 - R3 represent the null O_x-NO_x cycle which establishes a steady state O_3 concentration which depends upon the $\frac{NO_2}{NO}$ ratio and is given by Eq. 1.1

$$[O_3] = \frac{j_{NO_2}[NO_2]}{k_3[NO]} \tag{1.1}$$

The photostationary state relation given by Eq. 1.1 usually underestimates the O_3 concentration because reaction R3 is not the only mechanism to oxidize NO to NO_2. Additional O_3 formation occurs when volatile organic compounds (VOC) molecules are present.

In summary, when a generic VOC molecule (RH) is oxidized by an OH radical in the HO_x cycle (reactions R4 - R6) to form RO_2, then HO_2 and subsequently regenerate OH, two NO molecules are oxidized to NO_2. The NO_2 molecules then yield O_3 via reaction R1 after undergoing photolysis (reaction R2). Because in the presence of VOCs, NO molecules are oxidized to NO_2 via reactions R5 and R6 rather than through reaction with O_3 (reaction R3), net photochemical O_3 production occurs. Recycling of OH via reaction R6 and further reactions of $R'CHO$ until it is fully converted to CO_2 leads to additional O_3 formation.

$$RH + OH + O_2 \longrightarrow RO_2 + H_2O \tag{R4}$$

$$RO_2 + NO + O_2 \longrightarrow NO_2 + R'CHO + HO_2 \tag{R5}$$

$$HO_2 + NO \longrightarrow NO_2 + OH \tag{R6}$$

Formaldeyde (HCHO) and glyoxal (CHOCHO) are two examples of $R'CHO$ and are measurable by the instruments described as a part of the thesis and their retrieval is presented in Chapter 3.

Formation of nitric acid (HNO_3) by HO_x-NO_x termination reaction (R7) and hydrogen peroxide by HO_x-HO_x termination reaction (R8) effectively quenches the O_3 formation chain reaction as they remove NO_x and HO_x from the cycle.

$$OH + NO_2 + M \longrightarrow HNO_3 + M \tag{R7}$$

$$HO_2 + HO_2 \longrightarrow H_2O_2 + O_2 \tag{R8}$$

Thus, the O_3 formation chemistry is a nonlinear process which depends upon both NO_x and VOC levels as either chain propagation or chain termination reactions are favored. Depending upon the relative abundances of VOC to NO_x, the O_3 formation chemistry can be designated as either (1) NO_x limited, (2) VOC limited or (3) transition state.

Figure 1.1 shows the O_3 production rate as a function of NO_x concentration for different production rates of HO_x (P_{HO_x}). It shows that for a given P_{HO_x}, increasing NO_x concentration gradually increases O_3 production rate (P_{O_3}) initially until it reaches a turnover point beyond which further increase in NO_x results in decrease in P_{O_3}. Thus the region left of the turnover point is called the NO_x limited conditions, where increase in NO_x results in increase in P_{O_3}. The region to the right of the turnover point is known as the NO_x suppressed or VOC limited, where increase in NO_x results in decrease in P_{O_3} and O_3 concentration. The region around the turnover point represent the transition state from NO_x limited to NO_x suppressed conditions and vice versa.

Most of the urban areas in the world, especially the mega cities with large anthropogenic emissions, are in the NO_x suppressed or VOC limited conditions of O_3 formation chemistry as they are the major source regions for NO_x. In consequence, decrease in NO_x emission from vehicles on weekends leads to enhanced O_3 levels on weekends, a phenomenon commonly known as the

"weekend O_3 effect". The weekend O_3 effect in the South Coast Air Basin (SCAB) in California is a common phenomenon and has been widely studied. A chapter of this thesis presents the analysis of the state of the weekend O_3 effect in the SCAB (Chapter 5) while another chapter focuses on production rate of NO_2 and O_x from urban areas (Chapter 4).

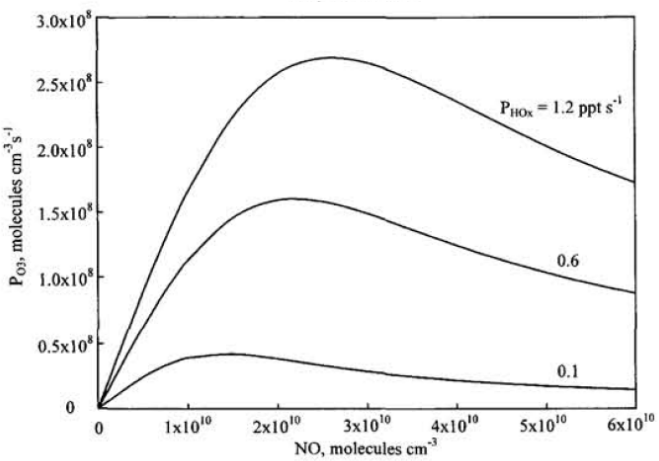

Figure 1.1: O_3 production rate as a function of NO at different HO_x production rates (adopted from Seinfeld and Pandis, 2006).

1.1.2 Sources and Sink of NO_2

Anthropogenic activities involving fossil fuel combustion is the main source of NO_x in the atmosphere. It represents more than 60% of the global source. Table 1.1 list the contribution of various NO_x sources to the global NO_x budget estimate for the year 2000 (Seinfeld and Pandis, 2006). Natural sources of NO_x include biomass burning, emission from soil, and lightning. During lighting, N_2 and O_2 in the atmosphere can decompose and recombine to form NO_2. This is the major source of NO_x in the free troposphere. Natural emission of NO_x from soil is further enhanced by application of nitrogen based fertilizers in the farms. The stratosphere and aircraft are only minor sources of NO_x contributing only about 1% of the global budget individually, but still represent a large fraction in the free troposphere where they are emitted.

Nitric acid (HNO_3) is the main sink for NO_x. During daytime NO_2 reacts directly with OH

radical to form HNO_3 (reaction R7). At night, NO_2 reacts with O_3 to form nitrate radical (NO_3) which then reacts with another NO_2 molecule to form N_2O_5. Reaction of N_2O_5 with H_2O produces HNO_3.

$$NO_2 + O_3 \longrightarrow NO_3 + O_2 \tag{R9}$$

$$NO_2 + NO_3 + M \longrightarrow N_2O_5 + M \tag{R10}$$

$$N_2O_5 + H_2O \longrightarrow 2HNO_3 \tag{R11}$$

Peroxyacetyl nitrate (PAN, $CH_3C(O)O_2NO_2$) is an important temporary reservoir for NO_x. PAN is formed by the reaction between peroxy radical and NO_2 molecule as shown in reaction R12. PAN enables long range transport of NO_x. Thermal decomposition of PAN ultimately releases NO_2 which can then take part in O_3 formation or aerosol formation in the atmosphere.

$$CH_3C(O)O_2 + NO_2 \longrightarrow CH_3C(O)O_2NO_2 \tag{R12}$$

Table 1.1: Estimate of global NO_x tropospheric emissions for the year 2000 (adopted from Seinfeld and Pandis, 2006).

Sources	Emissions, Tg N yr^{-1}
Fossile fuel combustion	33.0
Aircraft	0.7
Biomass burning	7.1
Soils	5.6
NH_3 oxidation	-
Lightning	5.0
Stratosphere	<0.5
Total	51.9

1.1.3 Global Trend in NO_2 and O_3

Global emissions of anthropogenic NO_x has been gradually increasing over time (Granier et al., 2011). Figure 1.2 shows the map of tropospheric vertical column of NO_2 derived from SCIAMACHY satellite borne instrument for the year 2004 (van der A et al., 2008). The NO_2 column can be assumed to be proportional to NO_x emissions as parameters affecting their levels, namely the life time of NO_x and NO_2 to NO_x ratio, can be assumed to be independent of NO_x concentration (Richter et al., 2005). It is clearly evident that the hotspots for NO_2, as expected, are in and around the mega cities in the world with little to no NO_2 over the oceans.

Observations from the space show that NO_2 levels in the United States and Europe, especially the mega cities, have been decreasing at a rate of 5-8% per year for the last decade (Richter et al., 2005; van der A et al., 2008; Russell et al., 2010). This decrease in the NO_2 column is a direct result of efforts to reduce emissions by the use of catalytic converters on automobile exhaust systems, transition to cleaner fuels, changing economic conditions, and stringent regulations such as Clean Air Act in U.S., in place in North America and Europe (Akimoto, 2003; Richter et al., 2005). The role of changing economic circumstances on NO_x emissions is evident in the enhanced reduction in NO_x emissions observed during the most recent economic recession that started in 2008 (Castellanos and Boersma, 2012; Russell et al., 2012). Some cities in Europe saw a one year decrease as large as 30% in 2010 (Castellanos and Boersma, 2012). The decrease in NO_2 due to economic recession in United States was much more modest compared to Europe, but some cities like Los Angeles did see a large reduction ($\sim$15%) (Russell et al., 2012). The effect of this large NO_x emission reduction on weekend O_3 effect in SCAB is presented in Chapter 5.

In contrast, NO_2 columns in the developing countries, especially in fast changing economies like China and India, are rapidly increasing (Richter et al., 2005; van der A et al., 2008). NO_2 levels in China have increased drastically since 2001 ($\sim$12%) (Richter et al., 2005; He et al., 2007) with some cities like Shanghai, China showing increases of up to 29% per year (van der A et al., 2008). The dramatic increase in NO_2 over eastern China is illustrated in Fig. 1.3, which shows

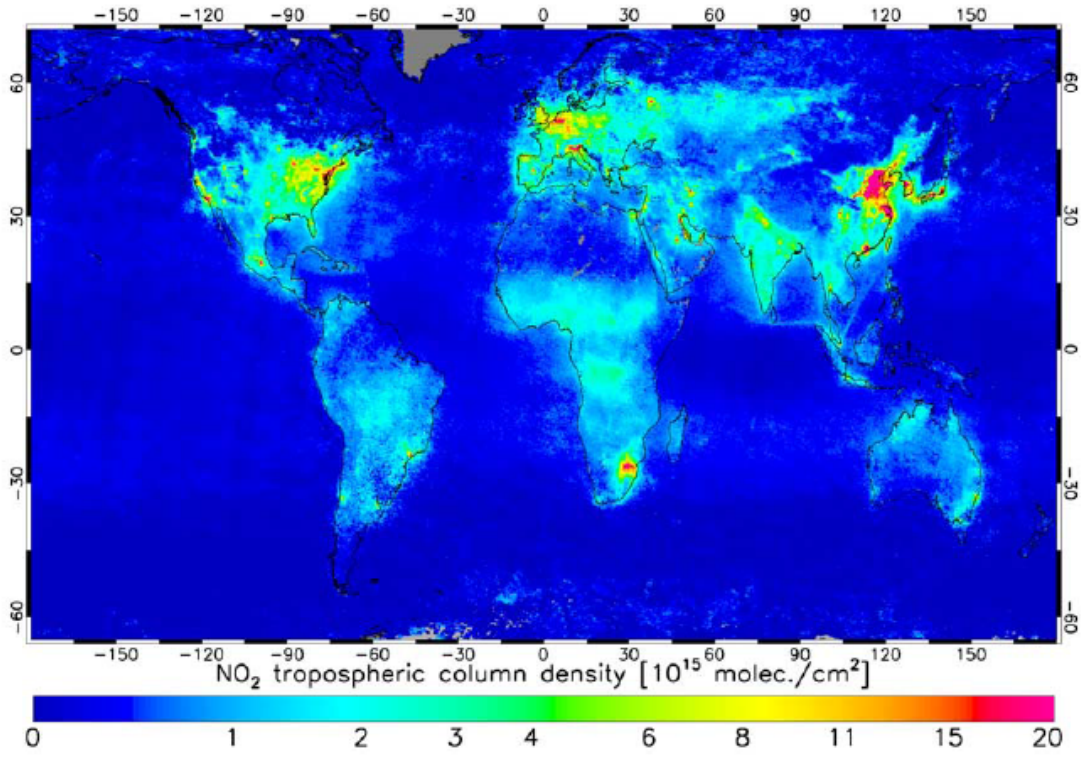

Figure 1.2: Global map of NO_2 vertical column retrieved from the SCIAMCHY observations for the year 2004 (adopted from van der A et al., 2008).

monthly mean NO_2 column observed from the space by SCIAMACHY and GOME instruments. NO_2 columns over major urban areas in India increased by 5-10% per year over the similar time period (van der A et al., 2008; Ghude et al., 2011). Overall NO_x emissions in Asia increased by a factor of 2.8 between 1990 and 2003 (Monks et al., 2009). NO_x emissions in Asia have already surpassed those from Europe and North America and continue to rise (Akimoto, 2003). As a result, reductions in NO_x emissions in Europe and North America are having little impact on the global NO_x trend.

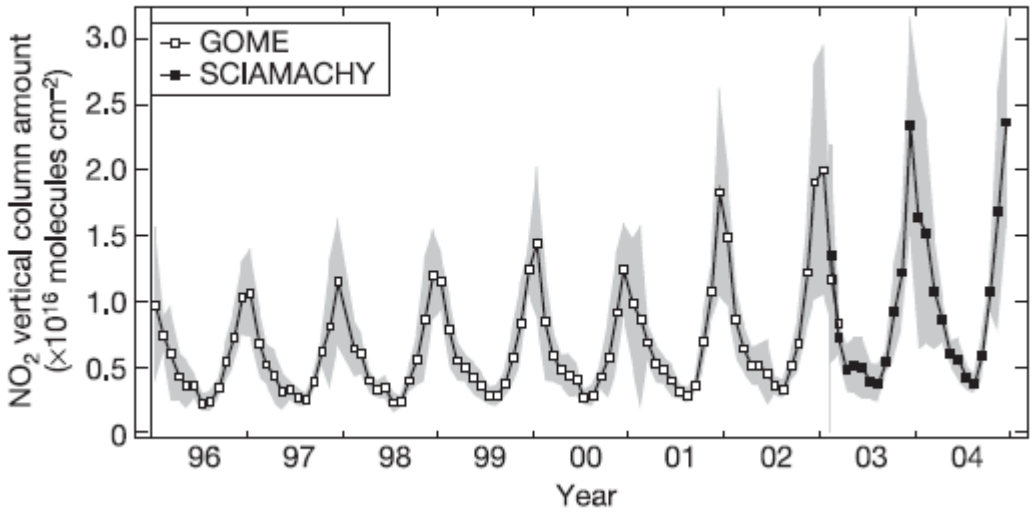

Figure 1.3: Time series of montly mean NO_2 vertical column over eastern China observed from space by the SCIAMACHY and GOME instruments (adopted from Richter et al., 2005).

O_3 levels in the urban areas in the North America and Europe have been decreasing slowly over time as a result of regulations in place to reduce emissions of precursor molecules and is expected to decrease in the future (Parrish and Stockwell, 2015; The Royal Society, 2008). Due to the complex non-linear nature of O_3 formation chemistry, the decrease in O_3 concentrations have not been as large as reductions in precursor emissions. For example, VOC and NO_x emissions in the SCAB have been reduced by a factor of 50 and 4 respectively from 1960 to 2010 but the O_3 has only decreased by factor of 4 in the same period, see Fig. 1.4 (Parrish and Stockwell, 2015; Pollack et al., 2013). Despite this decrease in O_3 levels, most large cities in U.S. still violate the

health based O_3 standard (U.S. Environmental Protection Agency, 2015). O_3 concentrations in developing countries have been going up and is projected to increase in the future as emissions of precursor molecules increase with rapid urbanization and economic development (The Royal Society, 2008). Thus the developing countries all over the world are now facing the same severe O_3 and other air quality issues that the North America and Europe faced 10-50 years ago. However, as North America and Europe continue to reduce emissions in the future, long range transport of pollutants from the developing countries will start to affect the air quality in these nations. Rural sites in both North America and Europe are already showing increasing trend in O_3, see Fig. 1.5 (Parrish et al., 2012a) . The cause for this increase in background O_3 is not fully understood. O_3 is slowly but increasingly becoming a global problem and not just a local air quality issue (The Royal Society, 2008).

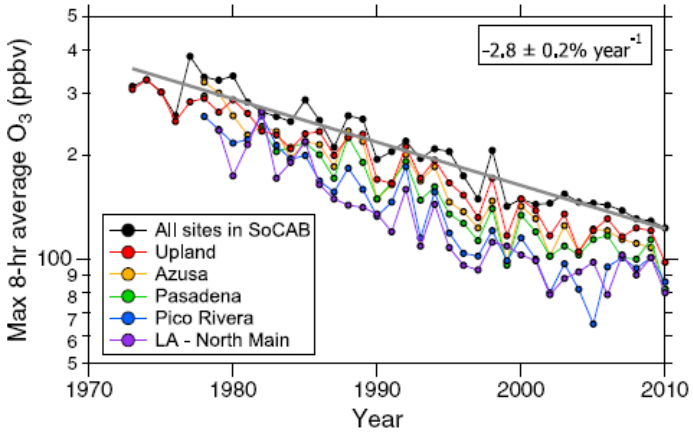

Figure 1.4: Trend in yearly maximum 8 hour average O_3 mixing ratio measured at different surface monitoring stations in the South Coast Air Basin (adopted from Pollack et al., 2013).

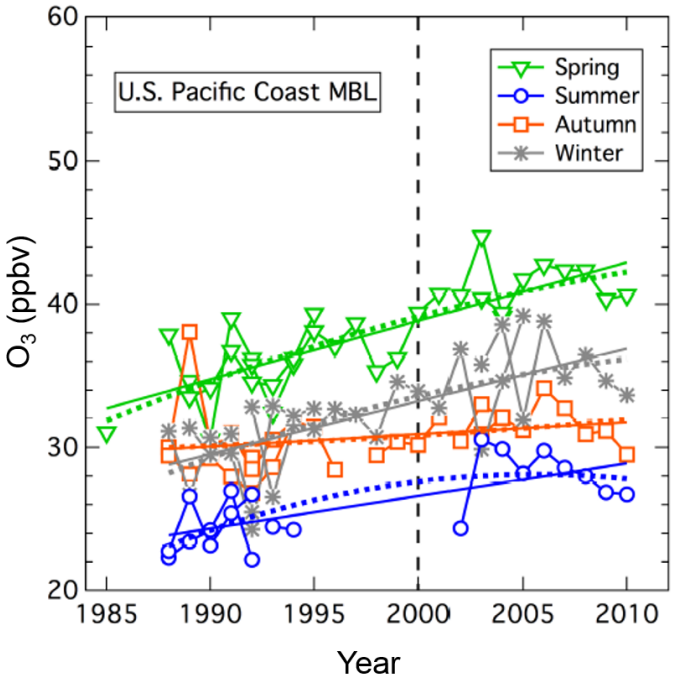

Figure 1.5: Trend in seasonal mean O_3 measured in the U.S. Pacific coast marine boundary layer (adopted from Parrish et al., 2012a).

1.2 Differential Optical Absorption Spectroscopy

Instruments characterized and developed as a part of this thesis use the differential optical absorption spectroscopy (DOAS) method (Platt and Stutz, 2008) for data analysis. In this section a brief overview of the technique is presented.

1.2.1 The Lambert-Beer Law

The attenuation of light with intensity I at a given wavelength λ as it passes through a infinitesimally small parcel of air in the atmosphere with the thickness ds is given by:

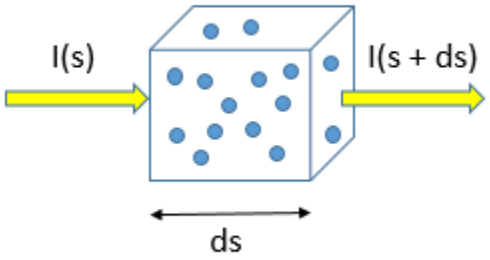

Figure 1.6: Attenuation of light by an infinitesimally small air parcel.

$$dI(\lambda) = -I(\lambda) \cdot \sum_i c_i \sigma_i(\lambda) ds \tag{1.2}$$

where $\sigma_i(\lambda)$ is the absorption cross section and c_i is the concentration of the i^{th} absorber in the air parcel. Absorption cross section is wavelength, pressure and temperature dependent and has a unit of cm^2 molec^{-1}.

Integration of Eq. 1.2 along the light path, L from top of the atmosphere to the observer results in the familiar Lambert Beer Law which describes the relationship between the incident light intensity $I_0(\lambda)$ and the transmitted light intensity $I(\lambda)$ through the absorber layer and is the basis of absorption spectroscopy.

$$I(\lambda) = I_0(\lambda) \cdot exp(-\sum_i \int_0^L c_i \sigma_i(\lambda) ds) \tag{1.3}$$

Rearranging Eq 1.3 to obtain logarithm of the ratio of the transmitted and incident light intensity gives a quantity commonly known as optical density.

$$\tau = ln\left(\frac{I_0(\lambda)}{I(\lambda)}\right) = \sum_i \int_0^L c_i \sigma_i(\lambda) ds \tag{1.4}$$

Eq 1.4 can be further simplified as absorption cross sections σ_i can be considered as independent of temperature and pressure along the light path.

$$\tau = ln\left(\frac{I_0(\lambda)}{I(\lambda)}\right) = \sum_i \sigma_i(\lambda) \cdot \int_0^L c_i ds \tag{1.5}$$

The term inside the integral in Eq. 1.5 can be defined as the integrated column density along the light path and has the units of molecules per unit area. When the light path is not often vertical such as for the instrument developed as part of this thesis, this quantity is referred as slant column density (SCD).

$$SCD_i = \int_0^L c_i ds = \frac{\tau_i(\lambda)}{\sigma_i(\lambda)} \tag{1.6}$$

1.2.2 The DOAS Method

Lambert-Beers law as defined in Eq. 1.5 cannot be used in the atmospheric measurements using scattered sunlight or direct sunlight as the light source since the incident light intensity $I_0(\lambda)$ is not known or not practical to obtain. Additional complications arise due to Rayleigh and Mie scattering by molecules and aerosols in the atmosphere.

The DOAS method which is a modification of Lambert-Beers law enables the retrieval of SCDs from atmospheric measurements using sunlight as the light source. It relies on the observation that Rayleigh and Mie scattering process results in broadband structure, whereas molecular absorptions include highly structured narrow banded features. In order to disentangle molecular absorptions

from scattering processes, the cross section is divided into two components, (i) a continuous feature (σ^b) and (ii) a differential features (σ^0) as shown in Fig. 1.7 and Eq. 1.7.

$$\sigma(\lambda) = \sigma^0(\lambda) + \sigma^b(\lambda) \tag{1.7}$$

The optical density given by Eq. 1.5 can then be split into a differential component and a broad band component. The broad band components, including caused by scattering processes, are accounted for in the DOAS method using a low order polynomial. And since $I_0(\lambda)$ is not available, a spectrum taken by the instrument with the least amount of absorber is used as the reference spectrum $I_{ref}(\lambda)$. Then Eq. 1.5 can be rewritten as:

$$\tau = ln\left(\frac{I_{ref}(\lambda)}{I(\lambda)}\right) = \sum_i \sigma_i'(\lambda) \cdot \Delta SCD_i + \sum_j a_j \lambda^j \tag{1.8}$$

The final retrieved quantity from the above equation is a differential slant column density (dSCD) of an absorber which is the difference of slant column between a measurement and reference spectrum.

1.3 Outline of the Dissertation

This work focuses on the measurements of vertical columns and profiles of NO_2, HCHO, and CHOCHO from two newly developed mobile DOAS instruments for air quality research in an urban environment.

Chapter 2 describes an airborne multi-axis DOAS instrument for measuring column abundances of NO_2, HCHO, CHOCHO, H_2O, and O_4. The instrument was first deployed aboard the NOAA Twin Otter research aircraft in California during the CalNex and CARES field campaigns in summer 2010. A total of 52 flights were performed over a two month period from May 19-July 19, 2010 and covered the entire state of California with particular focus in the SCAB and Sacramento Valley. We demonstrate the capabilities of the new instrument to retrieve vertical columns and profiles of the above mentioned trace gases. During the campaign the NOAA Twin Otter made

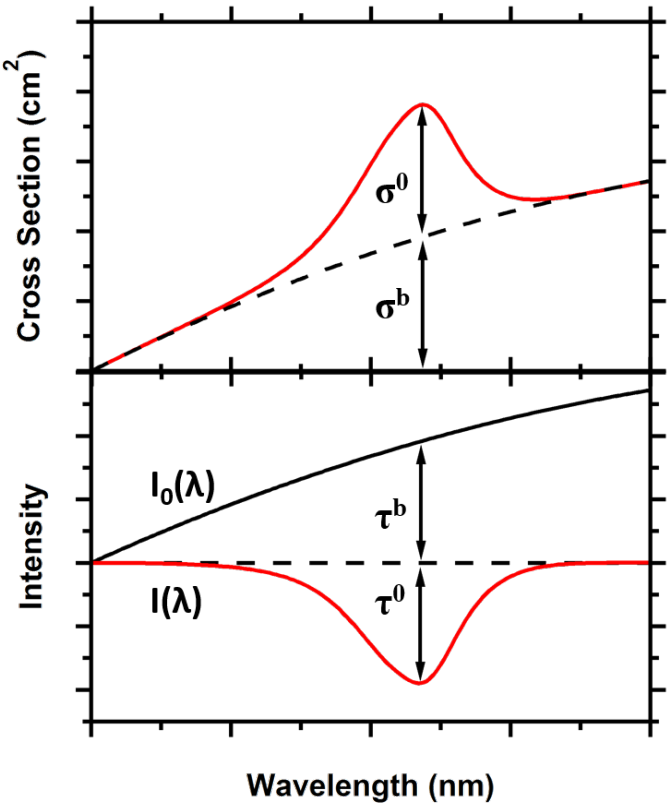

Figure 1.7: Graphical representation of differential cross section and optical depth. The σ^0 represents the differential portion and σ^b shows the broad band portion of the cross section. The bottom panel shows the attenuation of light by the above cross section and corresponding optical depths (adopted from Coburn, 2014).

routine overflights of 3 ground based sites with MAX-DOAS measurements of NO_2. Comparison of column NO_2 from the ground based and airborne instruments showed excellent agreement (within 5%) and good correlation ($R^2 = 0.86$) for a highly inhomogeneous NO_2 field in the urban SCAB.

Chapter 3 presents a method to retrieve vertical columns of HCHO and CHOCHO using spectra collected at various elevations angles (EAs)above and below the plane by the AMAX-DOAS. The signal to noise for HCHO and CHOCHO are relatively low compared to NO_2 and hence information from additional viewing geometries are used to constrain vertical columns for these trace gases. EA scans at flight altitude can be used to retrieve vertical profiles of trace gases. The uncertainty in the retrieved profiles are relatively large but the integrated columns are robust. The retrieval is further constrained by using the vertical profiles of these trace gases measured during low approaches from the same flight as a priori profile. We show example HCHO and CHOCHO columns maps in the SCAB. Comparison of the measured HCHO and CHOCHO vertical columns with atmospheric models using different emission inventories showed that the models under represented both HCHO and CHOCHO especially with the newest California Air Resource Board (CARB) 2010 emission inventory.

Chapter 4 demonstrates the potential of a synergistic use of active and passive atmospheric remote sensing measurements to quantify NO_2 and O_x (O_3 + NO_2) productions from urban areas. During the CalNex and CARES field campaigns NO_2, O_3, and wind profiles were measured aboard the NOAA Twin Otter by the CU AMAX-DOAS, NOAA TOPAZ LIDAR, and NCAS Doppler LIDAR, respectively. To show the potential, we focused our analysis on a case study over Bakersfield, CA on June 15, 2010. The flight plan was aimed at quantifying emissions from the Bakersfield region and included boxes around the city, and upwind and downwind of the city. We used the mass balance approach to quantify NO_2 and O_x productions within each box. As expected highest NO_2 production was observed over the city, but surprisingly the largest O_x production was found upwind of the city over an area with active oil and natural gas activities. The calculated NO_x emissions was compared with the CARB 2010 NO_x emission inventory and found to agree well. Concurrent measurements of all three species in similar time and spatial scale minimized uncertainty in the

calculated production rates.

In chapter 5, we explore the state of the weekend O_3 effect in the SCAB using the measurements aboard the NOAA Twin Otter and the CARB surface monitoring stations. Weekend O_3 effect, where higher O_3 is observed on the weekend compared to weekday due to reduction in NO_x emissions from motor vehicles on the weekend, is a very common phenomenon observed in the SCAB and most major urban areas in the world. To put the observation of a normal weekend or reverse weekend O_3 effect during a hot weekend in July 2010 in perspective with the usual weekend O_3 effect, we examined the trend in probability of weekend O_3 effect occurrence in the SCAB. Results showed a recent trend in the weakening of the weekend O_3 effect. This was more prevalent in the eastern part of the basin which suggests shrinking of the area affected by the weekend O_3 effect. The decreasing probability also indicates that increasingly more weekends are transitioning to NO_x limited O_3 formation conditions in the SCAB.

Chapter 6 shows the confirmation of sand signature spectrum used by satellite-borne instruments in order to improve retrieval of NO_2 vertical columns. Based on the relative decrease in sand signal observed from nadir to forward and zenith viewing geometry of the AMAX-DOAS measurements and radiative transfer calculations, we show that the sand signal is a surface property and originates as a result of reflection from the surface. In addition, the sand fit coefficient from Ozone Monitoring Instrument (OMI) was found to be strongly correlated with independent surface albedo measurements aboard the NOAA Twin Otter. The correlation was fairly weak with the sand fit coefficient from the AMAX-DOAS nadir viewing geometry and is likely due to the difference in spatial scale probed by the two sensors. We also show that the sand reference cross section is not necessary for DOAS analysis of trace gases from the AMAX-DOAS measurements. However inclusion of the sand reference cross section do not affect retrieval of trace gases, especially O_4 which has the peak at the same wavelength as the sand reference spectrum.

Chapter 7 presents the development of a mobile solar tracker for direct sun DOAS observations of trace gases such as NO_2, HCHO, and CHOCHO in the UV-visible spectra and alkanes, CH_4, and NH_3 in the infrared region simultaneously. Simultaneous measurements of column hy-

drocarbons and nitrogen oxides in the similar spatial and temporal scale hold a unique potential to understand/quantify O_3 formation using the method presented in Chapter 4. The new alt-azimuthal tracker couples existing motion compensation system from the AMAX-DOAS instrument described in Chapter 2 with an imaging feedback loop for high precision autonomous solar tracking from a mobile laboratory. The tracker was first deployed during the FRAPPE 2014 field campaign in Colorado. The tracker is capable of tracking the sun with an angular precision of 0.052° while in motion. This tracking precision is verified by retrieval of center-to-limb darkening (CLD) correction from spectral data. NO_2 vertical columns are presented to demonstrate the feasibility of measuring atmospheric trace gases using the tracker as the telescope. Comparison of NO_2 vertical columns with a co-located MAX-DOAS showed overall an excellent agreement amid a highly heterogeneous conditions.

Chapter 2

The CU Airborne MAX-DOAS Instrument: Vertical Profiling of Aerosol Extinction and Trace Gases

This chapter was published as : Baidar, S., Oetjen, H., Coburn, S., Dix, B., Ortega, I., Sinreich, R., and Volkamer, R.: The CU Airborne MAX-DOAS instrument: vertical profiling of aerosol extinction and trace gases, Atmos. Meas. Tech., 6, 719-739, doi:10.5194/amt-6-719-2013, 2013.

The University of Colorado Airborne Multi Axis Differential Optical Absorption Spectroscopy (CU AMAX-DOAS) instrument uses solar stray light to detect and quantify multiple trace gases, including nitrogen dioxide (NO_2), glyoxal (CHOCHO), formaldehyde (HCHO), water vapor (H_2O), nitrous acid (HONO), iodine monoxide (IO), bromine monoxide (BrO), and O_2-O_2 collision complexes (O_4) at multiple wavelengths (absorption bands at 360 nm, 477 nm, 577 nm, 632 nm) simultaneously, in the open atmosphere. The instrument is unique, as it (1) features a motion compensation system that decouples the telescope field of view from aircraft movements in real-time ($< 0.35^\circ$ accuracy), and (2) includes measurements of solar stray light photons from nadir, zenith, and multiple elevation angles forward and below the plane by the same spectrometer/detector system. Sets of solar stray light spectra collected from nadir to zenith scans provide some vertical profile information within 2 km above and below the aircraft altitude, and the vertical column density (VCD) below the aircraft is measured in nadir view. Maximum information about vertical profiles is derived simultaneously for trace gas concentrations and aerosol extinction coefficients over similar spatial scales and with a vertical resolution of typically 250 m during aircraft ascent/descent.

The instrument is described, and data from flights over California during the CalNex and

CARES air quality field campaigns is presented. Horizontal distributions of NO_2 VCDs (below the aircraft) maps are sampled with typically 1 km resolution, and show good agreement with two ground based MAX-DOAS instruments (slope = 0.95 ± 0.09, R^2 = 0.86). As a case study vertical profiles of NO_2, CHOCHO, HCHO, and H_2O concentrations and aerosol extinction coefficients, ε at 477 nm calculated from O_4 measurements from a low approach at Brackett airfield inside the South Coast Air Basin (SCAB) is presented. These profiles contain ∼12 degrees of freedom (DOF) over a 3.5 km altitude range, an independent information approximately every 250 m. The boundary layer NO_2 concentration, and the integral aerosol extinction over height i.e. aerosol optical depth (AOD) agrees well with nearby ground-based in-situ NO_2 measurement, and AERONET station. The detection limits of NO_2, CHOCHO, HCHO, H_2O_{442}, ε_{360}, ε_{477} for 30 seconds integration time spectra recorded forward of the plane are 5 ppt, 3 ppt, 100 ppt, 42 ppm, 0.004 km^{-1}, 0.002 km^{-1} in the free troposphere (FT), and 30 ppt, 16 ppt, 540 ppt, 252 ppm, 0.012 km^{-1}, 0.006 km^{-1} inside the boundary layer (BL), respectively. Mobile column observations of trace gases and aerosols are complimentary to in-situ observations, and help bridge the spatial scales probed by ground-based observations, satellites, and predicted by atmospheric models.

2.1 Introduction

Airborne Differential Optical Absorption Spectroscopy (DOAS) measurements of different trace gases in the atmosphere by solar stray light started in late 1980s and has come a long way since then. Early studies were focused on obtaining column integrals of stratospheric trace gases like nitrogen dioxide, NO_2 (Wahner et al., 1990a), chlorine dioxide, OClO (Schiller et al., 1990), and bromine oxide, BrO (Wahner et al., 1990b) from zenith measurements. First retrievals of trace gas concentrations close to the aircraft altitude were reported by Petritoli et al. (2002) for stratospheric ozone, O_3. These studies were followed by the application of the Airborne Multi-Axis DOAS (AMAX-DOAS) technique to obtain tropospheric columns for NO_2 (Melamed et al., 2003; Heue et al., 2005; Wang et al., 2005) and sulfur dioxide, SO_2 (Wang et al., 2006; Melamed et al., 2008) over polluted regions. These instruments used multiple telescopes, most notably zenith and

nadir to collect scattered sunlight. Over the past few years, building on the well-established limb observation technique (e.g., McElroy, 1988; Weidner et al., 2005, and references within), the focus has shifted towards retrievals of vertical distribution of trace gases from the aircraft using several limb viewing telescopes. Figure 2.1 shows the conceptual viewing geometry of the so-called AMAX-DOAS technique. Individual elevation angles (EAs) contain different amounts of information from different layers in the atmosphere and hence can be used to infer vertical distributions of trace gases. Bruns et al. (2006) first reported profiles of NO_2 over the Po valley from an airborne MAX-DOAS instrument with four telescopes, pointing at fixed EAs. A boundary layer NO_2 profile was obtained by Dix et al. (2009) using multiple lines of sight (LOS) and a descent of an aircraft. Prados-Roman et al. (2011) used the LOS parallel to the plane and the aircraft descent to retrieve vertical profiles of bromine oxide, BrO in the Arctic. Most recently, a limb scanning airborne DOAS instrument was developed at Belgium Institute for Space Aeronomy (BIRA) to obtain vertical distribution of trace gases like NO_2 (Merlaud et al., 2011). Most airborne DOAS instruments use either a single or multiple fixed LOS and use a spectrum collected from the same EA as the reference spectrum for DOAS analysis. However these instruments lack active control of the viewing geometry of the telescope during the flight. Pitch and roll information from the aircraft is used during post-processing to calculate the true viewing angle at the time of measurement during the flight. This often leads to a range of EAs assigned to measurements and results in a loss of sensitivity to a given layer in the atmosphere compared to when the elevation angle is actively controlled, to retrieve vertical profile information of trace gases. Active control of EA along with careful selection of EA also allows for maximization of the degrees of freedom (DOF).

Here we describe CU AMAX-DOAS instrument, a new and improved AMAX-DOAS instrument with capabilities to motion stabilize and collect spectra from multiple axes using a single telescope. The CU AMAX-DOAS instrument has the capability to access zenith, nadir and limb viewing geometry by means of a single, rotatable prism telescope which is coupled to a motion compensation system. The motion compensation system includes angle sensors to measure pitch and roll angles of the aircraft and a feedback loop to correct the telescope position for pitch and roll

angles in real-time. This ensures a constant desired EA is maintained during spectra acquisition in flight. Isolation of the telescope from the aircraft movements enables us to systematically probe the atmosphere with desired sets of EAs to retrieve vertical profiles of trace gases and aerosol extinction simultaneously, and with the highest possible information content. The use of a single telescope to collect spectra from zenith, and other EAs (nadir, and forward of the plane) further enables the zenith spectra to be used as the Fraunhofer reference spectrum in the DOAS analysis. Zenith spectra usually contain the least amount of tropospheric absorbers, and the ability to record zenith spectra close in time to other EA spectra assures that absorbers above the plane are characterized with minimum difference in radiation fields, and makes the instrument inherently more sensitive to absorbers near and below the aircraft altitude (Volkamer et al., 2009a).

The CU AMAX-DOAS instrument was successfully deployed from 19 May-19 July, 2010 as part of two air quality studies in California, namely the California Research at the Nexus of Air Quality and Climate Change (CalNex) (see overview paper by Ryerson et al., 2013) and the Carbonaceous Aerosols and Radiative Effects Study (CARES) (see overview paper by Zaveri et al., 2012). A total of 52 research flights were performed during this deployment and here we focus on results from one flight on 16 July, 2010 to describe the technique, and characterize instrument performance. In section 2.2 the CU AMAX-DOAS instrument is described, and the instrument configuration is introduced. Section 2.3 describes the DOAS analysis procedures, radiative transfer model (RTM) calculations, and algorithms to retrieve vertical column densities (VCD) and vertical profiles of the trace gas concentrations and aerosol extinction. Section 2.4 demonstrates the capability of the new instrument. As a case study, vertical profiles of NO_2, CHOCHO, HCHO, H_2O and aerosol extinction at 477 nm are retrieved from a low approach at Brackett airfield in the South Coast Air Basin (SCAB). Finally, as a validation, CU AMAX-DOAS NO_2 VCDs are compared with VCDs measured by two ground based MAX-DOAS instruments that were regularly over-passed during flights; the boundary layer NO_2 concentration retrieved from the vertical profile is compared to a ground-based in-situ sensor concentration, and the integral aerosol extinction over height i.e. AOD is compared with data from an AERONET station.

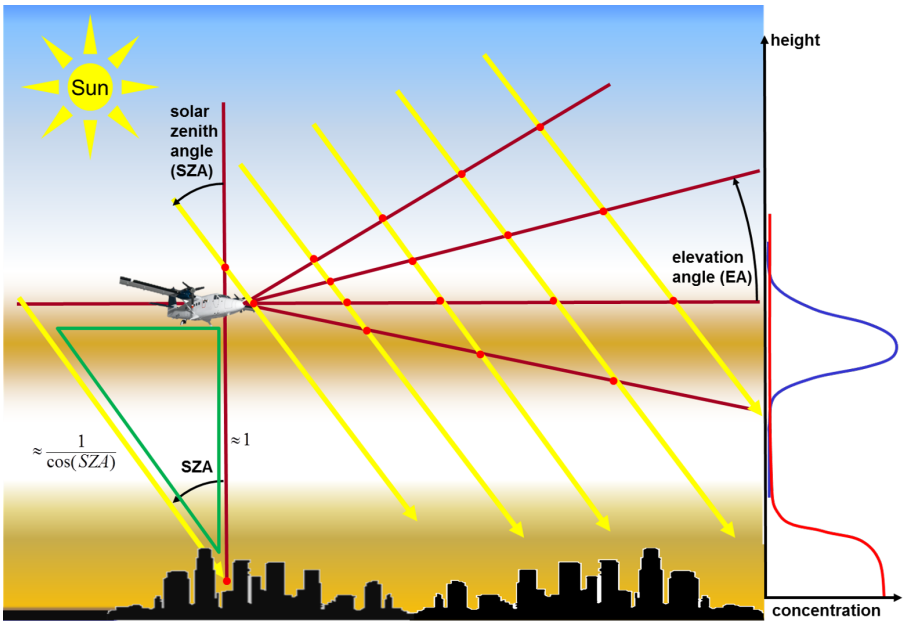

Figure 2.1: Schematic of the AMAX-DOAS measurement principle. Individual elevation angles (EA) contain different amounts of information from different layers in the atmosphere. The inset (green triangle) illustrates the geometric approximation used to convert nadir dSCDs to VCDs.

2.2 The CU AMAX-DOAS Instrument

The CU-AMAX-DOAS instrument collects spectra of scattered sunlight between 330 and 720 nm at different EAs. The scattered sunlight spectra are analyzed for the presence of absorbers like NO_2, CHOCHO, HCHO, H_2O, HONO, IO, BrO, O_4 using the DOAS method (Platt and Stutz, 2008). NO_2, CHOCHO, HCHO, H_2O and O_4 data will exemplarily be presented in this paper. The instrument consists of a telescope pylon mounted outside of a window plate on a NOAA Twin Otter Remote Sensing research aircraft. The collected photons are transferred via optical fibers to two synchronized spectrometer-detector systems that are housed inside the aircraft fuselage. An optical fiber switch box is placed in between the light sources (telescopes and Hg calibration lamp) and the spectrometer-detector systems to select between different light sources at a given time. The Hg calibration lamp is used to characterize the optical resolution of the spectrometer-detector system. The instrumental setup is shown in Fig. 2.2.

2.2.1 Telescope System

The telescope is designed for high light throughput and a very narrow vertical field of view (FOV), 0.3° x 5.89°. It comprises a $\frac{1}{2}''$ rotating prism, a $\frac{1}{2}''$ lens tube with a $\frac{1}{2}''$ f/4 lens and a stepper motor. All the telescope components are housed in a telescope pylon, an aluminum housing with quartz windows, which is mounted outside of a window plate on a NOAA Twin Otter research aircraft. The rotating prism is installed with 0° EA parallel to the aircraft heading and is driven by a stepper motor with an internal encoder to rotate vertically. The prism is capable of making a complete 360° rotation and hence allows characterization of the air masses above, below and in front of the aircraft using the same telescope. Viewing directions behind the aircraft are not accessible due to the structural design of the pylon including the placement of viewing ports. An additional telescope with a fixed EA is therefore present in the pylon to reach some of the inaccessible viewing geometries of the rotating prism. This telescope was rarely used during the CalNex and CARES campaign and data from this telescope is not presented in this paper. The viewing ports on the

pylon are heated to prevent formation of ice at higher altitudes. The pylon also includes two webcams; a downward and a forward looking one, to capture atmospheric conditions during the flight and filter for clouds during post processing of data. The light collected by the rotatable prism is focused via a lens tube onto a 12 m long fiber bundle consisting of 72 x 145 μm fibers. The fiber bundle is configured into two rows of 36 fibers at the telescope end and a circular arrangement at the other. The ends of the fibers away from the telescope are connected to a custom-made optical fiber switch box.

2.2.2 Optical Fiber Switch Box

The optical fiber switch box is used to select between different incoming light sources. It consists of a translational stage mounted to a stepper motor linear actuator. The fibers from the telescopes and Hg calibration lamp are connected to one end of the box. Hg spectra were taken before, after and at regular intervals during flights to check the stability of the spectrographs optical resolution. A 10 m long 1.7 mm diameter silica mono-fiber, which is used as a mixing fiber to minimize polarization effects, is mounted on the translational stage opposite the incoming fibers from the light sources. The motor of the linear actuator drives the platform to place the mono-fiber directly in front of the desired fiber with the incoming light at a given time. The other end of the mono-fiber is connected to a bifurcated fiber bundle (72 x 145 μm) to deliver light to two spectrometers simultaneously. The bifurcated ends are aligned in a single row of 36 fibers to connect to the spectrograph entrance slit.

2.2.3 Spectrometer and Detector System

Two spectrometers and their respective detectors are housed in a standard 19″ aluminum instrument rack (19″ x 22″ x 10.5 ″) with modifications to the bottom and top plates for added stability. The spectrometers are Princeton Instrument Acton SP2150 Imaging Czerny-Turner spectrometers with PIXIS 400 back illuminated charge coupled devices (CCD) detectors. The first spectrometer (later referred to as the O_4 spectrometer) is equipped with a 500 grooves/mm grat-

ing, blazed at 330 nm. It covers 350-720 nm and is used to measure all four major O_4 absorption bands at 360, 477, 577 and 630 nm. The second spectrometer (later referred to as trace gas (TG) spectrometer) covers a wavelength range from 330-470 nm with a custom 1000 grooves/mm (250 nm blaze wavelength) grating. It is used to measure all other trace gases. The optical resolution of the O_4 and TG spectrometers were ∼2.2 nm (∼7.7 pixels) and ∼0.7 nm (∼6.7 pixels), respectively, inferred from the full-width at half-maximum (FWHM) of a representative Hg line. The CCDs are cooled to -30 °C to reduce dark current. The temperatures of the spectrometers are actively controlled with heaters while the instrument rack box temperature is actively cooled using peltier cooling units assuring a constant temperature over a range of varying ambient temperatures. Please refer to Coburn et al. (2011) for additional information on temperature stability, data acquisition and electronic and dark current correction for a comparable instrument. To suppress spectrometer stray light from longer wavelength (above 470 nm) and to gain maximum intensities in our regions of interest, i.e. between 330-470 nm, in the TG spectrometer, two filters, a BG3 and a BG38, were placed immediately after the shutter.

2.2.4 Motion Compensation System

The motion compensation system is used to correct the viewing geometry of the telescope for the aircraft pitch and roll effects during the flight. It consists of a PC104 computer connected to the prism motor and two angle sensors, a Systron Donner Inertial MMQ-G, and an electronic inclinometer. The MMQ-G is a small robust Global Positioning System (GPS) based Inertial Navigation System (INS). It provides accurate 3-dimensional position, time, velocity, and attitude. It is primarily used to measure the pitch and roll angles of the aircraft for our application and has an angle accuracy of 5 mrad (∼0.29°). The information from the sensor is processed by custom LabVIEW software into the coordinate system along the horizon. It is then used to drive the stepper motor of the prism to a new position such that it corrects for the aircrafts movement and keeps the telescope at the desired EA. The software has capability for 100 Hz loop rate, and was typically operated at 10 Hz. The stepper motor has a precision of 0.01° but is limited by the resolution of the

internal encoder (0.2°) to precisely read back the position of the motor. The MMQ-G, inclinometer and the telescope prism are mounted on planes parallel to the ground such that the elevation angle of the telescope and the pitch of the aircraft read zero simultaneously. The inclinometer is used as a backup during flights for situations when the GPS signal required for the MMQ-G is lost. The theoretical angle accuracy of the motion compensation system is 0.35° considering the MMQ-G accuracy of ∼0.29° (1σ) and motor internal encoder resolution of 0.2°. The system is configured to reset the motor when it does not reach a given position within a desired tolerance level by a fixed time interval. The same motion compensation system has also been integrated as part of another telescope pylon designed for adaptation of the CU AMAX-DOAS instrument aboard the NSF/NCAR GV HIAPER aircraft.

2.2.5 Performance of the Motion Compensation System

Figure 2.3 shows the performance of the system during research flights aboard the GV HIAPER and Twin Otter aircrafts. GV HIAPER flights provide an excellent opportunity to test the system as the aircraft pitch and roll angles measured by the aircraft avionics system during the flight are recorded, while avionics data for the Twin Otter flights are not available. The histogram of differences in aircraft pitch angle recorded at 1 Hz frequency measured by NSF/NCAR GV HIAPER aircraft avionics and our MMQ-G recording during a research flight (∼8 hours) on 24 February 2012 is plotted as a probability density function in Fig. 2.3a. A Gaussian fit (black line) to the histogram has a 1σ deviation of 0.15° which is less than the 1σ accuracy (0.3°, yellow line in Fig. 2.3a) of the MMQ-G pitch measurement. Some of the difference could also be due the wing flex. Note that AMAX-DOAS is mounted on the wing of the HIAPER aircraft. This shows that the MMQ-G measures the aircraft pitch and roll angles with sufficient accuracy, which are then being used for real-time pointing corrections. Figure 2.3b shows the difference in desired elevation angle and the real-time elevation angle read back from the motor internal encoder as a probability density for the same flight. The 1σ of the Gaussian fit to the histogram (0.12°) is smaller than the resolution of the motor internal encoder confirming that the telescope position was corrected

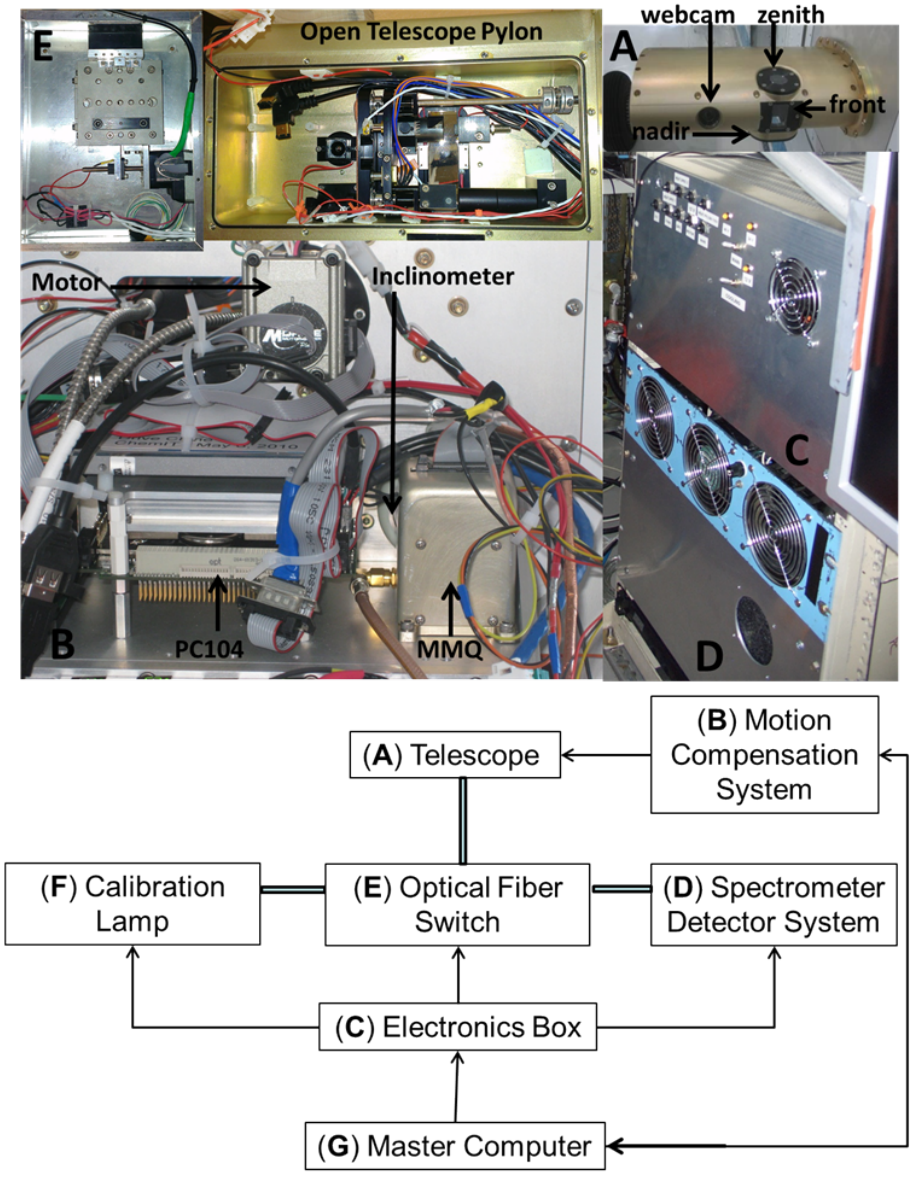

Figure 2.2: CU AMAX-DOAS instrument setup aboard the NOAA Twin Otter during the CalNex and CARES campaigns.

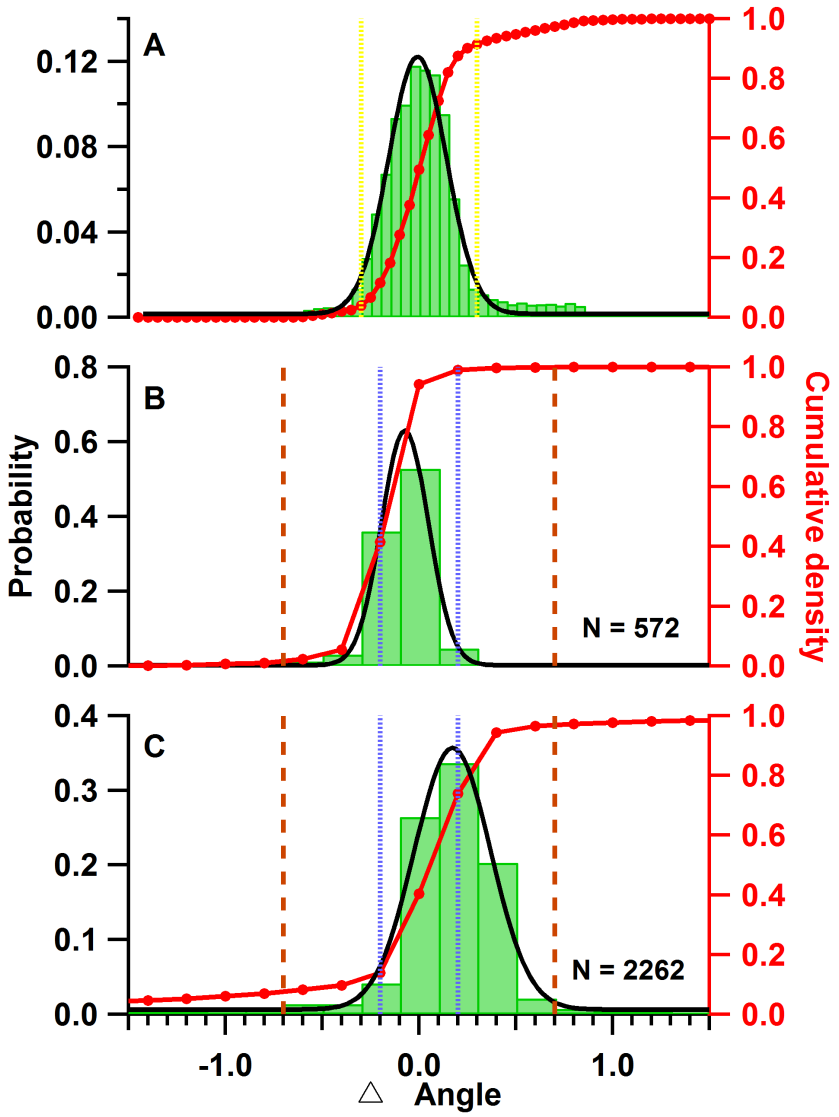

Figure 2.3: (A) Distribution of difference in pitch angle of the aircraft measured at real time by the MMQ-G angle sensor of the CU-AMAX-DOAS and aircraft avionics system of the NSF/NCAR GV HIAPER aircraft during a research flight on 24 February, 2012. 1 σ angle accuracy (0.29°) of the MMQ-G sensor is shown in yellow dotted lines. 1σ for the Gaussian fit (black line) is 0.15°. Distribution of elevation angle accuracy of the CU AMAX-DOAS telescope (B) from the above mentioned flight on the NSF/NCAR GV HIAPER flight, (C) during RF#46 aboard the NOAA Twin Otter on 16 July, 2010. 1σ for the Gaussian fits (black lines) are 0.12° and 0.2° for instrument aboard the HIAPER and Twin Otter aircraft, respectively, and are within the resolution of the motor internal encoder (0.2°), shown in blue dotted lines. Brown dashed lines represent the motor tolerance level (0.7°) set in the software before an automatic reset of the motor position takes place. The red lines represent the cumulative densities.

for the aircraft movements within our ability to read back the motor position. The width of the histograms (Fig. 2.3b and 2.3c) is chosen based on the resolution of the motor internal encoder, i.e. 0.2°.

A similar plot from a research flight (∼4 hours) on 16 July, 2010 aboard the NOAA Twin Otter is shown in Fig. 2.3c and the 1σ of the Gaussian fit is 0.2°. This slightly larger distribution is within the resolution of the motor internal encoder. The fact that the 1σ for both platforms is less than or equal to the ability with which we can accurately read the position of the motor demonstrates that this motion compensation is suitable for a wide range of moving platforms. Since the precision of the stepper motor is 0.01°, an order of magnitude better than resolution of the motor internal encoder, it is very likely that the difference between the real-time and desired EA is smaller than what is being read back from the internal encoder and the overall angle accuracy (1σ) of the motion compensation system is better than 0.35°. The offset of 0.17° for the Gaussian fit in Fig. 2.3c is probably due to some remaining misalignment between the angle sensor and the motor but is smaller than the accuracy of the angle sensor.

The tolerance level (brown dashed lines in Figs. 2.3b and c) above which the motor performs an automatic reset was set to 0.7° (2σ theoretical accuracy) for the campaigns described here. The statistical distribution of the elevation angle difference indicates that the desired position of the motor was achieved after the reset.

2.2.6 Field Deployment and Operation during CalNex and CARES

The CU AMAX-DOAS instrument was deployed aboard the NOAA Twin Otter remote sensing research aircraft during the CalNex and CARES field campaign from 19 May-19 July, 2010 in California after test flights in 2008 and 2009. The pylon was modified significantly after 2009. The aircraft is an unpressurized twin engine turboprop with an altitude ceiling of ∼4 km above sea level (without supplemental cabin oxygen). It has a normal cruising speed of ∼65 ms^{-1} and ascent rate of ∼10 ms^{-1} making it particularly suitable for surveying vertical and horizontal distributions of trace gases in a polluted urban environment. During CalNex, the NOAA Twin

Otter aircraft was stationed at Ontario, CA, and joined the CARES campaign from 16-29 June, 2010 at Sacramento, CA. The plane was equipped with a suite of remote sensing instruments: the University of Colorado deployed (1) CU AMAX-DOAS instrument, (2) two 4-channel radiometers (zenith and nadir viewing) to measure surface albedo (SA); further, NOAA/ESRL/CSD deployed (3) a nadir-pointing Tunable Ozone Profiler for Aerosol and oZone (TOPAZ) lidar (Alvarez II et al., 2011), which measures vertical distribution of ozone (O_3), and (4) the National Center for Atmospheric Science (NCAS) Doppler lidar (Pearson et al., 2009), which measures radial derived 3-dimensional wind fields, as well as (5) a nadir pointing infrared pyrometer, and (6) an in-situ O_3 monitor.

The purpose of the CU AMAX-DOAS deployment was to measure horizontal and vertical distributions of NO_2, HCHO, CHOHO and aerosol extinction over California, particularly over the SCAB, characterize boundary conditions for comparison with atmospheric models, and probe for pollutant concentrations above the boundary layer. NO_2, HCHO and CHOCHO play important roles in atmospheric chemistry and strongly influence air quality. NO_2 is a precursor molecule for tropospheric O_3 formation. Oxidation of nitrogen oxides (NO_x = NO + NO_2) in the atmosphere results in formation of nitric acid and aerosol nitrates causing acid deposition and visibility degradation. HCHO is the most abundant volatile organic compound (VOC) and produces HO_x radicals upon photolysis, a major oxidizer in the atmosphere, which sustains photochemical production of O_3 and secondary organic aerosols (SOA) (Griffin et al., 2004; Volkamer et al., 2010). CHOCHO also forms HO_x radicals upon photolysis and is a direct precursor for SOA. Studies conducted in Mexico City have suggested that CHOCHO could be responsible for 10- 15% of SOA formation in Mexico City (Volkamer et al., 2007). Aerosols directly affect human health and have been linked to increase in morbidity and mortality (Pope et al., 2009). A total of 52 research flights, each lasting up to ∼4 hours, were carried out over the two months period (206 flight hours). Flight plans were developed with the scientific objectives of mapping out horizontal and vertical distribution as well as characterizing transport of pollutants and validation of satellite retrievals. As this was the first deployment of this specific instrument pylon, different integration times and EA sequences were

explored as well as the LabVIEW acquisition software was updated during the early portion of the campaign for optimization. Spectra were collected with 2 seconds integration time during the second half of the campaign and all the data presented in this paper are 2 seconds data unless otherwise noted. The most commonly used EA sequence included EAs 90° (zenith), 20°, 10°, 5°, 2°, 0°, -2°, -5°, -10°, -20° and -90° (nadir) with 0° corresponding to a view parallel to the horizon. The FOV of the telescope at nadir viewing geometry gives a footprint of ∼0.55 km while flying at 4 km altitude. Typically, nadir spectra were recorded every 12-15 seconds, corresponding to a horizontal resolution of ∼1 km.

Table 2.1: List of trace gas references used for DOAS analysis.

No.	Molecule	References
1	NO_2 (220 K)	Vandaele et al. (1998)
2	NO_2 (294 K)	Vandaele et al. (1998)
3	O_3 (223 K)	Bogumil et al. (2003)
4	O_3 (243 K)	Bogumil et al. (2003)
5	O_4 (298 K)	Hermans (2002)
6	CHOCHO (298 K)	Volkamer et al. (2005)
7	HCHO (298 K)	Meller and Moortgat (2000)
8	H_2O	Rothman et al. (2005)
9	O_4	Greenblatt et al. (1990)

2.3 Data Analysis

2.3.1 DOAS Analysis

The measured spectra were analyzed for NO_2, CHOCHO, HCHO, H_2O and O_4 using the DOAS method (Platt and Stutz, 2008) that is implemented in the WinDOAS software (Fayt and Van Roozendael, 2001). In DOAS, measured spectra are analyzed against a Fraunhofer reference spectrum, and absorption cross-sections of different absorbers in the atmosphere are fitted simultaneously in a selected wavelength interval applying a non-linear least-square fitting routine. A low order polynomial to account for scattering processes and broadband absorption in the atmosphere as well as broadband instrumental features, a Ring reference spectrum to account for the filling in of

Fraunhofer lines due to rotational Raman scattering (Grainger and Ring, 1962) , and an additional intensity offset to account for instrumental stray light were also included in the fitting procedure. The Ring spectrum is calculated from the Fraunhofer reference (Bussemer, 1993). The Twin Otter aircraft being an unpressurized aircraft, the pressure in the cabin changed from 1010-665 mbar over a 3.5 km altitude range for typical flights (e.g., see Fig. 2.7). The change in the refractive index, as well as any pressure differentials that could give rise to a wavelength shift equally affect the Fraunhofer lines, and Earth atmospheric absorbers, and are accounted for by including a linear shift of the measurement spectrum during analysis. The observed shifts are up to 0.18 nm for the TG spectrometer between the spectra taken at the highest and the lowest altitude. A high altitude ($\sim$4 km) zenith spectrum from a clean, cloud free region of the same flight was included for the analysis of the individual flight data. The choice of the zenith spectrum as the Fraunhofer reference spectrum minimizes the amount of tropospheric absorbers in the reference spectrum, allowing for the detection of trace gases more sensitively. Since measured spectra are analyzed with respect to a reference spectrum, the quantity retrieved from the DOAS analysis is a differential slant column density (dSCD), which is the integrated difference in concentration of the absorber along the light path length with respect to the reference. The trace gas absorption cross sections and other analysis settings for the retrievals of the different trace gases are listed in Table 2.1 and 2.2, respectively. Examples for spectral fits of NO_2, CHOCHO, HCHO, O_4, and H_2O from the data measured during the CalNex and CARES campaign are shown in Fig. 2.4. Detection limit for CU AMAX-DOAS instrument in clean free troposphere (FT) and polluted urban boundary layer (BL) such as the SCAB for 30 and 2 seconds integration time is listed in Table 2.3. It is roughly equivalent to the 3σ DOAS fit error for typical clean FT (near Rayleigh atmosphere) and polluted urban BL atmospheric conditions (see Fig. 2.10b for aerosol extinction profile). Note that detection limit highly depends upon the atmospheric conditions during the time of measurement.

We included 2 Ring spectra (Bussemer, 1993), calculated for two different temperatures (298 and 230 K), in HCHO retrieval to account for the temperature dependence of rotational Raman scattering, which leads to the so-called filling-in of the Fraunhofer lines (Ring effect). The inclusion

of a second Ring cross section in the HCHO retrieval (1) improved the HCHO fit, (2) minimized fitting residuals and (3) reduced scatter in the retrieved HCHO slant columns. A second Ring cross-section was not needed to achieve comparable results for other trace gases, where the Ring structures are relatively smaller. New HCHO reference cross-section has recently been reported by Chance and Orphal (2011). We compared the dSCD retrieved with new cross-section to the one from Meller and Moortgat (2000) (used in this work) and found the mean difference of 6.0 x 10^{14} molecules cm^{-2}, which is well below the DOAS fit error for our retrieval. For a mean HCHO dSCD of 3.0 x 10^{16} molecules cm^{-2} for 0° EA at all flight altitudes for the exemplary flight presented here, the difference is only 2%.

We used O_4 cross-section by Greenblatt et al. (1990) for NO_2 and CHOCHO retrievals. O_4 cross-section by Hermans (2002) has some non-physical structures in the baseline around the weak O_4 absorption band at 446 nm, which seems to affect NO_2 and CHOCHO fits. The non-physicality of these structures has been verified by our laboratory (Thalman and Volkamer, 2013). At the time of writing this manuscript, these new O_4 reference spectra were subject to ongoing measurements. Hence for this particular wavelength range, we prefer using Greenblatt et al. (1990).

The quantity retrieved from a DOAS analysis, the dSCD is converted to tropospheric VCD (VCD_{trop}) by using an air mass factor (AMF). AMF is light path enhancement in the atmosphere for a particular viewing geometry relative to vertical path through the atmosphere. The VCD_{trop} is the integral absorber concentration per unit area in the troposphere.

$$VCD_{trop} = \left[\frac{dSCD}{dAMF}\right] \tag{2.1}$$

dAMF is usually calculated with the help of a radiative transfer program to convert the measured dSCD to a VCD_{trop} and is a difference in AMF between the measured and the reference viewing geometry. It requires a-priori knowledge of trace gas vertical concentrations and aerosol extinction coefficients along with other input parameters such as pressure, temperature, surface albedo (SA), aerosol asymmetry parameter, g, and aerosol single scattering albedo (SSA). NO_2

concentrations, profile shapes and aerosol scenarios are highly variable in the SCAB because of the variable sources and hence could result in a significant amount of error in radiative transfer calculations of AMFs. Instead, we applied a simple geometric approximation for the nadir viewing geometry to convert dSCDs to VCDs. The geometric approach, its validity and error associated with this approximation are further discussed in section 2.3.3.

Table 2.2: Summary of DOAS analysis settings for different trace gases. 2 Rings (warm and cold) were fitted for HCHO retrievals, and spectra collected from SZA $<\sim 65^{\circ}$ were only analyzed and hence BrO was not included in the fit.

Trace gases	Wavelength range (nm)	Fitted absorbers	Polynomial order
NO_2	433-460	1, 2, 3, 6, 8, 9	3
CHOCHO	433-460	1, 2, 3, 6, 8, 9	3
HCHO	335-357	1, 2, 3, 4, 5, 7	3
H_2O	435-455	1, 2, 4, 5, 6, 8	3
O_4	350-386	1, 2, 3, 4, 5	3
O_4	440-490	1, 2, 4, 5, 8	5

2.3.2 Radiative Transfer Modeling

Since the AMAX-DOAS measurements are carried out in the open atmosphere using scattered sun light as the light source, the solar radiative transfer during the time of measurement needs to be modeled to interpret the retrieved data. The radiative transfer program McArtim (Monte Carlo atmospheric radiative transfer inversion model) (Deutschmann et al., 2011) used here is a fully spherical model and simulates radiative transfer in the atmosphere in the UV/vis/NIR spectral range using a Monte Carlo approach. In McArtim, the 3-D atmosphere is simulated as a 1-D modeled atmosphere divided in concentric spherical shells. The atmospheric conditions during the time of measurement in each vertical layer are assumed to be horizontally and vertically homogeneous. McArtim has the capability to simulate Jacobians of trace gases and aerosols needed for the interpretation of AMAX-DOAS data. Auxiliary input parameters used in the radiative transfer program were either measured aboard the aircraft (i.e. SA), on the ground at CalNex

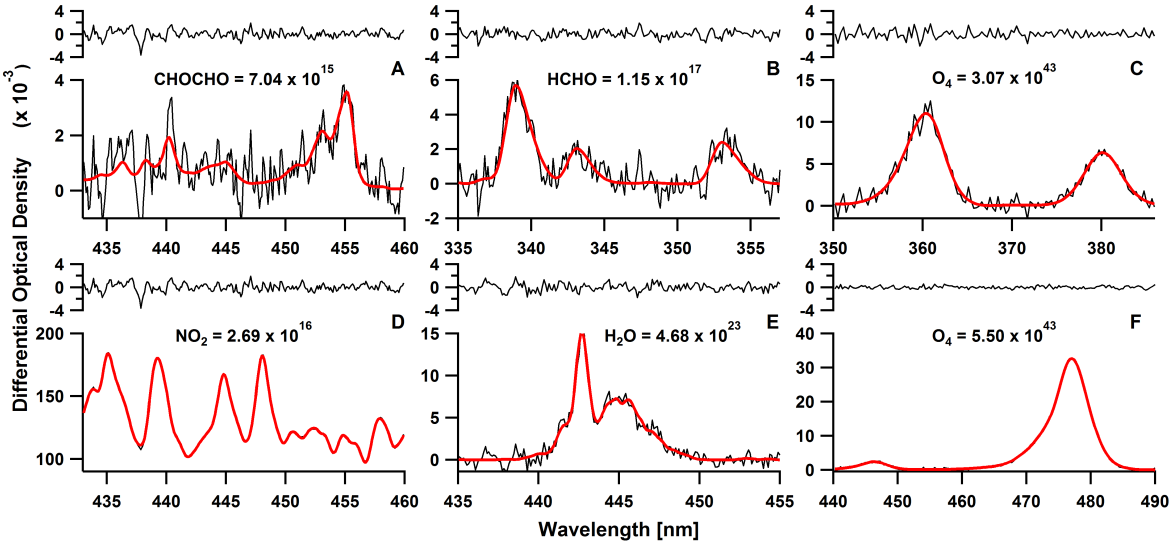

Figure 2.4: Spectral proofs for the detection of: (A) CHOCHO, (B) HCHO, (C) O_4 at 360 nm, (D) NO_2, (E) H_2O and (F) O_4 at 477 nm. CHOCHO and NO_2 fits are from 14 July, 2010 at 22:08 UTC (SZA: ∼42°) at ∼150 m AGL. HCHO and H_2O fits are from 16 July, 2010 at 20:19 UTC (SZA: ∼24°) at ∼600 m AGL. O_4 fits are from the same flight at 20:11 UTC (SZA: ∼23°) at ∼3000 m AGL. The black lines represent the measured spectra and red lines are fitted reference cross sections. Note that for NO_2 and O_4 at 477 nm, the absorption is so strong that the black lines are not visible. All the fits are for 0° EA. The units for retrieved dSCDs for CHOCHO, HCHO, NO_2 and H_2O is molecules cm^{-2} and for O_4 is molecules^2 cm^{-5}.

Table 2.3: Detection limits of the CU AMAX-DOAS instrument in the clean free troposphere and the boundary layer in polluted urban conditions like the SCAB for different integration times. Detection limit was calculated as 1σ RMS detection limit for the aerosol scenario presented in Fig. 2.10

Trace gas	Free troposphere (FT) (ppt)		Boundary layer (BL) (ppt)	
	30 s	2 s	30 s	2 s
NO_2	5	30	30	120
CHOCHO	3	16	16	65
HCHO	98	290	540	1355
H_2O_{442nm} (ppm)	42	210	252	760
ε_{477nm} (km^{-1})	0.002	0.002	0.006	0.006
ε_{360nm} (km^{-1})	0.004	0.004	0.012	0.012

ground site (Ryerson et al., 2013) (i.e. aerosol SSA), California Air Resources Board (CARB) (http://www.arb.ca.gov/homepage.htm) monitoring stations or typical values for urban environments based on previous studies (e.g., Dubovik et al., 2002).

2.3.3 Geometric Approximation for Conversion of dSCDs to VCDs

Under the geometric approximation, it is assumed that all the photons get scattered only once very close to the ground or are reflected from the surface before entering the telescope in nadir geometry. The geometric air mass factor (geoAMF) is then only a function of the solar zenith angle (SZA) and is given by

$$geoAMF = \left[1 + \frac{1}{cos(SZA)}\right] \tag{2.2}$$

The schematic of the geometric approximation is shown in the Fig. 2.1 inset.

In our DOAS analysis, a high altitude zenith spectrum from a clean background area is used as the reference spectrum. Assuming this background zenith spectrum has no tropospheric NO_2, the nadir dSCDs can be considered as tropospheric SCDs for most flight performed at low SZA. At high SZA, stratospheric NO_2 contribution changes with SZA and hence requires independent removal. For such flights (18 out of 52), stratospheric NO_2 contribution was corrected by fitting a polynomial through all the zenith dSCDs above 1.8 km flight altitude and subtracting the polynomial from the nadir measurements. The resulting quantity is defined as the tropospheric SCDs. This quantity is then converted to VCDtrop $\left(VCD_{trop} = \frac{SCD_{trop}}{geoAMF}\right)$, and is defined as VCD below the aircraft.

Sensitivity studies using the radiative transfer model (RTM) McArtim were performed to estimate uncertainties associated with the geometric approximation. A range of conditions that could potentially occur during the time of measurements were explored for this study. A representative sample of the results is summarized in Table 2.4, where the relative error in the geoAMF assumption compared to AMFs calculated using the RTM for different scenarios specified in the table. The results for most likely atmospheric state in the SCAB (surface albedo, SA = 0.1; single scattering albedo, SSA = 0.94; asymmetry parameter, g = 0.68; AOD = 0.4, boundary layer height,

BLH = 1.0 km; NO_2 mixing ratio = 10 ppb) is also shown in Table 2.4; it is based on ancillary measurements aboard the aircraft, CalNex ground site at Pasadena, CA and CARB ground monitoring stations or climatology of urban aerosol. Thomson et al. (2012) reported an average value for SSA of 0.92 at 532 nm during the entire CalNex campaign at Pasadena. They find SSA values to be slightly higher during the day time, when our measurements were taken. AOD measured at the AERONET station at Pasadena, CA showed AOD values to be lower than 0.4 at 440 nm for almost all of summer 2010, and the AOD of 0.4 likely represents an upper limit to provide a conservative estimate of relative error. The value of asymmetry parameter, g is based on the climatology of urban aerosol (e.g., Dubovik et al., 2002) and agrees well with measurements at the AERONET station at Pasadena, CA (range for the entire campaign: 0.63 - 0.80). AMFs calculated for this range of g values were within 3% of AMF relative to g = 0.68. It should be noted that these quantities are wavelength dependent. The largest source of error was found to be SA (see Table 2.4), which is constrained using the measurement aboard the aircraft. Notably, our SA measurements also provide means to filter data for conditions where the error may exceed 10%. The error from using the geoAMF compared to AMF calculated for the most likely atmospheric state in the SCAB is plotted as a function of SZA in Fig. 2.5. Based on this, a SZA cutoff of 65° was used to constrain the error in the NO_2 vertical columns. With these filters, the error in geoAMF is <7% for most conditions (85% of flight time with SZA <65°), and slightly larger (error <25% in all cases) for SZA ∼65° or during high altitude flights over low SA. The error associated with the geoAMF is consistent with previous airborne DOAS studies which used the geometric approximation. Melamed et al. (2003) estimated the error in NO_2 VCD from the geometric approximation to be ∼20% based on the discrepancies between measured and modeled O_2 AMF. To the best of our knowledge, there have been no previous deployments of AMAX-DOAS with simultaneous SA measurements by independent sensors. The high SA value of ∼10% at 477 nm is found widespread in the SCAB, and has the favorable effect to reduce errors from the geoAMF assumption due to compensating effects in the radiative transfer calculations.

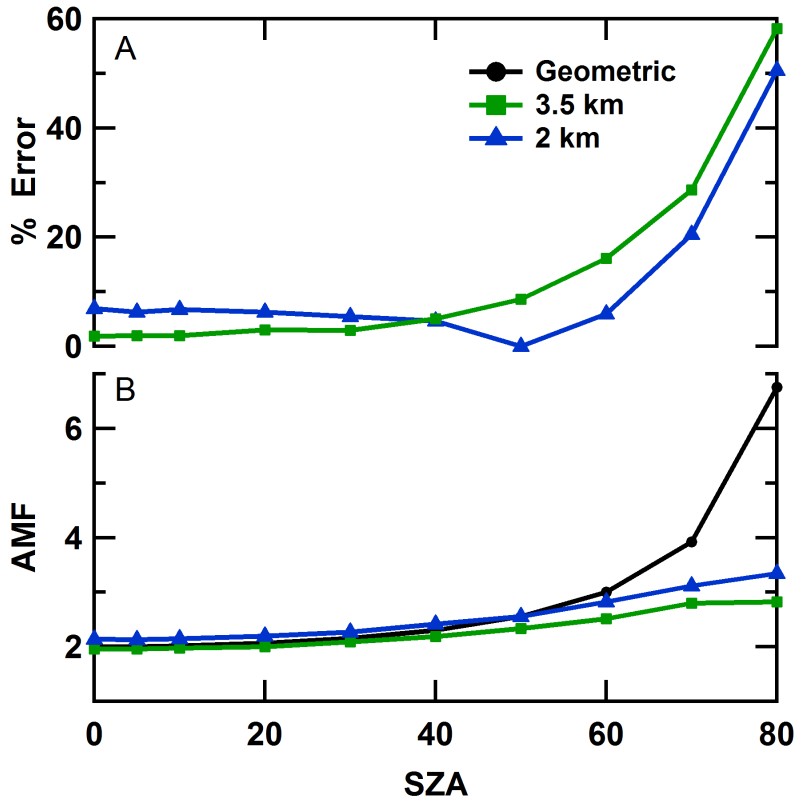

Figure 2.5: (A) Relative error of geometric air mass factor (geoAMF) compared to AMF for nadir geometry calculated using RTM, McArtim for flight altitude of 3.5 km (green) and 2 km (blue) AGL, for the most likely atmospheric conditions in the South Coast Air Basin (SCAB). (B) AMF calculated using McArtim (green and blue) and geoAMF (black). Most likely atmospheric state in the SCAB: surface albedo = 0.10, single scattering albedo = 0.94, g parameter = 0.68, aerosol optical depth = 0.4, boundary layer height = 1 km and NO_2 mixing ratio = 10.0 ppb.

Table 2.4: Relative error of geometric approximation compared to AMF calculated for nadir viewing geometry at 455 nm using radiative transfer program McArtim under different scenarios.

Altitude [km]	Solar zenith angle (SZA)	Most probable conditions*	Boundary layer height [m]		NO_2 concentration [ppb]		Surface albedo (SA)		Single scattering albedo (SSA)		Aerosol optical depth (AOD)	
			500	1500	5	20	0.05	0.15	0.90	0.99	0.10	0.80
2 (low)	20	6.3	3.3	9.0	7.2	5.6	3.0	12.2	4.4	9.6	4.3	6.7
	40	4.7	1.0	5.6	5.1	3.2	5.7	9.4	1.1	6.9	2.9	2.6
	60	5.9	7.3	6.3	6.0	7.0	15.3	0.7	8.0	3.3	3.4	11.0
3.5 (high)	20	3.0	6.3	0.3	2.8	3.2	15.2	5.3	5.3	0.30	4.6	1.0
	40	5.4	8.6	3.1	4.1	5.1	15.9	2.8	7.6	2.1	6.9	4.9
	60	16.1	16.4	14.0	14.5	16.5	25.0	8.3	17.5	11.6	14.2	19.3

* Most probable atmospheric conditions in SCAB: surface albedo = 0.10, single scattering albedo = 0.94, g parameter = 0.68, aerosol optical depth = 0.4, boundary layer height = 1 km and NO_2 mixing ratio = 10.0 ppb.

2.3.4 Aerosol Extinction Profile Retrieval

In the near-UV and visible wavelength range, under cloud free conditions, the change in photon path length compared to a Rayleigh atmosphere and hence the measured dSCDs of a trace gas depend mainly on the aerosol extinction profile. Thus, if the vertical distribution of an absorber is well known, the dSCD measurements of such species can be exploited to infer aerosol properties. The collisional complex of oxygen, O_4 is one such species (Honninger et al., 2004; Wagner et al., 2004; Wittrock et al., 2004; Clemer et al., 2010). The O_4 concentration varies with the pressure, temperature and square of the concentration of O_2. Hence, the dSCD measurements of O_4 can be used to calculate the aerosol extinction profiles. O_4 dSCD measurements from ground-based and airborne MAX-DOAS have previously been used for aerosol extinction profile and aerosol optical depth (AOD) retrievals (Clemer et al., 2010; Merlaud et al., 2011, and references within). Aerosol inversion is a non-linear problem and hence requires an iterative method. We used an iterative forward model approach to obtain the aerosol extinction profile. Under this approach a set of measured O_4 SCDs, y, is related to the aerosol extinction vertical profile, x_i, by forward model F such that

$$y = F(x_i, b) + \varepsilon \tag{2.3}$$

where b are forward model parameters that are not retrieved, i represents the iteration index and ε is the sum of measurement and model error. For 0° EA, i.e. parallel to the horizon, under cloud free conditions, the measurement is almost entirely sensitive to the altitude of measurement and nearly all of the vertical information contained in the SCD comes from that particular altitude. We exploit this property and retrieve the aerosol extinction profile by using a modified onion peeling algorithm using 0° EA O_4 SCD measurements. First the extinction above the highest altitude is constrained using upward EA scans performed at that altitude. Then the aerosol extinction values at the subsequent altitudes during the descent are determined iteratively using the set of 0° EA O_4 SCD measurements at those altitudes. Aerosol extinction below the lowest aircraft altitude is

obtained using downward EA scans performed at the lowest altitude. The process is repeated to account for any information on O_4 SCDs for 0° EA at a given altitude from O_4 column below the measurement altitude, until measured and modeled O_4 SCDs agree. The profile is then verified using other angles in the EA scans during the descent/ascent. It should be noted that this approach is feasible only due to the ability to maintain the desired EAs within narrow error bound also during descent/ascent of the aircraft, as discussed in Section 2.2.5.

The relative error in O_4 slant column densities (SCDs) at different altitudes in the atmosphere for different pointing uncertainties for a 0° EA is illustrated in Fig. 2.6. An uncertainty of 1-2° in pointing accuracy, which can easily happen on an airborne platform, could result in 20-80% O_4 SCD error above 10 km. Even though, the O_4 concentration is very small above 10 km (around 10% of the near surface at 10 km), the SCD at EA 0° can still be measured at good signal-to-noise, because of the much longer photon path lengths in the less dense air. Hence, the high sensitivity towards the pointing accuracy is the limiting source of error. Considering a non-linear relationship between O_4 SCD and aerosol extinction, this could result in even larger errors when O_4 SCDs are used to retrieve the aerosol extinction profile. This highlights the need for a motion compensation system to maintain pointing accuracy of the telescope.

2.3.5 Trace Gas Vertical Profile Retrieval

Trace gas vertical profile retrieval algorithm is based on the concept of Optimal Estimation (Rodgers, 2000). The use of this technique for profile retrieval from AMAX-DOAS measurements have been described in detail before (e.g., Bruns et al., 2004) and hence will only be introduced here briefly. A set of measurements y, which in our case are trace gas SCDs for different LOS can be related to a vertical distribution, x by the forward model F as shown in Eq. 2.3. Considering that we use a high altitude clean environment zenith reference spectrum, SCD of the reference spectrum is/can be considered to be negligible for tropospheric pollutants. Equation 2.3 can be rewritten in a linearized form as:

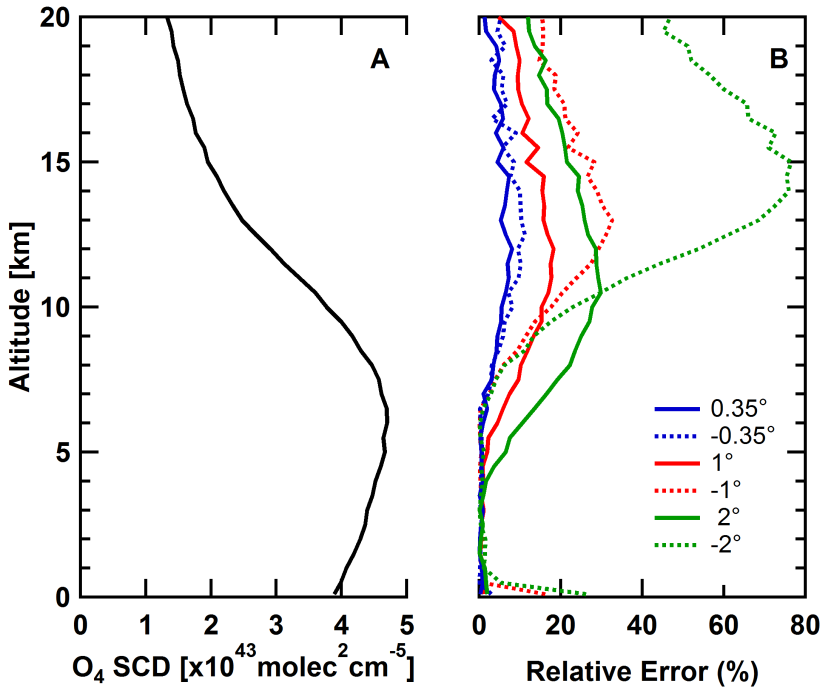

Figure 2.6: (A) Vertical profile of O_4 SCDs calculated for 0° EA at 477 nm using McArtim (US standard atmosphere with exponential aerosol extinction profile with extinction of 0.2 km^{-1} at the ground and 2.5 km scale height) (B) Relative error in O_4 SCDs for 0.35° (blue), 1° (red) and 2° (green) pointing error of the telescope at 0° EA. The solid and dashed lines represent angles above and below the horizon, respectively.

$$y = Kx + \varepsilon \tag{2.4}$$

where K defined as $\frac{\partial SCD}{x_i}$ is the weighting function matrix which expresses the sensitivity of measurement, y to x. We used the maximum a posteriori solution as described in Rodgers (2000) to solve Eq. 2.4:

$$x = x_a + \left(K^T S_\varepsilon^{-1} K + S_a^{-1}\right)^{-1} K^T S_\varepsilon^{-1} \left(y - K x_a\right) \tag{2.5}$$

where x_a is the a priori profile and S_a and S_ε are the a priori error and measurement error covariance matrices, respectively. The a priori profile is used to constrain the above described problem as it is generally ill-posed. S_ε was constructed using the square of the DOAS fit error as the diagonal elements of the matrix, the non-diagonal elements were set to 0. The apriori error covariance matrix, S_a was used as a tuning parameter; maximizing the information content while avoiding spurious oscillations in retrieved profiles (Schofield et al., 2004). The non-diagonal elements in S_a matrix accounts for correlation of trace gas values between different altitude layers and were included as Gaussian function shown in Eq. 2.6 (Barret et al., 2002; Hendrick et al., 2004):

$$S_{a_{ij}} = \sqrt{S_{a_{ii}} S_{a_{jj}}} \exp\left[(-\ln 2)\left(\frac{z_i - z_j}{\gamma}\right)^2\right] \tag{2.6}$$

where z_i and z_j are the altitudes at the i_{th} and j_{th} layers respectively and γ is the half width at half maximum (HWHM). The value of γ was set to half the width of vertical grid considered for inversion (Hendrick et al., 2004).

The solution given by Eq. 2.5 is a weighted mean of the a priori profile and the information from the measurement. This weight is given by the averaging kernel matrix A,

$$A = \left(K^T S_\varepsilon^{-1} K + S_a^{-1}\right)^{-1} K^T S_\varepsilon^{-1} K \tag{2.7}$$

The retrieval at any layer is an average of the whole profile weighted by the row of the averaging kernel matrix corresponding to that layer. The averaging kernel matrix also contains

information about the number of independent pieces of information retrieved, and an estimate of the vertical resolution of the retrieved profile at a given level. The trace of the averaging kernel matrix, A, gives the DOF, i.e. number of independent pieces of information retrieved. The FWHM of the main peak of an averaging kernel at any layer gives the estimate of the vertical resolution of the retrieved profile at that layer. For an ideal retrieval scenario, A is the identity matrix, the DOF equal the number of retrieved profile layers and the averaging kernels peak at their corresponding altitudes. In reality, the retrieved profile is a smoothed version of the true profile.

EA scan at flight altitude can be used to retrieve vertical profiles (e.g., Bruns et al., 2004) but the sensitivity of such scans are limited to mostly 2 km above and below the plane. Box AMF calculations for EAs 5° and 10° above and below the horizon show that the sensitivity of these EAs falls below 50% of the peak value above and below 2 km of the aircraft. Roscoe and Hill (2002) showed that vertical resolution can be improved by oversampling provided that the random error is degraded. Sensitivity can be improved by combining EA scan with aircraft ascent/descent. We exemplarily present vertical profiles from actively controlled EA scans during an aircraft descent at Brackett airfield in the Los Angeles basin, CA.

2.3.6 Error Analysis

Measurement noise, forward model parameter (e.g. SA) uncertainties and smoothing error due to finite resolution of the inversion grid contributes to the uncertainties in the retrieved profiles. The actual model error itself is neglected here as they are very small (Hendrick et al., 2006; Wagner et al., 2007). So, the total error in the retrieved profile is given by

$$S_{total} = S_m + S_f + S_s \tag{2.8}$$

where S_m is retrieval noise covariance, S_f is forward model parameter covariance, and S_s is smoothing error covariance matrices. Since the a priori covariance matrix, S_a is used as a tuning parameter, the smoothing error is also not considered but could be estimated from the averaging kernel matrix, A.

The error due to measurement noise is given by the retrieval noise covariance,

$$S_m = G^T S_\epsilon^{-1} G \tag{2.9}$$

where

$$G = \left(K^T S_\varepsilon^{-1} K + S_a^{-1}\right)^{-1} K^T S_\varepsilon^{-1} \tag{2.10}$$

is the gain matrix and expresses the sensitivity of retrieved profile to measured SCDs.

Sensitivity studies were performed to estimate the error in the retrieved profiles due to uncertainties in forward model parameters including EA accuracy. For each forward model parameter, b, we retrieved a new profile, x' such that

$$y = F(x', b') \tag{2.11}$$

where b' is the perturbation to the forward model parameter b. The difference between retrieved profiles, x with forward model parameter, b and x' with b' gives an estimate of the forward model error caused by uncertainties in parameter, b. The square of the differences constitutes the diagonal element of the corresponding forward model parameter covariance matrix, S_f.

We studied the effects of uncertainties in SA, SSA, asymmetry parameter, temperature, and EA on aerosol extinction coefficients at 477 nm. Results from the study are summarized in Table 2.5. The asymmetry parameter uncertainty ($g = 0.68 \pm 0.07$) could result in as much as 10% relative error in extinction values. A 5 °C temperature uncertainty could also result in similar relative error as the O_4 concentration in the atmosphere is temperature dependent (density effect). We used temperature measured aboard the aircraft to minimize this error. Angle accuracy uncertainty was found to result in large extinction errors (>0.01 km^{-1}) in the transition layer at the top of the boundary layer and around elevated layers. It points to the possibility of uncertainty in altitude of aerosol layers in the extinction profile and results in a blurring effect (Kritten et al., 2010). Angle accuracy uncertainties is often not considered for error estimates for vertical profiles from airborne DOAS measurements, but it could be the most important and largest source of error in the retrieved

profiles, especially for transition layers. The error bars in the aerosol extinction profile (Fig. 2.10b) reflects uncertainty due to measurement error, uncertainty in SSA, g parameter, SA and EA.

Uncertainties in aerosol extinction coefficients and EA were only considered as forward model parameter affecting the retrieved trace gas profiles as other forward model parameters (e.g. SA) have already been considered in aerosol extinction coefficients retrieval.

Table 2.5: Uncertainty in aerosol extinction coefficient due to uncertainty in model input parameters.

Parameter	Uncertainty in parameter	Uncertainty in extinction coefficient
Surface albedo	±0.05	<2%
Single scattering albedo	±0.05	<2%
Asymmetry parameter	±0.07	up to 10%
Temperature	±5°C	up to 10%
Pointing accuracy	±0.35°	mostly in transition layer

2.4 Results and Discussion

2.4.1 Nadir Observations

2.4.1.1 Horizontal distribution of NO_2

As an example, a map of NO_2 VCD distribution in the SCAB from RF# 46 on 16 July, 2010 (10:30-14:10 PDT) is shown in Fig. 2.7. The small footprint (∼1 km along the flight track) of the measurement allows us to clearly identify local hotspots and pollution sources. The NO_2 map in Fig. 2.7 reflects our understanding of the NO_x sources and its relatively short life time (∼4 hours). Clear NO_2 hotspots can be observed around downtown Los Angeles and Ontario, along the major highway, State Route 210 and at intersections of major highways. In contrast, very little NO_2 is seen in the eastern part of the basin, and over the High Desert to the northeast, where there are no significant local sources of NO_x. The footprint of CU AMAX-DOAS is comparable to air quality models, and smaller than that of current solar stray light satellite observations, which also measure VCDs of trace gases; this makes this data set an excellent opportunity to evaluate emissions in air

quality models and validate satellite observations. A first application of CU AMAX-DOAS to test NASA NO_2 VCD retrievals from the OMI/AURA satellite instrument is published in Oetjen et al. (2013).

2.4.1.2 Validation of NO_2 vertical column

To validate the retrieval of our NO_2 VCDs by CU AMAX-DOAS using the geometric approximation, we compared our observations with NO_2 VCDs from ground based MAX-DOAS instruments. Two MAX-DOAS instruments (Sinreich et al., 2010; Coburn et al., 2011) were deployed at the CalNex ground site (Ryerson et al., 2013) in Pasadena, CA, the Fontana Arrows CARB monitoring network station and the CARES T1 (Zaveri et al., 2012) site in Cool, CA at various times of the campaign. MAX-DOAS operates in the same principle as AMAX-DOAS. Spectra measured at off-axis angles were analyzed for NO_2 using a closest zenith reference spectrum in time. The retrieved NO_2 dSCDs for 20° EA were converted to VCDs using a dAMF calculated by McArtim. This EA was chosen to minimize the effect of uncertainties in model parameters, especially NO_2 profile shape and magnitude and aerosols. Sensitivity studies were performed to estimate the error in calculated dAMF due to model parameter uncertainties and is estimated to be around 8%. Considering ∼3% dSCD retrieval error and ∼8% dAMF error, we estimate the overall error in MAX-DOAS VCDs to be around 10%. MAX-DOAS instruments at Pasadena and Fontana Arrows were pointing in both east and west directions while the one at the CARES T1 site was looking north and south. Those MAX-DOAS instruments are capable of making a full 180° EA scan.

The NOAA Twin Otter was frequently routed over these ground sites. The correlation plot between the CU AMAX-DOAS and MAX-DOAS instruments is shown in Fig. 2.8. Correlations showed sensitivity to filtering data by criteria such as the distance of the plane and ground site, the relative azimuth angle between plane heading and ground viewing, and inhomogeneous air mass. The inhomogeneity of air mass was measured by MAX-DOAS, which observed differences in NO_2 VCDs in the east and west view of up to 2.5 x 10^{16} molecules cm^{-2} NO_2 VCD. Figure 2.7 gives an

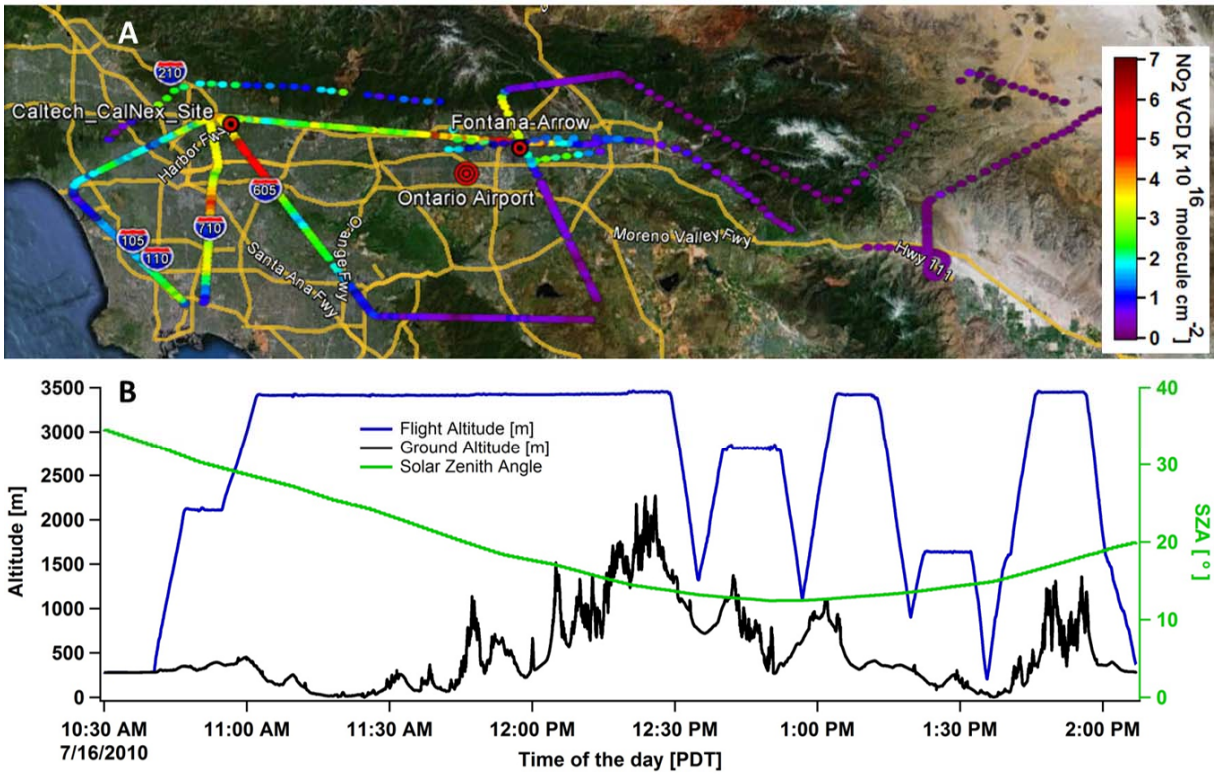

Figure 2.7: (A) Map showing horizontal distribution of NO_2 VCDs below the aircraft derived from nadir measurements from RF # 46 on 16 July, 2010 (10:30-14:10 Pacific Daylight Time, PDT) in the SCAB. MAX-DOAS instruments deployment sites and the base airport for the Twin Otter are shown as red targets. (B) Time trace of flight altitude (blue), ground altitude (black) and SZA (green) from the same flight.

idea of the NO_2 VCD variability as mapped by the CU AMAX-DOAS. Filtering for data within 5 km radius of the ground site, clouds (via two webcams installed on the aircraft), SZA $< 65°$, aircraft altitude $<$ 4 km, and $<$ 1.5 x 10^{16} molecules cm^{-2} NO_2 VCD difference in east/west view of MAX-DOAS instruments in the SCAB, as well as coincident measurements within a 10 minute of the aircraft overpass, resulted in a correlation with slope 0.86 $\pm$ 0.03, and offset in VCD of -0.8 $\pm$ 3.7 x 10^{14} molecules cm^{-2} ($R^2 = 0.96$) (grey dots in Fig. 2.8). The slope of the linear fit line is skewed by the measurements at the CARES T1 site which are near and/or below the detection limit of both the instruments but nevertheless still a very good agreement between the two instruments. If only measurements in the SCAB are considered, and filtering is further constrained (relative azimuth angle between plane heading and ground viewing $< \pm 15°$, and variability in NO_2 VCD for both instruments $<$ 8 x 10^{15} molecules cm^{-2}), the slope increases to 0.95 $\pm$ 0.09, offset in VCD of 2.5 $\pm$ 1.4 x 10^{15} molecules cm^{-2} ($R^2 = 0.86$)(Fig. 2.8). This sensitivity to filtering criteria reflects upon the inhomogeneity of the SCAB air mass and also points to the validity of geometric approach under horizontally inhomogeneous conditions.

2.4.2 Limb Observations

Vertical profiles of aerosol extinction coefficient and trace gas concentrations were retrieved for a low approach at Brackett airfield, CA during RF# 46. The aircraft was flying at $\sim$3.1 km above ground level (AGL), made a slow descent to an altitude of $\sim$0.6 km AGL at the airport, and then ascended again. The telescope was scanning a set of EAs (-90°, -5°, -2°, 0°, 2°, 5°, 90°) during the low approach. A complete set of EAs was also measured at the highest altitude just before the descent and at the lowest point before starting to ascent in order to characterize the air mass above and below the aircraft. The descent portion of the low approach took $\sim$8 minutes. Low approach is a maneuver over an airport in which the pilot intentionally does not make a contact with the runway.

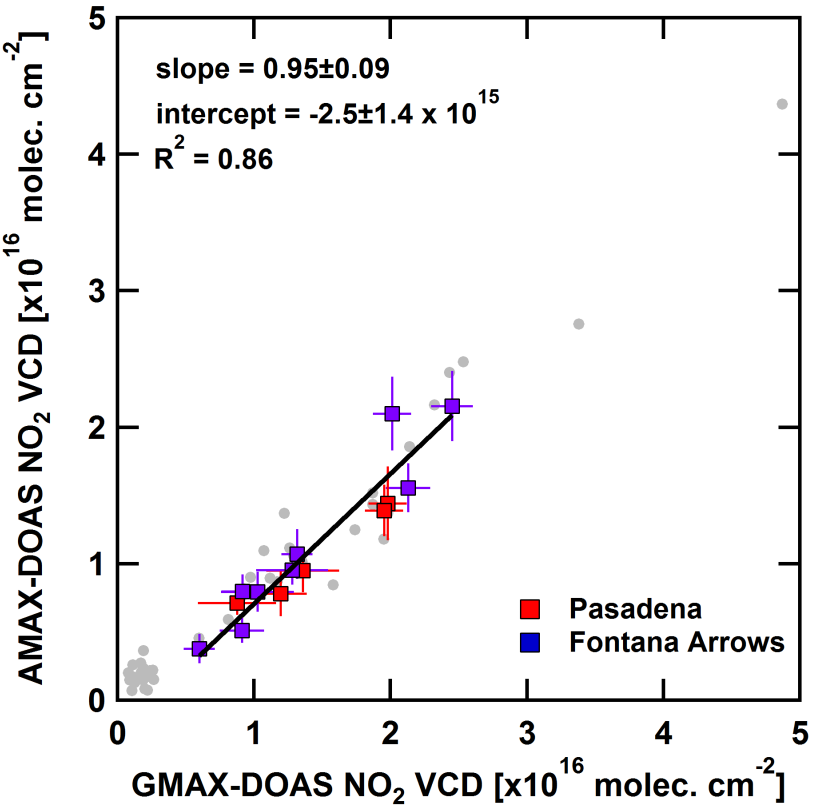

Figure 2.8: Correlation plot of NO_2 VCDs between the CU AMAX-DOAS and two MAX-DOAS instruments deployed in California during the CalNex and CARES field campaigns. Grey dots represent all data from both campaigns (see text for filtering conditions). Data from the CalNex further constrained for relative azimuth between plane heading and MAX-DOAS viewing geometry $< \pm 15°$ and NO_2 VCD variability < 8 x 10^{15} molecules cm^{-2} are shown in red and blue. Black line is the linear fit through the colored points.

2.4.2.1 Determination of O_4 SCD in the reference spectrum

The scale height of O_4 in the atmosphere is ~4 km and as our measurements were usually performed below 4 km altitude, it is important to quantify the O_4 SCD contained in the reference spectrum (SCD_{ref}) in order to accurately retrieve the aerosol extinction profile. Merlaud et al. (2011) used a linear regression between measured dSCD and calculated SCD for airborne measurements above 5.5 km in the Arctic to determine SCD_{ref} and the dSCD correction factor,α:

$$SCD = \alpha \text{ x } dSCD + SCD_{ref} \tag{2.12}$$

The dSCD correction factor (α) has been used to scale measured O_4 dSCDs to bring inferences of aerosol extinction into agreement with other sensors, like AERONET (e.g., Clemer et al., 2010). It is an empirical observation that some MAX-DOAS applications find measured O_4 dSCDs to be too large compared to modeled O_4 dSCDs for Rayleigh atmosphere. The non-physicality of α different from unity is a subject of ongoing debate in the DOAS community. For example, the value for the correction factor is different between different environments and research groups, and wavelengths, and ranges from 0.75 to 0.89 (Wagner et al., 2009; Clemer et al., 2010; Merlaud et al., 2011; Zieger et al., 2011). It has been speculated that the need for α could be due to the temperature dependence of the O_4 absorption cross-section (Wagner et al., 2009, Clemer et al., 2010). Indeed, a temperature uncertainty in the O_4 absorption cross-section has been reported (Blickensdorfer and Ewing, 1969; Wagner et al., 2002, and references within).

We employed the same approach as Merlaud et al. (2011) to determine SCD_{ref} and α. Temperature and pressure as measured on the plane were used to prescribe the vertical distribution of O_4 in the model. Temperature and pressure profiles were extrapolated to the ground using the lapse rate and scale height determined from the measurements respectively. The temperature was 36.7 °C and the pressure was 966 mbar at the ground. Comparison of extrapolated temperature and pressure values at the ground with measurements at the nearest CARB monitoring stations showed good agreement within ± 2 °C and ± 10 mbar respectively. Profiles above the aircraft were

extrapolated based on the mean temperature and pressure profiles measured at Joshua Tree, CA. The O_3 profile was also constructed similarly and was measured by the NOAA TOPAZ lidar aboard the plane. Based on the regression analysis shown in Fig. 2.9, between simulated and measured O_4 SCDs at 477 nm for a low approach at the Brackett airfield during RF# 46 (see more details below) , we determine $\alpha = 0.99 \pm 0.01$ for 477 nm. Hence it is concluded that a scaling factor is not needed to explain our measurements. An O_4 reference SCD of 9 x 10^{42} molecule^2 cm^{-5} based on the regression has been added to the measured dSCDs to convert them to SCDs.

2.4.2.2 Aerosol extinction coefficient profiles

Aerosol extinction coefficient vertical distribution retrieved at 477 nm is shown in Fig. 2.10b. The extinction profile was retrieved by iteratively minimizing the residual between measured and simulated O_4 SCDs, see section 2.3.4. Figure 2.10a illustrates the agreement between the measured and modeled O_4 SCDs at 477 nm for EA 0°. The corresponding aerosol extinction profile is presented in Fig. 2.10b. The aerosol extinction profile in Fig. 2.10b indicates that most of the aerosols are located inside the boundary layer (up to 0.9 km, indicated by the decrease in NO_2 and aerosol) with a 500 m thick elevated layer at ∼2.5 km. The error contribution in retrieved extinction due to EA uncertainty of 0.35° is shown Fig. 2.10c and it illustrates that pointing accuracy is needed especially to minimize error in transition layers and elevated layers.

Integration of the extinction coefficient profile over altitude gives aerosol optical depth (AOD), the total load of aerosols in the atmosphere. AOD at 477 nm from the profile in Fig. 2.10b is 0.16 ± 0.03, and agrees well with 0.18 ± 0.02 at 500 nm measured by AERONET station located at Pasadena. The AOD values for the AERONET station reported here are hourly averages and standard deviations for the hour of the low approach. Pasadena is located 30 km west of the Brackett airfield; the telescope was pointing towards the west during our low approach, and the measurements inherently averages over spatial scales of typically few 10 km. Based on the Koschmieder visibility formula for the visible wavelength region, visibility = 3.91/extinction coefficient (see e.g., Horvath, 1971), the visibility at 477 nm during the time of our measurement would be ∼39 km. The excellent

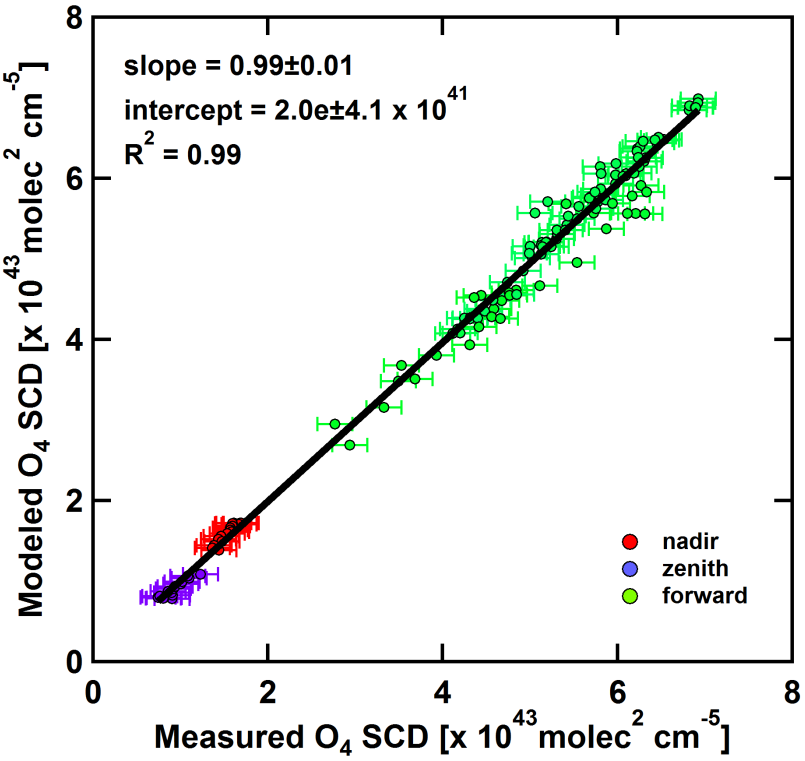

Figure 2.9: Correlation plot of modeled and measured O_4 SCDs at 477 nm for the case study shown in Fig. 2.10b. SCD of the zenith reference (9 x 10^{42} molecules^2 cm^{-5}) has been added to the measured O_4 dSCDs. Forward viewing geometry includes 0°, ±2° ±5° EAs.

agreement between the AOD calculated from our profiles and AERONET station adds confidence to our retrieval approach and accuracy of the retrieved profile. To our knowledge this is the first demonstration of quantitative retrieval of aerosol extinction from O_4 dSCD observations that does not require a correction factor.

2.4.2.3 Trace gas vertical profiles

Figure 2.11 shows the retrieved NO_2, CHOCHO, HCHO and H_2O mixing ratio profiles from the same low approach. The NO_2, CHOCHO, and HCHO vertical profiles have a very similar shape with most of the trace gases located inside the boundary layer. This is not surprising since most of the sources for these gases are close to the surface. On the other hand, the H_2O profile is almost linearly decreasing with altitude. The retrieved NO_2 profile shows an average urban boundary layer value of 14.2 ± 1.3 ppb (at the surface: 1 ppb ≈ 2.46 x 10^{10} molecules cm^{-3} at sea level, and 298 K temperature). The hourly NO_2 data recorded at the nearest CARB monitoring station at Pomona is 13 ppb. Pomona station is located ∼3 km south of the Brackett airfield. Our retrieved NO_2 surface mixing ratio agrees well with the measurement at the ground station. The CHOCHO profile shows a BL value of 274 ± 28 ppt. It also exhibits an elevated layer of glyoxal with ∼33 ± 8 ppt at around 2.5 km (Fig. 2.11b). The lower error bars in the FT compared to the BL is due to two reasons: 1) With both the reference spectrum and the measured spectrum taken under very similar conditions, i.e. FT with lower aerosol load compared to BL, the DOAS retrieval error is smaller in the FT compared to the BL. 2) In our low approach, the aircraft only descended down to an altitude of ∼ 600 m AGL and a set of downward EAs at that altitude was used to probe the lower altitudes. Hence, the measurement has lower sensitivity below 600 m (see Appendix A Fig. A.1). The observation of 33 ppt glyoxal in a layer aloft that is decoupled from the boundary layer coincides with the altitude where a layer of enhanced aerosol is observed in the aerosol extinction profile (Figure 2.10b). The coexistence of glyoxal and aerosol aloft could indicate the in-situ production of glyoxal from oxidation of VOCs that have been transported along with the aerosols. Laboratory studies show consistent evidence of glyoxal uptake by aerosols forms SOA (Liggio et al.,

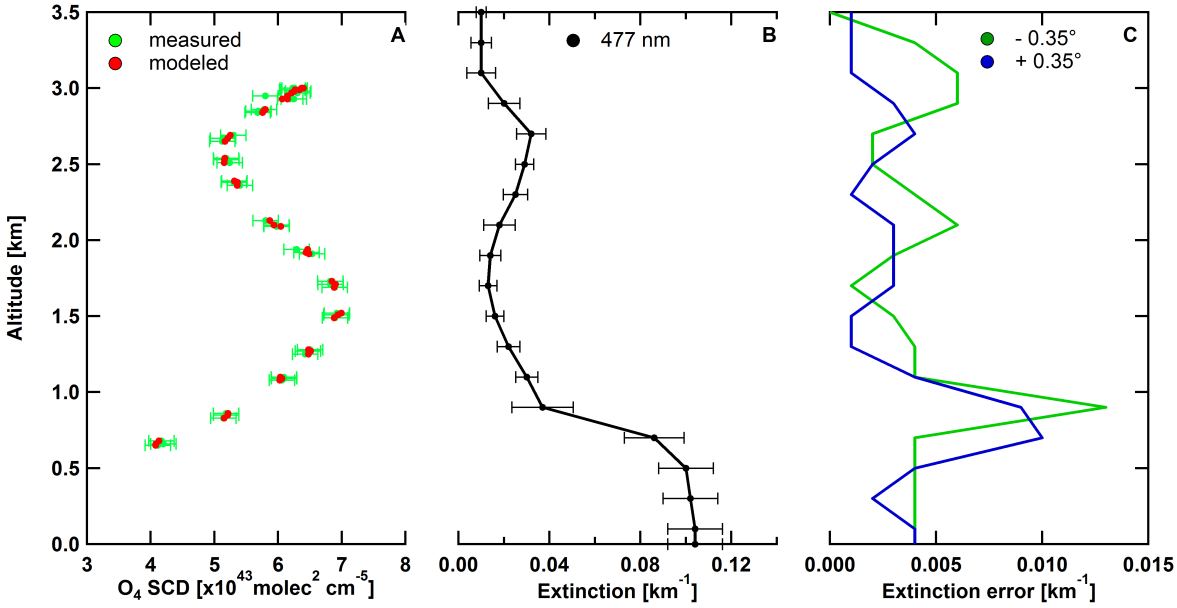

Figure 2.10: (A) Measured (green) and simulated (red) vertical profiles of O_4 SCDs for EA 0° at 477 nm from a low approach at the Brackett airfield during RF# 46 on 16 July, 2010 in the SCAB (B) Corresponding aerosol extinction vertical profile retrieved at 477 nm (C) Error contribution in extinction due to angle uncertainty of ±0.35°. Note that the aircraft only flew down to ∼600 m AGL during the low approach and a set of downward EAs at that altitude was used to probe the lower altitudes.

2005b; Volkamer et al., 2009b; Trainic et al., 2011). However, if this process is partly reversible, the collocation of glyoxal and aerosol could also point to aerosols as a source of glyoxal aloft (Kroll et al., 2005; Kampf et al., 2013). It should be noted that while glyoxal dSCDs at the elevated layers are close to the detection limit for our 2 second data, this detection limit can be improved by longer averaging times. An elevated layer of O_3 is also observed in the NOAA TOPAZ lidar data at the same altitude (pers. communication, C. Senff, CIRES & NOAA, 2012) and is included in the RTM calculations for aerosol extinction and trace gas inversion. The water vapor mixing ratio inside the BL corresponds to a relative humidity, RH = 23 ± 5%. Coincident measurements of RH at nearby CARB monitoring stations varied from RH = 23% (Ontario International Airport) to RH = 34% (Upland). The good agreement of RH demonstrates control of radiation fields in the inversion. HCHO vertical profile was retrieved using aerosol extinction profile independently obtained using O_4 dSCD measurements at 360 nm (see Appendix A Fig. A.2).

A 250 m altitude grid was chosen for the retrieval of trace gases. This grid height was chosen based on the FOV of the telescope, rate of aircraft descent and time it took to complete one EA scan cycle during the descent. The averaging kernels for all the trace gases indicate a constant sensitivity for the whole low approach except the lowest layer at the surface. The DOF are 12.5, 11.5, 11.6, and 11.8 for NO_2, CHOCHO, HCHO, and H_2O, respectively confirming the presence of independent information approximately every 250 m. The sensitivity of the retrieved profile to different a priori profiles was also tested, and found the lowest layer inside the BL to be the most susceptible (upto 20%), the layer with the least measurement sensitivity. The lower averaging kernels below 600 m are explained from the observing geometry of the low approach (see above). While this decrease in sensitivity for other EAs compared to 0° for a given atmospheric layer does not appear to limit our ability to infer meaningful information near the surface (see this section above), it highlights the benefit of capabilities to maintain EA 0° during aircraft ascent/descent to systematically probe the atmosphere with maximum sensitivity, and vertical resolution.

The averaging kernels (Fig. 2.11) appear as if there were no other EAs but 0° EA used for the profile retrievals. In fact they peak at the altitude of 0° EA measurements. This highlights the

fact that 0° EA is the most sensitive EA during ascent and descent of the aircraft and provides the most independent information. This has also been reported by Merlaud et al. (2011). Bruns et al. (2004) performed theoretical sensitivity study regarding choice of EA for maximizing DOF while flying at a constant altitude. Based on the study by Bruns et al. (2004) and our experiment, we recommend maintaining EA 0° actively aligned during descent/ascent and scanning only at the lowest and highest point during the ascent/descent to maximize DOF.

2.5 Conclusion

An Airborne MAX-DOAS instrument equipped with a motion-stabilized scanning telescope to collect solar stray light photons provides accurate means to probe atmospheric composition in terms of the horizontal and vertical distributions of multiple trace gases and aerosols simultaneously and sensitively by means of a single, portable, instrument.

The CU AMAX-DOAS instrument is validated by comparison with NO_2 VCDs measured by ground-based MAX-DOAS. A sensitivity study using radiative transfer modeling reveals that the geometric approximation is a viable option to convert NO_2 SCD to VCD for measurements below the plane. This approximation is found to be accurate over southern California, where elevated surface albedo ($\sim$10% at 477 nm wavelength, measured aboard the plane) compensates for reduced sensitivity due to aerosols. We estimate the error in the NO_2 vertical columns due to the geometric approximation to be less than 7% under most conditions for SZA $< 65°$; a slightly larger error ($<$25% in all cases) is found for SZA $\sim$65° or during high altitude flights over low surface albedo. These results emphasize benefits of measuring surface albedo and AOD by independent sensors.

For a case study, vertical profiles of NO_2, CHOCHO, HCHO, H_2O, and aerosol extinction coefficient at 477 nm showed that trace gases and aerosols are located mostly inside the BL, though the presence of an elevated pollution layer was observed as well. Sensitivity studies show that the main error sources in the retrieved vertical profiles of aerosol extinction are due to the asymmetry parameter of aerosol scattering. Further, sensitivity studies highlight the need of pointing accuracy of the telescope on moving platforms like an aircraft to accurately retrieve vertical distributions of

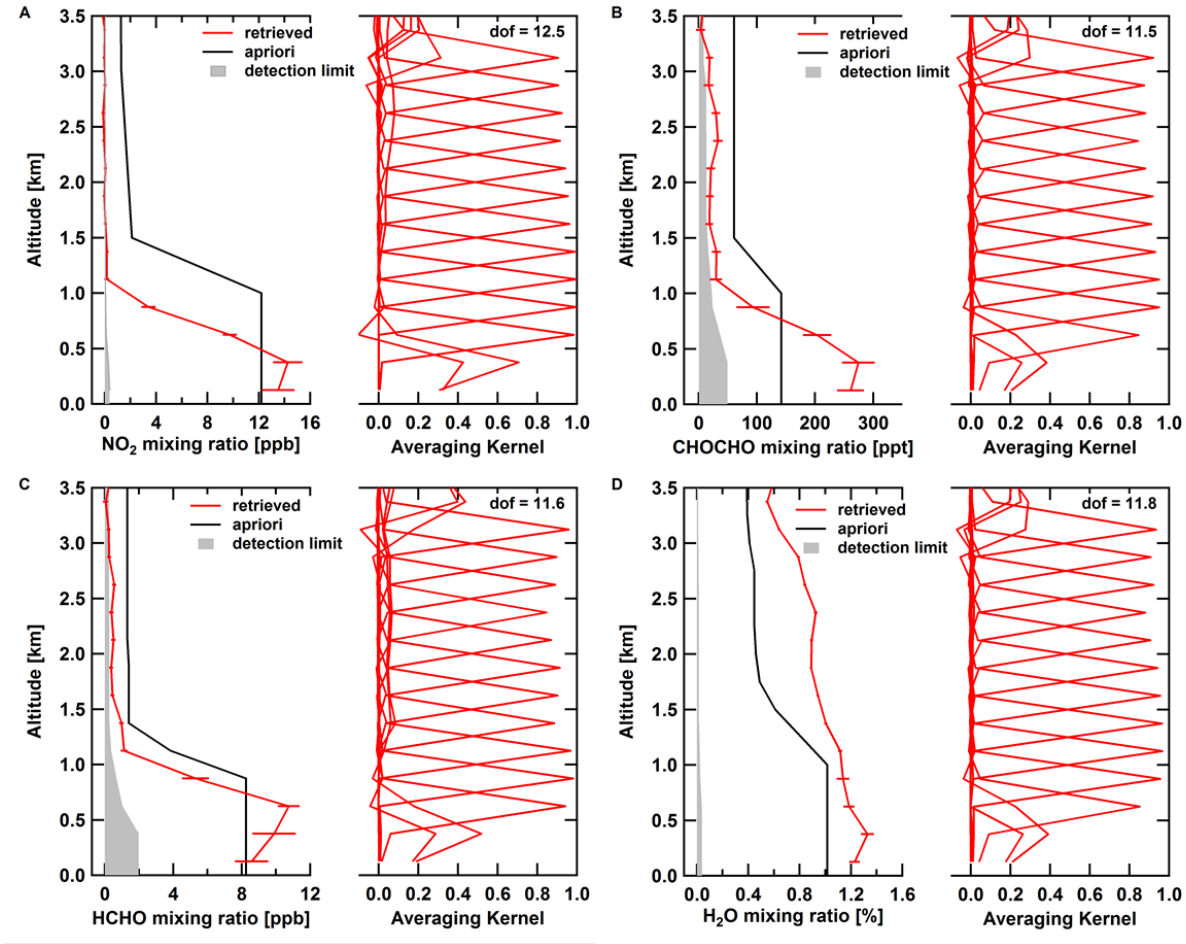

Figure 2.11: Retrieved vertical profiles and corresponding averaging kernels for (A) NO_2, (B) CHOCHO, (C) HCHO and (D) H_2O from the low approach at the Brackett airfield. NO_2, CHOCHO and HCHO profiles show most of the trace gases are located close to the source region inside the BL. Averaging kernels indicate almost constant sensitivity for all trace gases over the entire altitude range. Grey shaded area represents detection limit for each profile.

trace gases and aerosol extinction coefficients. The accuracy of our motion compensation is found to be $<0.35^{\circ}$ by comparison with an independent inertia system.

An $\sim$500 m thick layer at around 2.5 km altitude AGL was observed that was decoupled from the BL, and contained 33 $\pm$ 8 ppt CHOCHO, NO_2 below the detection limit (30 ppt, for 2 seconds integration time), 545 $\pm$ 114 ppt HCHO, 0.029 $\pm$ 0.004 km^{-1} ε_{477}, corresponding to a partial vertical columns of 4.14 ± 1.12 x10^{13} molecules cm^{-2} CHOCHO, 7.10 ± 1.75 x10^{14} molecules cm^{-2} HCHO, and partial AOD of 0.047 ± 0.007 at 477nm. This elevated layer contained ratios of CHOCHO/HCHO of 0.06 ± 0.02, compared to 0.027 ± 0.006 inside the BL. The concurrent location of elevated aerosol extinction at the same altitude indicates either collocated glyoxal sources from VOC oxidation, or the release of glyoxal that was initially taken up as SOA back to the gas-phase. The increase in the CHOCHO/HCHO ratio with altitude appears to be outside error bars, and the cause for this altitude dependence deserves further investigation.

The capabilities of CU AMAX-DOAS are not limited to the parameters presented here, and include also measurements of reactive species, like halogen oxide radicals, and aerosols at other wavelengths. The absence of sampling lines, and inherent averaging over extended spatial scales enable the AMAX-DOAS technique to bridge between ground-based networks, atmospheric models, and satellites, and holds as yet unexplored potential to advance airborne atmospheric observations, and improve our understanding of the processes taking place in the atmosphere. The CU AMAX-DOAS deployment during the CalNex and CARES field campaigns makes a 10 week long data set available that we plan to apply for such studies.

Chapter 3

Measurements of Formaldehyde and Glyoxal Vertical Columns

Formaldehyde (HCHO) and glyoxal (CHOCHO) are important atmospheric chemistry tracer molecules for photochemistry. We present an algorithm for obtaining HCHO and CHOCHO vertical columns from CU AMAX-DOAS measurements. The algorithm is based on optimal estimation and leverages measurements from multiple elevation angles (EA) at a constant flight altitude to retrieve vertical columns below the aircraft. The dependence of retrieved vertical columns on aerosol load and a priori profiles were systematical tested using synthetic data and were found to result in ∼7% and ∼12% uncertainty, respectively. We show example maps of HCHO and CHOCHO vertical columns over the South Coast Air Basin (SCAB) in California. The measured columns for both species were found to be higher than predicted by atmospheric models using different emission inventories, while the glyoxal-to-formaldehyde ratio over the SCAB was consistent with GOME-2 observations. These maps of HCHO and CHOCHO columns would be very useful in evaluating current atmospheric models and satellite retrievals over California.

3.1 Introduction

Formaldehyde (HCHO) and glyoxal (CHOCHO) play important roles in atmospheric chemistry as tracer molecules for photochemistry. HCHO photolysis produces HO_x radicals, a major oxidizer in the atmosphere, which sustains photochemical production of ozone (O_3) and secondary organic aerosols (SOA) (Finlayson-Pitts and Pitts Jr, 2000). Sources of HCHO include direct emissions from biomass burning (Lee et al., 1997), vehicular exhaust, industrial activities (Anderson

et al., 1996; Parrish et al., 2012b) as well as secondary production from hydrocarbons like alkanes and alkenes (Finlayson-Pitts and Pitts Jr, 2000; Parrish et al., 2012b). Contributions of primary vs secondary sources for HCHO differ greatly by location. For example, Garcia et al. (2006) reported >30% contribution from primary sources in Mexico City. In contrast, the contribution from primary sources was only around 5% in Houston, Texas (Parrish et al., 2012b). It is very important to differentiate primary and secondary sources of HCHO for regulatory purposes in order to identify appropriate control measures. Because of its relatively large secondary source, HCHO is also used as a proxy for VOC oxidation.

Glyoxal, the simplest alpha dicarbonyl, is a novel indicator molecule for active photochemistry (Volkamer et al., 2005). Sources for CHOCHO in the atmosphere are dominated by secondary productions from oxidation of precursor hydrocarbons with two or more carbon atoms (Calvert et al., 2002; Volkamer et al., 2007). Our knowledge on the primary sources of CHOCHO is currently very limited, but minor amounts have been reported in tailpipe emissions (Grosjean et al., 2001; Kean et al., 2001) and biomass burning (Fu et al., 2008). CHOCHO is a known direct precursor for SOA (Liggio et al., 2005b,a; Volkamer et al., 2007, 2009b). The role of SOA as a source of CHOCHO is currently an active field of research in atmospheric chemistry (e.g., Washenfelder et al., 2011; Waxman et al., 2013). Recent results show that uptake of CHOCHO to SOA could be reversible (Kroll et al., 2005; Kampf et al., 2013). Glyoxal is a short lived species with average atmospheric life time of ∼3 hours (Fu et al., 2008; Myriokefalitakis et al., 2008) and hence airborne measurements of CHOCHO can be used to identify photochemical hot spots for VOC oxidation and SOA formation.

CU AMAX-DOAS (Volkamer et al., 2009a; Baidar et al., 2013a) measurements during CalNex (Ryerson et al., 2013) and CARES (Zaveri et al., 2012) field campaigns in summer 2010 provided an opportunity of retrieve high resolution maps of HCHO and CHOCHO in California especially in the South Coast Air Basin (SCAB) and Sacramento area. Here, we present a case study from two morning flights on July 16 and 17, 2010 in the SCAB to demonstrate the potential and feasibility of HCHO and CHOCHO vertical column retrieval from the CU AMAX-DOAS measurements. Brief

discussions on the retrieval technique, horizontal distribution of the two species, and the glyoxal to formaldehyde ratio are presented. We also compared model HCHO and CHOCHO outputs from two atmospheric models: Community Multi-scale Air Quality model (CMAQ) using CARB 2010 emission inventory (EI); and Weather Research and Forecasting model coupled with chemistry (WRF-Chem) using NEI 2005 and CARB 2010 EIs with the measured vertical columns.

3.2 Data Retrieval

Analysis of the CU AMAX-DOAS measured atmospheric absorption spectra for HCHO and CHOCHO was performed using the DOAS method (Platt and Stutz, 2008). Briefly, the DOAS approach relies on the separation of the narrow band absorption signatures of trace gases from broad band absorption and scattering features. A quantity known as differential slant column density (dSCD) of trace gases are retrieved in a set wavelength window by simultaneously fitting the absorption cross-sections of the known absorbers in that window using a non-linear least square fitting procedure (see section 1.2). For HCHO dSCD retrievals, a spectral region of 335-357 nm was chosen and absorption cross-sections of NO_2 (at 220 K and 294 K) (Vandaele et al., 1998), O_3 (at 223 K and 243 K) (Bogumil et al., 2003), O_4 (Hermans, 2002) and HCHO (Meller and Moortgat, 2000), a Ring spectrum (Bussemer, 1993), and a third order polynomial included in the fit. Absorption cross-section of NO_2 (at 220 K and 294 K), O_3 (223 K), O_4 (Greenblatt et al., 1990), H_2O (Rothman et al., 2005), and CHOCHO (Volkamer et al., 2005), a Ring spectrum, and a third order polynomial was fitted in the wavelength window of 433-460 nm for CHOCHCO dSCD retrievals. Multiple spectra (typically 3-10) with 2 seconds integration time for each elevation angle (EA) were added to improve the signal to noise for HCHO and CHOCHO DOAS retrievals. The 1σ RMS dSCD detection limit for the nadir viewing geometry were around 5 x 10^{14} molecules cm^{-2} and 1.0 x 10^{16} molecules cm^{-2} for CHOCHO and HCHO, respectively.

The retrieved HCHO and CHOCHO dSCDs were converted to vertical column densities (VCDs) using the concept of optimal estimation by Rodgers (2000). This technique was also used to retrieve vertical profiles of trace gases (NO_2, CHOCHCO, HCHO and H_2O) from the CU

AMAX-DOAS measurements during low approaches and is described in detail in section 2.3.5. Generally, dSCDs are converted into VCDs using a quantity known as differential air mass factor (dAMF; dAMF $=\frac{dSCD}{VCD}$). Calculation of dAMF requires knowledge of vertical distribution of trace gas of interest as well as aerosol extinction. Since the magnitude as well as vertical distribution of pollutants such as HCHO and CHOCHO is highly variable in polluted urban environment like the Los Angeles Basin, we used EA scans performed at flight altitude >1500 m above ground level (AGL) to constrain the problem and retrieve VCD using the inversion based on optimal estimation. Sensitivity studies showed that vertical columns retrieved using this technique are very robust (see section 3.3). The EA scan at flight altitude usually included the following angles; ±90°, ±20°, ±10°, ±5°, ±2°, and 0° with +90° being the zenith view and -90° being the nadir view. A set of EA scans containing all or some of these angles were used to retrieve the vertical columns of HCHO and CHOCHO.

The vertical column retrieval algorithm builds on the algorithm used to retrieve vertical profiles and hence will only be introduced here briefly. In the linearized form, a set of measured trace gas SCDs, y is related to the trace gas vertical profile, x such that

$$y = Kx + \varepsilon \tag{3.1}$$

where K is the weighting function matrix that expresses the sensitivity of measurement y to true profile x. The maximum a posteriori solution to the above problem using optimal estimation is given by

$$x = x_a + \left(K^T S_\varepsilon^{-1} K + S_a^{-1}\right)^{-1} K^T S_\varepsilon^{-1} \left(y - K x_a\right) \tag{3.2}$$

where x_a is the a priori profile, and S_ε and S_a are the measurement error and a priori error covariance matrices respectively. An a priori profile is used to constrain the problem, as it is generally ill-posed. S_ε was constructed using the square of the DOAS fit error as the diagonal elements and the non-diagonal elements were set to 0 assuming the errors were uncorrelated. The a priori error

covariance matrix, S_a was constructed with the diagonal elements defined as

$$S_a[i,i] = (\alpha \cdot x_a[i])^2 \tag{3.3}$$

Here, α is the tuning parameter used to minimize the residual between the measured and modeled SCDs using the retrieved profiles while avoiding spurious oscillations in the retrieved profiles. The value of α was determined by the L curve method (e.g., Hansen, 1992; Steck, 2002). The L curve method is a popular technique to determine the regularization parameter in Phillips-Tikhonov regularization. In this work, the L curve was constructed by the residual norm, $||y - Kx||$ and the error norm of the solution, $||x_e||$. The residual norm decreases monotonically with increasing α while the error norm increases monotonically with each iteration. Thus, the curve formed by the error norm of the solution vs the residual norm has a characteristic L shape. Figure 3.1 shows the points of L-curve from the sensitivity studies (see section 3.3). The point with the maximum curvature balances the minimization of the residual norm and the error norm and provides the optimal solution. We used the triangle method as described in Castellanos et al. (2002) to determine the optimal solution for α. The triangle method determines the corner point by calculating the angle at the vertex of the successive triangles formed by two adjacent points and one fixed end point. The non-diagonal elements of S_a is defined as described in section 2.3.5.

The vertical column is then the sum of the individual elements of the retrieved profile and is given by

$$VCD = \sum_{i=1}^{n} x_i \cdot \Delta H_i \tag{3.4}$$

where x_i is the trace gas concentration at retrieval grid, i and ΔH_i is the height of that retrieval grid.

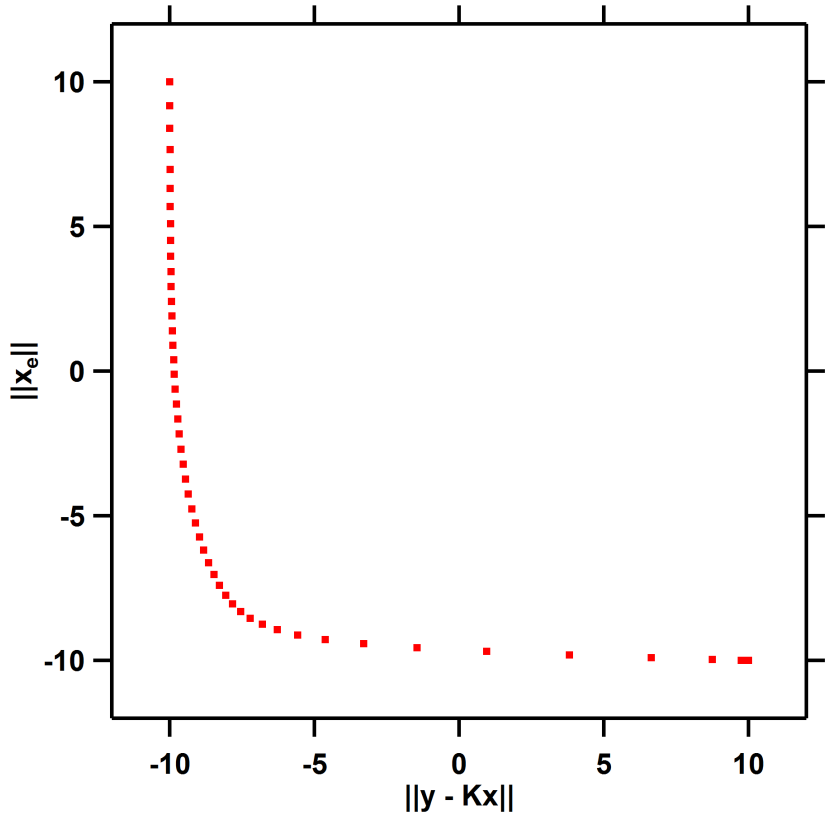

Figure 3.1: Example of L curve formed by the solution error norm vs the residual norm used to determine the optimal value of α.

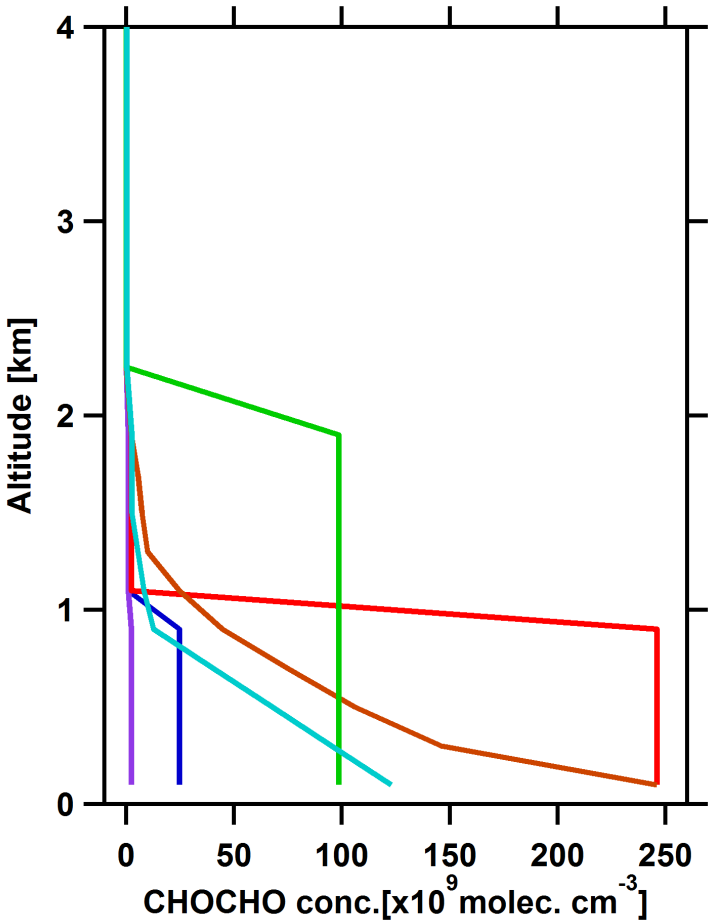

Figure 3.2: Different CHOCHO profiles used for the sensitivity studies. The vertical columns for the profiles range from 2.5 x 10^{14} - 2.5 x 10^{16} molecules cm^{-2}.

3.3 Sensitivity Studies

Sensitivity studies, using the radiative transfer model (RTM) McArtim, (Deutschmann et al., 2011) were performed to validate the method to retrieve the vertical columns as well as estimate uncertainties due to the a priori profile and aerosol load. Six CHOCHO profiles of various shapes with vertical columns ranging from 2.5 x 10^{14} to 2.5 x 10^{16} molecules cm^{-2}, and five different aerosol scenarios with aerosol optical depth (AOD) ranging from 0 to 0.5 was considered for the study. The different CHOCHO profiles used for this study are shown in Fig. 3.2. CHOCHO SCDs for different EAs were simulated for each CHOCHO profile with AOD=0.3 scenario using McArtim. A 10% Gaussian noise was added to the SCDs before using them as input SCDs in the inversion algorithm to retrieve vertical columns. Vertical columns were retrieved for the above mentioned five aerosol conditions using the six CHOCHO profiles as a priori profiles.

The correlation between the mean retrieved CHOCHO vertical columns for all the aerosol load and a priori conditions (n=30 for each point) and true CHOCHO vertical columns is shown in Fig. 3.3. The linear least square fit through the origin has a slope of 0.96 and a correlation coefficient of 0.99 indicating that the technique is well suited for retrieval of vertical columns of trace gases. The error bars in the y-axis represents the standard deviation of the retrieved vertical columns and is in the order of 9-14%. The variability between the retrieved vertical columns for a given aerosol scenario using different a priori CHOCHO profiles provides insight into the uncertainty due to a priori conditions. Similarly, the variability in VCDs for a given a priori profile but various aerosol loads gives uncertainty due to aerosol conditions. The a priori was found to be the larger source of uncertainty ($\sim$12%), while the aerosol load could lead to $\sim$7% uncertainty. Uncertainties due to other parameters such as surface albedo, single scattering albedo are expected to be very small (<2%) (see Table 2.5). Since high vertical resolution profiles measured from the same flight during low approaches (ascent/descent) will be used for column retrieval, the uncertainty due to the a priori profile is not likely to be a limiting factor for the retrieved vertical columns using this approach.

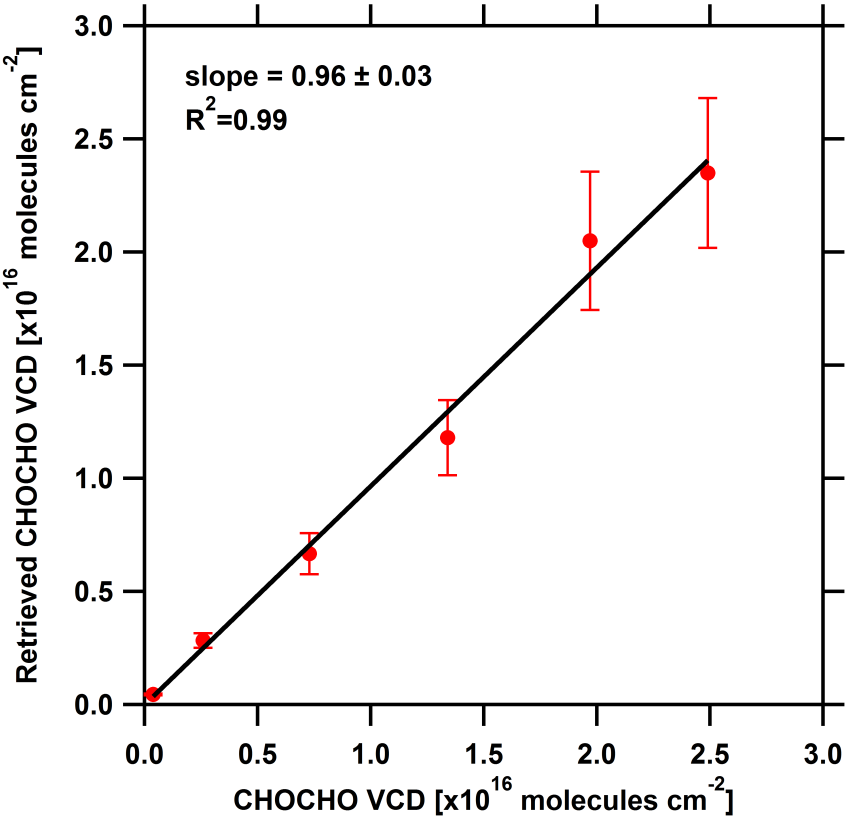

Figure 3.3: Correlation plot of mean retrieved CHOCHO vertical columns for the different aerosol and a priori conditions (see Fig. 3.2) and true CHOCHO vertical columns. Error bars represent standard deviation of the retrieved vertical columns for the different conditions.

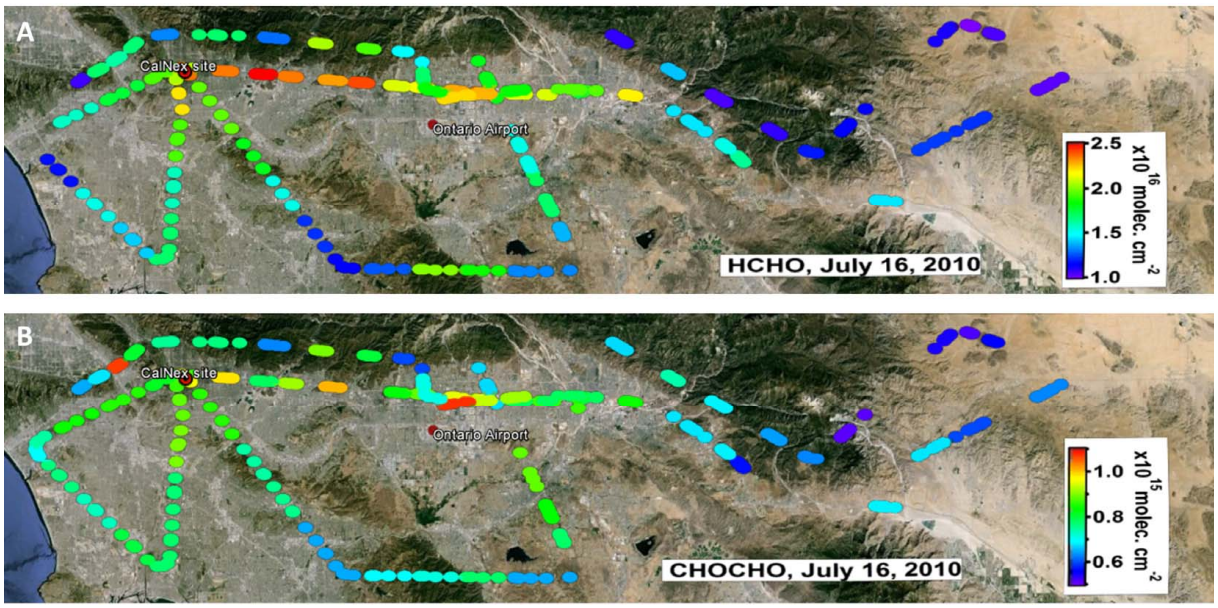

Figure 3.4: Vertical columns of (A) HCHO and (B) CHOCHO measured over the South Coast Air Basin during a flight on July 16, 2010.

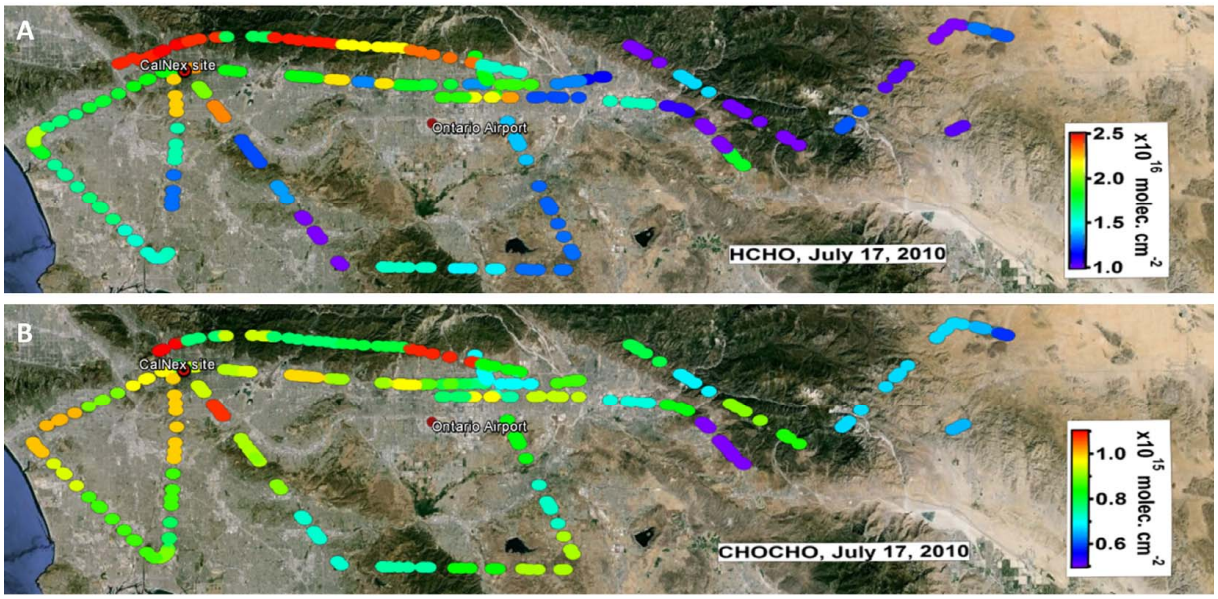

Figure 3.5: Vertical columns of (A) HCHO and (B) CHOCHO measured over the South Coast Air Basin during a flight on July 17, 2010.

3.4 Results

Figure 3.4 and 3.5 show maps of HCHO and CHOCHO VCD distribution in the SCAB from RF#46 on July 16, 2010 (10:30-14:10 PDT), and RF#48 on July 17, 2010 (10:30-14:10 PDT), respectively. Since the individual 2 second spectra were co-added for the DOAS analysis of HCHO and CHOCHO, the horizontal footprint is larger compared to NO_2 VCDs (see section 2.4.1.1). However, the maps reveal a clear trend in the spatial distribution of HCHO and CHOCHO inside the basin. Higher column amounts are observed over the western and central part of the basin especially along the foothills. The foothills in the SCAB is a major thoroughfare for the vehicular traffic (a primary source for pollutants), and this is clearly reflected in the maps. Further, the column amounts of HCHO are smaller along the foothills on July 17, a Saturday, when vehicular traffic is relatively lower compared to the weekday on July 16. In contrast, the eastern part of the basin show comparatively lower amount of HCHO and CHOCHO for both days. The uncertainty in the retrieved columns is around 20% based on the vertical column retrieval error and sensitivity studies above. The horizontal footprint of the CU AMAX-DOAS measurement of HCHO and CHOCHO VCD ($\sim$12 km) is comparable to air quality models (4 km^2) and satellite observations ($\sim$13 x 24 km^2). This makes the current dataset an excellent opportunity of evaluate air quality models and assess the value of satellite observations of HCHO and CHOCHO as a data source for air quality regulation over California.

3.5 Comparison with Models

3.5.1 HCHO

Figure 3.6 show time series of measured (black) and modeled HCHO vertical columns (red: WRF-Chem with CARB 2010 EI, green: WRF-Chem with NEI 2005 EI and orange: CMAQ with CARB 2010 EI) for the two flights on (A) July 16 and (B) on July 17, 2010. Note that the large variability in the measured columns is mostly due to the large spatial area covered by the Twin Otter during the flights. In general, the overall spatial trend as well as magnitude is better

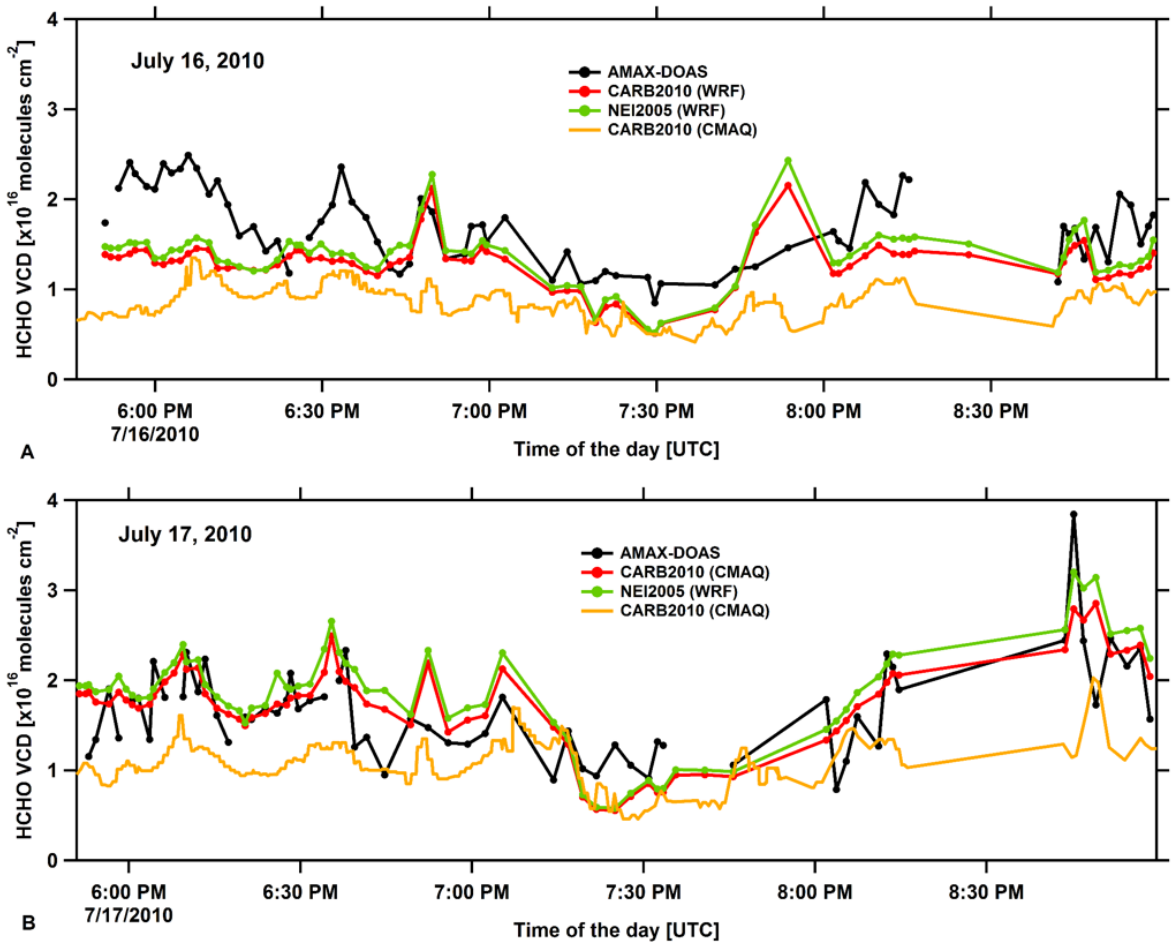

Figure 3.6: Time series of HCHO vertical columns measured (black) and modeled (red: WRF-Chem with CARB 2010 EI, green: WRF-Chem with NEI 2005 EI and orange: CMAQ with CARB 2010 EI) over the South Coast Air Basin during the flights on (A) July 16 and (B) July 17, 2010.

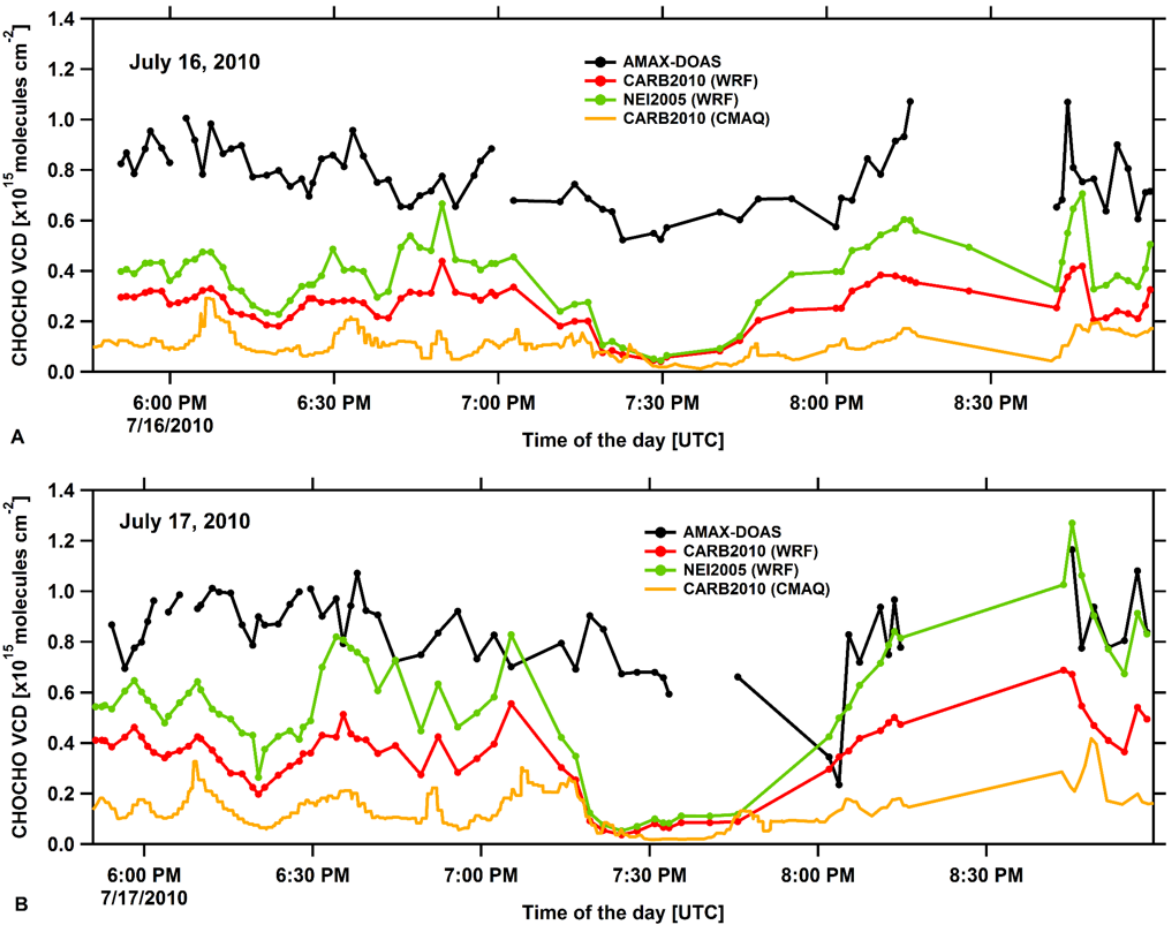

Figure 3.7: Time series of CHOCHO vertical columns measured (black) and modeled (red: WRF-Chem with CARB 2010 EI, green: WRF-Chem with NEI 2005 EI and orange: CMAQ with CARB 2010 EI) over the South Coast Air Basin during the flights on (A) July 16 and (B) July 17, 2010.

captured by the WRF-Chem simulations compared to the CMAQ. Considering one of the WRF-Chem simulations used the same emission inventory as the CMAQ, the difference in the two model outputs is likely due to the different VOC chemistry in the models.

3.5.2 CHOCHO

Figure 3.7 show the same plots as Fig. 3.6 but for CHOCHO. The model outputs seem to capture the spatial trend to some extent but CHOCHO is largely under predicted by both the models. Again, the WRF-Chem simulations are closer to the measurements. Interestingly, the WRF-Chem results with NEI 2005 EI are in better agreement with the measurements than CARB 2010 indicating that the VOC emissions might not have decreased as expected from 2005 to 2010. It is very likely that models are lacking the VOC oxidation chemistry to form CHOCHO in the atmosphere. The missing VOC source and chemistry in the models could have larger impacts on both O_3 production and SOA formation in the models.

3.6 Glyoxal to Formaldehyde Ratio, R_{GF}

The ratio of CHOCHO to HCHO (R_{GF}) has been hypothesized to reflect the speciation of VOCs in the atmosphere because of the differing yields from different classes of VOCs and similar atmospheric lifetimes of the two molecules (Vrekoussis et al., 2010; DiGangi et al., 2012; Chan Miller et al., 2014; Kaiser et al., 2015) This ratio has previously been used to determine the relative dominance of biogenic and anthropogenic VOC sources. A ratio between 0.04 and 0.06 has been reported for areas dominated by biogenic emissions based on satellite measurements of HCHO and CHOCHO (Vrekoussis et al., 2009, 2010). Lower values of R_{GF} (< 0.045) have been observed over polluted areas such as Mexico City. However, in-situ measurements in the forests over the Sierra Nevada and Rocky Mountain regions indicated the opposite, i.e. lower R_{GF} (<0.02) for biogenic emissions (DiGangi et al., 2012). More recently, Kaiser et al. (2015) suggested that R_{GF} depends not only on biogenic and anthropogenic VOC sources, but also classes of these biogenic and anthropogenic sources, based on their measurements over southeastern United States. They

observed lower R_{GF} (< 0.025) over isoprene emission dominated forests, while a relatively larger value was observed over areas with high monoterpene emission (> 0.03). This was found to be more consistent with more recent satellite borne OMI CHOCHO retrievals by Chan Miller et al. (2014). Kaiser et al. (2015) also reported a low R_{GF} over areas with active oil and natural gas production and no dependence of R_{GF} on anthropogenic emissions. Thus, there are still unresolved issues regarding R_{GF} in the scientific literature and this needs to be addressed before it could be used to determine speciation of VOC in the atmosphere.

Figure 3.8 shows maps of R_{GF} for the flights on July 16 and 17, 2010. For large part of the basin, R_{GF} is found to be between 0.04 and 0.06. R_{GF} close to or less than 0.04 is observed along the foothills of San Gabriel Mountains and downtown Los Angeles where we also observed higher NO_2 vertical columns (see Fig. 2.7). Thus, our observations support GOME-2 observed R_{GF} by Vrekoussis et al. (2010), i.e. increased influence of anthropogenic emission lowers R_{GF}. This is also corroborated by the R_{GF} from the vertical profiles of HCHO and CHOCHO over four different locations in the SCAB, Bakersfield, CA and high desert in Arizona (see Appendix A Fig. A.3 - A.8 for the profiles). Table 3.1 shows R_{GF} values for the six profiles. The lowest R_{GF} is observed at Brackett, located in the middle of the SCAB and with the highest NO_2 concentration, and the highest value is seen over the high desert. It is worth mentioning that a relatively lower R_{GF} (0.029) is observed over Bakersfield, CA, which is known to be more influenced by oil and natural gas production compared to the SCAB. This observation is more consistent with Kaiser et al. (2015) but is higher than reported by Kaiser et al. (2015) over such an area in southeastern U.S..

The basin wide average R_{GF} for the two days is 0.05 ± 0.01. This value is larger (but within the standard deviation of our measurements) than 0.041 reported by Vrekoussis et al. (2010) for Los Angeles based on GOME-2 measurements for a two year period from 2007 to 2008. A plausible explanation for the higher value is that the biogenic VOC emissions during the summer season are relatively higher in the SCAB. There could also be bias in the sampling between the two measurements due to large spatial scale covered by satellite pixels. The spatial variability in R_{GF}

over a relatively small area is intriguing by itself and deserves further investigation.

Vrekoussis et al. (2010) also reported an anti-correlation between R_{GF} and NO_2 column amounts i.e. R_{GF} decreases with increasing NO_2 amounts, based on two years of GOME-2 data. Figure 3.9 shows R_{GF} as a function of NO_2 VCD for the two flights and six profiles. There is clearly a correlation between R_{GF} and NO_2 amount in the SCAB and R_{GF} decreases with increasing NO_2. It would be interesting to investigate the correlation between observed R_{GF} and O_3 production in the basin to see how O_3 production relates to VOC speciation.

Our R_{GF} measurements over the SCAB supports observations from GOME-2 by Vrekoussis et al. (2010) while measurement in Bakersfield, CA show lower values over area affected by oil and gas production as reported by Kaiser et al. (2015). Thus, we conclude that VOC oxidation chemistry from various sources needs to be better understood before global satellite observations of R_{GF} can be used obtain information regarding VOC speciation. More importantly different R_{GF} thresholds might be necessary for different parts of the world depending upon the dominant source of VOCs in the area.

Table 3.1: Ratio of glyxoal to formaldehyde, R_{GF} for the vertical profiles at six different locations in California and Arizona, see Appendix A Fig. A.3 - A.8 for the profiles.

Site	R_{GF}
Page, AZ	0.050 ± 0.008
Bakersfield, CA	0.029 ± 0.003
Santa Monica, CA	0.048 ± 0.004
Brackett, CA	0.027 ± 0.003
Ontario, CA	0.039 ± 0.001
Banning, CA	0.044 ± 0.003

3.7 Conclusion

Retrievals of HCHO and CHOCHO VCDs along the flight track using EA scans of the CU AMAX-DOAS instrument are feasible and provide a means to obtain high spatial resolution maps of the two trace gases. The overall uncertainty in the retrieved columns are around 20% based on

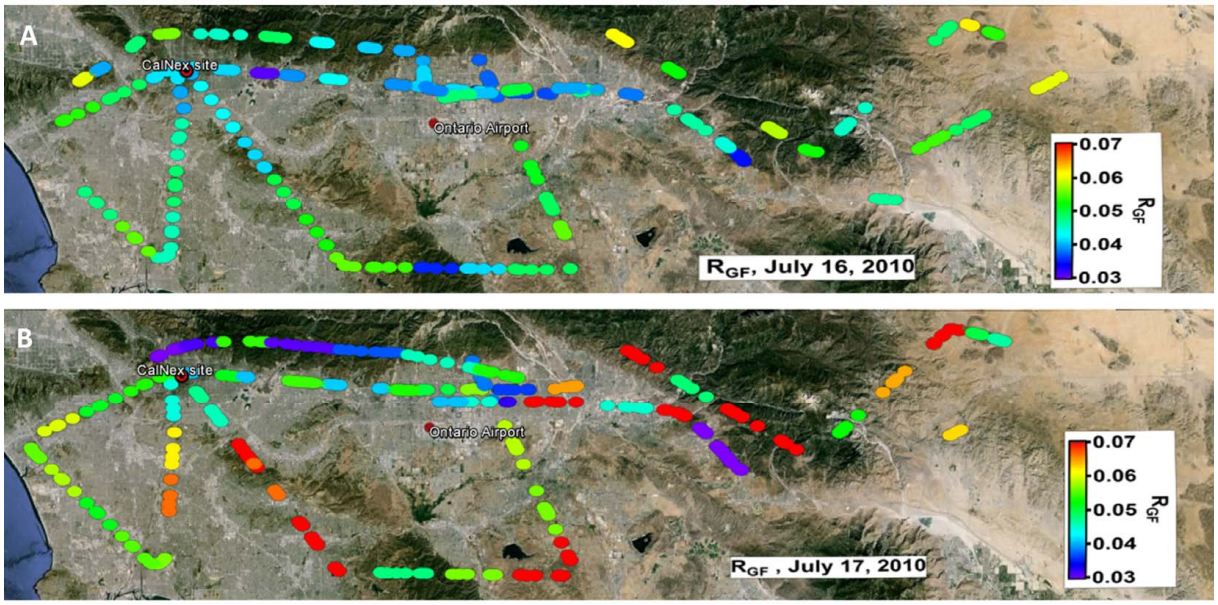

Figure 3.8: Ratio of glyoxal to formaldehyde, R_{GF} for the flights over the South Coast Air Basin on (A) July 16, 2010 and (B) July 17, 2010.

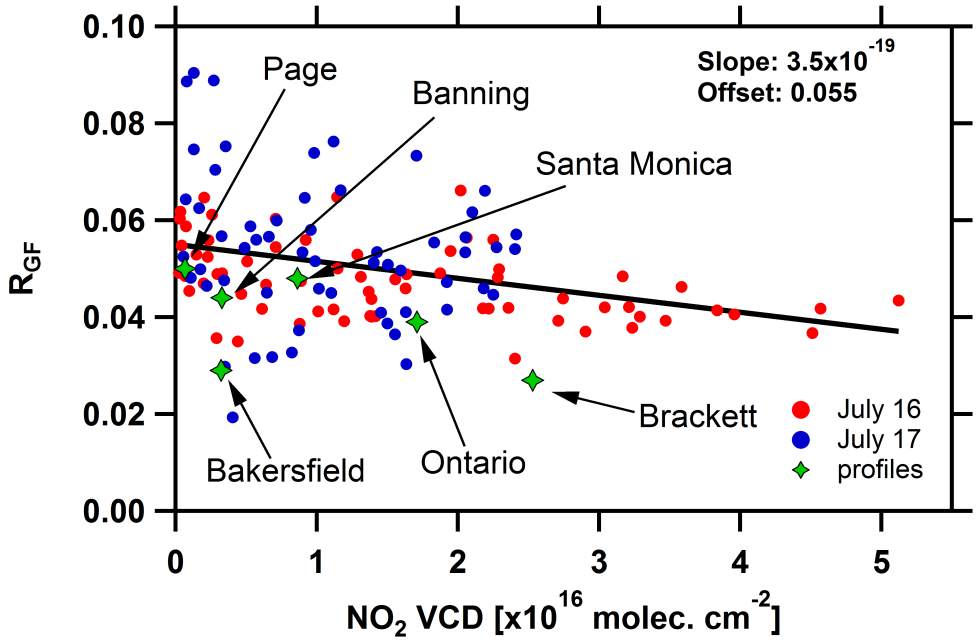

Figure 3.9: R_{GF} as a function of NO_2 vertical column.

the vertical column retrieval error and sensitivity studies on the aerosol and a priori profiles. Maps in the SCAB show higher amounts of HCHO and CHOCHO in the western and central parts of the basin, especially along the foothills. The ratio of glyoxal to formaldehyde indicates the foothills region is more influenced by anthropogenic emissions compared to the other parts of the basin, where biogenic influences are significant. Our measurements are more consistent with the GOME-2 interpretation of R_{GF}, i.e. R_{GF} decreases with increasing anthropogenic influence. However, it is very likely different R_{GF} thresholds are necessary for different regions depending upon the dominant VOC sources. Comparison of model outputs with different emission inventories showed that the models generally under estimate the amount of these gases, particularly CHOCHO. This is likely due to (i) missing VOC chemistry and (ii) lower VOC emission in the emission inventories.

HCHO and CHOCHO are indicator molecules for VOC oxidation chemistry. Maps of HCHO and CHOCHO provide powerful indicators to pinpoint location of active VOC photochemistry. The existing CU AMAX-DOAS dataset can retrieve high resolution maps of vertical columns of HCHO and CHOCHO for the identification of regions of active photochemistry and constrain VOC emission in California. These maps would also be very valuable in evaluating current atmospheric models and assessing the value of satellites as a source for data to assess air quality regulations over California.

Chapter 4

Combining Active and Passive Airborne Remote Sensing to Quantify NO_2 and O_x Production near Bakersfield, CA

This chapter was published as : Baidar, S., Volkamer, R., Alvarez, R., Brewer, A., Davies, F., Langford, A., Oetjen, H., Pearson, G., Senff, C. and Hardesty, R. M.: Combining Active and Passive Airborne Remote Sensing to Quantify NO_2 and O_x Production near Bakersfield, CA, British Journal of Environment and Climate Change, 3, 4, 566-586, doi: 10.9734/BJECC/2013/5740, 2013.

Three remote sensing instruments, namely the CU AMAX-DOAS, NOAA TOPAZ lidar and NCAS Doppler lidar, deployed aboard the NOAA Twin Otter research aircraft were used to quantify nitrogen dioxide (NO_2) and O'_x (background corrected $O_3 + NO_2$) production rates near Bakersfield, CA. By making concurrent measurements of the trace gases as well as the wind fields, we have reduced the uncertainty due to wind field in the production rates. The entire region near and around Bakersfield, CA was found to be a source for both NO_2 and O'_x. NO_2 production was highest over the city (1.35 kg hr^{-1} km^{-2} NO_2), and about 30 times lower at the background site (0.04 kg hr^{-1} km^{-2} NO_2). We also found that the NO_x emissions as represented in the CARB 2010 emission inventory agree well with our measurements over Bakersfield city (within 30%). However, emissions upwind of the city are significantly underestimated. The O'_x production was less variable, found ubiquitous, and accounts for 7.4 kg hr^{-1} km^{-2} O'_x at the background site. Interestingly, the maximum of 17.1 kg hr^{-1} km^{-2} O'_x production was observed upwind of the city. A plausible explanation for the efficient O'_x production upwind of Bakersfield, CA are favorable volatile organic compound (VOC) to NO_x ratios for O'_x production, that are affected by emissions from large oil and natural gas operations in that area. The data is probed over spatial scales that link closely

with those predicted by atmospheric models, and provide innovative means to test and improve atmospheric models that are used to manage air resources.

4.1 Introduction

Ozone (O_3) and nitrogen oxides (NO_x = NO + NO_2) are trace gases that are important components of air pollution. Health concerns of O_3 and NO_2 are related to respiratory illnesses such as chest pain, reduced lung function, asthma, emphysema whereas environmental concerns include reduced vegetation growth and acid rain. Due to these concerns both trace gases are recognized as air pollutants by air quality regulating agencies around the world, and are regulated by air quality standards and guidelines. The World Health Organization (WHO) air quality guideline recommends the standard to be set at 100 g m^{-3} (∼51 ppb) for O_3 (8 hour mean) and 40 g m^{-3} (∼21 ppb) for NO_2 (annual mean) (World Health Organisation, 2011). The National Ambient Air Quality Standard (NAAQS) set by U.S. Environmental Protection Agency are 75 ppb for O_3 (8 hour maximum) and 53 ppb for NO_2 (annual mean) (U.S. Environmental Protection Agency, 2012). Similarly, the current air quality standard for the European Union are 120 g m^{-3} (∼61 ppb) for O_3 (8 hour maximum) and 40 g m^{-3} (∼21 ppb) for NO_2 (annual mean) (European Comission, 2013). Further, O_3 is a greenhouse gas that is relevant to climate discussions (Intergovernmental Panel on Climate Change, 2013). The lifecycles of O_3 and NO_x are intimately coupled, because NO_2 photolysis by sunlight drives photochemical O_3 production, while emissions of NO destroy O_3 to form NO_2. The sum of O_3 and NO_2 is called O_x, and is a conserved quantity as it implicitly accounts for the destruction of O_3 by NO (O_3 titration). Excess O_x is formed from the oxidation of volatile organic compounds (VOCs) in the presence of NO_x (Haagensmit, 1952; Finlayson-Pitts and Pitts Jr, 2000; Seinfeld and Pandis, 2006). Fig. 4.1 shows a schematic diagram of photochemical O_3 production and evolution of NO, NO_2, O_3 and O_x concentrations upwind (I), within city limits (II) and downwind (III and IV) of an urban area. Different chemistry in these regions results in the characteristic spatial patterns in NO_x-O_3 distributions depicted in Figure 4.1, which are: (1) Background O_3 present in the upwind region (I). (2) Emission of NO_x in the city limits (II),

which leads to (3) O_3 removal via reaction with NO to produce NO_2 (titration reaction). (4) Photochemical production of O_3 from VOC-NO_x chemical cycles, which dominates downwind of the city center (III) and results in O_3 concentrations to accumulate. Further (5) the O_3 concentration does no longer accumulate in some distance downwind (IV), when NO_x has been oxidized to NO_y. NO_y is efficiently deposited or lost to aerosols resulting in insufficient NO_x to drive VOC-NO_x chemical cycles (NO_x limited region). Ultimately O_3 removal by photolysis and dry deposition leads to a slowly decreasing O_3 concentration here (Finlayson-Pitts and Pitts Jr, 2000; Seinfeld and Pandis, 2006; Stedman, 2004).

Due to their importance for air quality and human health, NO_2 and O_3 plumes from point sources and urban areas have been extensively studied. Previous studies have estimated NO_2 emission rates from point sources like power plants (Melamed et al., 2003), urban areas (Ibrahim et al., 2010; Wang et al., 2012; Beirle et al., 2011; Shaiganfar et al., 2011), O_3 production rates in urban plumes (Kleinman et al., 2002; Senff et al., 2010), the amount of O_3 transported from urban areas and its impact on regional background O_3 (Senff et al., 2010), and the relationship between O_3, NO and NO_2 as function of NO_x in urban areas (Clapp and Jenkin, 2001). However, despite decades of research, models that predict O_3 formations have not been constrained by observations at the scale of cities and immediately downwind of cities. The comparison at the local scale is important, because of uncertain and changing emission of VOCs (Warneke et al., 2012), NO_x (Kim et al., 2009), complicated transport (Langford et al., 2012, 2010; Neuman et al., 2012) over cities and downwind of cities, and also uncertainties in non-linear chemistry that couples VOCs, NO_x and O_3. Such chemistry is heavily parameterized in current atmospheric models used to predict O_3. The net O_3 production by VOC oxidation is related to the conversion of NO to NO_2 transformations by organic peroxy-and hydro peroxy radicals that are formed during the airborne oxidation of VOCs by atmospheric oxidants like OH, NO_3, O_3, and Cl radicals (Sillman, 1999). Under high NO_x conditions, the rate of O_3 production is limited by the availability of VOCs, while availability of NO_x controls the rate of O_3 production under low NO_x conditions (Sillman, 1999; Liu et al., 1987; Lin et al., 1988; Kleinman et al., 1997). For example, the testing of detailed chemical mechanisms

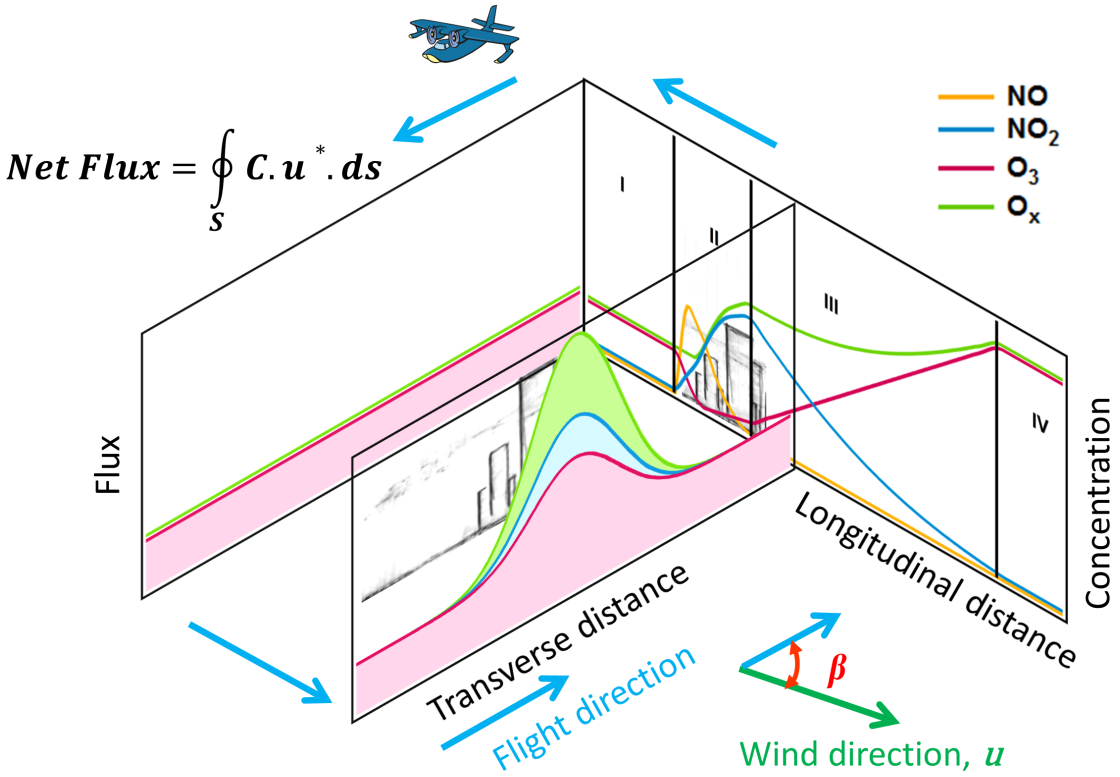

Figure 4.1: Schematic diagram showing cross-section of ozone formation in an urban area under steady wind conditions and horizontal flux divergence measurements in a closed loop for source strength calculations. Evolution of NO (orange), NO_2 (blue), O_3 (maroon) and O_x (green) over different urban regions: (I) upwind, (II) urban center, (III) downwind and (IV) further downwind are also illustrated.

of VOC oxidation using simulation chamber data (Carter and Lurmann, 1991; Carter, 1995), and field observations (Ren et al., 2003; Volkamer et al., 2010; Sheehy et al., 2010; Cazorla et al., 2012) often predict lower O_3 formation rates than that are actually being observed. The uncertainty in the chemistry of O_3 formation can be of similar relevance as uncertainties in emissions, and transport (Sheehy et al., 2010). Further, transport of O_x across city, state and international borders causes possible non-attainment of O_3 levels at sites downwind (Senff et al., 2010; Langford et al., 2010; Pusede and Cohen, 2012) and the changing boundary conditions complicates enforcement of regulations.

Over the course of the last decade, emission control policies aimed at reducing ambient O_3 levels have resulted into NO_x reductions in North America and Europe (Kim et al., 2009; Richter et al., 2005; van der A et al., 2008; Kim et al., 2006; Konovalov et al., 2008; Russell et al., 2010, 2012). NO_x sources in the troposphere are primarily related to anthropogenic emissions from on-road motor vehicles and power plants. With more than half of the world population now living in urban areas, cities have developed into hotspots for NO_x sources (Kim et al., 2009; Richter et al., 2005; van der A et al., 2008) and provide opportunities for NO_x reductions that are relevant on the global scale. This trend towards urbanization on global scales is unique in the history of mankind, and has the potential to change the planet. There is an increasing need for the development of analytical approaches that are effective at quantifying emissions of NO_x, provide experimental constraints to O_x production rates, and transport in order to refine atmospheric models that are used to manage air resources.

The primary objective of this study is to demonstrate the potential and feasibility of integrated use of passive and active remote sensing instruments and column observations to estimate the rate of NO_x emissions, and investigate the O_x production from an urban area. We use the mass conservation approach to estimate source strength for NO_2, and O_x from an urban area. Recently, ground based mobile differential optical absorption spectroscopy (DOAS) measurements have been used to estimate NO_x emissions from urban areas using this approach (Ibrahim et al., 2010; Wang et al., 2012; Shaiganfar et al., 2011). A similar approach has also been used to probe NO_x emission

from megacities using satellites (Beirle et al., 2011). We have made simultaneous measurements of NO_2 vertical columns, O_3 and wind profiles for the first time from a research aircraft. The data set provides an opportunity to estimate production of individual species and investigate the conserved quantity, O_x, which could be significantly impacted by O_3 titration in NO_x source areas such as city centers. As a case study, data from a research flight on June 15, 2010 over Bakersfield, California is presented.

4.2 Methodology

We use a mass conservation approach to estimate the emission and production source strength of NO_2 and O_x. Neglecting the molecular diffusivity term in the mass conservation equation, the NO_2 and O_x source strengths within a given volume can be estimated from their time rate of change within the volume and the horizontal flux divergence across the boundaries enclosing the volume. We have conducted measurements of vertical columns of NO_2, O_3, and wind profiles aboard a research aircraft that flew box patterns over and near an urban area. Figure 4.1 shows a conceptual schematic illustrating our approach for measuring NO_2 and O_x production rates.

Three remote sensing instruments namely (1) the University of Colorado Airborne Multi-Axis Differential Absorption Spectroscopy instrument (CU AMAX-DOAS), (2) the National Oceanic and Atmospheric Administration (NOAA) Tunable Optical Profiler for Aerosol and Ozone (TOPAZ) lidar and (3) the National Center for Atmospheric Science (NCAS) Doppler lidar were deployed aboard the NOAA Twin Otter research aircraft. The configuration of the three instruments aboard the Twin Otter is shown in Fig. 4.2. A total of 52 research flights were conducted over the course of two months (May 19-July 19, 2010) as part of the California Research at the Nexus of Air Quality and Climate Change (CalNex) (Ryerson et al., 2013) and the Carbonaceous Aerosol and Radiative Effects Study (CARES) (Zaveri et al., 2012) field campaigns in California during summer 2010. Most of the flights were focused on the Los Angeles basin and Greater Sacramento area. More details on the individual Twin Otter research flights can be found in Ryerson et al. (2013). One of the foci of this deployment was to constrain the emission and production of NO_2 and O_3 upwind,

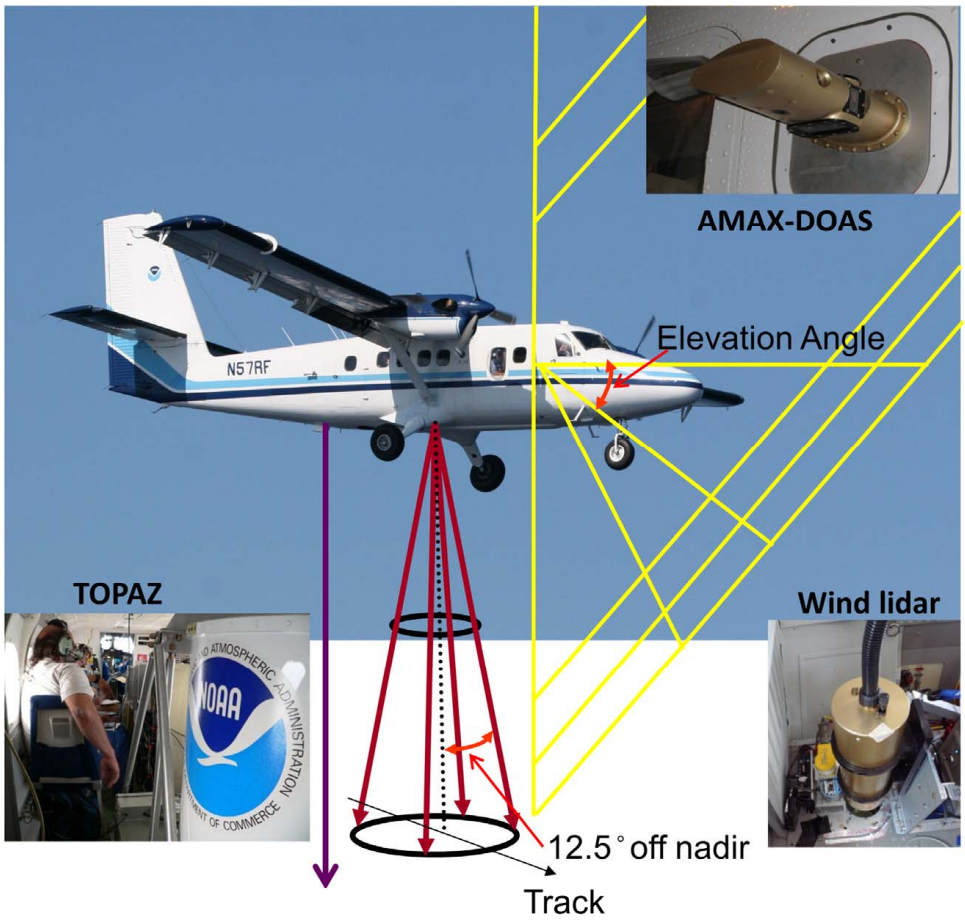

Figure 4.2: Instrumental setup of CU AMAX-DOAS, NOAA TOPAZ lidar and NCAS Doppler wind lidar aboard the NOAA Twin Otter research aircraft during CalNex and CARES field campaigns. The yellow, purple and maroon lines represent viewing geometry of CU AMAX-DOAS, NOAA TOPAZ lidar and NCAS Doppler wind lidar respectively. The three instruments are also shown in the insets.

within and downwind of urban areas.

4.2.1 AMAX-DOAS

The CU AMAX-DOAS instrument (Volkamer et al., 2009a; Baidar et al., 2013a) uses scattered sunlight as the light source (passive remote sensing). The scattered sunlight spectra are analyzed for the presence of absorbers like NO_2, glyoxal (CHOCHO), formaldehyde (HCHO) and oxygen dimer (O_4) among others using the DOAS method (Platt and Stutz, 2008). The instrument and its performance during the CalNex and CARES field campaigns are described in detail in Baidar et al. (2013a). Briefly, a telescope pylon is mounted on the outside of the window plate of the aircraft and includes a rotatable prism to collect scattered photons from different elevation angle (EA) i.e. angle relative to the horizon. Spectra collected from different EA contain information from different layers in the atmosphere and hence can be used to obtain information about vertical distribution of trace gases. The collected photons are transferred to a spectrometer / charge coupled device (CCD) detector system via optical glass fiber bundle. Here we will only present data from nadir viewing geometry from the flight over Bakersfield.

The measured spectra were analyzed, for NO_2 in a wavelength range from 433 to 460 nm, against a fixed zenith reference spectrum recorded during the same flight in a clean environment and flying at relatively high altitudes (3-5 km; 3.5 km for this flight). Zenith spectra were recorded frequently, and are used to correct for stratospheric NO_2 contributions and NO_2 above the aircraft. The nadir NO_2 differential slant column densities (dSCDs) are observed below the plane and correspond to the average integrated difference in concentration of the absorber along the light path with respect to the reference. Since most of the NO_2 sources in an urban environment are located close to the surface, the retrieved nadir dSCD was considered to be the boundary layer slant column ($dSCD_{bl}$). NO_2 nadir measurements were performed every 20-25 s and hence NO_2 data points are available every $\sim$1.5 km horizontally. For the conversion of nadir NO_2 $dSCD_{bl}$ into boundary layer vertical column densities, VCD_{bl}, the geometric Air Mass Factor (AMF_{geo}) approximation was applied.

$$AMF_{geo} = 1 + \frac{1}{cos(SZA)} = \frac{SCD_{bl}}{VCD_{bl}} \tag{4.1}$$

Here, SZA refers to solar zenith angle at the time of the measurement. This approach is in good agreement with explicit radiative transfer calculations for California while flying between 2 and 4 km. Radiative transfer calculations for the conditions of the Bakersfield case study (flight altitude: 2 km, SZA: <25°), and comparisons with ground based vertical columns consistently reveal the uncertainty in AMFgeo to be less than 7% (Baidar et al., 2013a). The overall uncertainty in NO_2 VCD for the Bakersfield case study is estimated to be around 9% (AMFgeo : <7%, NO_2 cross-section: ∼5%, DOAS fit: ∼3%) (Baidar et al., 2013a; Oetjen et al., 2013).

4.2.2 TOPAZ

NOAAs nadir-looking TOPAZ differential absorption lidar is a compact, solid-state-laser-based O_3 lidar that emits pulsed laser beams at three tunable wavelengths in the UV spectral region between about 285 and 300 nm (Alvarez II et al., 2011). The differential attenuation of the three wavelengths due to O_3 permits the retrieval of O_3 concentration profiles along the laser beam path (Browell et al., 1985). TOPAZ O_3 profiles were computed every 10 s (or about 600 m horizontally) with a vertical resolution of 90 m. The ozone profiles extend from about 400 m beneath the plane to near the ground. O_3 values in the lowest two measurement bins (lowest 180m) above ground level (AGL) are typically not used because of poor signal to noise ratio.

The TOPAZ lidar also provided aerosol backscatter profiles for the longest (and least absorbed by O_3) of the three emitted wavelengths near 300 nm. The time resolution of the aerosol backscatter profile measurements is the same as for O_3, but the vertical resolution is much finer at 6 m. We used these highly resolved lidar backscatter profile data to retrieve boundary layer height (BLH) by employing a Haar wavelet technique (Davis et al., 2000). This approach is based on the (often valid) assumption that the aerosol concentration is higher in the boundary layer (BL) than in the lower free troposphere (FT). The altitude at which the strongest aerosol gradient is found by the wavelet technique is used as an estimate of the BLH. At times, the contrast in aerosol backscatter

between the BL and the overlying FT is not sufficient to yield reliable results, and the BLH is not reported for such scenarios.

We used the BLH estimates and O_3 profiles measured with the TOPAZ lidar to compute O_3 column data integrated over the depth of the BL. To fill in data gaps in the O_3 profiles close to the ground, we averaged the ozone measurements in the lowest two gates with usable data (typically 200 - 300 m AGL) and extrapolated this value to the ground. We then integrated these extrapolated ozone profiles from the surface to the top of the BL to yield BL O_3 column density along the flight track at 10-s resolution. When BLH estimates were not available from the backscatter profile for a given O_3 profile, BLH was interpolated from adjacent measurements to compute O_3 vertical column over the BLH. TOPAZ O_3 measurements have been extensively compared to and agree well ($\pm$2-9%) with in situ airborne O_3 observations (Langford et al., 2011).

4.2.3 Doppler Wind lidar

Information on the wind structure below the aircraft was provided by the NCAS Doppler lidar (Pearson et al., 2009) mounted in the Twin Otter cabin. The lidar measures the Doppler shift of radiation scattered from atmospheric aerosol particles to estimate the component of wind along the lidar line of sight. Typical precision of the lidar radial wind measurements under acceptable aerosol loading is better than a few tens of cm s^{-1}. The lidar was mounted in the cabin with the beam transmitted vertically though a small camera port located on the underside of the aircraft (Fig. 4.2). In order to measure the horizontal component of the winds a rotatable refractive wedge mounted in the port directed the beam to 12.5° off nadir. The original scanner design included two wedges, which provides greater beam deflection and enables vertical pointing; however poor optical quality of the wedges forced us to eliminate the second wedge to reduce total attenuation through the scanner.

During flight operations the wedge was rotated to four different azimuth angles (45, 135, 225, 315°) relative to the flight track. Dwell time at each azimuth angle was 1 s for most of the Doppler measurements during CalNex. A complete rotation among the four azimuths required 8

s, including the time required to rotate the wedge to a new position. At the nominal Twin Otter speed of 60 m s^{-1} a complete 4-beam scan was completed about every 500 m. Vertical resolution of the lidar wind measurements was roughly 50 m.

Information on aircraft speed and orientation was obtained from the CU AMAX-DOAS motion compensation system (Baidar et al., 2013a). Additionally, we used the surface return at the four look angles, for which the only Doppler shift results from motion of the aircraft, to provide additional information on aircraft orientation and velocity. For the case described here, a 19-beam running average of the radial wind estimates at each of the four azimuth angles was computed to improve precision of measurements. After removal of the Doppler shift induced by aircraft motion, the velocities from the four azimuth angles were combined in a least-squares type algorithm to estimate the mean wind speed and direction in each of the 50 m range gates where backscatter was high enough to provide a strong signal. The wind speed and direction were averaged up to the BLH before further calculations of horizontal flux. The uncertainty in the wind measurement is estimated to be around 6% based on the difference between wind retrievals from a longer (19-beam) and a shorter (3-beam) running average wind fits.

4.2.4 Bakersfield Case Study

Bakersfield is a city located in the southern part of the Central Valley, CA, surrounded mostly by agricultural area and oil and natural gas operations. In the summer months, wind blows predominantly from the northwest down the valley providing steady wind conditions necessary for the method presented here. The Bakersfield area also makes for an interesting case study to probe NO_2 and O_x production from a large city influenced by intense agriculture and petrochemical production. In particular, we have probed (i) background air unaffected by urban anthropogenic emissions, (ii) air upwind, influenced by agricultural and petrochemical production, (iii) urban emissions from the city, and, (iv) the chemical evolution downwind, after it is perturbed by urban emission inputs.

The flight plan of the Twin Otter on June 15, 2010 (see Fig. 4.3) was designed to inter-

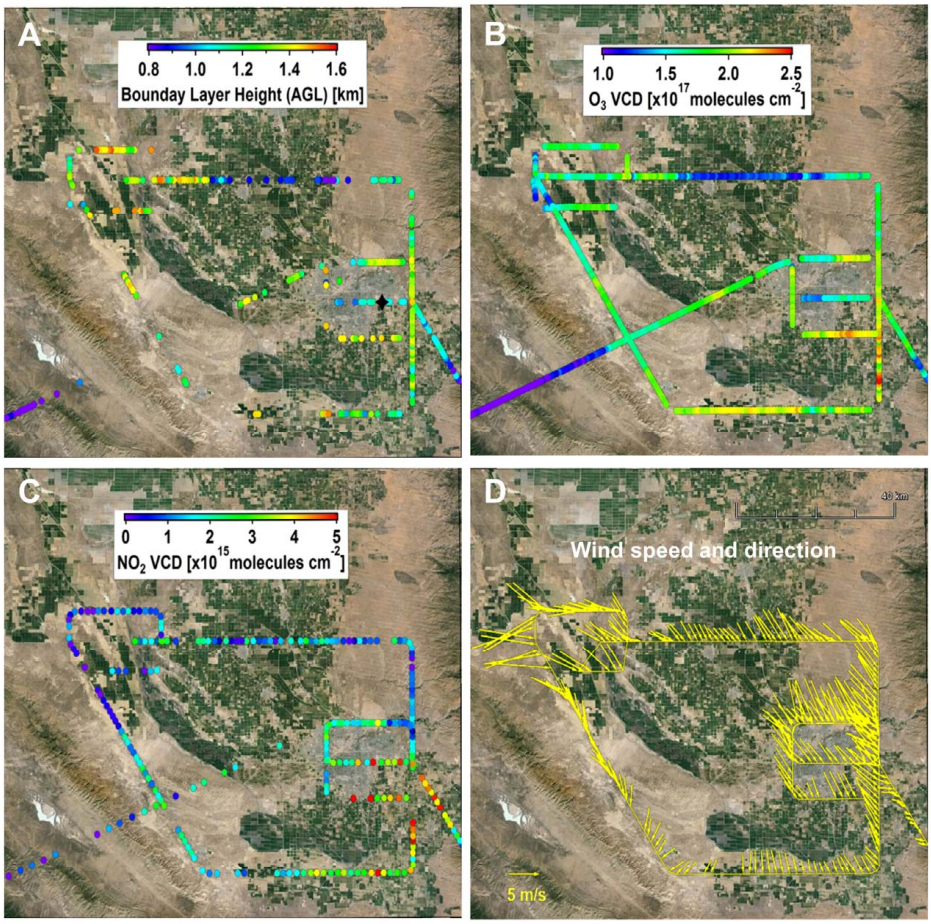

Figure 4.3: Maps of (A) Boundary layer height (BLH) above ground level, (B) O_3 vertical columns up to the BLH, (C) NO_2 vertical columns and (D) wind speed and direction from the flight over Bakersfield, CA on June 15, 2010. BLH and O_3 columns were measured by the NOAA TOPAZ lidar, NO_2 vertical columns by the CU AMAX-DOAS and wind speed and direction by the NCAS Doppler wind lidar. Black diamond on panel A shows the location of the CalNex Bakersfield supersite.

rogate NO_x emissions and constrain the O_3 production from different source regions enclosed by "boxes"applying the mass balance approach. The flight plan included an enclosed box, over areas with no major emission sources, in the northwest of Bakersfield to characterize the background conditions (Box A; see Fig. 4.4). Two boxes (Box C and D; D is twice the size of C) were flown over the city of Bakersfield to constrain emissions/productions from the city. In order to contrast NO_2 and O_3 production upwind and downwind of Bakersfield, two additional boxes (Box B and E) were created by interpolating the measured NO_2, O_3 and wind data for the western legs (shown as diamonds in Fig. 4.4). A larger trapezoid (Box F) was flown, connecting the three boxes, and enclosing the entire greater Bakersfield region. It took approximately 15, 13 and 18 minutes to complete boxes A, C and D respectively while the larger Box F took ∼75 minutes. The entire box patterns were flown at a constant altitude (∼2000 m above sea level), well above the BL. Details related to the times and meteorological conditions encountered for each boxes are summarized in Table 4.1.

4.2.5 Horizontal Flux and Source Strength

For each transect, the gas flux at a point, x along the flight path is obtained by multiplying the column measurement at that location, column(x) by the corresponding wind speed averaged over the BLH, $u^*_{avg}(x)$ (Ibrahim et al., 2010; Wang et al., 2012). The flux calculation through a surface area, A is shown in Eq. 4.2:

$$\int \overrightarrow{J} \cdot d\overrightarrow{A}_{area} = \int_{x1}^{x2} \int_{0}^{BLH} conc(z) \cdot u^*(z) \cdot dz \cdot dx = \int_{x1}^{x2} u^*_{avg}(x) \cdot column(x) \cdot dx \qquad (4.2)$$

where $\overrightarrow{J}$ corresponds to flux at any location, x to the flight direction, z to the altitude, u^* to the wind speed orthogonal to the flight direction (x) and is assumed to be constant over the BLH, u^*_{avg} to wind speed averaged up to the BLH, and

$$column = \int_{0}^{BLH} conc(z) \cdot dz \qquad (4.3)$$

Table 4.1: Meteorological conditions on June 15, 2010 for the closed boxes flown near Bakersfield, CA.

Box	Area (km x km)	Time (UTC)	wind Speed (m/s)	wind direction (°)	boundary layer height (m, AGL)	
			mean ± sdev	mean ± sdev	min	max
A	20 x 14	20:24-20:38	5.6 ± 1.7	283 ± 44	1005	1548
B	20 x 19		4.3 ± 1.6	314 ± 41	760	1425
C	20 x 9	19:41-19:54	4.1 ± 1.5	317 ± 49	936	1425
D	20 x 18	21:07-21:25	4.7 ± 0.9	317 ± 26	1049	1481
E	20 x 18		3.0 ± 0.8	328 ± 27	1066	1450
F	67 x 56	19:54-21:11	3.3 ± 1.8	313 ± 41	760	1524

$$u^* = u \cdot \sin(\beta) \tag{4.4}$$

Here u is wind speed and β is angle between wind direction and flight heading.

Flux measurement in a closed loop can be used to estimate source strength within the enclosed volume (Ibrahim et al., 2010; Wang et al., 2012). The general continuity equation in the integral form is given in Eq. 4.5 and is the basis for the source strength calculation. It involves three terms: source, flux divergence and rate of change of concentration.

$$Q_{net} = \oint_S \overrightarrow{J} \cdot d\overrightarrow{A}_{area} + \int_{Vol} \frac{\partial conc}{\partial t} \cdot dV_{Vol} \tag{4.5}$$

i.e. the net source strength of an enclosed volume, Q_{net} is the sum of fluxes through all areas along the closed loop (incoming and outgoing) and change in concentration inside the volume.

We assumed that the time dependence of concentration in the enclosed volume is zero over the time scale of our measurement. Our measurements were performed during the midday when rate of change of NO_2 and O_3 concentrations in the Bakersfield area is very small (see Fig. 4.5). Hence, we neglected the second term on the right hand side in Eq. 4.5. We also assumed that the net vertical exchange and deposition are negligible over the timescale of our measurement. Hence, the net flux i.e. the difference in fluxes entering and leaving the enclosed volume through the walls gives the source strength of the particular enclosed area for the species at the time of the measurement.

4.2.6 Daily NO_x Emission

Daily NO_x emission was estimated based on the computed NO_2 source strength, diurnal profile of NO_2 and the NO_x to NO_2 ratio measured at the California Air Resource Board (CARB) monitoring station at Bakersfield. It is computed as:

$$NO_x\ emission = \sum_{t=10}^{20} E \cdot \frac{NO_2(t)}{NO_2(t_0)} \cdot \frac{NO_x(t)}{NO_2(t)} \tag{4.6}$$

where E is the computed NO_2 production rate from Eq. 4.5, t is hour of the day, t_0 is the hour of our measurement. Therefore, the daily NO_x emission is the sum of product of measured NO_2 emission rate at time t_0, ratio of NO_2 at time t and t_0 and ratio of NO_x to NO_2 at time t over the course of the day. In order to minimize potential bias created due NO_x accumulation overnight, we only calculated daily NO_x emission for the period when NO_2 and NO_x measurements at the CARB station were stable (10:00-20:59 PST). Figure 4.5 shows NO_2, NO_x and O_3 mixing ratios measured hourly at the Bakersfield CARB monitoring station on that day. The time period of our measurement and time frame for the daily NO_x emission calculation are also shown in Fig. 4.5.

4.3 Results and Discussion

The measurement on June 15, 2010 over Bakersfield, CA was performed at mid-day when the change in NO_2 and O_3 concentration is very small, providing chemically stable conditions most suitable for source strength calculations. This is supported by NO_2 and O_3 measurements at the CARB monitoring station at Bakersfield (see Fig. 4.5). Column O_3, BLH from the NOAA TOPAZ lidar, column NO_2 from the CU AMAX-DOAS, and wind speed and direction from the NCAS Doppler lidar are shown in Fig. 4.3. Figure 4.3a shows the BLH at the time of the measurement retrieved from the TOPAZ backscatter profiles. In general, the highest O_3 and NO_2 VCDs were measured in the southeastern corners of the boxes especially for boxes with significant emission sources (Fig. 4.3b and 4.3c), consistent with the prevailing wind conditions. We calculated NO_2 and O_x production rates for the six boxes.

The wind speed and direction and BLH during the time of measurements for different boxes are given in Table 4.1. The wind was blowing predominantly from the northwest and provided ideal conditions as horizontal flux divergence measurements require steady wind fields (also see Fig. 4.3d). The variability in wind speed and direction was larger for upwind boxes (A and B) compared to downwind boxes (D and E). The BLH range for boxes D and E were also smaller compared to other boxes. The observed BLH variability is most likely a combination of land use changes (irrigated fields vs. dry land vs. urban heat island) and the fact that upslope flow over

the foothills east of Bakersfield favor BLH growth, while strong subsidence over the middle of the valley acts to suppress BL growth. We use the BLH variability to estimate the amount of BL air column susceptible to exchange with the FT (see section 4.3.1). Since all the parameters needed to quantify flux are constrained by measurements here, the horizontal variability in the BLH does not pose a limitation to our approach. Notably, the variability of BLH remains difficult to predict by atmospheric models, and warrants further investigation.

Background corrected O_x (O'_x from here on) column up to the BLH, computed as the sum of NO_2 and background corrected O_3 columns, is shown in Fig. 4.4. Background correction for O_3 is needed as we are interested in the source strength of the area at the time of measurement i.e. the amount that is being produced locally. The background correction also minimizes any potential biases due to BL-FT exchange in case of strongly varying BLH. If the BLH is constant over a box, then background correction is not necessary, because incoming and outgoing background fluxes are the same and cancel each other. Note that we measure column amount of O_3 and NO_2. Background O_3 levels were calculated based on the mean O_3 concentration over the BLH in the northwestern corner of the Box A (see Fig. 4.4). We note that background air in the Central Valley is affected by transport of pollution emitted upwind; indeed we find significant production of O'_x in Box A. However, low and similar amounts of NO_2 are transported into and out of Box A, and net production of measured species is the lowest observed anywhere. We find no evidence for major emission sources within Box A. The mean and the standard deviation of the background O_3 concentration was 1.20 $\pm$ 0.03 x 10^{12} molecules cm^{-3} (48.8 $\pm$ 1.2 ppbv, 1 ppbv = 2.46 x 10^{10} molecules cm^{-3}). It was assumed that this background O_3 concentration is representative of the entire area. A background O_3 column for each measurement point along the flight track was then calculated by multiplying the background O_3 concentration with BLH at that location. This background column was then subtracted from the measured O_3 column to determine O'_3, which corresponds to the excess O_3 column at each point along the flight track. NO_2 VCDs were used without further corrections as they were below the detection level over that area (4.2 x 10^{14} molecules cm^{-2}, $\sim$130 pptv). The average column NO_2 to O'_x partition ratio increased from 2%

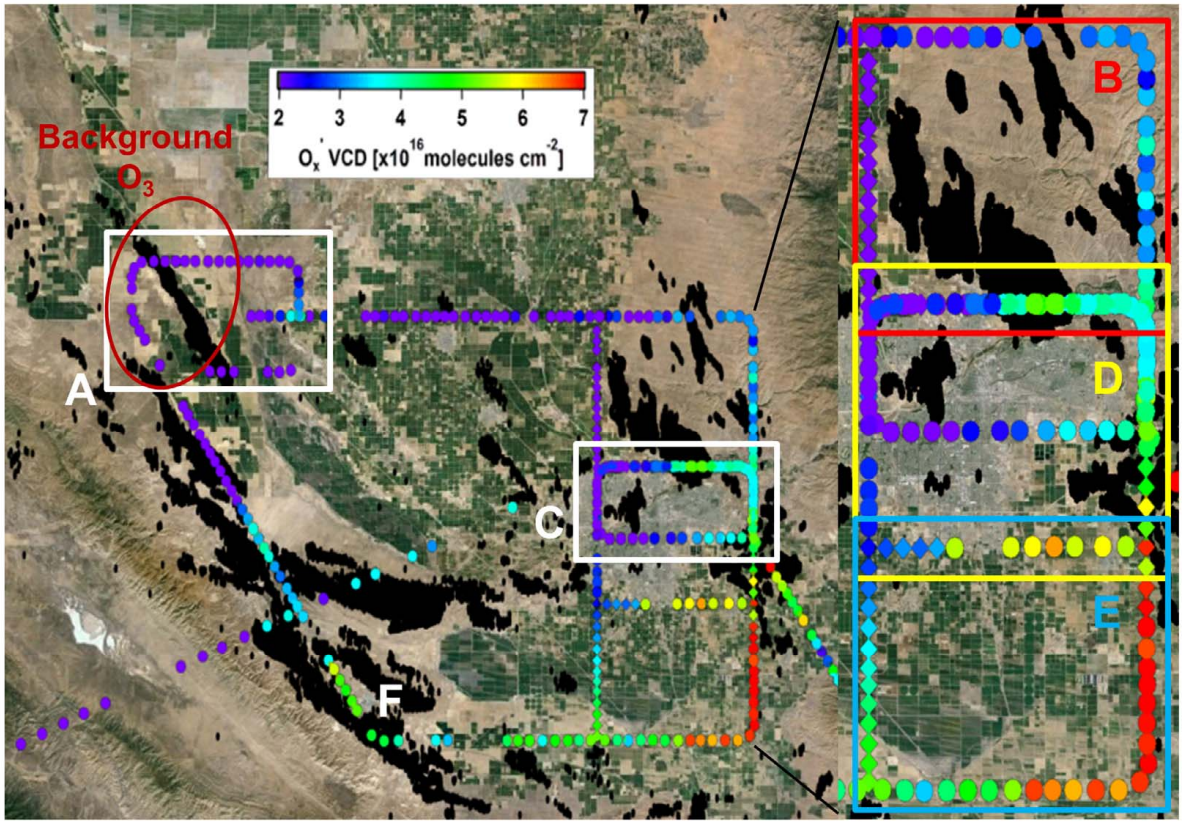

Figure 4.4: Map of O'_x vertical columns up to the BLH. Rectangles represent different boxes flown over Bakersfield: (A) upwind background area, (C) over the city, and (F) over the entire area. Colored rectangles in the inset highlight three boxes: (B) upwind, (D) over the city, and (E) downwind. Box B and E were created for comparison purposes by interpolating the western legs. Interpolated data are shown as diamonds. Black areas in the map show active oil and gas wells in the region.

over the background site to 7% over the city of Bakersfield. Thus, NO_2 gas forms a significant portion of O'_x over the urban area and would result in a bias if O_3 production rates were calculated instead of O_x. By investigating O'_x we eliminate the uncertainty due to titration of O_3 by NO to form NO_2 in the NO_x source regions.

The minimum, maximum and mean mixing ratios of NO_2 and O_3 for each box are also given in Table 4.2. The average NO_2 and O_3 concentrations were lowest for the background box. The NO_2 concentrations show higher variation within a box as well as between the boxes, indicating highly local NO_2 sources in the area. The mean O_3 does not vary much between the boxes (see Table 4.2). Notably, the maximum O_3 concentrations were observed to be generally related to the O'_x production rates in the box upwind of a given box, which is expected. Both O_3 and NO_2 showed the highest average concentration over the downwind box (E). Considering that the production rates are lower compared to the boxes upwind (B and D), there could be some accumulation of NO_2 and O_3 taking place in this box.

The enclosed areas are sources for both NO_2 and O'_x for all the boxes investigated. The NO_2 and O'_x production rates calculated for different boxes are given in Table 4.2. The production rates were calculated using Eq. 4.5 and have been normalized for the area of the boxes so that they can be directly compared to each other. As expected, the background, Box A, has the lowest production rate for both NO_2 and O'_x. The NO_2 production rate in the background box was 0.04 kg hr^{-1} km^{-2}. The NO_2 production rate was highest for Box D and amounts to 1.35 kg hr^{-1} km^{-2} above Bakersfield. This is consistent with the present knowledge that urban city limits are the dominant source for NO_x emissions in California (Kim et al., 2009). Boxes C and E, located in the northern half of Box D, and immediately downwind of Box D respectively, show about 13 times lower NO_2 production rate, indicating that the NO_2 sources from the urban area are highly localized. Interestingly, the site upwind of Bakersfield (Box B) was also found to be a significant source for NO_2 compared to the downwind site (Box E).

The O'_x production rate for the background box was 7.4 kg hr^{-1} km^{-2}, the lowest of all boxes. Box A likely represents the O'_x production rates for regions in the Bakersfield area that are

Table 4.2: NO_2 and O_3 mixing ratios and NO_2 and O'_x production rates normalized by area of the boxes for each box near Bakersfield, CA on June 15, 2010. Error in the production rates represents total propagated measurement uncertainty.

Box	Mixing ratio[1]		Production rates[4]	
	NO_2 (pptv)	O_3 (ppbv)	NO_2[2] ($x10^{-2}$ kg hr^{-1} km^{-2})	O_x'[3] (kg hr^{-1} km^{-2})
	min / max / mean	min / max / mean		
A	22 / 864 / 298	45 / 59 / 51	4 ± 8	7.4 ± 0.6
B	38 / 951 / 497	47 / 62 / 58	60 ± 6	17.1 ± 0.8
C	145 / 2425 / 852	47 / 67 / 58	11 ± 15	11 ± 2
D	149 / 1554 / 694	52 / 68 / 60	135 ± 12	13 ± 1
E	563 / 1948 / 1183	56 / 76 / 66	12 ± 10	11 ± 1
F	22 / 1948 / 582	45 / 76 / 59	39 ± 1	9.4 ± 0.1

[1] Mixing ratio is calculated assuming that the NO_2 and O_3 are uniformly distributed over the boundary layer. Conversion: 1 pptv = 2.46 x 10^7 molecules cm^{-3} and 1 ppbv = 2.46 x 10^{10} molecules cm^{-3}.
[2] Molecular weight of NO_2 (MW_{NO_2}) = 46 g/mole.
[3] Molecular weight of O_x ($MW_{O'_x}$) = 48 g/mole.
[4] Error in the production rates represents total propagated measurement uncertainty. Details are provided in section 4.3.1.

not affected directly by the urban emissions. Notably, the NO_2 production from within box A was the lowest we have observed in this case study. However, our approach does not attempt to make a correction for NO_2 losses due to photochemistry and deposition, and as such the reported NO_2 production has to be considered a lower limit. While the measured NO_2 flux was essentially zero within error of the measurements, this indicates that comparable amounts of NO_2 enter and exit the box, and that enough NO_x was present to produce O_3. This was confirmed by our observations of elevated O_x production in box A. Interestingly, the O'_x production rates over the Bakersfield city limit (Box C and D) and downwind site (Box E) only showed small enhancement (< factor of 1.75) over the background O'_x production rate. This indicates that even though the NO_2 levels in the wider area surrounding Bakersfield are relatively small (∼330 pptv), there is enough NO_x to sustain photochemical O'_x production in the entire region. Surprisingly, the upwind box (Box B) was found to have the largest O'_x production rate (17.1 kg hr^{-1} km^{-2}, 2.3 times that of Box A). The O'_x production rate in Box B was 133% that of urban Box D while the NO_2 production was only about 40% of the urban box. A plausible explanation for our observation of efficient and high O'_x production from Box B could be from enhanced VOC levels due to large oil and natural gas operations in the area, creating favorable conditions for enhanced O_3 production (high VOC/NO_x ratio). Oil and natural gas production is a source for atmospheric methane, a greenhouse gas, and other more reactive hydrocarbons as well as NO_x. The observed elevated emissions of NO_x in Box B indicate emissions are active in this area. However, the NO2 concentration was only 40% higher, while the O_3 production rate was 2.3 times higher than in background air. While higher NO_2 is likely to contribute to the higher O_3 production rate, additional VOC emissions are needed to explain such a high increase in the O_3 production rate. We are unable to conclude about additional VOC sources from our data at this point, but note that some emissions of reactive hydrocarbons are expected from the oil and natural gas production in the area that could help accelerate O_3 formation. Notably, the O_3 produced within Box B was only partially transported into the downwind boxes, where lower O_3 production rates were observed. This decrease in O_3 production rates downwind of Box B are probably related to higher NO_2 concentrations, and a

different VOC/NO_x ratio as air mixes with urban sources. The net effect of the added emissions from urban sources was a lowering of the O_3 production rates. The black areas in Fig. 4.4 represent active oil and gas wells in the region (California Department of Conservation, 2013).

The measured NO_2 production rates were used along with the diurnal profile of NO_2 and NO_x measured at the CARB monitoring network station of Bakersfield (see Fig. 4.5) to provide an estimate of daily NO_x emissions in Table 4.3. We only considered the daylight hours (10:00-20:59 PST) when the measured NO_2 and NO_x at the CARB station were stable in order to minimize potential bias due to NO_x accumulation overnight. The uncertainty in Table 4.3 only considers error in measured production rates and does not include spatial and temporal variability in NO_x and NO_2 across the region. The daily NO_x emission from Bakersfield was estimated to be around 10.7 metric tons for June 15, 2010 from 10:00-20:59 PST, compared with 13.5 tons NO_x for the same time frame in CARB 2010 emission inventory (CalNex-2010 modeling inventory) (California Air Resource Board, 2013). There is a mismatch in the location of NO_x emissions within Bakersfield. Our measurements suggest that the large portion of the emission occurs in the southern half of Box D. Note that NO_x emissions of Box C were also part of Box D (i.e., form the northern half of Box D). Emissions in Box C were comparatively very small. In contrast, emissions from Box C form a significant portion of overall emission of Box D in the CARB 2010 emission inventory. The NO_x emissions for the entire study area (Box F: 32.1 tons) were comparable to those in the CARB 2010 emission inventory in the same area (29.2 tons). However, there are differences in the locations of the NO_x emissions here as well. The background NO_x emissions are higher in the emission inventory whereas emissions over the oil and natural gas operations are significantly underestimated. Table 4.3 also compares hourly emission rates for the hour of our measurement. The measured emissions were lower for all the boxes except for the upwind box, B. Considering that the daily emission estimates are in better agreement compared to the hour of measurement, there is a discrepancy in the timing of NO_x emission in the emission inventory. The diurnal profile of NO_2 and the NO_x to NO_2 ratio varies between days as well as seasons and hence we do not attempt to scale up to the yearly NO_x emission. However with regular flights over different times

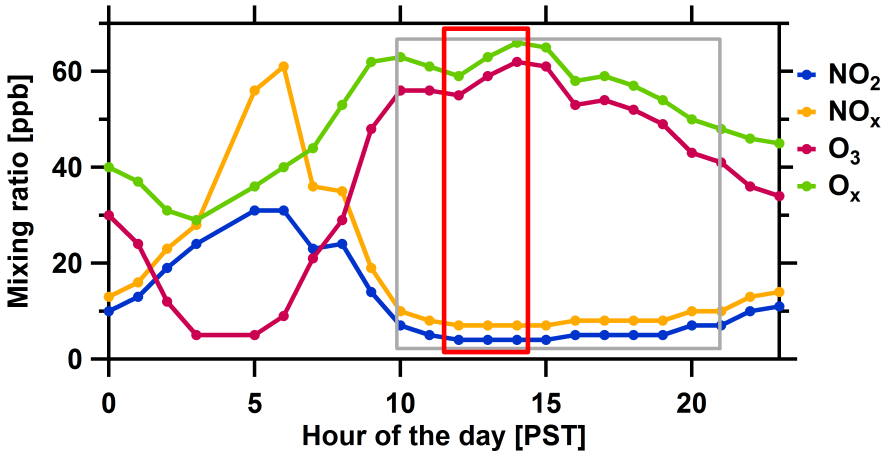

Figure 4.5: Diurnal variation of NO_2, NO_x, O_3 and O_x measured at the Bakersfield CARB monitoring station on June 15, 2010. The red and grey rectangles represent the time frame of our measurement and time period used for daily NO_x emission calculation respectively.

of the day and course of different seasons, the combination of active and passive remote sensing has the potential to constrain and improve NO_x emissions in emission inventories.

4.3.1 Error Estimates

Error in calculated fluxes and source strengths are a function of uncertainties in the measurements of individual species, winds, uncertainties about sinks (dry deposition and oxidation), and the variability of atmospheric state. Previous source strength calculations have found the uncertainty in the wind to be the largest source of error as it was not measured concurrently (Ibrahim et al., 2010; Wang et al., 2012). The uncertainty in the wind measurements in this study is estimated to be around 6%. Thus, the uncertainty in the wind measurement itself has a relatively small effect on the production rates in our study. This uncertainty is very likely not representative of wind variability within the boxes but the variability in wind are captured as part of individual wind measurements.

The overall uncertainty in NO_2 VCD is ∼9%. The contributions of different error sources in NO_2 VCD uncertainty is given in section 4.2.1. It is assumed that all of NO_2 were located inside the BL. Based on the amount of NO_2 above the BL in the vertical profile through the city center (see Fig. 4.6) we estimate this leads to a systematic error of around a few percent. The lidar O_3 profile measurements at 90 m vertical resolution have an error of typically 6-10% and can be improved by integration and averaging (Alvarez II et al., 2011; Langford et al., 2011). O_3 data were integrated vertically (∼10 points) and horizontally (2-3 points) for flux calculations at each location. As a result, the statistical uncertainties in the integrated O_3 are reduced to ∼2%. O_3 data to the ground were extrapolated from measurement at lowest two gates assuming a well-mixed BL (see section 4.2.2). Based on the difference between measurement at the CARB stations and extrapolated values, we estimate this systematic error to be around 5%. The uncertainty in BLH retrieval for TOPAZ backscatter profile is ∼7%. Considering the standard deviation of background O_3 concentration (∼4%), BLH uncertainty, O_3 column uncertainty and NO_2 column uncertainty, the overall error in the O'_x column is ∼8%. Thus the total measurement uncertainty in the individual

Table 4.3: Daily NO_x emissions calculated for June 15, 2010 using derived NO_2 production rate and NO_x and NO_2 diurnal profiles measured at CARB monitoring station at Bakersfield, CA. Error represent error due to uncertainty in the NO_x to NO_2 ratio and NO_2 diurnal variation estimated based on difference in diurnal profiles measured at Bakersfield and Shafter monitoring stations and error in the NO_2 production rates.

Box	NO_x Emissions[1] (metric tons)			
	This work		CARB 2010 emission inventory	
	Daily[2]	Hourly[3]	Daily[2]	Hourly[3]
A	0.2 ± 0.5	0.02 ± 0.04	1.1	0.11
B	5.1 ± 0.5	0.40 ± 0.04	1.1	0.11
C	0.4 ± 0.6	0.03 ± 0.05	10.6	1.05
D	10.7 ± 0.9	0.85 ± 0.07	13.5	1.33
E	0.9 ± 0.8	0.07 ± 0.06	2.2	0.22
F	32.1 ± 0.9	2.56 ± 0.07	29.2	2.91

[1] Molecular weight of NO_x (MW_{NO_x}) = 46 g/mole.
[2] Daily = 10:00-20:59 PST.
[3] Hourly = hour of our measurement.

flux measurement is ∼10-11%. The error for production rates of NO_2 and O'_x tabulated in Table 4.2 represents the overall uncertainty due to propagated error in individual column of the species and wind speed and direction for each box.

Vertical transport, atmospheric sinks and chemical transformations over the transport time between the source and the sampling regions are other potential sources of errors in the measured production rates for NO_2 and O'_x. Our approach assumes that all transport through the enclosed box occurs horizontally. Entrainment flux is a product of entrainment velocity (w_e) and the difference in trace gas concentrations between the FT and the BL (ΔC), $E_{flux} = w_e \times \Delta C$. To constrain the magnitude of potential vertical flux, we have used the rate of BLH growth as the entrainment velocity. This neglects the potential contribution of large-scale, mean vertical velocity and BLH advection. The northern legs for Box C and D overlap in location, but were flown ∼90 minutes apart and provide an opportunity to calculate the BLH growth rate. It was estimated to be 1.2 cm s^{-1}. NO_2 and O_3 concentrations were determined from the vertical profiles obtained from the low approach over the Bakersfield airport (see Fig. 4.6). We estimate the vertical flux to be 2.30 x 10^{-3} kg km^{-2} hr^{-1} for NO_2 and 0.21 kg km^{-2} hr^{-1} for O'_x for Box D. Hence, the potential error due to vertical transport is likely to be smaller than 2%.

Typical dry deposition velocities, w_d, for O_3 and NO_2 in the continental environment are 0.4 and 0.1 cm s^{-1} respectively (Finlayson-Pitts and Pitts Jr, 2000; Seinfeld and Pandis, 2006; Hauglustaine et al., 1994). We calculated the depositional flux as $D_{flux} = w_d \times C$, where C is the trace gas concentrations at the lowest layer. This could result in error of ∼10% in the O'_x and ∼1% in the NO_2 production rates. For an air mass transport time of 1 hour (between production and measurement), Ibrahim et al. (2010) estimated the error in the production rate due to chemical transformation of NO_x, based on average atmospheric NO_x lifetime, to be around 10%. Considering that the transport time for our conditions is around 0.5 hour, we estimate the error due to chemical transformation of NO_2 to be less than 5%. The atmospheric lifetime of O_3 is more than 3 times that of NO_x. Hence, we estimate the error in O'_x production rate due to chemical transformation to be smaller than 2%. Thus, the potential error due to entrainment, dry deposition and chemical

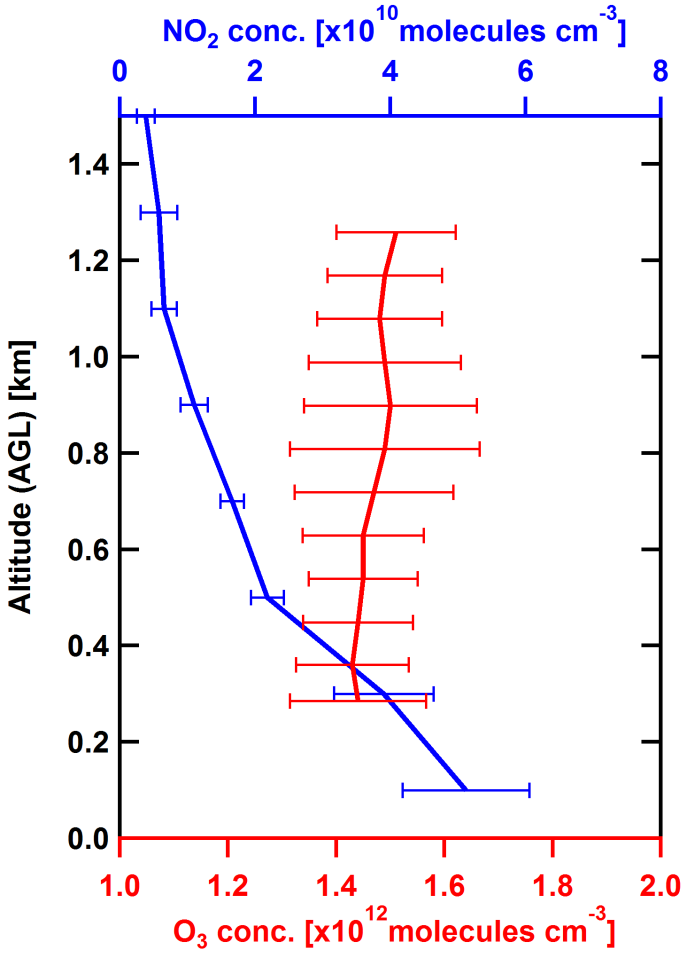

Figure 4.6: Mean O_3 profile measured by the NOAA TOPAZ lidar for Box D and NO_2 profile measured by the CU AMAX-DOAS from a low approach at the Bakersfield airport. Error bars for O_3 profile is the standard deviation of the mean and NO_2 shows measurement uncertainty.

transformation is in the same order as the total measurement uncertainty in the production rates.

We observed very high local variation in the BLH and this could also potentially result in error in the calculated production rates. The BLH variability makes the air column susceptible to exchange with the FT via horizontal transport. We have tried to bind the magnitude of this exchange in two ways: Method A calculates it as a product of the relative amount of air column (with respect to the average) susceptible to this exchange based on the difference in the average BLH measured for the upwind and downwind legs and our measured production rates; Method B calculates the same number based on the maximum and minimum BLH, assuming they occur equally frequent within each box. This is likely an upper limit estimate of such transport, since BLH is something in between most of the time. Note that we only know the BLH along the edge of the boxes and not within the boxes. We find that the uncertainty due to this potential FT exchange accounts for 1-8% (method A) of the overall horizontal flux. Method B yields 15-30% as an upper limit for FT exchange. To our knowledge the horizontally variable BLH as a mechanism for BL-FT exchange has not previously been studied, and deserves further investigation. We consider the error in horizontal fluxes from method A to be most likely representative of uncertainty in the production rates listed in Table 4.2 due to such an exchange.

4.4 Conclusion and Outlook

We demonstrated the feasibility of co-deployed active and passive remote sensing instruments aboard a research aircraft to study NO_x emissions and O_x production rates out of an urban area. NO_2 vertical column, O_3 vertical profile and wind profile measurements aboard the aircraft were used to calculate NO_2 and O'_x fluxes from source areas along the flight track.

The advantages to co-deployment of these three remote sensing instruments on a mobile platform for this kind of study are as follows:

(1) The flux calculations are fully experimentally constrained. In particular, measurements of wind and BLH along the flight track decouple horizontal and vertical transport; col-

umn measurements integrate pollutant concentrations over the BLH, and are inherently insensitive to vertical inhomogeneity.

(2) Measurements constrain NO_2, O_3, O_x (O_3 + NO_2), enabling studies of NO_x emissions and O_x production rates also over NO_x source areas, i.e., under conditions when O_3 concentrations are reduced due to NO emissions (O_3 titration to form NO_2).

(3) Colocation of all three sensors on a single platform minimizes error, and makes the flux calculation straightforward by assuring sampling on similar temporal and spatial scales.

The horizontal flux divergence approach presented here for a case study in the Bakersfield area has comparatively small error for the largest box (Box F) and larger error for the smallest box (Box C). The overall measurement uncertainty in the individual flux measurement is in the order of 10-11%. The potential error due to entrainment, dry deposition and chemical transformation is of a similar magnitude, and can in the future be further reduced through coupling with atmospheric models. Our measured NO_2 and O'_x production rates reveal higher O_3 production upwind of Bakersfield in an area with active oil and natural gas production. This finding is highly significant within experimental error, and spatially well separated from urban source areas. Comparison of NO_x emissions with the CARB 2010 emission inventory suggest that the NO_x emissions from the urban area are well represented in the inventory. However, the location and timing of the NO_x emissions within the urban area could be improved. In contrast, NO_x emissions over areas with active oil and natural gas production were found to be significantly under estimated; higher background emissions compensate for these local effects over the entire study area. The atmospheric impacts of emissions from oil and natural gas production deserve further investigation.

Models that predict O_3 formation have not previously been constrained by observations at the scale of cities and immediately downwind of cities. The synergistic benefit of combining active and passive remote sensing instruments demonstrated here holds great potential as an innovative tool to improve NO_x emission inventories (emitted amounts and location) as well as constrain O_x production rates experimentally, and over extended areas. The local variations in the BLH deserve

further investigation as to their role in the exchange of air between the BL and the FT. Further, other trace gases (e.g., formaldehyde and glyoxal) can be measured by the AMAX-DOAS and hold largely unexplored potential to extend this approach to the study of VOC oxidation rates. The co-deployment of AMAX-DOAS, TOPAZ lidar and Doppler wind lidar during 51 remaining flights provide a valuable dataset to locate and constrain NO_x emissions over much of California especially the South Coast Air Basin, the Bay area, as well to assess the transport of NO_2 and O_x across the US-Mexican border.

Chapter 5

Weakening of the Weekend Ozone Effect in California's South Coast Air Basin

Higher surface ozone (O_3) concentrations on weekends (WE) compared to weekdays (WD) in urban areas (weekend ozone effect) are typically due to the reduction in emissions of nitrogen oxides (NO_x) on weekends. We have analyzed the spatial extent and the trend in the probability of weekend ozone effect occurrences (P_{WEO3}) using measurements of nitrogen dioxide (NO_2) and O_3 from aircraft (summer 2010), and surface monitoring measurements of NO_2, O_3 and temperature from 1996-2014 at 9 different stations in South Coast Air Basin (SCAB). In recent years P_{WEO3} has decreased significantly compared to a decade ago. The major decrease happened during the economic recession from 2007-2009, after which P_{WEO3} has stabilized at a 20-35% lower level throughout most of the basin. Furthermore, the area affected by higher O_3 on weekends is decreasing in recent years. Future NO_x reductions are likely to be increasingly effective at reducing O_3 pollution in the coming decade.

5.1 Introduction

The occurrence of the weekend O_3 effect was first reported in the 1970s in New York City, Washington DC and Los Angeles (Cleveland et al., 1974; Lebron, 1975; Elkus and Wilson, 1977) and has been observed in most major urban areas in the United States (Heuss et al., 2003). The weekend O_3 effect has been particularly well studied in the Los Angeles area or South Coast Air Basin (SCAB) in California (Blanchard and Tanenbaum, 2003; Chinkin et al., 2003; Fujita et al., 2003; Pollack et al., 2012, and references within). In early 2000s, the California Air Resource Board

(CARB) conducted a major study to better understand the weekend O_3. Reduced emissions of NO_x on weekends and subsequent chemical feedback are considered to be the dominant cause for the weekend O_3 effect phenomenon (Marr and Harley, 2002a,b; Blanchard and Tanenbaum, 2003; Fujita et al., 2003; Yarwood et al., 2003, 2008; Pollack et al., 2012).

Ozone formation is a complex nonlinear process. Reductions in volatile organic compounds (VOC) and NO_x precursors can increase, decrease or leave the O_3 levels unchanged depending upon the state of the O_3 formation chemistry. Large reduction in heavy duty diesel engine vehicles on weekends results in a significant reduction in weekend NO_x emissions (Marr and Harley, 2002a; Chinkin et al., 2003; Harley et al., 2005). In contrast, VOC emissions are similar between weekdays and weekends (Marr and Harley, 2002a; Warneke et al., 2013). Thus, the decrease in NO_x emissions from weekday to weekend provides an inadvertent naturally occurring test of O_3 sensitivity to changes in NO_x emissions. It holds the key information regarding whether expected future reductions in precursor emissions due to new regulations will increase or decrease O_3 concentrations. Due to its implications for O_3 control strategies, weekend O_3 is of particular interest to policymakers.

Long term trends in NO_x, VOCs and O_3 in the SCAB have been extensively investigated in various studies (e.g., Pollack et al., 2013; Warneke et al., 2012). However only few studies exist that have investigated multi-year change in the weekend O_3 effect. Wolff et al. (2013) investigated the difference in WD and WE O_3 levels to examine the changing prevalence of weekend O_3 effect in the U.S. Here we show that years of reduction in precursor emissions due to stringent regulations combined with the most recent economic recessions has led to a significant weakening of the weekend O_3 effect due to NO_x emission reduction in the SCAB during the summer months.

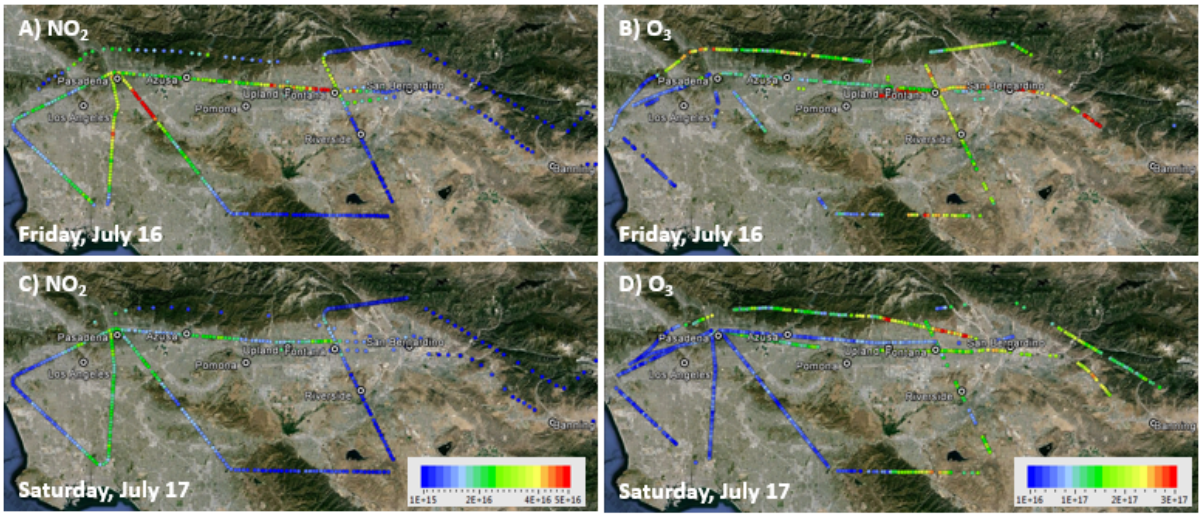

Figure 5.1: Map of the South Coast Air Basin showing locations of surface monitoring sites used in this study and distribution of NO_2 and O_3 during a weekday and a weekend. A) NO_2 vertical column measured by CU AMAX-DOAS during a research flight on Friday July 16, 2010. B) O_3 vertical column measured by NOAA TOPAZ lidar during the same flight. C) NO_2 vertical column measured on Saturday July 17, 2010. D) O_3 vertical column measured during that day. Flights on both days took place from 9:30-13:10 PST.

5.2 Observations

5.2.1 Airborne Observations

Figure 5.1 shows maps of NO_2 and O_3 vertical column inside the boundary layer measured by the CU AMAX-DOAS (Baidar et al., 2013a; Volkamer et al., 2009a) and NOAA TOPAZ lidar (Alvarez II et al., 2011) respectively on Friday July 16, 2010 and Saturday July 17, 2010 as a part of the CalNex field campaign (Ryerson et al., 2013). Description of the CU AMAX-DOAS and NOAA TOPAZ lidar measurements during CalNex can be found in Baidar et al. (2013b). The maps show the horizontal distribution of vertical columns of the two pollutants inside the SCAB on a weekday and a weekend. Column measurements are insensitive to local variations and hence should be spatially more representative and also robust. For the purpose of comparison with surface measurements in the later section, these NO_2 columns are converted to surface concentration amounts using boundary layer height measured along the flight track by the TOPAZ lidar. A very clear distinction can be observed in the spatial distribution of the two pollutants in terms of location of their highest values. NO_2 is located mostly close to the downtown Los Angeles whereas highest O_3 is seen downwind in the eastern part of the basin along the foothills. NO_2 was 35% lower on the Saturday relative to the Friday and is clearly visible in the NO_2 maps. However despite the usual decrease in NO_x on the weekend, O_3 was found to be lower on the weekend over the entire basin. The lower O_3 on the Saturday was widespread over the SCAB. Note that the meteorological conditions on both days were same with daily maximum reaching around 40 °C and the flight on both days followed identical flight plan. In order to put this unusual event in perspective with the usual weekend O_3 effect we analyzed the long term trend in the in the probability of weekend O_3 effect occurrence throughout the basin.

5.2.2 Surface Observations

CARB monitoring stations measure hourly O_3, NO_2 and temperature throughout the SCAB. Here we have analyzed data from 1996-2014 summer months (June - September) at 9 different moni-

toring stations to calculate the P_{WEO3} i.e. the probability that the O_3 on the weekend is higher than on the weekday that it followed. We focus our analysis on probability as it captures the statistical distribution in difference in WE to WD O_3 (see Appendix A Fig. A.11 - A.12) and better informs about the changing nature of the WE O_3 effect. Locations of the 9 monitoring stations inside the SCAB are also shown in Fig. 5.1. We directly compared daily mean O_3 values between 12:00-16:00 PST for Thursday and Friday (weekday) with corresponding Saturday and Sunday (weekend) O_3 values to compute the probability. Saturday and Monday are often considered transition days as they are affected by preceding weekday and weekend. Hence, the Monday-Tuesday pair was not considered for the comparison but Saturday was included to improve statistics for the weekend. A sensitivity study was carried out to test the effect of excluding Saturday as the weekend day (see Appendix A Fig. A.13). In addition for individual days to be eligible for comparison, consecutive days within the given weekday-weekend pair needed to be between 34 and 45 °C. Biogenic VOC emission such as Isoprene has been found to be temperature dependent (Guenther et al., 1993) and Pusede et al. (2014) recently reported a temperature dependent component of VOCR in San Joaquin Valley, CA. Ambient O_3 data in the SCAB also show clear distinction between different temperature ranges (see Appendix A Fig. A.9 and A.10). Note that ambient temperature reached above 40 °C when we observed lower O_3 on the weekend during CalNex. A 3 ppb equal O_3 threshold was defined as the O_3 level where weekday and weekend O_3 are statistically the same. This threshold value is based on the 1 σ confidence interval reported for mean O_3 values at the surface monitoring stations in the SCAB for summer 2010 by Pollack et al. (2012). Corresponding daily mean (12:00-16:00 PST) NO_2 values were also required to be lower on the weekend compared to the weekday as we were interested in the effect of NO_x reduction on the weekend O_3 levels. However this constrain was found to mostly filter out days when NO_2 data were not/partially available. Additionally to make the results more relevant for policy implications, only weeks when O_3 value was greater than 70 ppb (California 8 h O_3 standard) (O_3 threshold from here on) for at least one of the four days being compared in that week were included in the analysis.

Temperature in the basin was based on daily maximum temperature (12:00-16:00 PST) mea-

sured at the San Bernardino monitoring station and was considered representative for the entire basin. San Bernardino was chosen as it had the most complete data record. We don't expect the temperature to be very different at different sites within the SCAB. To determine the robustness of the results with respect to the choice of parameters, sensitivity studies were performed for the following parameters: (i) only considering Sunday as the weekend day, (ii) changing the equal O_3 threshold value from 3 ppb by ± 1 ppb, (iii) changing the O_3 threshold value from 70 ppb to 60 and 80 ppb, (iv) changing the temperature range to 25-45 °C, (v) using temperature from Upland surface monitoring station in the middle of the basin as opposed to San Bernardino, (vi) changing the time period for daily mean O_3 calculation from 12:00-16:00 PST to 11:00-17:00 PST, and (vii) changing the parameter from mean O_3 to maximum O_3.

Sensitivity studies indicated that the results were robust regardless of the parameters chosen. Effect of changing most of the parameters was found to be negligible in the P_{WEO3} across the SCAB. Some differences were observed for the western part of the SCAB when O_3 threshold was lowered to 60 ppb and maximum O_3 instead on mean O_3 was used as the statistical parameter being compared however, the overall trend remain the same. Excluding Saturday from the weekend only had the effect of worsening the statistics as half of the data points are not eligible for comparison but the trend remained the same (see Appendix A Fig. A.13). Further details from the sensitivity studies are included in the Appendix A (Fig. A.13 - A.19).

5.3 Results

Figure 5.2A shows the four year P_{WEO3} at the 9 surface monitoring sites inside the SCAB for year 2003-2006 and 2011-2014. During the four year period from 2003-2006, the P_{WEO3} was around 80-90% for the entire basin from downtown Los Angeles to San Bernardino in the east. The P_{WEO3} for the most recent four year period is 20-35% lower across most of the basin except for the western part where the decrease is around 10% (Azusa and Pasadena) or has increased (downtown Los Angeles). While the P_{WEO3} was nearly the same for the entire basin for the period 2003-2006, the P_{WEO3} gets gradually lower further east away from downtown Los Angeles for the 2011-2014

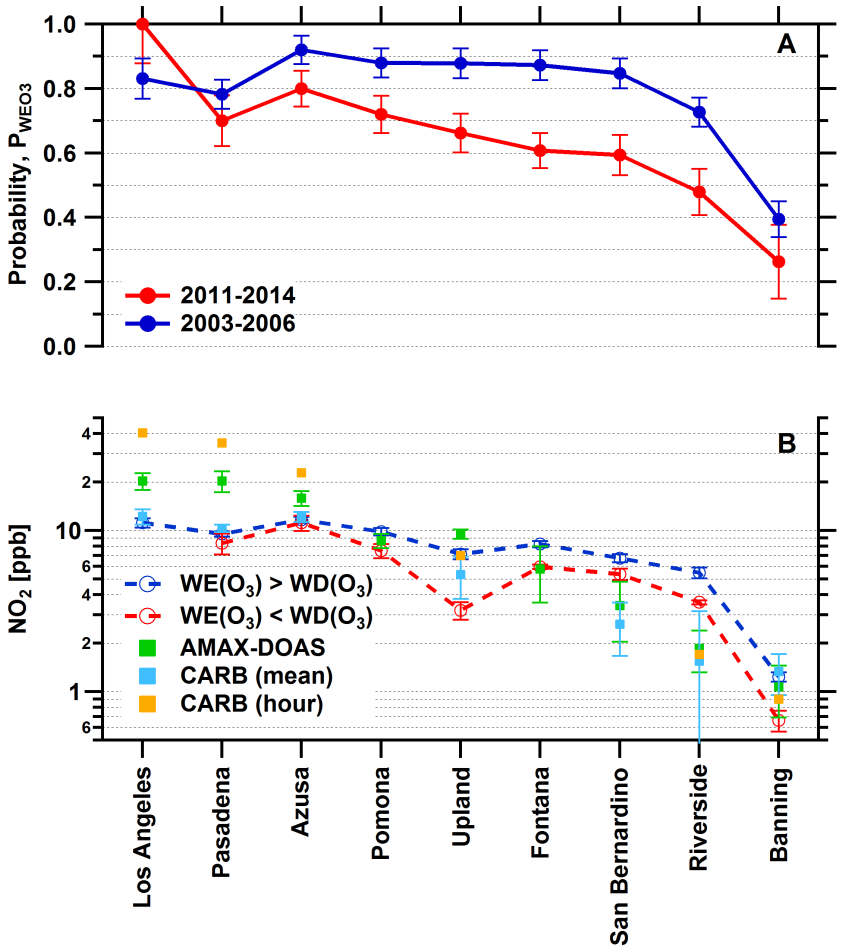

Figure 5.2: Four year probability of weekend O_3 effect occurrences (P_{WEO3}) and mean NO_2 values at different sites in the SCAB. A) Four year P_{WEO3} for 2003-2006 (blue) and 2011-2014 (red). The error bars represent uncertainty in the counting statistics. B) Mean NO_2 when weekend O_3 is higher than weekday (blue) and weekend O_3 is lower than weekday (red) for the year 2011-2014. The error bars represent standard error of the mean. AMAX-DOAS NO_2 data from Saturday, July 17 2010 at/close to the measurement sites are shown as green squares. NO_2 vertical columns were converted into mixing ratio using boundary layer height measured by NOAA TOPAZ lidar. The error bars represent standard deviation. Mean afternoon and hour of AMAX-DOAS measurement NO_2 values for July 17 2010 from the surface monitoring stations are shown as turquoise and orange squares respectively.

period. More recently, P_{WEO3} is at 60% in San Bernardino and below 50% at Riverside. P_{WEO3} was generally low in the easternmost part of the SCAB.

Figure 5.2B shows the mean NO_2 values for the last 4 years (2011-2014) when (i) weekend O_3 is higher than weekday O_3, and (ii) weekend O_3 is lower than weekday O_3. The NO_2 values are consistently found to be higher for (i) than (ii) at all sites. The error bars represent the standard error in the mean. The difference in NO_2 between when O_3 is higher and lower on the weekend is about 2 ppb for most sites. The mean NO_2 value ranges from 12 ppb in the western part of the basin to <1 ppb in the eastern most site at Banning and shows the gradual decrease in NO_x levels towards the eastern part of the SCAB.

Figure 5.3 shows the three year time series of P_{WEO3} for 4 sites in the SCAB. The probability over the downtown Los Angeles has been gradually increasing over time from around 60% in 1997 to 100% in 2014. For Upland, Riverside and Banning, the probability remained fairly constant around 80-90% for a decade from 1997-2006. A very sharp decrease is observed between 2007 and 2010 after which it increased slightly and then settled to a new probability level. Other 4 sites in the middle of the basin not shown here also followed a similar trend with a sharp decrease around 2008.

5.4 Discussion

The widespread reduction in NO_2 and O_3 affects the entire SCAB area during the hot weekend case study (ambient maximum temperature reaching around 40 °C in the SCAB). Analysis of surface monitoring data from 1996-2014 showed that the likelihood of such events is increasing in recent years, and is particularly more frequent on hot weekends (34-45 °C) during summer months in the SCAB. A decreasing trend in P_{WEO3} is also observed if the temperature constraint is effectively removed, though in this case P_{WEO3} is 5-10% higher , see Appendix A Fig. A.16. The larger decrease in P_{WEO3} on hot weekends is consistent with the temperature dependence of VOCR (Pusede et al., 2014), but the trend for widespread and decreasing P_{WEO3} is independent of temperature. Between 2003 and 2006 P_{WEO3} remained fairly constant at above 80% inside the

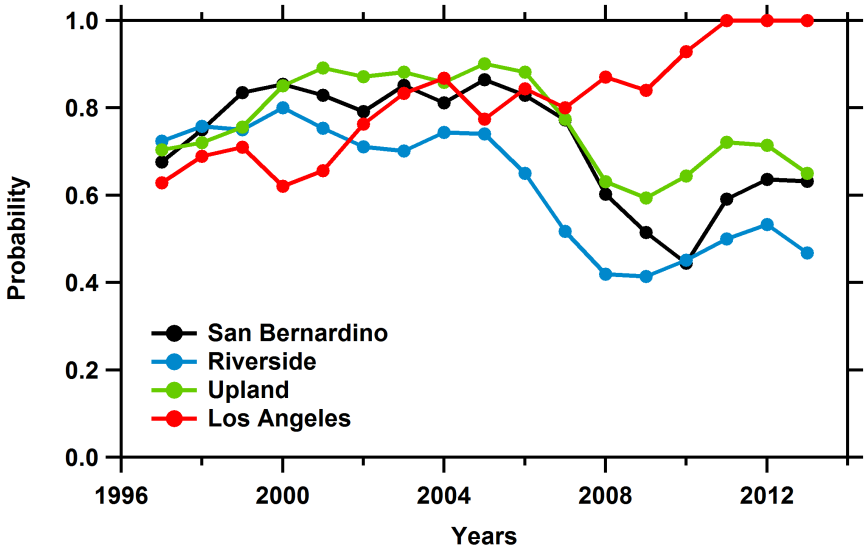

Figure 5.3: Time series of three year probability of weekend O_3 effect occurrences (P_{WEO3}) from 1996-2014 for downtown Los Angeles (red), Upland (green), Riverside (blue) and San Bernardino (black) monitoring stations in the SCAB.

SCAB indicating that the WE O_3 effect was ubiquitous over the entire basin. For the most recent four year period, the probability has not only gone down but it has decreased disproportionately over the basin compared to a decade ago. The eastern part of the basin has lower NO_x levels, and experienced a larger decrease in P_{WEO3} compared to the western part (downtown Los Angeles). This disproportionate decrease in P_{WEO3} indicates not only the weakening of the WE O_3 effect in the SCAB but also gradual shrinking of the area where NO_x reductions cause higher O_3 on the weekends. In the last four years P_{WEO3} has decreased below 50% in Riverside and is around 60% in San Bernardino and Fontana. A faster photochemical processing of VOCs and NO_x due to NO_x emission reduction on weekends has been observed over the SCAB (Pollack et al., 2012; Warneke et al., 2013). Such faster chemical processing of precursor molecules results in higher O_3 being produced closer to the sources, and it is supported by the observation of P_{WEO3} remaining the same or increasing over the western part of the SCAB (downtown Los Angeles, Pasadena, Azusa). This gradual shrinking in area affected by WE O_3 effect away from the eastern part of the basin is in sharp contrast to a decade ago when Fujita et al. (2003) reported eastward expansion of WE O_3 effect.

The VOC-to-NO_x ratio plays a critical role for the O_3 formation chemistry. At low VOC/NO_x ratio (<10 ppb C to ppb NO_x) typically seen over urban area, VOC is generally the limiting reactant. This represents VOC limited or NO_x suppressed chemical conditions for O_3 formation, and a further decrease in NO_x emissions results in more efficient O_3 production. This is considered to be the primary cause for the weekend O_3 effect. At high VOC/NO_x ratio (>10), NO_x becomes the limiting reactant and less O_3 is formed upon further decreasing NO_x emissions. This is known as NO_x limited conditions for O_3 formation (Finlayson-Pitts and Pitts Jr, 2000; Seinfeld and Pandis, 2006). The decreasing trend in P_{WEO3} over the year means that there is a higher probability that NO_x reductions on weekends result in lower WE O_3 now than any time before. As our analysis was constrained by temperature as proxy for VOC reactivity, this decreasing trend in P_{WEO3} indicate likely shift of the O_3 production chemistry on the weekends to NO_x limited conditions on increasingly more weekends. This is further supported by the observations that NO_2 values

are indeed lower when lower O_3 on the weekend is observed. Thus depending upon the extent of NO_x decrease on the weekend, the O_3 formation chemistry remains either NO_x suppressed on the weekend (increasing WE O_3), or transitions to NO_x limited conditions resulting in lower O_3 on the weekend. Figure 5.2B shows the NO_2 concentrations when the O_3 formation chemistry is in (i) the NO_x suppressed and (ii) the NO_x limited conditions at various locations in the basin. NO_x limited conditions for O_3 formation had NO_2 concentrations that ranged from 7.5 ppb (Pomona) to 3.5 ppb (Riverside) in the east. In the western part of the basin (Azusa, Pasadena and Los Angeles) where P_{WEO3} decrease was lowest, the highest NO_2 is observed. NO_2 concentrations measured by the AMAX-DOAS on Saturday, July 17, 2010 in the eastern part of the SCAB are lower than the average NO_2 typical of NO_x limited O_3 formation conditions based on the surface monitoring data (see Fig. 5.2B). Thus, this low NO_2 level is likely the reason for lower O_3 observed by the TOPAZ lidar for the case study shown in Fig. 5.1. Higher NO_2 values were observed over the western part of the basin during morning rush hour, and are consistent between AMAX-DOAS and the monitoring network (Fig. 5.2B). During the afternoon hours the NO_2 values in the western basin were near or below the NO_x limited conditions (see Fig. 5.2B). A recent study by Hong et al. (2015) showed that additional reduction of vehicular traffic due to a freeway closure in the SCAB popularly known as "Carmageddon" resulted in lower O_3 on the weekend. An average reduction in 14% in vehicular traffic due to the closure resulted in 16% lower O_3 compared to non-closure weekends. This is consistent with our observations, and provides corroborating evidence that O_3 formation chemistry is near or at the peak on weekends, and that additional NO_x reductions are increasingly likely to result in lower O_3 on weekends also in the western basin in the future.

NO_x emission in the SCAB has been decreasing over the last 5 decades (Pollack et al., 2013). It is expected to continue to go down in the SCAB in coming years as a result of new stringent emission regulations in place (California Code of Regulations, 2008, 2012). NO_x reduction can be expected from both heavy-duty diesel vehicles as well as cars and light duty trucks. In order to expedite the benefits of the national new stringent NO_x emissions standard for heavy duty vehicles, CARB is requiring all vehicles owners to retrofit or replace half of the in-use heavy duty engines

in large fleets by 2014 and all vehicles by 2023 (California Code of Regulations, 2008). This is expected to reduce summertime diesel NO_x emission in Los Angeles area by greater than 50% over the five years from 2010 to 2015 and a slower reductions in the following decade from 2015 to 2025 (Millstein and Harley, 2010). Further, the Advanced Clean Cars Program in California is expected to reduce NO_x emission by 75% from cars and light duty vehicles by year 2025 (California Code of Regulations, 2012). With the O_3 formation chemistry already near its peak, and/or even in NO_x limited conditions for an increasing number of weekends, these regulations aimed at reducing NO_x emission are likely to be progressively more effective at reducing O_3 pollution in the SCAB in the decade ahead.

5.4.1 Effect of Economic Recession

The period of sharp decrease in P_{WEO3} observed between 2007 and 2010 coincides with the most recent economic recession. Satellite observations have shown a much larger than average decrease in NO_x in many parts of the world during the economic slowdown. Russell et al. (2012) reported around 15% per year, 3 times faster than usual, NO_x reduction in Los Angles for the period 2007-2009 based on Ozone Monitoring Instrument (OMI) observations from space. Similarly, fuel sales data for diesel fuel and on road diesel NO_x emission in the SCAB showed a 17-20% decrease between 2007 and 2009 (McDonald et al., 2012). Before 2007 fuel sales data for diesel fuel and on road diesel NO_x emissions showed a gradually increasing trend. After the recession as the economy recovered the P_{WEO3} increased slightly but seems to have settled at a new level in recent years. Satellite observations also show a much slower decrease in NO_x after the recession ($\sim$2% per year from 2009-2011; Russell et al. (2012)). The decrease observed for diesel fuel sales and on road diesel NO_x emission also stopped after 2009 (McDonald et al., 2012). Thus our analysis showed that the economic recession not only had an impact on NO_x emissions, but this sharp decrease very likely has also expedited a reduction in P_{WEO3}. More importantly, the more recent value of P_{WEO3} is significantly different than what it was a decade ago.

The change in P_{WEO3} is driven by the relative O_3 trend on WE vs WD. If both show a similar

trend, then P_{WEO3} remains the same. Prior to the recession (2000-2006) O_3 on both WD and WE followed similar trends, and as a result P_{WEO3} did not exhibit a significant trend. During the recession, larger NO_x reduction likely fueled increasing WD O_3 while it resulted in decreasing WE O_3. This contrasting behavior contributed to the significant trend for decreasing P_{WEO3}. After the recession both WD and WE O_3 are again following the same decreasing trend, and P_{WEO3} has settled to a new lower value (see Appendix A Fig. A.9 and A.10 for trends in WD and WE O_3). This recent lower level of P_{WEO3} is most likely the result of new technology used is diesel trucks, which had been expected to result in reductions of NO_x emissions after 2010 (Millstein and Harley, 2010), though a more detailed analysis of the drivers for the lower P_{WEO3} deserves further investigation.

5.5 Conclusion

We observed a widespread lower O_3 in the SCAB despite the usual decrease in NO_x on a hot weekend during summer 2010. This observation was found to be spatially representative of the surface measurement networks inside the SCAB. Analysis of P_{WEO3} based on the routine measurements of NO_2, O_3 and temperature at 9 different CARB surface monitoring stations showed the observation during the hot weekend in summer 2010 is happening more frequently now. The P_{WEO3} was around 80-90% throughout the basin in 2003-2006 and has decreased by 20-35% in recent years at all monitoring sites except in the western part of the basin where the decrease is smaller ($\sim$10% for Pasadena and Azusa) or has increased (downtown Los Angeles). This decrease in P_{WEO3} was robust for a range of temperatures; P_{WEO3} decrease was highest for hot weekends, and 5-10% lower when a larger temperature range (25-45 °C) was considered. The decrease in P_{WEO3} was larger over the eastern part of the basin compared to the western part of the basin closer to downtown Los Angeles. This suggests that the area affected by the weekend O_3 effect is shrinking and the eastern part of the basin is less likely to be affected by this phenomenon in the future. Comparison of NO_2 values when weekend O_3 is either lower or higher than weekday indicated O_3 formation chemistry on weekends is at its peak in the SCAB and future regulations

aimed at reducing NO_x emissions are likely to be more effective in decreasing O_3 pollution on weekends in the coming decade.

Chapter 6

Confirmation of Sand Signature Observed by Satellite Borne Instruments

Quality of trace gas retrieval using DOAS method from remote sensing data from satellite, airborne and ground based systems depend upon the accurate representation of both atmospheric and surface properties at the time of measurements. Recently, a need for a reference spectrum for sand was demonstrated for NO_2 retrieval over desert regions from satellite borne instrument, GOME-2. We present evidence for the sand signature observed by the satellite borne instruments to be a surface property of the measurement location. CU AMAX-DOAS measurements aboard the NOAA Twin Otter over the desert in Nevada and Arizona observed the largest sand signal at nadir viewing geometry and gradually decreased away from nadir towards zenith indicating that the sand signal originates at or near the surface. This decrease in sand fit coefficient was consistent with decrease in ground scattered photons expected at different EAs. We also show that the observed sand fit coefficients from OMI satellite borne instrument correlates strongly with independent surface albedo measurements aboard the NOAA Twin Otter. The correlation was fairly weak for the CU AMAX-DOAS nadir measurements and is likely due to difference is spatial scale probed by the two sensors. The sand reference spectrum was found to be non critical for DOAS analysis of trace gases from AMAX-DOAS measurements. However, including the sand reference spectrum in the analysis does not affect retrieval of O_2-O_2 collision complexes (O_4).

6.1 Introduction

Remote sensing signal of trace gases such as NO_2 in the atmosphere is affected by both atmospheric and surface properties. Proper representation of these effects in the data processing is critical for accurate retrieval of trace gases from the measured signal using a technique like Differential Optical Absorption Spectroscopy (DOAS) (Platt and Stutz, 2008). The quality of the retrieval is given by the root mean square (RMS) of non-linear least square fitting. During the process of improving the nitrogen dioxide (NO_2) retrieval from GOME-2 satellite instrument (Callies et al., 2000) using the DOAS method, Richter et al. (2011) discovered a need for an additional spectral feature specific to sand or soil over the desert regions. A sand reference spectrum was empirically determined using two nadir spectra; one with the sand signature and one without the sand signature and included in the fit. Figure 6.1 shows the smoothed reference sand spectrum derived by Richter et al. (2011). They also found a similar structure from laboratory measurement of reflectance from sand using a MAX-DOAS instrument. Inclusion of the empirically determined sand signature reference spectrum in the DOAS analysis improved the NO_2 retrieval over the desert regions. The map of retrieved GOME-2 sand signal for August 2007 is shown in Fig. 6.2 and it clearly shows enhanced sand signal over the desert area, especially the Saharan desert. However, they did not rule out the possibility that the empirically determined cross section of sand is not affected by other atmospheric and/or instrumental contributions.

Merlaud et al. (2012) showed that inclusion of GOME-2 derived sand reference cross section in the DOAS analysis of NO_2 from an airborne DOAS instrument improved the RMS while flying over the Saharan desert and other regions with bare soil. They also identified several episodes of enhanced soil signal that were coincident with sand storms. This supported that the empirically determined sand reference spectrum has a geophysical origin and very likely the source of the signal is sand. The DOAS instrument deployed on the ultralight aircraft as described on Merlaud et al. (2012) only had one viewing geometry; forward pointing telescope with a field of view (FOV) of 25°. Hence, the exact nature of source of the sand signal i.e. whether it is atmospheric and/or

surface property is not clear from these measurements.

CU AMAX-DOAS instrument (Baidar et al., 2013a; Volkamer et al., 2009a) consists of a fully rotatable telescope prism and hence, capable of making measurements above, forward and below the aircraft. During the CalNex (Ryerson et al., 2013) and CARES (Zaveri et al., 2012) field campaigns in 2010, CU AMAX-DOAS made measurements over wide range of surface properties from urban areas to deserts. These measurements above, forward and below of the aircraft especially over the deserts provide a unique opportunity to (i) potentially unambiguously pinpoint whether the sand signal observed by both Richter et al. (2011) and Merlaud et al. (2012) have their origin in the atmosphere, surface or both properties, and (ii) assess the need for the sand reference spectrum for the DOAS analysis of trace gases from AMAX-DOAS measurements. Here we examined a flight over the desert in Nevada and Arizona on July 19, 2010 to gain further insight on the source of the sand signal. Further, the NOAA Twin Otter also included independent surface albedo measurements and we investigated the correlation between the surface albedo and the sand signal. We also examined the correlation between the surface albedo measured on the aircraft and the sand signal observed by the satellite borne Ozone Monitoring Instrument (OMI) (Levelt et al., 2006).

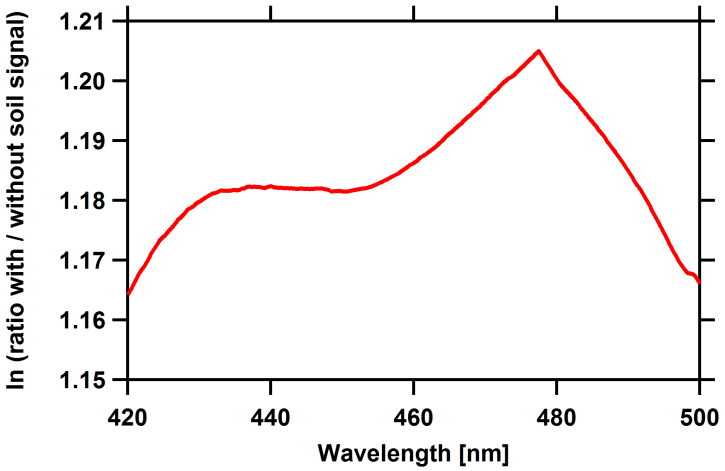

Figure 6.1: Sand reference cross-section derived from GOME-2 measurements by Richter et al. (2011).

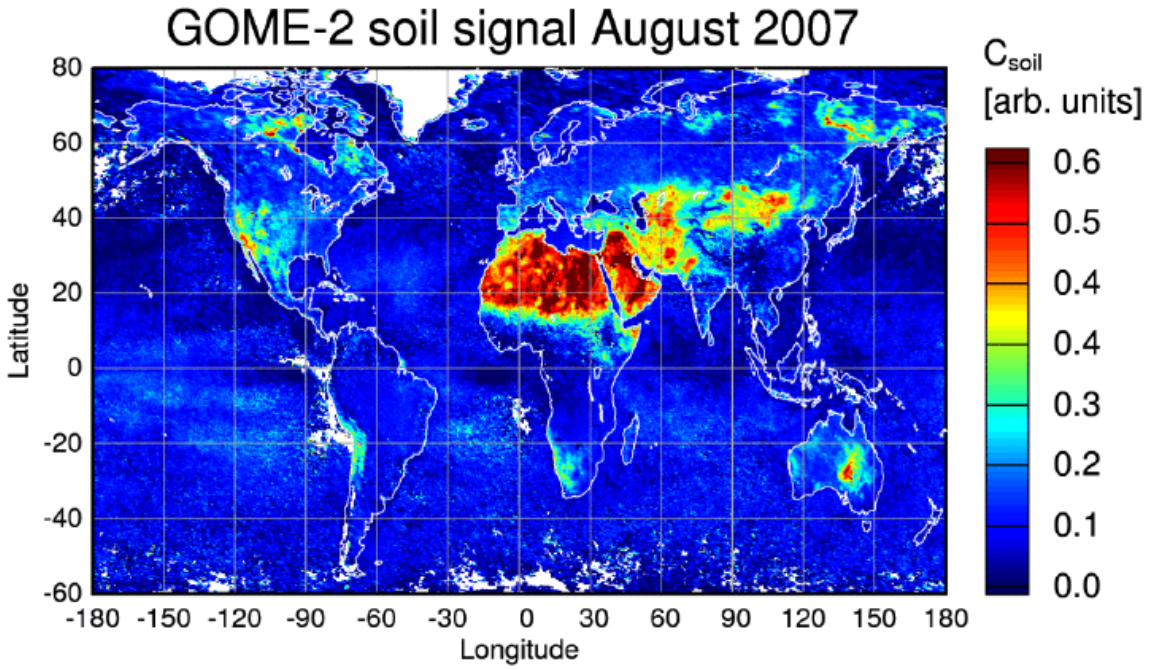

Figure 6.2: Map of sand fitting coefficient from GOME-2 for August 2007 (Richter et al., 2011).

6.2 Experimental

6.2.1 CU-AMAX DOAS measurements on July 19, 2010

The CU AMAX-DOAS instrument uses scattered sunlight as the light source. The scattered sunlight spectra are analyzed for the presence of absorbers like NO_2, glyoxal (CHOCHO), formaldehyde (HCHO) and O_2-O_2 collision complexes (O_4) among others using the DOAS method. The instrument and its performance during the CalNex and CARES field campaigns are described in detail in Baidar et al. (2013a). Briefly, a telescope pylon is mounted on the outside of the window plate of the aircraft and includes a rotatable prism to collect scattered photons from different elevation angles (EA) i.e. angle relative to the horizon. Spectra collected from different EA contain different amount of information from different atmospheric layers and hence is generally used to obtain information about vertical distribution of trace gases. They also contain different amount of ground scattered photon signal and hence could be used to gain insight into surface properties. The collected photons are transferred to a spectrometer/charge coupled device (CCD) detector system via optical glass fiber bundle. The spectrometer-detector system consists of a two spectrometer-detector combination. Here we will only present data from the spectrometer used primarily for the measurement of O_4, which is equipped with a 500 grooves/mm grating, blazed at 330 nm and covers the wavelength range of 350-720 nm. It is used to measure all four major O_4 absorption bands at 360, 477, 577 and 630 nm.

The research flight on July 19, 2010 took place from Ontario, CA to Page, AZ on route to Broomfield, CO. The flight left Ontario, CA at around 3:00 PM UTC and arrived at Page, AZ at ~6:45 PM UTC. We focused our analysis during the level leg of the flight at ~5000 m above sea level (ASL) from 3:30 - 6:05 PM UTC. The EA scan during the level leg included 0°, ±2°, ±5°, ±10°, ±20°, ±90° angles with 0° being horizontal, +90° representing zenith and -90° representing nadir viewing geometry. EAs -20° and -90° were included 3 times and 2 times respectively in each EA scan sequence. The spectra collected at these EAs were analyzed using the DOAS method with a zenith spectrum from the same flight as the Fraunhofer reference spectrum. Depending upon

the location of the source of the signal, the relative distribution of signal in different EAs would be different. If the source of the sand signal is primarily the sand particles in the air e.g. sand storm, the shallower EAs (0°, -2°, -5°, -10°) would likely have higher sand fit coefficient compared to nadir. In contrast, if the source of the sand signal is mainly due to the surface property, we expect to see the largest signal for the nadir viewing geometry and subsequently decreasing away from the nadir viewing geometry.

6.2.2 DOAS Analysis

Measured spectra from the O_4 spectrometer were analyzed for O_4 in a wavelength range from 425-497 nm using a fixed zenith reference spectrum recorded during the same flight (4:30 PM UTC). Reference cross sections for O_4 (Hermans, 2002), NO_2 (Vandaele et al., 1998), O_3 (Bogumil et al., 2003), H_2O (Rothman et al., 2005), and sand (Richter et al., 2011) were fitted along with a Ring cross section to correct for the Ring effect (Grainger and Ring, 1962) using the WinDOAS software (Fayt and Van Roozendael, 2001). In addition a 3^{rd} order polynomial was included in the fit to account for Mie and Rayleigh scattering. This analysis setting is representative of the GOME-2 NO_2 retrieval setting and is considered case #1 of our analysis. We used 3 additional analysis settings to verify the need for the sand reference spectrum and also to test for the effect of using higher order polynomial. The analysis settings for the 4 cases are described in Table 6.1. Case #2 is same as case#1 except for the exclusion of the sand reference cross section and is used to test the need for a separate sand reference cross section in the retrieval. We also tested the effect of using polynomial 5 with and without the sand cross section as our standard O_4 retrieval setting uses fifth order polynomial (Baidar et al., 2013a). The empirically determined sand reference spectrum from GOME-2 was included in the DOAS analysis (see Fig. 6.1). We focused our analysis on O_4 retrieval rather than NO_2 due to coarse resolution of the O_4 spectrometer ($\sim$2.2 nm).

Table 6.1: Different analysis settings used for sensitivity studies of sand signal retrieval.

Case #	Polynomial order	Sand reference	comments
1	3	yes	new GOME-2 NO_2
2	3	no	
3	5	yes	
4	5	no	standard AMAX O_4

6.2.3 Radiative Transfer Modeling

We used radiative transfer model (RTM), McArtim (Deutschmann et al., 2011), to help interpret the retrieved sand signal. McArtim is described in detail in section 2.3.2. We calculated fraction of ground scattered photons (Ph_{gs}) observed by the CU AMAX-DOAS instrument at different EAs along the flight track. Ancillary input parameters pressure and temperature was obtained from NCEP/NCAR reanalysis, while surface albedo (SA) was measured aboard the aircraft (Oetjen et al., 2013). A one km thick aerosol layer with optical depth of 0.15 (representative value based on AERONET stations near the flight area) was also included in the model. As our goal was to qualitatively, rather than quantitatively, interpret the retrieved sand signal, we did not account for the effect of changing aerosol and terrain along the flight track. A 3-dimensional RTM calculations would be required to properly account for changing atmospheric and surface conditions along the flight track.

6.3 Results and Discussion

6.3.1 Proof of need for Sand Reference Spectrum

Figure 6.3 shows time series of the RMS for the nadir viewing geometry for the 4 different cases listed in Table 6.1. Case #1 represents the new GOME-2 NO_2 retrieval setting. Case #2 is same as the case #1 except for the lack of sand reference spectrum in the analysis. The RMS for the case #2 (green line) was found to be relatively very high compared to the case #1 (red line) and indicated the need for inclusion of the sand reference spectrum to improve the DOAS retrieval.

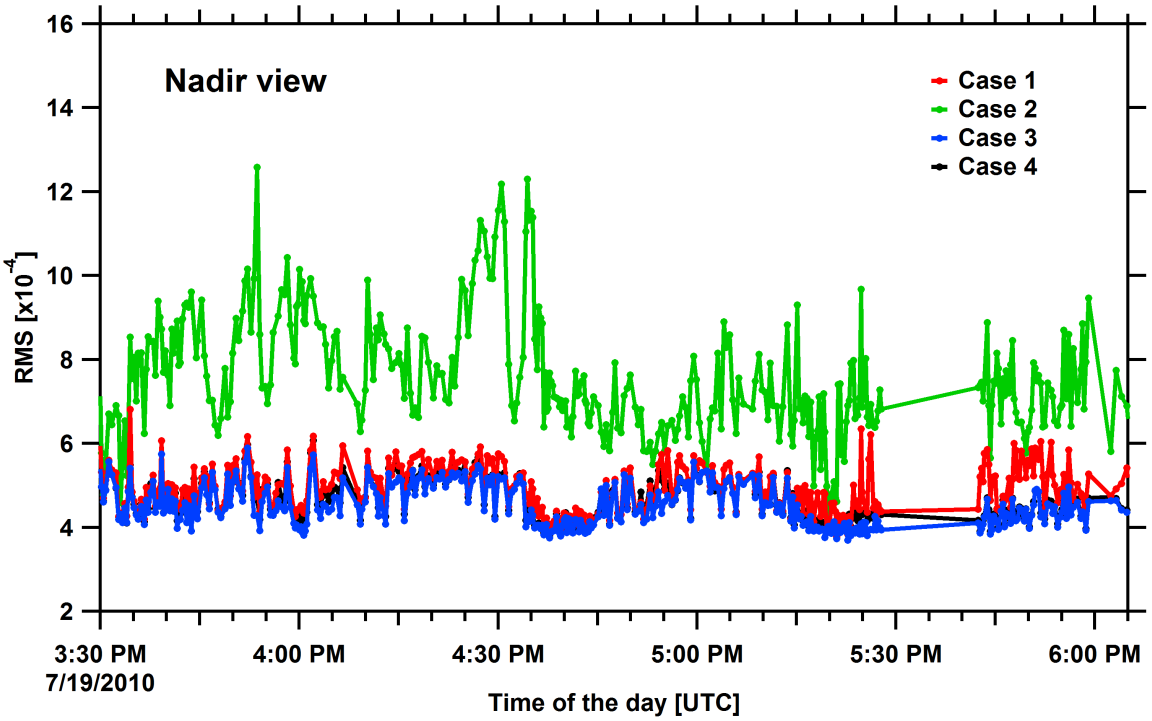

Figure 6.3: Time series of RMS for the nadir viewing geometry from the research flight on July 19, 2010 for the 4 different cases given in Table 6.1.

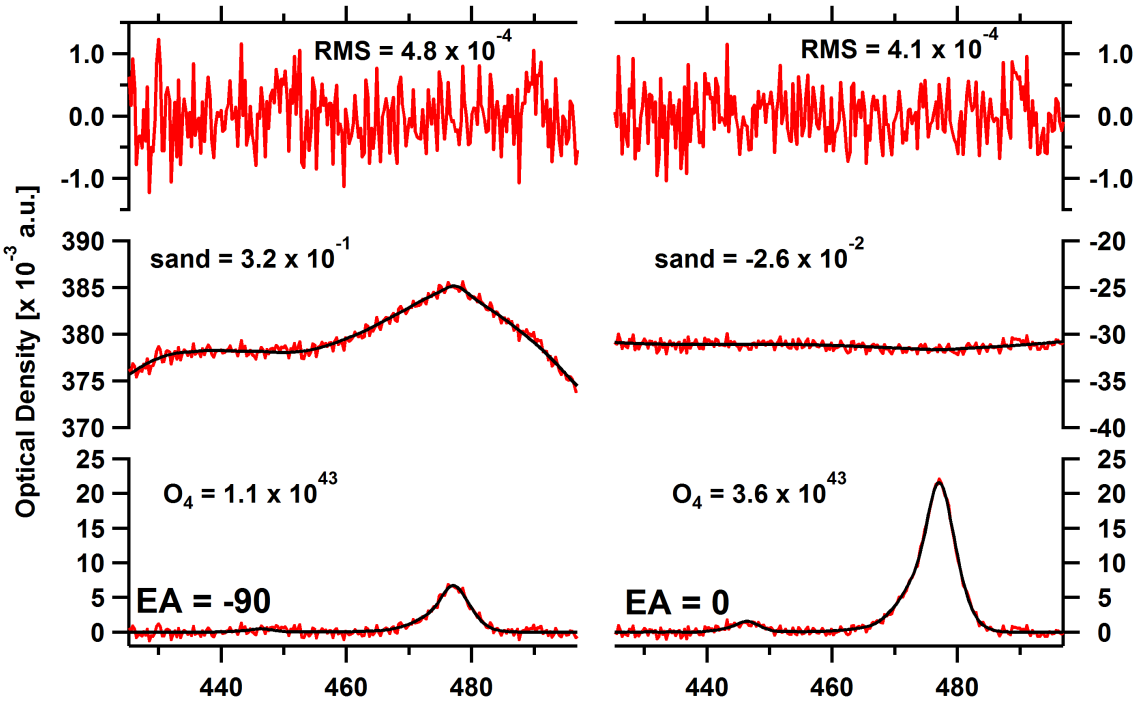

Figure 6.4: Spectral proofs of sand for EA -90° (nadir; panel A) and EA 0° (horizontal; panel B) viewing geometry. The red and black lines represent measured signal and fitted reference cross section respectively. Fits for O_4 and residual are also shown.

The blue and black lines show the RMS for case #3 and case #4 respectively. Both the case #3 and 4 used polynomial 5 and the only difference was the inclusion of the sand reference cross-section in the case #3 and lack of in the case #4. With polynomial 5, we clearly observed that there was no need to include the sand reference spectrum in the DOAS fit. It did not improve the fit results and more importantly it did not seem to worsen the analysis either. Polynomial 5 was able to compensate the need for the sand reference spectrum that was observed when using polynomial 3. Note that polynomials are used in the DOAS analysis to account for broad structures such as Rayleigh and Mie scattering. Hence, we concluded that inclusion of the sand reference spectrum is not critical for retrieval of O_4 in the CU AMAX-DOAS data as long as polynomial order 5 is used in the analysis but needed if a lower order polynomial is included.

Spectral proofs of detection of sand signal for spectra from two EAs, -90° and 0°, are shown in Fig. 6.4. The top row shows the residuals of the DOAS fits for the two spectra. The RMS value of the residual for both spectra is also included in the figure. The residual indicate the quality of the retrieval and both the residuals do not show systematic structures. The retrieved sand signal and O_4 for both spectra are shown in second and third row respectively. The observed sand signal was much stronger for EA -90° compared to EA 0° (see section 6.3.2). The red and black lines represent measured signal and fitted reference cross section respectively. The good O_4 fits in third row also indicate that the inclusion of the sand reference likely do not interfere with retrieval of O_4 dSCDs (see section 6.3.5 for further details).

6.3.2 Separation of EAs

Figure 6.5 shows the time series of the sand fit coefficient for EAs 90°, 0°, -5°, -10°, -20° and -90° from the case #1 analysis. The largest sand fit coefficient was observed for EA -90° (nadir, green line) and decreased away from nadir. Further, the signal was around zero for both zenith and EA 0° indicating very small change in the source of sand signal at the flight altitude and above the aircraft. We used a zenith reference spectrum from the same flight as a Fraunhofer reference spectrum and hence the measured signals are differentials with respect to the reference spectrum.

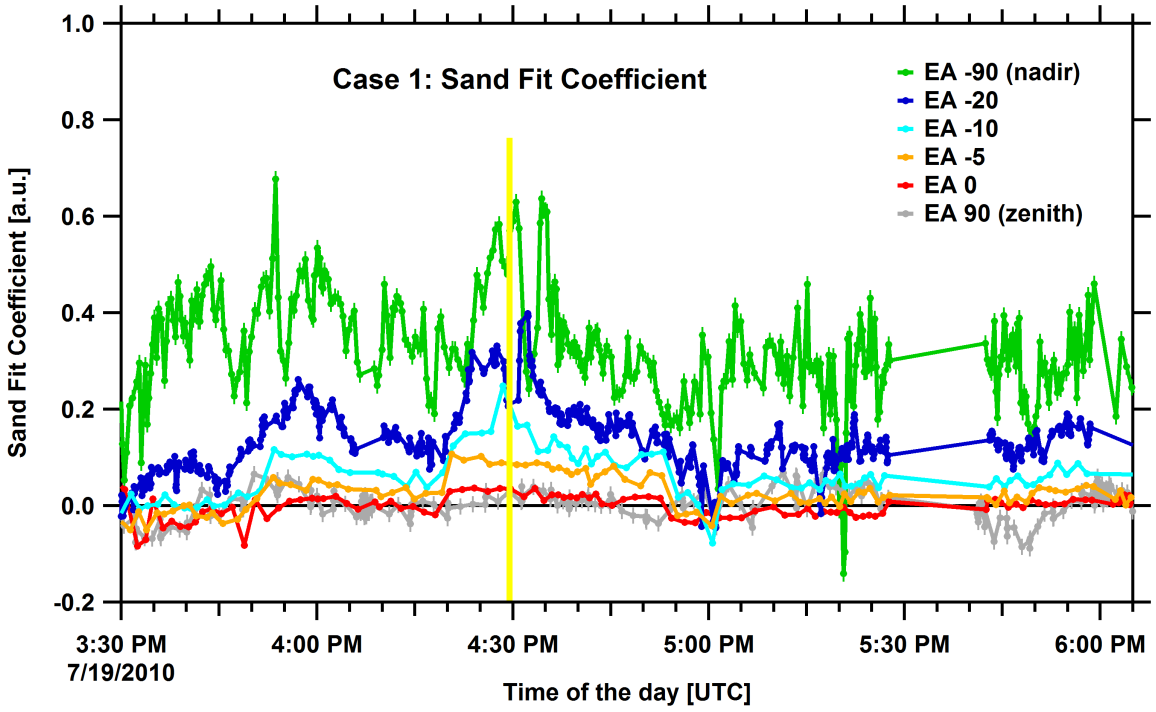

Figure 6.5: Time series of sand signal retrieved using analysis setting case #1 for EAs 90° (zenith, grey), 0° (red), -5° (orange), -10° (turquoise), -20° (blue) and -90° (nadir, green) along the flight track for the flight on July 19, 2010. The yellow vertical line shows the time of the zenith reference used for the analysis.

The time of the zenith reference spectrum is indicated by the yellow vertical line in Fig. 6.5. The decreasing trend in the sand signal from nadir to EA 0° provides a strong evidence that the source of the sand signal is at the surface. The high variability for the nadir viewing geometry compared to EAs -10° and -20° is very likely due to the inhomogeneity in the surface properties along the flight track. Note that the signals for EAs -10° and -20° are averaged horizontally over a larger area compared to nadir. Figure 6.5 also shows that the sand signal for EAs -10°, -20° and -90° follow similar temporal trend. The increase and decrease in the sand signal is first observed in time for EA -10°, then -20° and finally -90°. This is consistent with their viewing geometry as EA -10° looks further forward compared to EAs -20° and -90° and hence observes the same signal first.

The nadir sand signal measured over the desert in Nevada and Arizona on July 19, 2010 overlaid on a Google Earth map is shown in Fig. 6.6. Qualitatively, the larger signals were observed over relatively brighter areas on the Google Earth image. Note that the Google Earth image and our measurements were not concurrent and hence this qualitative agreement could very well be coincidence. More interestingly, the lowest value was observed over a lake. This further supports the geo-physicality of the sand signal. Here we should also mention that an additional flight over a thick cloud deck inside the Los Angeles basin also did not show presence of sand signal. Maps of the sand signals from additional flights inside the LA basin are included in the Appendix section (see Fig. A.20). All flights showed similar separation of EAs for the sand signal.

6.3.3 RTM Results

We calculated the ratio of modeled ground scattered photons observed at EA -10° and EA -20° relative to EA -90° along the flight track (i.e. percentage of EA -90° ground scattered photon observed at EAs -10° and -20°). The mean modeled ratios of 0.52 and 0.25 for EA -20° and -10° respectively were in good agreement with the mean measured ratio of sand fit coefficient values of 0.48 and 0.22. This good agreement between measured and modeled ratios further supports that the measured sand signal is largely due to the surface property. If the measured sand signal originated at the surface then the photons carrying this signal must have been reflected from the

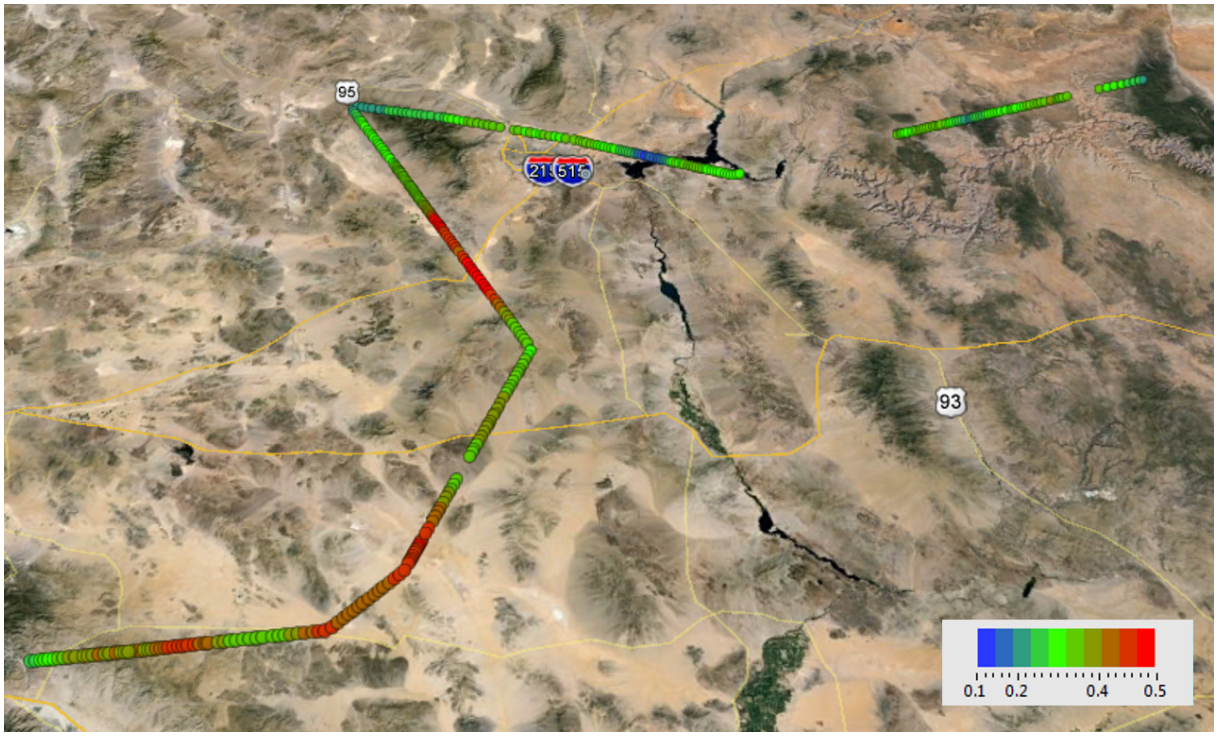

Figure 6.6: Map of sand signal over the desert in Nevada and Arizona measured by the CU AMAX-DOAS during the flight on July 19, 2010.

surface and the observed and the modeled ratios should have similar values. Note that this is only a qualitative comparison since the effects of changing terrain and aerosol were neglected in the RTM and the variability in the modeled ratio was only due to the surface albedo. As a result the high variability observed in the measurement especially for the nadir viewing geometry was not reproduced by the model (see Appendix A Fig. A.21 for details).

6.3.4 Correlation with Surface Albedo

Figure 6.7A shows correlation of the sand fit coefficient retrieved from the CU AMAX-DOAS and the surface albedo along the flight track measured aboard the NOAA Twin Otter during the same flight. The surface albedo measurement aboard the NOAA Twin Otter is described in Oetjen et al. (2013) and is shown in the Appendix section (see Fig. A.22 and A.23). The correlation between the AMAX-DOAS derived sand and surface albedo was found to be fairly weak ($R^2 = 0.22$). However a trend of increasing sand fit coefficient with increasing surface albedo was noticeable. The correlation was found to be much stronger for the OMI derived sand fit coefficients (Fig. 6.7B, $R^2 = 0.80$). The OMI flies on the NASA Aura satellite which was launched into a near-polar sun-synchronous orbit in 2004 (Levelt et al., 2006). The OMI sand fit coefficients are monthly averages for ground pixels along the NOAA Twin Otter flight track for the month of July 2010. The strong correlation between the OMI retrieved sand signal and the independently measured surface albedo further supports that the sand signal is a surface property.

The stronger correlation for the OMI derived sand and a weak one for the AMAX-DOAS with the surface albedo is likely due to the difference in spatial scale probed by each sensor. The instantaneous footprint of the surface albedo measurements while flying at 5 km is a circle with ~5 km radius. This data is further averaged for 30 s to improve the signal to noise. Thus the footprint of the 30 s averaged surface albedo measurement is ~7 x 5 km^2. This is comparable to the size of the ground footprint for the OMI (13 x 24 km^2 at nadir, increases across the swath towards the edges). In comparison the FOV of the CU AMAX-DOAS telescope gives a nadir footprint of ~25 m across and ~650 m along the track while flying at 5 km altitude for 2 s integration times.

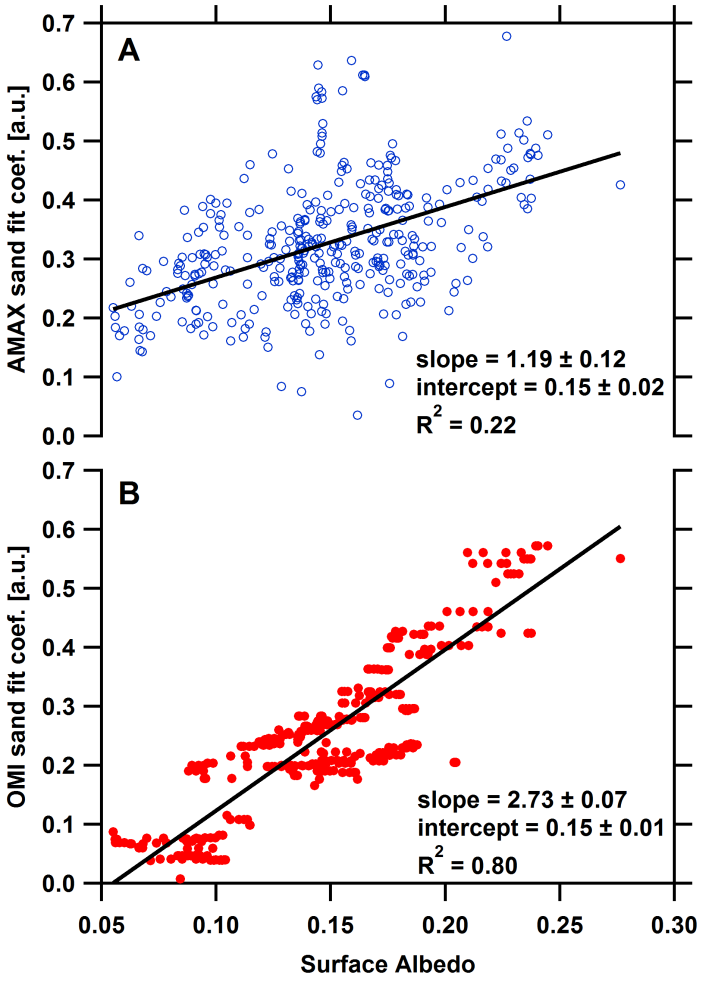

Figure 6.7: Correlation between sand fit coefficient retrieved from (A) CU AMAX-DOAS and (B) OMI and surface albedo measured along the flight track aboard the NOAA Twin Otter. OMI sand fit coefficient is the monthly average for the July 2010.

As a results the CU AMAX-DOAS measurements are affected by small scale variability in surface properties which are averaged out in both the albedo sensor and OMI measurements.

6.3.5 Effect on O_4 dSCD Retrievals

One of the concerns with including the sand reference spectrum in the DOAS retrieval is how it affects the O_4 fit in the analysis. The broad structure for the sand reference spectrum peaks at the same region as the O_4 peak at 477 nm. Hence inclusion of the sand reference spectrum could potentially fit into the O_4 signal and reduce the retrieved O_4 dSCDs. O_4 is an important trace gas for MAX-DOAS measurements as it is used to retrieve aerosol information which is a prerequisite for accurate interpretation of the measured trace gas dSCDs (e.g., Clemer et al., 2010, and references within). Figure 6.8 shows correlation between O_4 dSCD retrieved from the case #1 and case #4. The case #1 is representative of the new GOME-2 NO_2 analysis settings and included sand reference spectrum whereas the case #4 is the standard O_4 analysis settings for the CU AMAX-DOAS instrument and did not include the sand reference spectrum. The slope and intercept for the best line fit was 1.022 ± 0.001 and $-1.27 \pm 0.04 \times 10^{42}$. The agreement between the two retrievals decreased slightly if only nadir data was considered (slope = 0.96 ± 0.01, intercept = $-2.4 \pm 0.1 \times 10^{42}$; see Fig. 6.9) but was within the uncertainty of O_4 retrievals. Thus we concluded that the inclusion of the sand reference spectrum in the DOAS analysis does not affect the O_4 dSCD retrieval.

6.4 Summary and Conclusion

We used the CU AMAX-DOAS measurements over the desert in Nevada and Arizona to investigate the need as well as the origin of sand signal in the DOAS analysis, in the wavelength range of 425-497 nm, that was shown for the GOME-2 measurements. Sand reference cross section was indeed found to be needed to improve the DOAS fit but only when using a 3^{rd} order polynomial for the data set used in this study. Additionally, in this data a fifth order polynomial was found to compensate for the broad feature attributed to sand/soil and a separate sand reference cross section

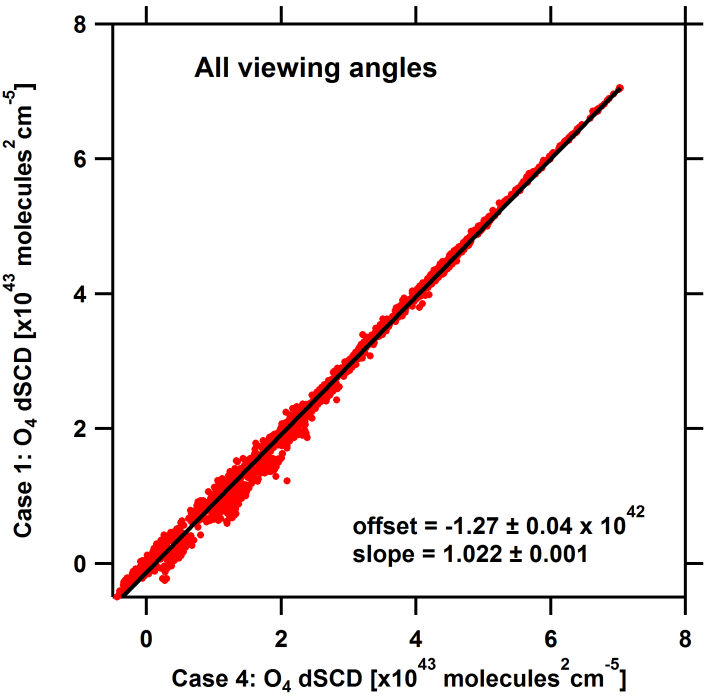

Figure 6.8: Correlation plot for O_4 dSCDs retrieved using the case #1 and case #4 analysis settings.

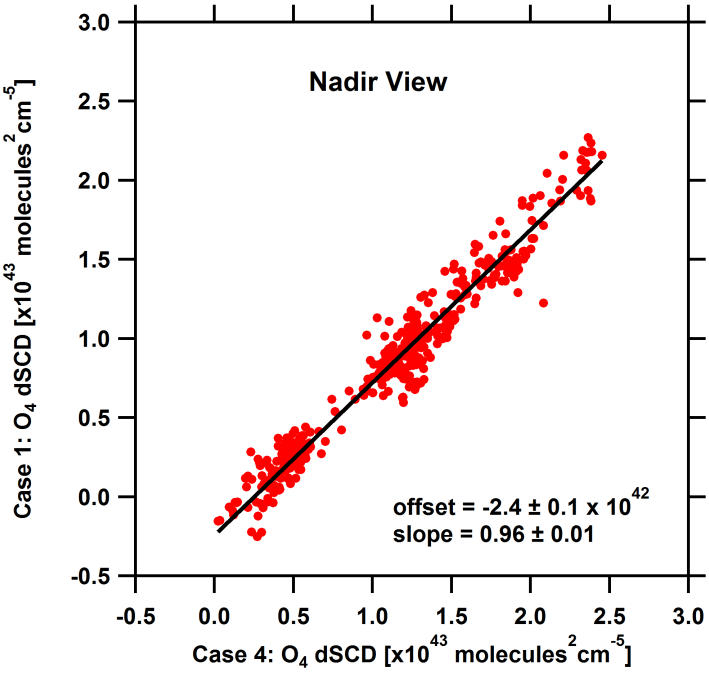

Figure 6.9: Correlation plot for O_4 dSCDs for nadir viewing geometry retrieved using the case #1 and case #4 analysis settings.

is not needed. However inclusion of the sand reference cross section was not found to negatively affect the fit for the higher order polynomial case.

The likely source of the observed sand signal is the surface. The relative decrease in the sand signal from nadir viewing geometry to zenith strongly indicated the ground surface as the source of the signal in the spectrum. This was further supported by the RTM calculation of percentage of ground reflected photons observed at different EAs. In addition, the OMI derived sand signal was found to be strongly correlated with an independent surface albedo measurements. This correlation was fairly weak for the CU AMAX-DOAS sand signal but this is likely due to the difference in the spatial scale probed by the two sensors. The strong correlation between the OMI sand signal and surface albedo opens up the potential to derive surface albedo maps from retrieved sand signal for satellite borne instruments.

Chapter 7

Development of a Mobile Solar Tracker

A new mobile solar tracker with an integrated motion compensation system and an imaging feedback loop is presented. The tracker can be simultaneously coupled to UV-vis and FTIR spectrometers making it possible to measure trace gases in the entire solar spectrum. The integrated system allows for the tracker to operate autonomously and track the sun at high precision while in motion. The tracker was deployed aboard a trailer during FRAPPE 2014 in Colorado, USA. We demonstrate that the tracker can achieve an angular precision of 0.052° during research drives. The tracking precision is verified qualitatively using the center to limb darkening (CLD) correction from spectral data. We also show that the tracking precision meets the requirement needed to measure trace gases such as nitrogen dioxide (NO_2) from a mobile laboratory. High photon flux from direct sun observation enables measurements of NO_2 vertical columns in unprecedented temporal and spatial detail from a mobile platform. Comparison of measured NO_2 with co-located MAX-DOAS shows overall an excellent agreement with very small bias amid a highly heterogeneous air mass.

7.1 Introduction

Solar Occultation Flux (SOF) measurement is a direct method of quantifying emissions using the direct sun light as the light source (Mellqvist et al., 2010). In this method, vertically integrated concentrations of trace gas species measured from a vehicle travelling around or upwind and downwind of target sources using direct solar beam as the light source are multiplied by the corresponding wind speeds along the drive track to obtain trace gas fluxes and ultimately trace

gas production rates from the target sources. The measurement principle of SOF measurements to estimate source strength for trace gases is illustrated in Fig. 7.1. The SOF method has previously been shown to be very useful for estimating fugitive VOC emissions especially from refineries (e.g., Mellqvist et al., 2010; Johansson et al., 2014a,b) and has been in use for last two decades. However this method has only been applied in handful of field studies and is limited to the infrared region of the solar spectrum (e.g., Mellqvist et al., 2010; Johansson et al., 2014a,b).

One of the most likely reasons for the limited use of this powerful technique is the challenge presented by tracking the sun from a mobile platform. Tracking the sun (0.53° angular diameter) from a mobile platform on a road is not a trivial undertaking considering the ever present uneven motions. Mobile solar tracking has been performed from a space shuttle (Farmer, 1987), research ship (Notholt et al., 1995, 2000; Bertleff, 2014), balloon (Hawat et al., 1996, 1998; Bosch et al., 2003) and research aircraft (Coffey et al., 2002, 2008). These platforms are generally more stable as well as the motion is more periodic compared to a vehicle on a busy highway or dirt road. Use of direct sun as a light source from a motor vehicle is comparatively very limited. Duffell et al. (2001) used solar tracker on the back of a moving pick-up truck to measure volcanic gas emission rates. Similar measurements were made by Mellqvist et al. (2010); Johansson et al. (2014a,b) to determine emission rates of VOCs from refineries. Description of the tracker and tracking precision of these system on a motor vehicle are currently not available.

Another deterrent for the widespread use of this technique could be due to the requirement for clear sunny days for measurements. Availability of other measurement techniques which do not pose the same logistical and meteorological challenge as tracking the sun while moving, such as mobile DOAS using scattered sunlight, likely hindered its application in the UV-vis region of the solar spectrum (e.g., Baidar et al., 2013b; Wang et al., 2005, 2012; Johansson et al., 2014a). The advantage of using direct sun measurement in the UV-vis region instead of scattered sunlight include (1) increased photon flux, (2) simple determination of air mass factor (depends only upon the solar zenith angle) and (3) no need for Ring effect correction. This ultimately results in the improved precision of the measurements.

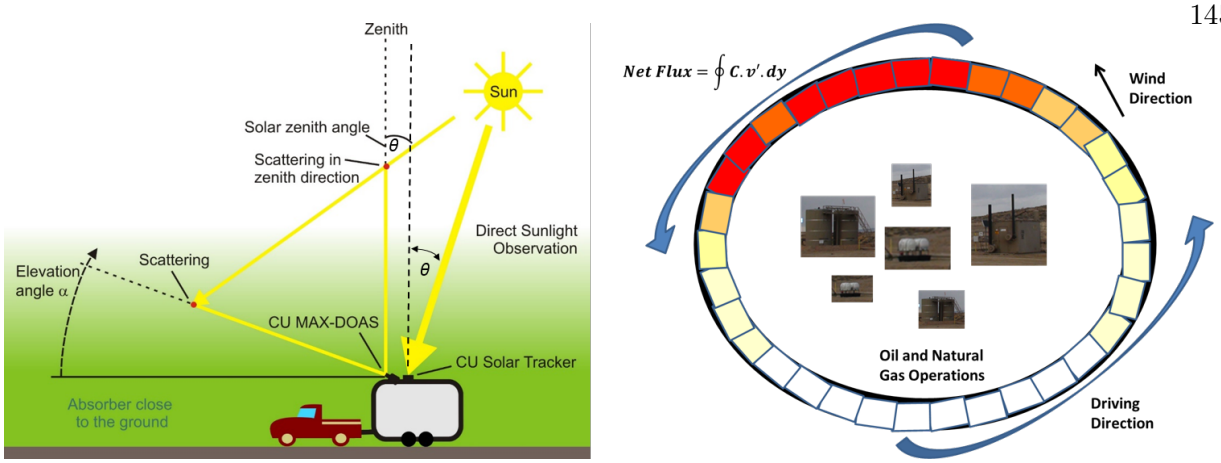

Figure 7.1: Illustration of measurement principle of the mobile solar tracker aboard the NCAR trailer during FRAPPE 2014 and Solar Occultation Flux (SOF) measurements for source strength calculations by making measurements in a closed loop around source regions.

In this work we present a new mobile solar tracker with capabilities to motion stabilize and track the sun at high precision. The new tracker includes an integrated motion compensation system and an imaging feedback loop. This enables the tracker to autonomously locate the sun while moving and also make measurements under thin cloud conditions. The tracker can be coupled simultaneously to an EM27 spectrometer for IR application and UV-vis spectrometers via optical fiber. Simultaneous measurement of VOC and NO_2 columns using a single instrument on the same spatial and time scale could be especially valuable in improving our understanding of O_3 formation.

This instrument was successfully deployed from 21 July-03 September, 2014 as part of the Front Range Air Pollution and Photochemistry Experiment (FRAPPE 2014) field study in Colorado. A total of 16 research drives (RD) were performed during this deployment. Here we show results from one research drive on 13 August, 2014 (RD#11) as an example to characterize the instrument performance. In section 7.2, we describe the new instrument and the configuration as deployed during FRAPPE 2014. The tracker performance is demonstrated in section 7.5. We show tracking precision based on the imaging data as well as UV-vis spectral data. In section 7.6, we present NO_2 vertical column data measured by the UV-vis spectrometer as an example of the data product with the new tracker as the telescope. As a validation, NO_2 vertical column measured with

the mobile solar tracker as the telescope is compared to NO_2 vertical column from a MAX-DOAS instrument also deployed on the trailer.

7.2 Instrumentation

The mobile solar tracker is an alt-azimuthal tracker consisting of two mirrors as shown in Fig. 7.2. The first mirror is mounted directly on a M17 plus stepper motor (Schneider Electric) and allows access to a range of elevation angles (EA). The direct coupling of the mirror permits fast backlash free movements. The second mirror is mounted at a 45° angle opposite to the first mirror. The two mirrors are mounted on a rotational stage (Standa) so that the desired azimuthal directions can be accessed. The rotational stage is driven by a second M17 plus stepper motor. The rotational stage is also coupled to a slip ring (Moflon) that allows transmission of signal and power to the elevation angle motor and permits unrestrained and continuous 360° rotation of the mirror system. The rotational stage and the slip ring have hollow axle diameters of 50 cm and 1.5 inch respectively for light beam to pass through. The light is focused onto an aperture plate with a 2 mm diameter aperture (see Fig. 7.2D) by a 2 inch f/4 lens. The light through the aperture is collected by 1.5 mm fiber bundle and transmitted to the UV-vis spectrometers. A diffuser plate is placed between the aperture plate and the fiber bundle to ensure homogeneous illumination of the fiber bundle. A 10 m long 1.7 mm diameter single core silica fiber is connected on the other end of the fiber bundle and used as a mixing fiber to minimize polarization effects. The other end of the monofiber is connected to a fiber bundle that delivers light to a single UV-Vis spectrometer or to a bifurcated fiber bundle connected to two UV-Vis spectrometers simultaneously. The mixing fiber was found to be critical for DOAS analysis of the UV-Vis spectra. Without the mixing fiber the root mean square (RMS) of the DOAS fit increased gradually over a short period of time. An absorptive neutral density filter with optical density of 1.6 was placed above the focusing lens to optimize the light entering the UV-vis spectrometer. The infrared wavelength beam is directed to an EM27 spectrometer by using a dichroic mirror positioned at an angle of 45° above the neutral density filter.

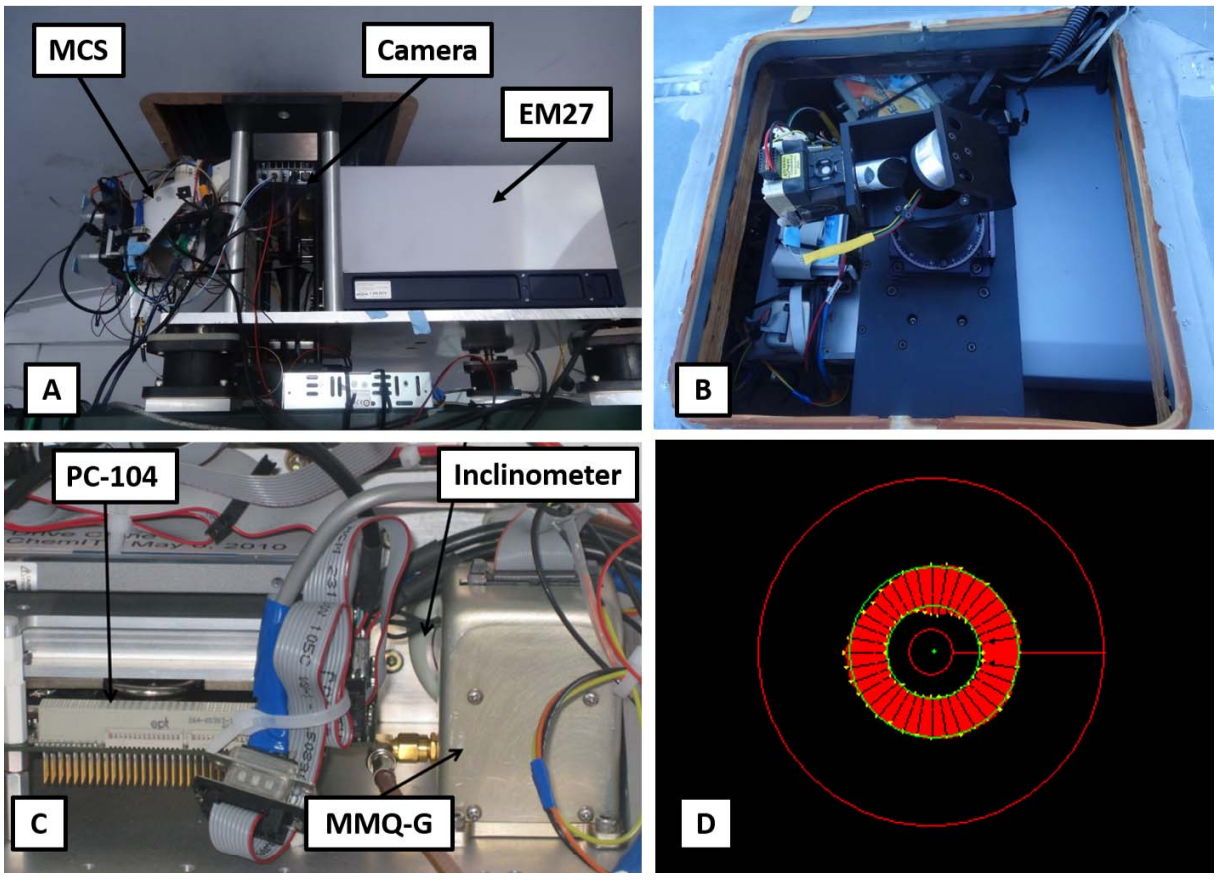

Figure 7.2: Instrumental setup during FRAPPE 2014. (A) as mounted on the trailer roof, (B) mirrors on the top of the roof, (C) motion compensation system, and (D) image of the solar disk on the aperture plate showing fitted circles.

The motion compensation system has been described in detail in Baidar et al. (2013a) as part of the airborne multi-axis DOAS instrument. The same motion compensation system is used here to correct the mirror angles for the vehicle pitch, roll and heading effects during the drive (Fig. 7.2C). It consists of a PC104 computer connected to the two motors, two angle sensors, a Systron Donner Inertial MMQ-G and an electronic inclinometer. The MMQ-G is a small robust global positioning system (GPS) based inertial navigation system (INS). It provides accurate 3-D position, time, velocity, and attitude. It is primarily used to measure the pitch, roll and heading angles of the vehicle and has an angle accuracy of 5 mrad ($\sim$0.29°). The information from the sensor is processed by custom LabVIEW software as Euler angles to calculate the astronomical solar position relative to the real-time vehicle orientation along the drive track. The two mirror angles are then sent to the stepper motors to bring the solar disk in the field of view (FOV) of the imaging camera. Once properly initialized the motion compensation system allows for the automatized operation of the tracker during the drive.

A smart camera from National Instrument (NI 1722) with an embedded PC (400 MHz) is used as an imaging feedback to monitor and control the pointing of the tracker once the solar disk is in the FOV of the camera. The imaging camera is mounted below the baseplate of the solar tracker at an angle of 20° and has a FOV of 5.2° x 3.9°. It is equipped with a standard lens and filter and records the image of the projected solar disk on the aperture plate at about 15-20 Hz. The solar disk has a diameter of about 140 pixels on the recorded images and results in angular size of about 0.0038° per pixel. The 2 mm aperture has a diameter of about 80 pixels. The images are evaluated for the centers of the solar disk and the aperture on the smart camera in real-time using the built in LabVIEW image processing algorithm to determine pixel difference between the centers of the two circles (see Fig. 7.2D). The pixel offset data is then sent to the motion compensation system for fine tracking of the sun. An additional correction is applied for pitch and roll difference between the time when the last image was taken and when the motor position will be updated. The corrected pixel offset data is then converted to mirror angles to update the mirror positons (see section 7.2.1 for details). Similar camera based feedback loop has previously been used to precisely

track the sun from a stationary setup (Gisi et al., 2011) and a research vessel (Bertleff, 2014).

The solar tracker was coupled to an Ocean Optics QE65000 spectrometer with Hamamatsu S7031-1006 TE cooled CCD array detector via an optical fiber bundle. The spectrometer covered the wavelength range of 390 to 520 nm with ∼0.55 nm resolution (full width at half maximum or FWHM). The optical resolution was determined by measuring Krypton emission line at 414 nm. This emission line was also used to determine the instrumental slit function and later to convolve high resolution literature cross section to the optical resolution of the instrument for DOAS analysis. The optical spectrometer bench was heated to a temperature of 40 °C to minimize changes in optical properties while the detector itself was cooled to -10 °C to reduce dark current. The temperature stability was maintained by using a two stage temperature controlled housing described in Coburn et al. (2011). The integration time for each spectrum was 2 seconds. The target CCD saturation level for the spectra was set and maintained at 85% in order to reduce effects of detector non-linearity. Integration time for individual scans are calculated at the beginning of the spectrum acquisition to account for changing light conditions and to maintain target saturation for the spectra. Scans which reached the maximum CCD capacity at least one wavelength channel of the detector because of light changes during acquisition were automatically rejected.

A second Ocean Optics QE 65000 spectrometer which covered the wavelength range from 300-420 nm was added during the last few drives to test the feasibility of making measurements in the UV and visible region simultaneously. However the absorptive neutral density filter optimized for the visible spectrometer cuts off very sharply below 400 nm and very little light was available in the UV region. Broadband absorptive neutral density filters which transmit light uniformly over the UV and visible region are not commercially available to our knowledge. A reflective neutral density filter which has a similar transmittance over both UV and visible region was found to create additional noise which increased the RMS of the DOAS fit over time and hence was not used. The source of this noise is currently not understood. Future improvement in the setup would involve adding separate neutral density filters at the spectrometer entrances in order to make measurements at both UV and visible wavelengths.

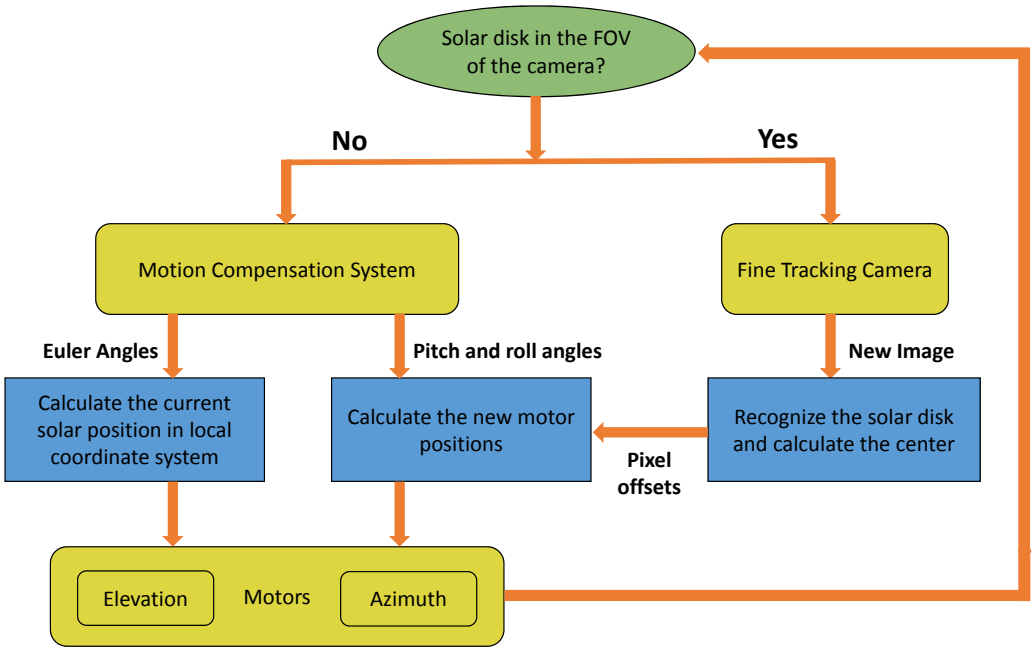

Figure 7.3: Flowchart showing instrument operation principle of the mobile Solar Tracker.

7.2.1 Principle of Operation

The operation of our mobile solar tracker is based on a two-level algorithm as shown in Fig. 7.3. First, based on real-time attitude of the platform, an astronomical algorithm is used to locate the sun in the sky. We use the real-time pitch, roll and heading information from the motion compensation system as Euler angles to locate the position of the sun in the sky relative to the vehicle orientation. The calculated sun position in the local vehicular coordinate system provide the coarse mirror angles to the motors to bring the solar disk in the FOV of the camera (see Appendix A.5.2 for details). Once the solar disk is in the FOV of the camera, recorded pictures are evaluated to determine the center position of the aperture and the solar disk. The steps involved in finding the center positions are similar to one described in Gisi et al. (2011). We use the built in LabVIEW circle and ellipse fitting algorithm from National Instruments. First an appropriate threshold is applied to the image to distinguish the bright solar disk from the dark aperture plate and aperture. The image is then converted to a binary form using the threshold. Next, depending upon the location of the solar disk relative to the aperture, either a circle or an ellipse fitting algorithm is applied to the contours. This is done for efficiency as well as due to limitation of the built in LabVIEW circle/ellipse fitting algorithms. The circle fitting algorithm is comparatively faster than the ellipse fitting algorithm as it only searches for circle to fit within a well-defined region of the camera image around the aperture whereas the ellipse fitting searches the entire camera pixel space. A consistency check is performed for the radii of fitted circles/ellipses before being used to calculate the difference in the center position of the solar disk and aperture. Once the deviation between the aperture and the solar disk centers are determined from the camera data, a small correction is applied to this to account for the motion of the platform between when the picture was taken and correction is applied to the mirrors. A polynomial is fitted to the recent pitch and roll data from the angle sensor and extrapolated to the future to account for the difference in attitude of the platform. It was empirically determined that we can only reliably predict the very next point using the most recent 4 data points. Hence a polynomial fit using the 4 most recent pitch and roll data

was used to make prediction for the next pitch and roll data i.e. current pitch and roll when the correction is being applied to the mirror positions. The corrected pixel data is then converted to mirror angles to update the mirror positions in order to align the two centers and subsequently keep them aligned (see Appendix A.5.3 for details on conversion of pixel offset data to mirror angles). An improvement in the tracking was indeed observed when correction based on the motion of the platform is applied to camera pixel offset data to determine the new mirror angles (see Appendix A Fig.A.25).

7.2.2 Advantages of Integrated Motion Compensation System and Imaging Setup

The advantages of the motion compensation system for a mobile instrument and an imaging setup for a stationary setup individually have been well documented in Baidar et al. (2013a) and Gisi et al. (2011) respectively. The primary function of the motion compensation system in the mobile solar tracker setup is to accurately determine the real time orientation of the platform in order to locate the sun in the sky while mobile. The secondary purpose is to make a small correction in the imaging data in order to account for the time difference between when the image is taken and the motors are updated. The theoretical angle accuracy of the motion compensation system is 0.35° (0.29° for the MMQ and 0.17° for the motors). The angular diameter of the solar disk in the sky is 0.53°. So, the motion compensation system by itself is not good enough to track the sun accurately while moving. The imaging setup has been documented for very high tracking precision in a ground based stationary system (Gisi et al., 2011) and a research vessel (Bertleff, 2014). However with the uneven motion on the road, the imaging setup alone cannot track the sun continuously during drives. By employing the imaging setup along with the motion compensation system tracking at a high level of angular precision and duty cycle can be achieved.

The advantages of the integrated motion compensation system and imaging feedback loop are:

(1) Accurately determine the position of the sun in the sky. Once the motion compensation system is initialized properly, the location of the sun relative to the vehicle local orientation

can be autonomously found if and when the solar disk is not in the FOV of the camera for various reasons such as bumps, trees or clouds.

(2) It minimizes the time needed to locate the sun in the sky. Currently reported mobile solar trackers utilize a "search mode" to locate the sun in the sky (e.g., Bertleff, 2014). Once the motion compensation system is initialized properly, it eliminates the need for such a search mode which could be time consuming and subsequently improves the duty cycle of the instrument.

(3) Minimizes the need for accurately orienting the tracker mirrors and the motion compensation system as the final tracking is based on the imaging setup.

(4) Higher precision tracking of the sun. The integrated system allows for higher precision tracking compared to motion compensation system alone which has a precision of 0.35°.

7.3 DOAS Analysis

The wavelength range of 433-460 nm was used for DOAS retrieval of NO_2. Trace gas reference cross sections for glyoxal (Volkamer et al., 2005), NO_2 (Vandaele et al., 1998), O_3 (Bogumil et al., 2003), H_2O (Rothman et al., 2013), and O_4 (Thalman and Volkamer, 2013) were simultaneously fitted using a nonlinear least square fitting routine. A fifth order polynomial to account for scattering processes and broadband absorption in the atmosphere as well as broadband instrumental features, a center to limb darkening (CLD) correction reference spectrum to account for CLD (Hestroffer and Magnan, 1998; Bosch et al., 2003) and an additional intensity offset to account from instrument stray light were also included in the fitting procedure. The CLD spectrum is calculated as described in Bosch et al. (2003) and accounts for uneven decreases in intensity of solar spectrum at the center and at the limb. The inclusion of CLD reference spectrum in the retrieval (1) improved NO_2 fit, (2) minimized residuals and (3) reduced scattering in the retrieved NO_2 slant columns. A spectrum from a clean background region was included as the Fraunhofer reference spectrum in the analysis. Figure 7.4 shows spectral fit for NO_2 and the corresponding residual from the DOAS

fit.

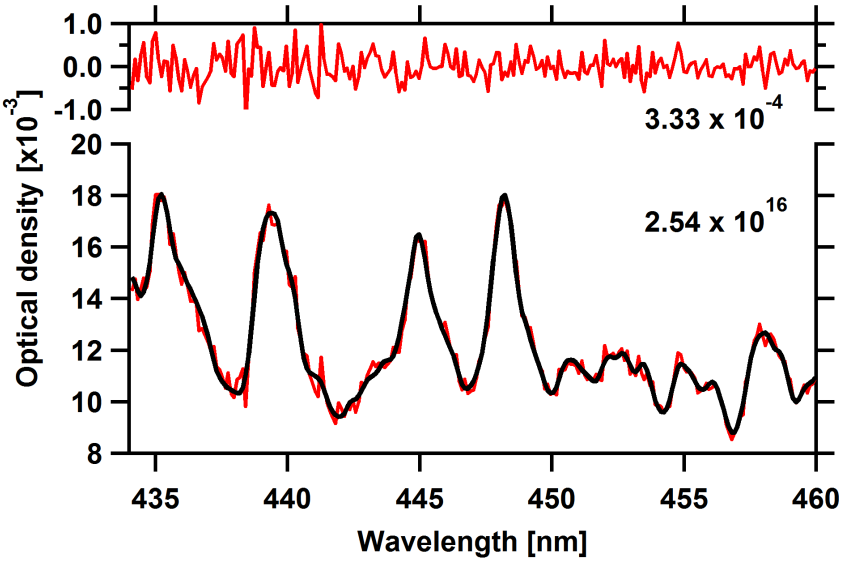

Figure 7.4: Spectral fits of NO_2 and corresponding residual (top panel) from the DOAS fit. The spectrum was taken at 16:59:00 UTC (SZA = 37.4°) during the RD#11 on August 13, 2014 shown in Fig. 7.11. The red line represents the measured spectrum and black line is the fitted cross section. The retrieved NO_2 dSCD and RMS for the DOAS fit are also shown.

7.4 Center to Limb Darkening

The effective emission temperature is higher for solar radiation coming from the center compared to the edges of the solar disk. This decrease in effective emission temperature results in observed decrease in solar intensity going from the center of the solar disk to the edges. This effect is known as the center-to-limb darkening (CLD) (Hestroffer and Magnan, 1998). However, the intensity of the Fraunhofer lines does not change across the solar disk as opposed to the continuous portion of the solar spectrum. In consequence, the optical depth (OD) of the solar Fraunhofer lines also decreases from the center to the edges of the solar disk and results in the need for CLD correction of spectra. The need for CLD correction for UV-vis solar occultation measurements is well documented (e.g., Bosch et al., 2003; Butz, 2006). DOAS analysis of atmospheric absorbers relies on proper correction for solar Fraunhofer lines using a reference Fraunhofer spectrum. As the

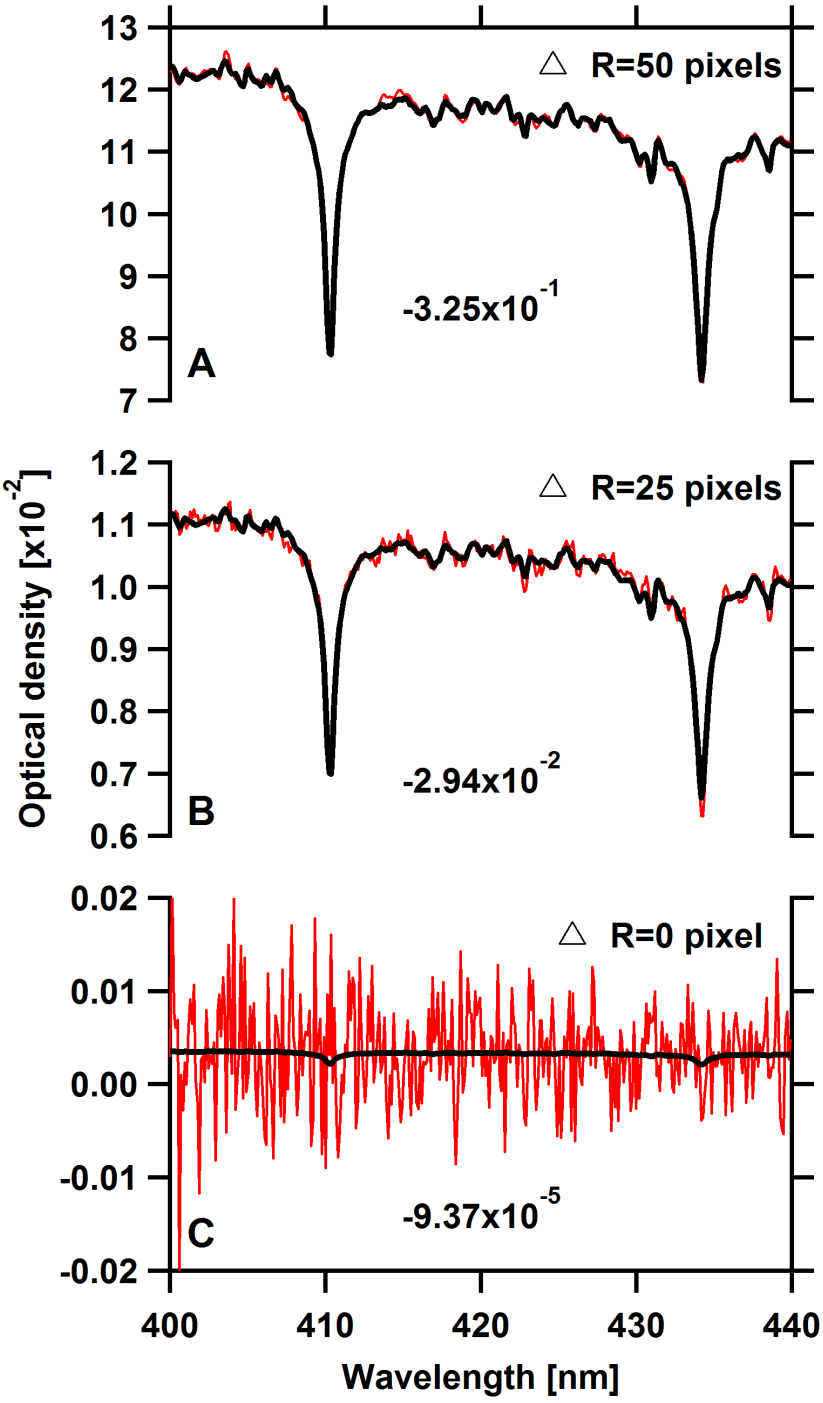

Figure 7.5: Spectral fits of CLD reference for spectra taken at 0, 25 and 50 pixels off of the center of the solar disk. The retrieved fit coefficient from DOAS fit are also shown.

optical density of Fraunhofer lines are 100-1000 times larger than atmospheric absorbers, even a small error in Fraunhofer line correction makes trace gas retrieval very difficult. An empirical approach to correct for the CLD effect was developed by Bosch et al. (2003) and showed that addition of CLD correction improved DOAS retrieval of IO and OClO from balloon borne solar occultation measurements. High resolution solar spectrum taken from the solar disk center and spectrum averaged over the solar disk were used to create a reference pseudo absorber CLD reference cross-section and included in DOAS fits.

In our set up only the radiation from the central portion of the solar disk is used for the UV-vis spectra. In consequence, as the pointing accuracy of the tracker deteriorates, the apparent Fraunhofer lines OD value changes and results in the need for CLD correction. Thus, the CLD correction from the DOAS analysis could also be used to estimate the effective tracking precision from spectral data. We evaluated the UV-vis spectra in the wavelength window from 400-440 nm for the CLD correction fit coefficient. This fit window was chosen to include two strong Fraunhofer lines (Hδ at 410.175 nm and Hγ at 434.047 nm) in the DOAS analysis. CLD reference spectrum was created as described in the Bosch et al. (2003) and included in the DOAS analysis. Figure 7.5 shows the spectral proofs of CLD correction fits for spectrum taken at the center of the solar disk, 25 pixels off of the center, and 50 pixels off of the center. Figure 7.5 clearly illustrates that the CLD correction becomes more important as spectra are collected further away from the center of the solar disk.

7.5 Tracking Accuracies

The pointing accuracy of the solar tracker can be directly determined from the deviation of the center of the two fitted circles (i.e. aperture and solar disk) shown in Fig. 7.2D. The deviation in X and Y direction in camera FOV can be converted to angular deviation using the relationship between the diameter of the sun in the camera picture and its angular diameter in the sky. The location of the centers of the solar disk for every circle/ellipse fit from the RD#11 ($\sim$8 hours) on August 13, 2014 are shown in Figure 7.6. Figure 7.7 depict the histograms showing the distribution

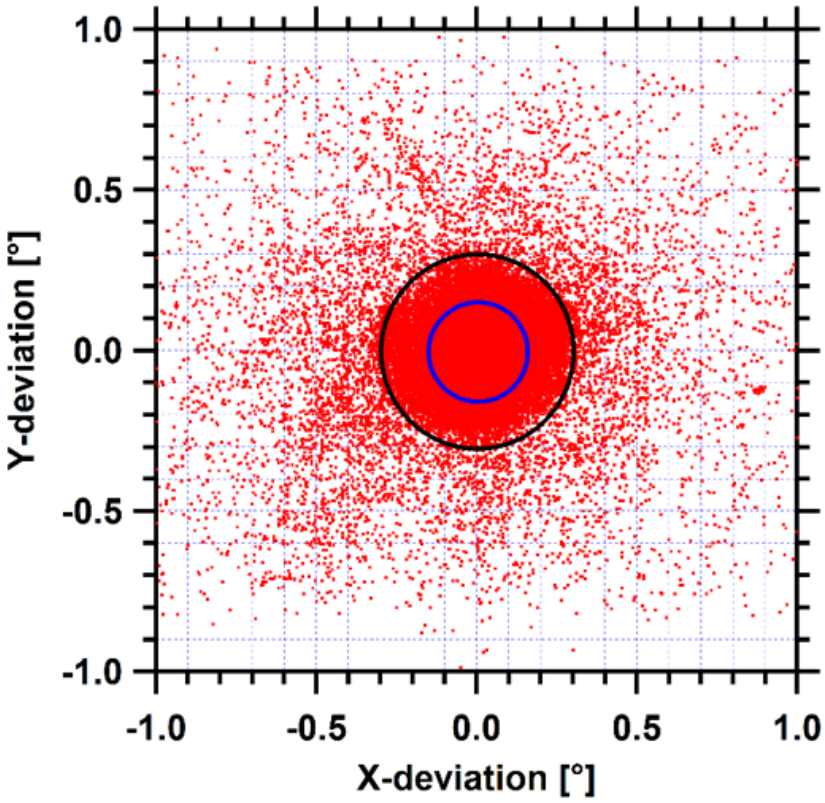

Figure 7.6: Position of the centers of the solar disk on the aperture plate during the RD#11 on August 13, 2014.

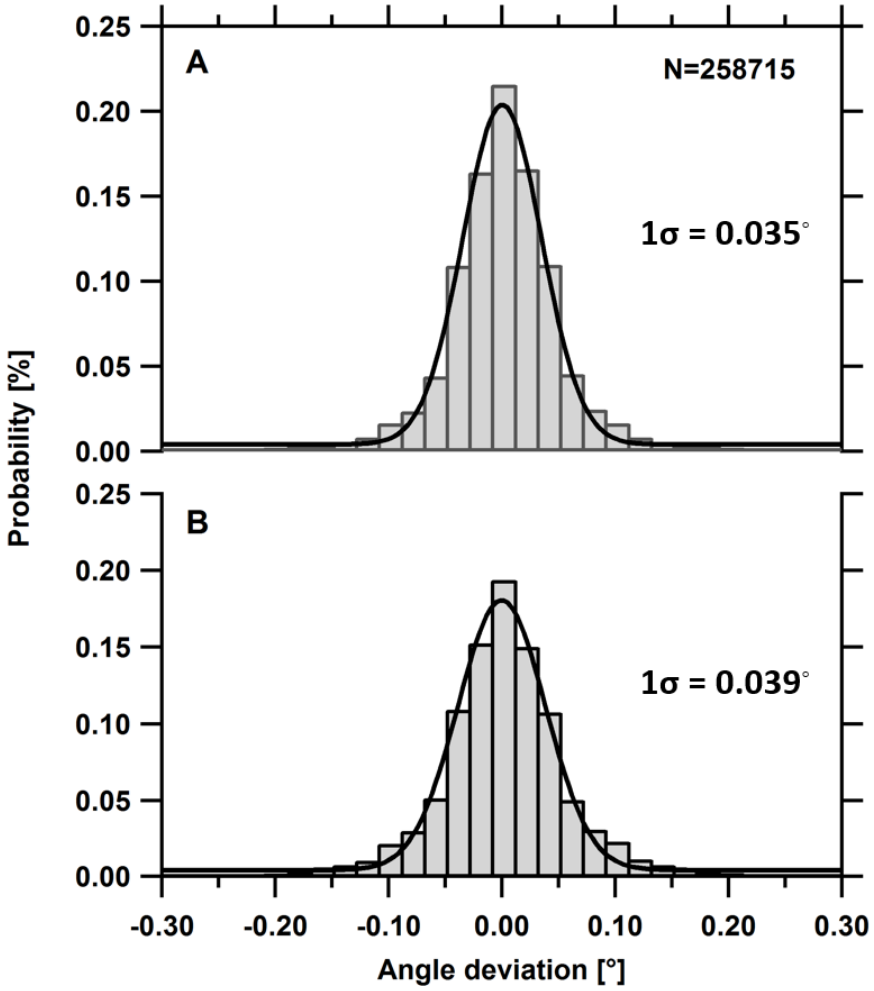

Figure 7.7: Pointing precision during the RD#11 on August 13, 2014. Distribution of deviation between solar disk center and aperture center in (A) x-direction, (B) y-direction. The black lines show the Gaussian fits to the data.

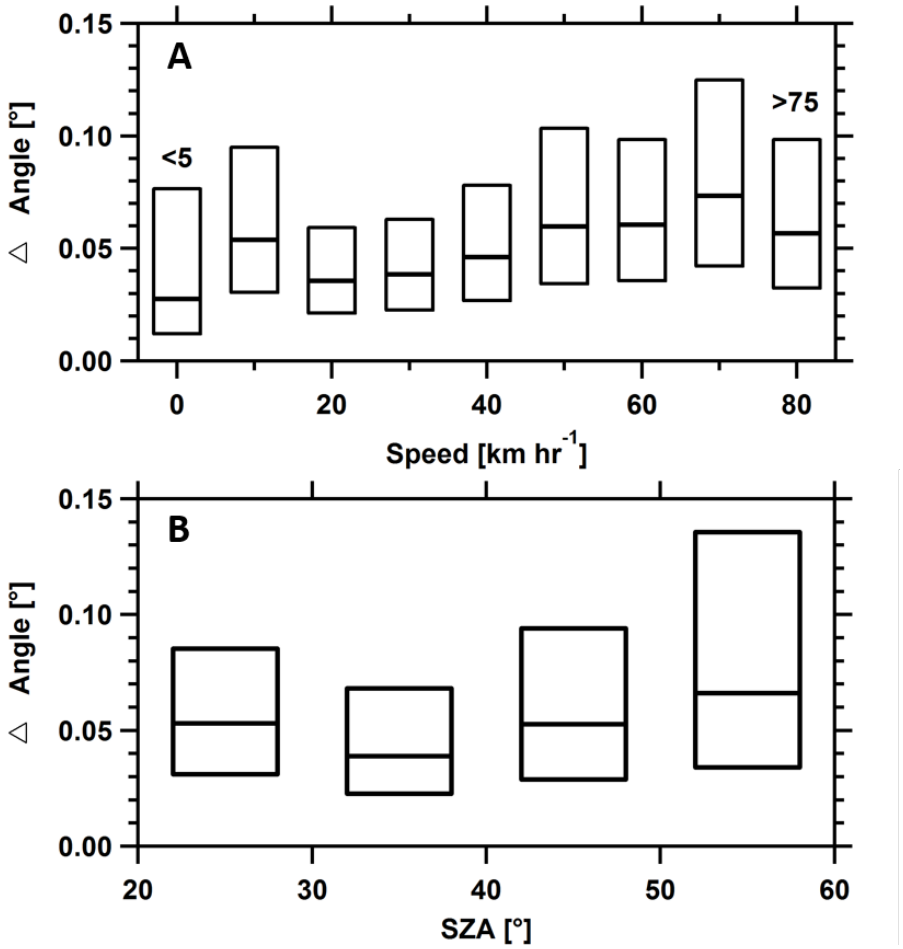

Figure 7.8: Pointing precision during the RD#11 on August 13, 2014 (A) as a function of vehicular speed and (B) as a function of solar zenith angle. The top and the bottom of the box represent 75^{th} and 25^{th} percentile.

of the angular deviation between the centers of the two circles in X and Y direction during the research drive (only the mobile data is included). The 1σ standard deviation in X and Y direction determined from Gaussian fits (black lines) were 0.035° and 0.039° respectively giving us an overall pointing precision of 0.052°. Hence the pointing precision (1σ) of about one-tenth of the of the solar disk angular diameter in the sky can be achieved while mobile. The 1σ mobile tracking precision for all the reasearch drives during FRAPPE 2014 is given in Table A.2. Note that any data point when the solar disk is not in the FOV of camera is excluded from this analysis.

Figure 7.8A and B show the box plot of angular deviation as a function of vehicular speed and solar zenith angle (SZA) respectively from the same research drive. The top and bottom of the box represent the 25^{th} and 75^{th} percentile of the data respectively while the middle line is the median. The distribution is relatively larger above 50° SZA. This is likely due to (1) at higher SZA, trees on the side of the road start to pose a problem as the sun gets intermittently blocked and the tracker has to go through the coarse alignment process more often. (2) A minor bug in the control loop code which gets progressively worse at higher SZA was discovered after the campaign. The distribution also gets slightly larger at higher speed and is likely due to the limitations in the loop rate of the control loop cycle. Future improvement in the tracker would involve incorporating faster camera and motor in order to decrease the control loop time. Some of this improvements have already begun but could not be fully implemented during FRAPPE as some mechanical modifications are required to integrate the new hardware.

As mentioned earlier CLD correction from DOAS analysis can also be used to determine effective tracking precision. Figure 7.9 shows CLD fit coefficient (absolute value) as a function of distance from the center. An absolute value is used as the center of the observed solar disk is not always the brightest spot but moves away from the center as SZA increases and hence the sign of the correction for CLD changes. The fit coefficient gradually increases with the increasing distance from the center of the disk until it is 25-30 pixels off of the center. After that the increase in the fit coefficient is much more dramatic. In fact from 0-30 pixels the CLD fit coefficient is not very sensitive to the pixel offset. This is because CLD is a power law function of distance from the

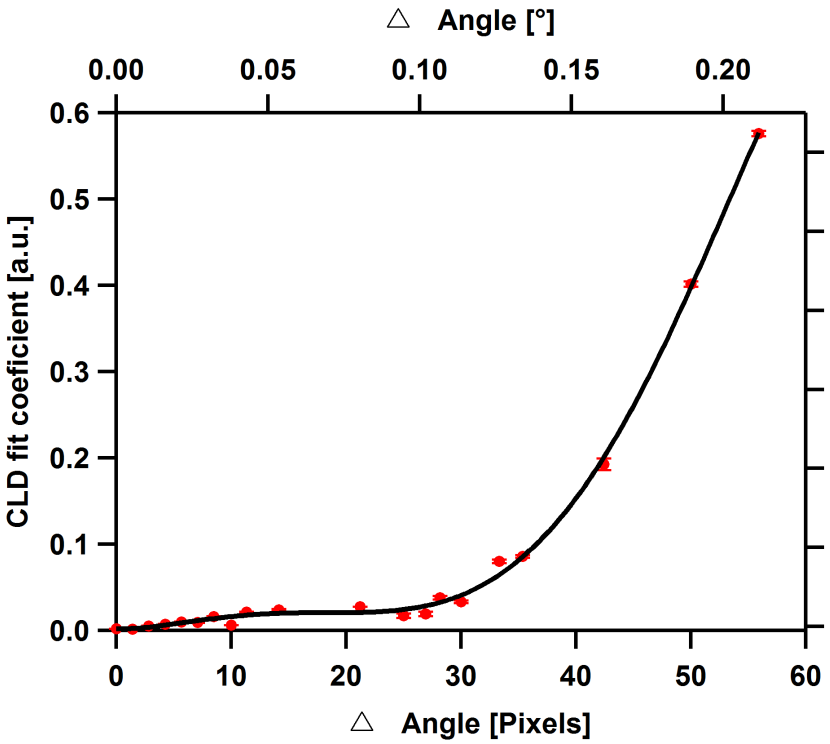

Figure 7.9: Relation between CLD fit coefficient and pointing deviation from the center of the solar disk. The error bars represent standard error.

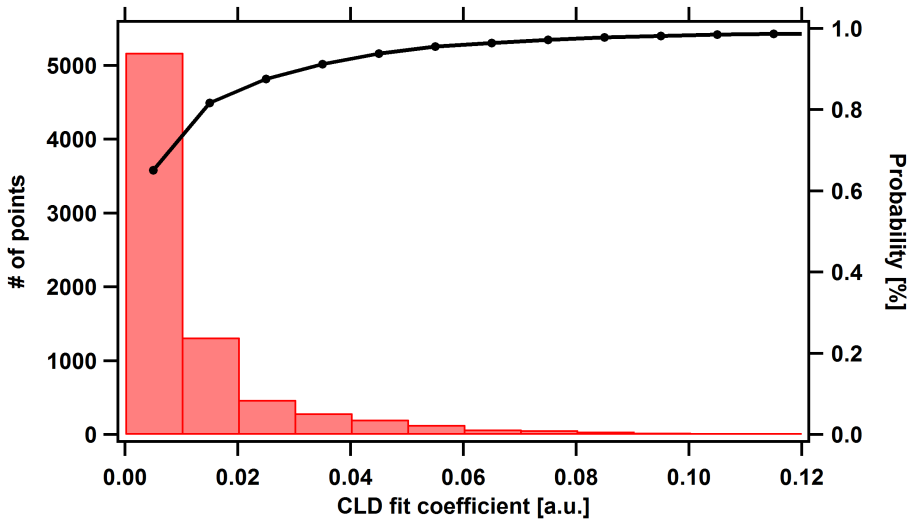

Figure 7.10: Histogram showing distribution of CLD fit coefficients for the spectra collected during the RD#11 on August 13, 2014. The black line shows the cumulative densities.

center of the solar disk to the limb and hence is not very sensitive close to the center (Hestroffer and Magnan, 1998). This insensitivity closer to the center is likely further pronounced in our setup due to (1) the size of the aperture used to collect the radiation for the UV-Vis spectra (∼40 pixels in radius). Thus the radiance weighted average spectra does not show significant need for CLD correction until it is 25-30 pixels off of the center. (2) As the solar zenith angle of the sun changes the apparent brightest spot on the solar disk in our image moves away from the true center resulting in CLD being less sensitive over small scales. (3) There could also be small misalignment between the aperture used to determine the center of the disk and the optical fiber entrance below it. However it is very clearly evident in Fig. 7.9 that the CLD fit coefficient are robust enough to quantitatively determine whether a spectra was taken within 30 pixels or outside this threshold.

The CLD correction fit coefficients from the DOAS analysis for the RD#11 on August 13, 2014 is shown in Fig. 7.10 as a histogram and a cumulative probability distribution function for different fit coefficient bins. Figure 7.10 shows that 95% of the data were within the fit coefficient of 0.05 which corresponds to pixel offset of ∼30 pixels or angular precision of about 0.12° (2σ). This is consistent with angular tracking precision of 0.052° (1σ) determined from the camera data. The precision of the CLD correction fit has been crosschecked using the CLD correction fit from the NO_2 retrieval window and showed excellent agreement (slope = 1.07, intercept = 1.77 x 10^{-3}, R^2 = 0.97; see SI Fig. A.26). The 7% increase in slope is very likely due to the wavelength dependence of CLD. A 9±3% increase in CLD fit coefficient is expected based on the wavelength dependence from 420 nm to 450 nm (Hestroffer and Magnan, 1998).

7.6 Application

Figure 7.11 shows the map of NO_2 vertical column from the RD#11 on August 13, 2014. Vertical column were calculated using the geometric airmass factor (geoAMF = $\frac{1}{cos(SZA)}$). The drive was designed to quantify emissions from various farms near Greeley, CO. We made loops around beef, dairy, and sheep farms as a part of the drive and is shown in Fig. 7.11 (left panel). The NO_2 detection limit and precision (1σ) for the instrument are 7 x 10^{14} and 3 x 10^{14} molecules cm^{-2}

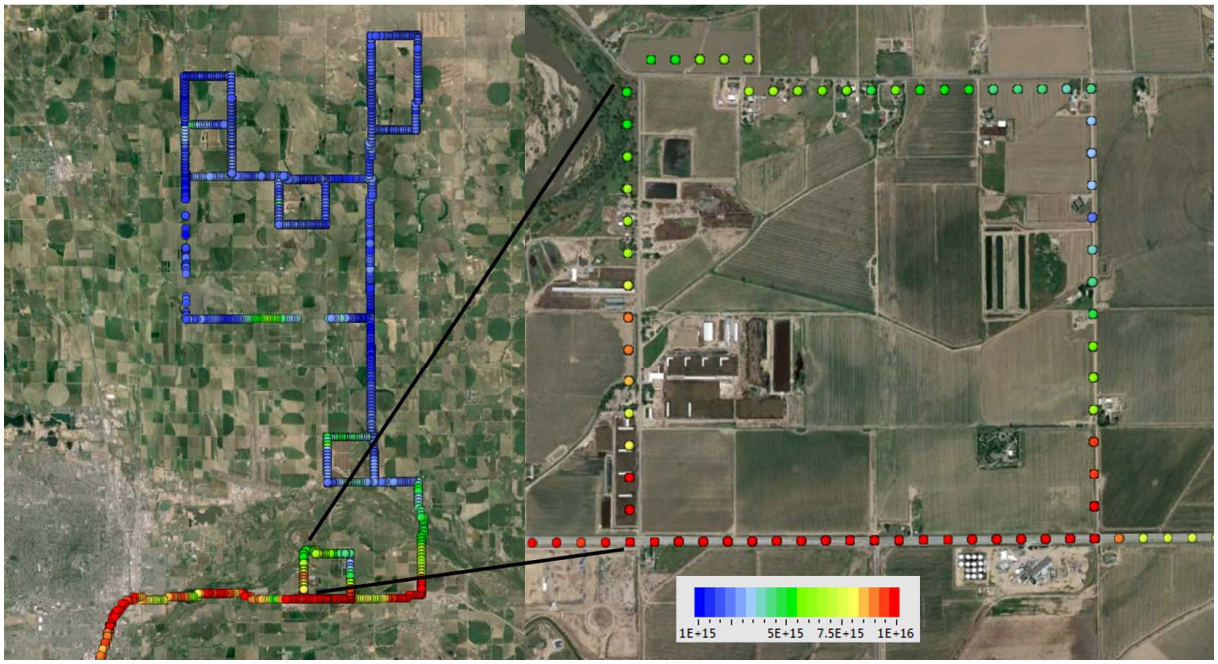

Figure 7.11: Map of NO_2 vertical column measured during the RD#11 on August 13, 2014 around various farms near Greeley, CO. The right panel shows the zoomed map around a beef farm.

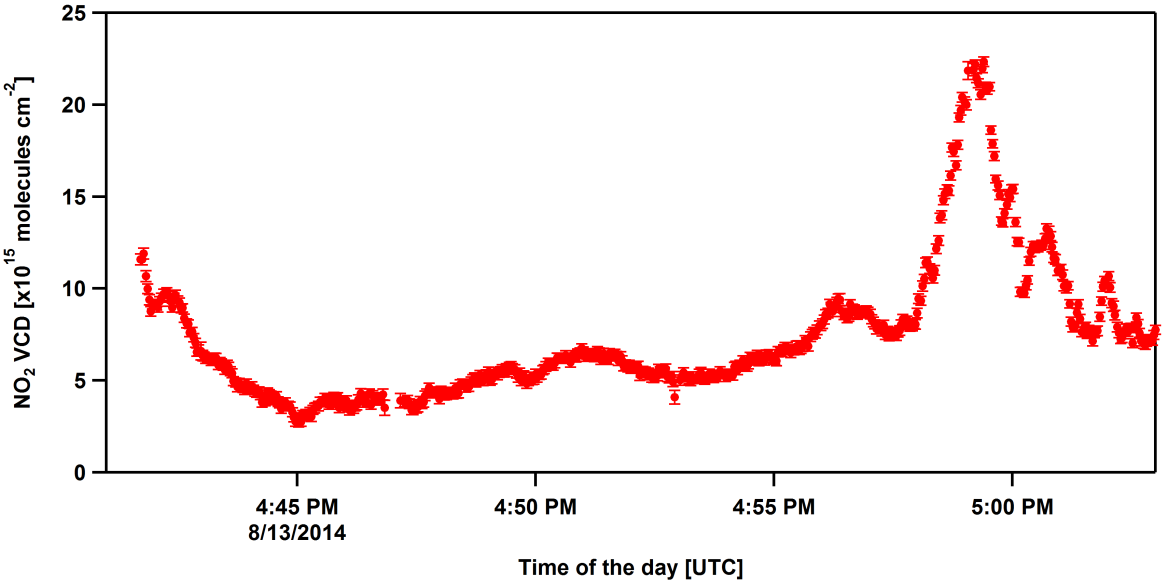

Figure 7.12: Time series of NO_2 vertical column measured around the beef farm shown in Fig. 7.11.

respectively for 2 seconds integration time. The right panel shows a zoomed map of NO_2 around a beef farm. Enhanced NO_2 in the bottom left corner of the box indicate potential location of a source close by. Higher NO_2 was also observed at the same corner during RD#10 which followed the same path on August 12, 2014 further supporting the presence of nearby NO_2 source (see Fig.A.27). The corresponding time series is shown in Fig. 7.12 and demonstrate the capability of the instrument to clearly resolve individual plumes of NO_2 in the spatial scale of few 100-1000 meters. Thus, the tracker can be used as a light source for measurement of NO_2 and other species and quantify emissions of trace gases from various sources such as power plants, refineries, farms, feedlots with an unprecedented detail. We do not quantify emissions from the sources sampled during the drive as it is beyond the scope of this chapter but it is clearly evident that the measurements from the new tracker can be used for such a purpose. It could also be used to measure horizontal distribution of these trace gases over a larger regional scale.

7.6.1 Comparison with MAX-DOAS

NO_2 vertical columns measured by the mobile solar tracker were compared with vertical columns from a co-located MAX-DOAS instrument. Description of the MAX-DOAS instrument can be found in Sinreich et al. (2010); Coburn et al. (2011). NO_2 dSCD from both instruments were converted into vertical column density (VCD) using geometric air mass factor (geoAMF = $\frac{1}{sin(EA)}$). MAX-DOAS measurements at 30° EA were used to calculate VCD. Figure 7.13 shows the time series of NO_2 VCD measured by the two instruments while parked near Boulder Atmospheric Observatory during the RD #13 on August 16, 2014. The time series shows very small to no bias between two instruments at very small NO_2 VCDs. The difference observed between two instruments is likely due to inhomogeneity in the atmosphere. The viewing geometry of the two instruments were 30-60° apart in azimuth direction and about 20-30° in elevation angle. The viewing geometry were closest at the later part to the time series.

Figure 7.14 shows the correlation plot between the NO_2 VCDs measured by the solar tracker and the MAX-DOAS during the RD #14 on August 18, 2014 in Northern Colorado. This particular

drive included a straight leg heading South when the Sun was located withing 30-60° off of the South and provided a good opportunity for comparison between the two instruments. The map of the drive with measured NO_2 used for the correlation plot is shown in Fig. A.28. The orthogonal distance least square fit between the two data sets showed excellent agreement within 5%. The intercept likely represent the difference in SCD between the Fraunhofer reference spectra used for the DOAS analysis of the two data sets but is within the uncertainty of the instruments. Even though the overall agreement was very good the inhomogeneity in the NO_2 field in the atmosphere is very clearly evident in the plot.

7.7 Conclusion and Outlook

The presented solar tracker design fulfills the requirement of being able to track the sun from a moving platform such as a mobile laboratory on the road and can provide an output solar beam with a pointing precision of 0.052°. The effective pointing precision was also verified using spectral data. These characteristics have proved to be adequate to acquire high resolution atmospheric absorption spectra with a high signal-to-noise ratio in the UV-Vis wavelengths. NO_2 vertical columns measured with the mobile solar tracker were compared with vertical columns from a co-located MAX-DOAS instrument and found to be in excellent agreement amid a highly inhomogeneous environment. The neutral density filters used for tuning down solar beam intensity entering the spectrometers could easily be replaced to maximize the signal in the UV wavelengths for retrieval of trace gases such as HCHO or for nighttime atmospheric measurements with the moon as a light source. In the future, arrangements could be made to add filters on the spectrometer end so as to optimize the different spectrometers, thus different wavelength regions, independently. Future improvement for the tracker would involve integrating a faster camera and motors to improve the control loop rates. These changes should lead to further improvements in the pointing precision of the tracker.

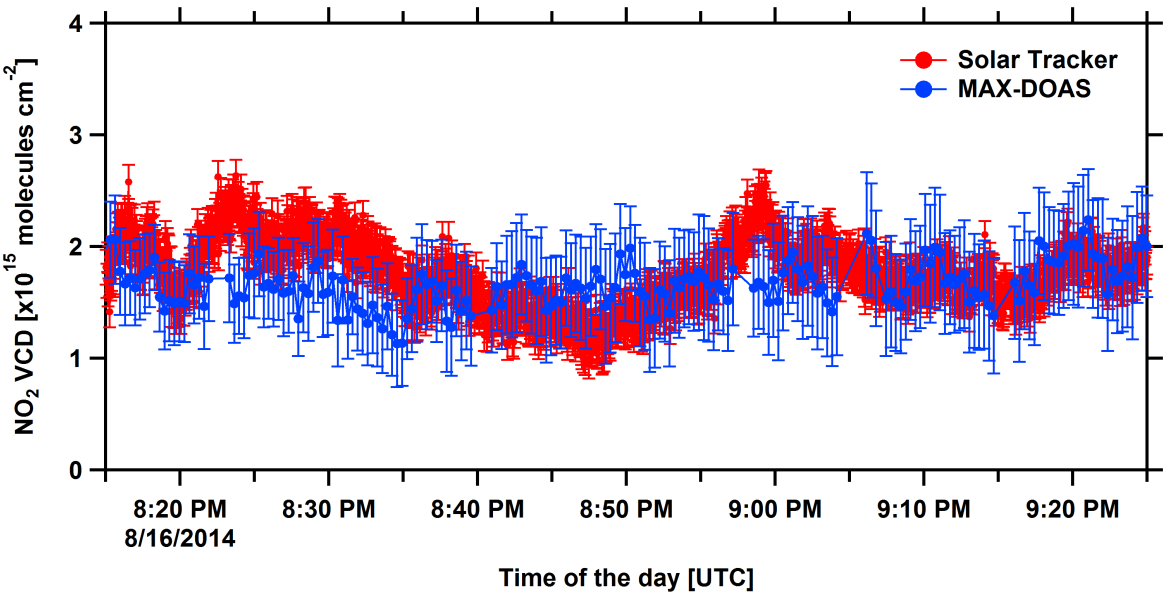

Figure 7.13: Time series of NO_2 vertical column measured by the solar tracker (red) and MAX-DOAS (blue) at Boulder Atmospheric Observatory during the RD#13 on August 16, 2014. The error bars represent 1σ fit error for respective instruments. The viewing geometry of the two instruments were 30-60° apart in azimuth direction and about 20-30° in elevation angle. The viewing geometry were closest at the later part to the time series.

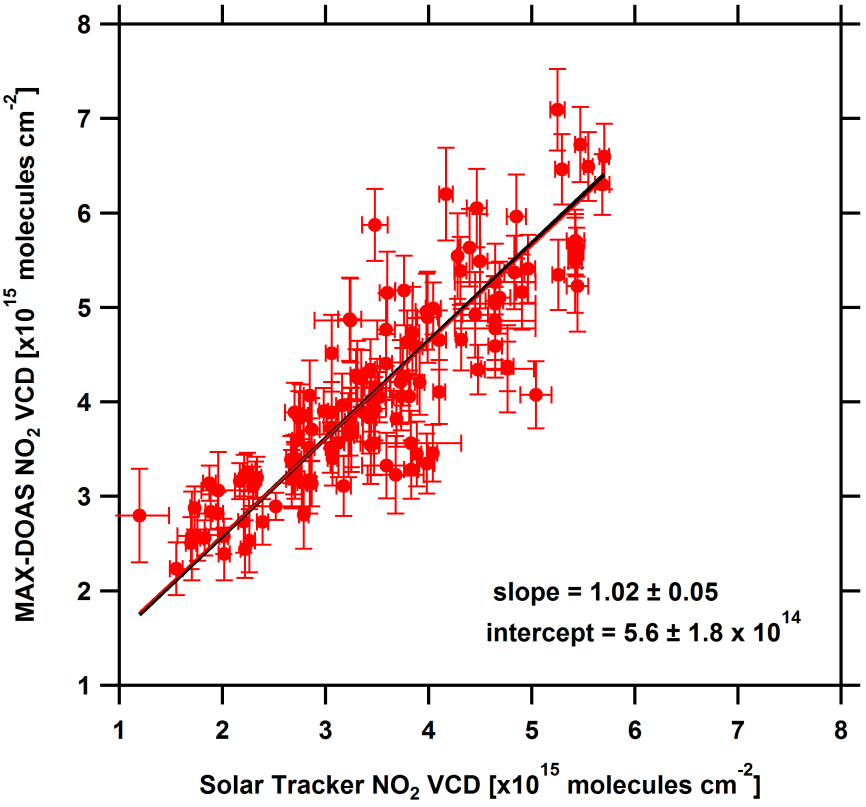

Figure 7.14: Correlation of NO_2 vertical column measured by the solar tracker and MAX-DOAS instruments during the RD#14 in Northern Colorado. The line shows orthogonal distance least square fit. The error bars represent 1σ fit error for respective instruments. The solar tracker data were averaged for 30 seconds in time.

Chapter 8

Summary and Outlook

This thesis developed and characterized AMAX-DOAS retrievals and developed a solar tracker for mobile direct sun measurements for air quality research in an urban environment. The AMAX-DOAS measures absorption of trace gases in the UV-visible wavelength using the scattered sunlight. The mobile solar tracker uses the direct solar beam and can be coupled simultaneously to UV-visible spectrometers and FTIR spectrometer (EM27). Only results from the UV-visible spectrometer is presented as part of this thesis. Data from both instruments are analyzed using the DOAS method. The findings of this work are as follows.

The motion stabilized fully rotatable telescope makes the CU AMAX-DOAS a very versatile instrument capable of measuring vertical profiles as well as vertical columns of trace gases such as NO_2, HCHO and CHOCHO. Maintaining horizontal viewing geometry (EA =0°) increases sensitivity of the instrument to various layers in the atmosphere as the aircraft descends/ascends and allows for vertical profile retrieval of trace gases at high vertical grid resolution (250 m). Vertical columns of the trace gases can be measured using a nadir viewing geometry or EA scan at flight altitude. NO_2 vertical columns is measured at a very high spatial resolution (∼1 km) using a nadir viewing geometry. Vertical columns of weaker and less abundant trace gases such as CHOCHO and HCHO can be retrieved at a relatively lower spatial resolution (∼12 km) by leveraging measurements from EA scans at flight altitude.

Passive and active remote sensing measurements from AMAX-DOAS, TOPAZ O_3 lidar and Doppler wind lidar aboard an aircraft is exploited to constrain NO_2 and O_3 production rates from

source regions on the scale of entire cities. Concurrent measurement of wind profiles in a similar spatial and temporal scale to the trace gases along the flight track significantly reduces uncertainty in the calculated individual flux quantities and subsequently the production rates for the trace gases.

The probability of the occurrences of the weekend O_3 effect in the SCAB has decreased significantly compared to a decade ago. The major shift happened during the economic recession of 2008 and is likely due to the large reduction in NO_x emission during that period. This decrease in probability is non uniform across the basin. A larger reduction is occurring in the eastern part of the basin indicating gradual shrinking of the areas affected by elevated O_3 during the weekends. The decreasing probability also suggests that O_3 formation chemistry is near or at its peak on summer weekends and increasingly more weekends are being transitioned to NO_x limited conditions reducing O_3 on those weekends. Future NO_x reductions are going to be increasingly more effective at reducing O_3 on the weekends.

The sand reference spectrum used in GOME-2 NO_2 retrieval has a geophysical origin and is very likely a surface property. Inclusion of sand reference spectrum is not critical for DOAS analysis of trace gases from the AMAX-DOAS measurements as long as a higher order polynomial capable of compensating for the broad sand absorbance is included in the fit. More importantly including the sand reference spectrum does not interfere with the DOAS O_4 retrieval. Sand measurements from satellite borne instruments are very well correlated with independent surface albedo measurements and indicate potential for deriving surface albedo from sand measurements for satellite borne instruments.

Integration of motion compensation system and imaging feedback loop enables the mobile solar tracker to track the sun at a very high precision while the vehicle is in motion. A tracking precision of up to 0.052°, one-tenth of the solar diameter, was achieved during research drives. The imaging setup also makes it possible to make measurements under thin cloud conditions. The achieved tracking precision meets the requirement for mobile measurement of NO_2. The high photon flux from the direct solar beam enables column measurements at very high temporal resolution and

capture changes in ambient NO_2 columns at unprecedented detail from a moving platform. Future improvement of the tracker would include incorporating a faster camera and motors to improve the tracker loop rate. Additional modification to include neutral density filters on the spectrometer entrance would make measurements of HCHO in the UV wavelengths possible with the setup.

8.1 Outlook

This work has demonstrated a novel and cost effective approach to measure horizontal and vertical distributions of NO_2 and oxygenated hydrocarbons (OVOC) over California. It developed tools to measure column abundances of HCHO and CHOCHO, an indicator of VOC oxidation and SOA precursor, from a research aircraft. For the two case studies over SCAB (section 3.5.1 and 3.5.2), atmospheric models were found to consistently and significantly underestimate both OVOCs in the boundary layer and in the free troposphere. These missing OVOC sources in atmospheric models above the boundary layer affect the photochemistry inside the boundary layer as air mixes down, and indicate uncertainties about VOC/NO_x ratios in the CARB 2010 EI, which translates into uncertain O_3 and secondary aerosol formation. Measurements of HCHO and CHOCHO VCD maps from research aircraft are scarce over California and also globally, yet the knowledge about OVOC distributions provide means to track missing VOC sources, evaluate VOC chemistry by constraining the rate of VOC oxidation, assess oxidative capacity in atmospheric models that is a key component to accurately predicting the secondary (inorganic and organic) aerosol source.

The following projects could benefit and build on the work presented as part of this thesis:

(1) Extend the divergence flux approach used to calculate NO_x emissions over Bakersfield to OVOC formation rates, and map fluxes over the SCAB, Bakersfield, Sacramento, across the US-Mexican border, and over high deserts through the integrated analysis of NOAA TOPAZ O_3, CU AMAX-DOAS OVOC and NO_2, and NCAS Doppler lidar wind data. Expanding the flux divergence technique towards OVOC could further help determine the sources and spatial distribution of OVOCs (which in part determine oxidative fields) and

missing VOC emissions (which would help close the carbon accounting gap and better inform SOA models).

(2) Measurements of soil surface temperature from a radiometer aboard the aircraft provide currently unexplored means to further investigate the source of the variable boundary layer height in the San Joaquin valley and Sacramento valley. Irrigation in the Central Valley is expected to cause variations of soil temperature over small spatial scales. The variability of boundary layer height in the Central Valley is currently not understood.

(3) Full angle scans by AMAX-DOAS, and the wavelength dependent absorption of NO_2 provide means to analyze range resolved NO_2 vertical profiles along the flight track. NO_2 at altitudes above 1 km provides a chemical indicator for recent mixing from the surface, and provides independent means to interrogate boundary layer height variability from a perspective of a short-lived chemical species. It further provides an opportunity to contrast the conditions in the San Joaquin and Sacramento valleys with those in the SCAB.

(4) Investigate missing sources for OVOC over the SCAB, San Joaquin valley and Sacramento valley that inform about VOC reactivity, O_3 and SOA formation. These three regions are chemically very different, yet continue to face problems of O_3 and PM non-attainment. The existing spectra hold largely unexplored potential to assess the VOC emission inventory, and test VOC oxidation chemistry in the models.

(5) Unexplained OVOC in the residual layer can affect the chemistry of O_3 and aerosol formation in the boundary layer upon down-mixing of pollution in the residual layer during morning hours. The available data set has only partially been analyzed and holds unexplored potential to map OVOC in the residual layer more comprehensively by analyzing additional vertical profiles, and investigate the impact of these OVOC on photochemistry.

(6) Investigate the sensitivity of O_3 formation to NO_x and VOC concentrations in California. HCHO to NO_x and CHOCHO to NO_x ratios enable us to determine sensitivity of an area to

NO_x and VOC control (Duncan et al., 2010). Further, CHOCHO to HCHO ratio provides a useful metric to identify biogenic vs. anthropogenic VOC influences. The comprehensive mapping of these ratios informs decisions about emission controls for NO_x and VOCs.

(7) It is now accepted that fine PM pollution is largely formed in the atmosphere as the result of photochemical transformation of gases (secondary aerosol) in addition to direct emissions (primary aerosol). By investigating the OVOC weekend effect, this dataset holds potential to inform control strategies to reduce fine PM that depend on knowledge about oxidative fields, as well as VOC precursors to PM from light-duty and heavy-duty vehicles.

(8) Assess quality of satellite retrievals of HCHO and CHOCHO in California over summer months for potential application in air quality monitoring from space. With the planned deployment of geo-stationary satellite instruments like Tropospheric Emissions: Monitoring of Pollution (TEMPO) in the near future, which will provide hourly measurements of NO_2, HCHO and CHOCHO among others, it would be very advantageous to assess the usefulness of the satellite data for air quality monitoring application.

Bibliography

Akimoto, H.
2003. Global Air Quality and Pollution. Science, 302(5651):1716–1719.

Alvarez II, R. J., C. J. Senff, A. O. Langford, A. M. Weickmann, D. C. Law, J. L. Machol, D. A. Merritt, R. D. Marchbanks, S. P. Sandberg, W. A. Brewer, R. M. Hardesty, and R. M. Banta
2011. Development and application of a compact, tunable, solid-state airborne ozone lidar system for boundary layer profiling. Journal of Atmospheric and Oceanic Technology, 28(10):1258–1272.

Anderson, L. G., J. A. Lanning, R. Barrell, J. Miyagishima, R. H. Jones, and P. Wolfe
1996. Sources and sinks of formaldehyde and acetaldehyde: An analysis of Denver's ambient concentration data. Atmospheric Environment, 30(12):2113–2123.

Baidar, S., H. Oetjen, S. Coburn, B. Dix, I. Ortega, R. Sinreich, and R. Volkamer
2013a. The CU Airborne MAX-DOAS instrument: vertical profiling of aerosol extinction and trace gases. Atmospheric Measurement Techniques, 6(3):719–739.

Baidar, S., R. Volkamer, R. J. Alvarez II, W. A. Brewer, F. Davies, A. O. Langford, H. Oetjen, G. Pearson, C. J. Senff, and R. M. Hardesty
2013b. Combining active and passive airborne remote sensing to quantify NO_2 and O_x production near Bakersfield, CA. British Journal of Environment and Climate Change, 3(4):566–586.

Barret, B., M. De Maziere, and P. Demoulin
2002. Retrieval and characterization of ozone profiles from solar infrared spectra at the Jungfraujoch. Journal of Geophysical Research-Atmospheres, 107(D24):4788.

Beirle, S., K. F. Boersma, U. Platt, M. G. Lawrence, and T. Wagner
2011. Megacity emissions and lifetimes of nitrogen oxides probed from space. Science, 333(6050):1737–1739.

Bertleff, M.
2014. Camera based sun tracking system for mobile platforms. Masters thesis, Karlsruhe Institute of Technology, Germany.

Blanchard, C. L. and S. J. Tanenbaum
2003. Differences between weekday and weekend air pollutant levels in southern California. Journal of the Air & Waste Management Association, 53(7):816–828.

Blickensdorfer, R. P. and G. E. Ewing
1969. Collision-induced absorption spectrum of gaseous oxygen at low temperatures and pressures .2. simultaneous transitions $^1\Delta_G + {}^1\Delta_g \leftarrow {}^3\Sigma_g^- + {}^3\Sigma_g^-$ and $^1\Delta_G + {}^1\Sigma_g^+ \leftarrow {}^3\Sigma_g^- + {}^3\Sigma_g^-$. Journal of Chemical Physics, 51(12):5284.

Bogumil, K., J. Orphal, T. Homann, S. Voigt, P. Spietz, O. Fleischmann, A. Vogel, M. Hartmann, H. Kromminga, H. Bovensmann, J. Frerick, and J. Burrows
2003. Measurements of molecular absorption spectra with the SCIAMACHY pre-flight model: instrument characterization and reference data for atmospheric remote-sensing in the 230-2380 nm region. Journal of Photochemistry and Photobiology A-Chemistry, 157(2-3):167–184.

Bosch, H., C. Camy-Peyret, M. P. Chipperfield, R. Fitzenberger, H. Harder, U. Platt, and K. Pfeilsticker
2003. Upper limits of stratospheric IO and OIO inferred from center-to-limb-darkening-corrected balloon-borne solar occultation visible spectra: Implications for total gaseous iodine and stratospheric ozone. Journal of Geophysical Research-Atmospheres, 108(D15):4455.

Browell, E. V., S. Ismail, and S. T. Shipley
1985. Ultraviolet dial measurements of O_3 profiles in regions of spatially inhomogeneous aerosols. Applied Optics, 24(17):2827–2836.

Bruns, M., S. A. Buehler, J. P. Burrows, K. P. Heue, U. Platt, I. Pundt, A. Richter, A. Rozanov, T. Wagner, and P. Wang
2004. Retrieval of profile information from airborne multi axis uv/visible skylight absorption measurements. Applied Optics, 43:4415–4426.

Bruns, M., S. A. Buehler, J. P. Burrows, A. Richter, A. Rozanov, P. Wang, K. P. Heue, U. Platt, I. Pundt, and T. Wagner
2006. NO_2 profile retrieval using airborne multi axis uv-visible skylight absorption measurements over central Europe. Atmospheric Chemistry and Physics, 6:3049–3058.

Bussemer, M.
1993. Der Ring-Effekt: Ursachen und einflu auf die spektroskopische messung stratosphrischer spurenstoffe. Diploma thesis, Ruperto Carola University of Heidelberg, Germany.

Butz, A.
2006. Case studies of stratospheric nitrogen, chlorine and iodine photochemistry based on balloon borne UV/Vis and IR absorption spectroscopy. Ph.D. dissertation, Ruperto Carola University of Heidelberg, Germany.

California Air Resource Board
2013. California Air Resource Board: 2010 CalNex Modeling Inventory. `http://orthus.arb.ca.gov/calnex/data/` (accessed: September 25, 2013).

California Code of Regulations
2008. Regulation to reduce emissions of diesel particulate matter, oxides of nitrogen and other criteria pollutants, from in-use heavy-duty diesel-fueled vehicles. `http://www.arb.ca.gov/regact/2008/truckbus08/truckbus08.htm` (accessed: April 15, 2015).

California Code of Regulations
2012. Zero emission vehicle standards for 2018 and subsequent model year passenger cars,

light-duty trucks, and medium-duty vehicles. http://www.arb.ca.gov/regact/2012/zev2012/zev2012.htm (accessed: April 15, 2015).

California Department of Conservation
2013. California Department of Conservation: GIS Mapping. http://www.conservation.ca.gov/dog/maps/Pages/GISMapping2.aspx (accessed: September 9, 2015).

Callies, J., E. Corpaccioli, M. Eisinger, A. Hahne, and A. Lefebvre
2000. GOME-2 - Metop's second-generation sensor for operational ozone monitoring. ESA Bulletin-European Space Agency, (102):28–36.

Calvert, J. G., R. Atkinson, K. H. Becker, R. M. Kamens, J. H. Seinfeld, T. J. Wallington, and G. Yarwood
2002. The Mechanisms of Atmospheric Oxidation of Aromatic Hydrocarbons. Oxford: Oxford University Press.

Carter, W. P. L.
1995. Computer modeling of environmental chamber measurements of maximum incremental reactivities of volatile organic-compounds. Atmospheric Environment, 29(18):2513–2527.

Carter, W. P. L. and F. W. Lurmann
1991. Evaluation of a detailed gas-phase atmospheric reaction-mechanism using environmental chamber data. Atmospheric Environment Part A-General Topics, 25(12):2771–2806.

Castellanos, J. L., S. Gomez, and V. Guerra
2002. The triangle method for finding the corner of the L-curve. Applied Numerical Mathematics, 43(4):359–373.

Castellanos, P. and K. F. Boersma
2012. Reductions in nitrogen oxides over Europe driven by environmental policy and economic recession. Scientific Reports, 2:265.

Cazorla, M., W. H. Brune, X. Ren, and B. Lefer
2012. Direct measurement of ozone production rates in Houston in 2009 and comparison with two estimation methods. Atmospheric Chemistry and Physics, 12(2):1203–1212.

Chan Miller, C., G. Gonzalez Abad, H. Wang, X. Liu, T. Kurosu, D. J. Jacob, and K. Chance
2014. Glyoxal retrieval from the Ozone Monitoring Instrument. Atmospheric Measurement Techniques, 7(11):3891–3907.

Chance, K. and J. Orphal
2011. Revised ultraviolet absorption cross sections of HCHO for the HITRAN database. Journal of Quantitative Spectroscopy & Radiative Transfer, 112:1509–1510.

Chinkin, L. R., D. L. Coe, T. H. Funk, H. R. Hafner, P. T. Roberts, P. A. Ryan, and D. R. Lawson
2003. Weekday versus weekend activity patterns for ozone precursor emissions in California's South Coast Air Basin. Journal of the Air & Waste Management Association, 53(7):829–843.

Clapp, L. and M. Jenkin
2001. Analysis of the relationship between ambient levels of O_3, NO_2 and NO as a function of NO_x in the UK. Atmospheric Environment, 35(36):6391–6405.

Clemer, K., M. Van Roozendael, C. Fayt, F. Hendrick, C. Hermans, G. Pinardi, R. Spurr, P. Wang, and M. De Maziere
2010. Multiple wavelength retrieval of tropospheric aerosol optical properties from MAXDOAS measurements in Beijing. Atmospheric Measurement Techniques, 3(4):863–878.

Cleveland, W. S., T. E. Graedel, B. Kleiner, and J. L. Warner
1974. Sunday and workday variations in photochemical air-pollutants in New-Jersey and New-York. Science, 186(4168):1037–1038.

Coburn, S.
2014. Development of optical spectroscopic instruments and application to field measurements of marine trace gases. Ph.D. dissertation, University of Colorado Boulder, USA.

Coburn, S., B. Dix, R. Sinreich, and R. Volkamer
2011. The CU ground MAX-DOAS instrument: characterization of RMS noise limitations and first measurements near Pensacola, FL of BrO, IO, and CHOCHO. Atmospheric Measurement Techniques, 4(11):2421–2439.

Coffey, M. T., J. W. Hannigan, A. Goldman, D. Kinnison, J. C. Gille, J. J. Barnett, L. Froidevaux, A. Lambert, M. Santee, N. Livesey, B. Fisher, S. S. Kulawik, and R. Beer
2008. Airborne fourier transform spectrometer observations in support of EOS Aura validation. Journal of Geophysical Research-Atmospheres, 113(D16):D16S42.

Coffey, M. T., W. G. Mankin, J. W. Hannigan, and G. C. Toon
2002. Airborne spectroscopic observations of chlorine activation and denitrification of the 1999/2000 winter Arctic stratosphere during SOLVE. Journal of Geophysical Research-Atmospheres, 108(D5):8303.

Davis, K. J., N. Gamage, C. R. Hagelberg, C. Kiemle, D. H. Lenschow, and P. P. Sullivan
2000. An objective method for deriving atmospheric structure from airborne lidar observations. Journal of Atmospheric and Oceanic Technology, 17(11):1455–1468.

Deutschmann, T., S. Beirle, U. Friess, M. Grzegorski, C. Kern, L. Kritten, U. Platt, C. Prados-Roman, J. Pukite, T. Wagner, B. Werner, and K. Pfeilsticker
2011. The Monte Carlo atmospheric radiative transfer model McArtim: Introduction and validation of Jacobians and 3D features. Journal of Quantitative Spectroscopy & Radiative Transfer, 112(6):1119–1137.

DiGangi, J. P., S. B. Henry, A. Kammrath, E. S. Boyle, L. Kaser, R. Schnitzhofer, M. Graus, A. Turnipseed, J.-H. Park, R. J. Weber, R. S. Hornbrook, C. A. Cantrell, I. Maudlin, R.L., S. Kim, Y. Nakashima, G. M. Wolfe, Y. Kajii, E. C. Apel, A. H. Goldstein, A. Guenther, T. Karl, A. Hansel, and F. N. Keutsch
2012. Observations of glyoxal and formaldehyde as metrics for the anthropogenic impact on rural photochemistry. Atmospheric Chemistry and Physics, 12(20):9529–9543.

Dix, B., C. A. M. Brenninkmeijer, U. Friess, T. Wagner, and U. Platt
2009. Airborne multi-axis DOAS measurements of atmospheric trace gases on CARIBIC long-distance flights. Atmospheric Measurement Techniques, 2(2):639–652.

Dubovik, O., B. Holben, T. F. Eck, A. Smirnov, Y. F. Kaufman, M. D. King, D. Tanre, and I. Slutsker
2002. Variability of absorption and optical properties of key aerosol types observed in worldwide locations. Journal of the Atmospheric Sciences, 59:590–608.

Duffell, H., C. Oppenheimer, and M. Burton
2001. Volcanic gas emission rates measured by solar occultation spectroscopy. Geophysical Research Letters, 28(16):3131–3134.

Duncan, B. N., Y. Yoshida, J. R. Olson, S. Sillman, R. V. Martin, L. Lamsal, Y. Hu, K. E. Pickering, C. Retscher, D. J. Allen, and J. H. Crawford
2010. Application of OMI observations to a space-based indicator of NO_x and VOC controls on surface ozone formation. Atmospheric Environment, 44(18):2213–2223.

Elkus, B. and K. R. Wilson
1977. Photochemical air-pollution - weekend weekday differences. Atmospheric Environment, 11(6):509–515.

European Comission
2013. European Commission: Air Quality Standards. `http://ec.europa.eu/environment/air/quality/standards.htm` (accessed: September 9, 2015).

Farmer, C. B.
1987. High-resolution infrared-spectroscopy of the Sun and the Earths atmosphere from space. Mikrochimica acta, 3(1-6):189–214.

Fayt, C. and M. Van Roozendael
2001. WinDOAS 2.1, software user manual, Belgian Institute for Space Aeronomy, Brussels, Belgium, available at: http://uv-vis.aeronomie.be/software/windoas/windoas-sum-210b.pdf (last access: 29 May 2012).

Finlayson-Pitts, B. J. and J. N. Pitts Jr
2000. Chemistry of the Upper and Lower Atmosphere. San Diego, CA: Academic Press.

Fu, T.-M., D. J. Jacob, F. Wittrock, J. P. Burrows, M. Vrekoussis, and D. K. Henze
2008. Global budgets of atmospheric glyoxal and methylglyoxal, and implications for formation of secondary organic aerosols. Journal of Geophysical Research-Atmospheres, 113(D15):D15303.

Fujita, E. M., W. R. Stockwell, D. E. Campbell, R. E. Keislar, and D. R. Lawson
2003. Evolution of the magnitude and spatial extent of the weekend ozone effect in California's South Coast Air Basin, 1981-2000. Journal of the Air & Waste Management Association, 53(7):802–815.

Garcia, A. R., R. Volkamer, L. T. Molina, M. J. Molina, J. Samuelson, J. Mellqvist, B. Galle, S. C. Herndon, and C. E. Kolb
2006. Separation of emitted and photochemical formaldehyde in Mexico City using a statistical analysis and a new pair of gas-phase tracers. Atmospheric Chemistry and Physics, 6:4545–4557.

Ghude, S. D., P. S. Kulkarni, S. H. Kulkarni, S. Fadnavis, and R. J. Van Der A
2011. Temporal variation of urban NO_x concentration in India during the past decade as observed from space. International Journal of Remote Sensing, 32(3):849–861.

Gisi, M., F. Hase, S. Dohe, and T. Blumenstock
2011. Camtracker: a new camera controlled high precision solar tracker system for FTIR-spectrometers. Atmospheric Measurement Techniques, 4(1):47–54.

Grainger, J. and J. Ring
1962. Anomalous Fraunhofer line profiles. Nature, 193(4817):762.

Granier, C., B. Bessagnet, T. Bond, A. D'Angiola, H. D. van der Gon, G. J. Frost, A. Heil, J. W. Kaiser, S. Kinne, Z. Klimont, S. Kloster, J.-F. Lamarque, C. Liousse, T. Masui, F. Meleux, A. Mieville, T. Ohara, J.-C. Raut, K. Riahi, M. G. Schultz, S. J. Smith, A. Thompson, J. van Aardenne, G. R. van der Werf, and D. P. van Vuuren
2011. Evolution of anthropogenic and biomass burning emissions of air pollutants at global and regional scales during the 1980-2010 period. Climatic Change, 109(1-2):163–190.

Greenblatt, G. D., J. J. Orlando, J. B. Burkholder, and A. R. Ravishankara
1990. Absorption-measurements of oxygen between 330nm and 1140nm. Journal of Geophysical Research-Atmospheres, 95(D11):18577–18582.

Griffin, R. J., M. K. Revelle, and D. Dabdub
2004. Modeling the oxidative capacity of the atmosphere of the South Coast Air Basin of California. 1. ozone formation metrics. Environmental Science & Technology, 38(3):746–752.

Grosjean, D., E. Grosjean, and A. W. Gertler
2001. On-road emissions of carbonyls from light-duty and heavy-duty vehicles. Environmental Science & Technology, 35(1):45–53.

Guenther, A. B., P. R. Zimmerman, P. C. Harley, R. K. Monson, and R. Fall
1993. Isoprene and monoterpene emission rate variability - model evaluations and sensitivity analyses. Journal of Geophysical Research-Atmospheres, 98(D7):12609–12617.

Haagensmit, A. J.
1952. Chemistry and physiology of Los Angeles smog. Industrial and Engineering Chemistry, 44(6):1342–1346.

Hansen, P. C.
1992. Analysis of discrete ill-posed problems by means of the L-curve. SIAM Review, 34(4):561–580.

Harley, R. A., L. C. Marr, J. K. Lehner, and S. N. Giddings
2005. Changes in motor vehicle emissions on diurnal to decadal time scales and effects on atmospheric composition. Environmental Science & Technology, 39(14):5356–5362.

Hauglustaine, D. A., C. Granier, G. P. Brasseur, and G. Megie
1994. The importance of atmospheric chemistry in the calculation of radiative forcing on the climate system. Journal of Geophysical Research-Atmospheres, 99(D1):1173–1186.

Hawat, T., C. Camy-Peyret, and R. Torguet
1998. Suntracker for atmospheric remote sensing. Optical Engineering, 37(5):1633–1642.

Hawat, T., R. Torguet, C. CamyPeyret, P. Jeseck, and S. Payan
1996. The pointing and the sun-tracker system for the LPMA gondola, volume 2739 of Proceedings of the Society of Photo-Optical Instrumentation Engineers (SPIE).

He, Y., I. Uno, Z. Wang, T. Ohara, N. Sugirnoto, A. Shimizu, A. Richter, and J. P. Burrows
2007. Variations of the increasing trend of tropospheric NO_2 over central east China during the past decade. Atmospheric Environment, 41(23):4865–4876.

Hendrick, F., B. Barret, M. Van Roozendael, H. Boesch, A. Butz, M. De Maziere, F. Goutail, C. Hermans, J. C. Lambert, K. Pfeilsticker, and J. P. Pommereau
2004. Retrieval of nitrogen dioxide stratospheric profiles from ground-based zenith-sky uv-visible observations: validation of the technique through correlative comparisons. Atmospheric Chemistry and Physics, 4:2091–2106.

Hendrick, F., M. Van Roozendael, A. Kylling, A. Petritoli, A. Rozanov, S. Sanghavi, R. Schofield, C. von Friedeburg, T. Wagner, F. Wittrock, D. Fonteyn, and M. De Maziere
2006. Intercomparison exercise between different radiative transfer models used for the interpretation of ground-based zenith-sky and multi-axis DOAS observations. Atmospheric Chemistry and Physics, 6:93–108.

Hermans, C.
2002. Measurement of absorption cross sections and spectroscopic molecular parameters: O_2 and its collisional induced absorption. `http://spectrolab.aeronomie.be/o2.htm` (accessed: April 25, 2013).

Hestroffer, D. and C. Magnan
1998. Wavelength dependency of the solar limb darkening. Astronomy & Astrophysics, 333(1):338–342.

Heue, K. P., A. Richter, M. Bruns, J. P. Burrows, C. von Friedeburg, U. Platt, I. Pundt, P. Wang, and T. Wagner
2005. Validation of SCIAMACHY tropospheric NO_2 columns with AMAXDOAS measurements. Atmospheric Chemistry and Physics, 5:1039–1051.

Heuss, J. M., D. F. Kahlbaum, and G. T. Wolff
2003. Weekday/weekend ozone differences: What can we learn from them? Journal of the Air & Waste Management Association, 53(7):772–788.

Hong, A., L. Schweitzer, W. Yang, and L. C. Marr
2015. Impact of temporary freeway closure on regional air quality: A lesson from Carmageddon in Los Angeles, United States. Environmental Science & Technology, 49(5):3211–3218.

Honninger, G., C. von Friedeburg, and U. Platt
2004. Multi axis differential optical absorption spectroscopy (MAX-DOAS). Atmospheric Chemistry and Physics, 4:231–254.

Horvath, H.
1971. Applicability of Koschmieder visibility formula. Atmospheric Environment, 5(3):177.

Ibrahim, O., R. Shaiganfar, R. Sinreich, T. Stein, U. Platt, and T. Wagner
2010. Car MAX-DOAS measurements around entire cities: quantification of NO_x emissions from the cities of Mannheim and Ludwigshafen (Germany). Atmospheric Measurement Techniques, 3(3):709–721.

Intergovernmental Panel on Climate Change
2013. Climate Change 2013: The Physical Science Basis. Cambridge, United Kingdom and New York, NY, USA: Cambridge University Press.

Johansson, J. K. E., J. Mellqvist, J. Samuelsson, B. Offerle, B. Lefer, B. Rappenglueck, J. Flynn, and G. Yarwood
2014a. Emission measurements of alkenes, alkanes, SO_2, and NO_2 from stationary sources in southeast Texas over a 5 year period using SOF and mobile DOAS. Journal of Geophysical Research-Atmospheres, 119(4):1973–1991.

Johansson, J. K. E., J. Mellqvist, J. Samuelsson, B. Offerle, J. Moldanova, B. Rappenglueck, B. Lefer, and J. Flynn
2014b. Quantitative measurements and modeling of industrial formaldehyde emissions in the Greater Houston area during campaigns in 2009 and 2011. Journal of Geophysical Research-Atmospheres, 119(7):4303–4322.

Kaiser, J., G. M. Wolfe, K. E. Min, S. S. Brown, C. C. Miller, D. J. Jacob, J. A. deGouw, M. Graus, T. F. Hanisco, J. Holloway, J. Peischl, I. B. Pollack, T. B. Ryerson, C. Warneke, and F. N. Keutsch
2015. Reassessing the ratio of glyoxal to formaldehyde as an indicator of hydrocarbon precursor speciation. Atmospheric Chemistry and Physics Discussions, 15(5):6237–6275.

Kampf, C. J., E. M. Waxman, J. G. Slowik, J. Dommen, L. Pfaffenberger, A. P. Praplan, A. S. H. Prevot, U. Baltensperger, T. Hoffmann, and R. Volkamer
2013. Effective Henry's law partitioning and the salting constant of glyoxal in aerosols containing sulfate. Environmental Science & Technology, 47(9):4236–4244.

Kean, A. J., E. Grosjean, D. Grosjean, and R. A. Harley
2001. On-road measurement of carbonyls in California light-duty vehicle emissions. Environmental Science & Technology, 35(21):4198–4204.

Kim, S. W., A. Heckel, G. J. Frost, A. Richter, J. Gleason, J. P. Burrows, S. McKeen, E. Y. Hsie, C. Granier, and M. Trainer
2009. NO_2 columns in the western United States observed from space and simulated by a regional chemistry model and their implications for NO_x emissions. Journal of Geophysical Research-Atmospheres, 114:D11301.

Kim, S. W., A. Heckel, S. A. McKeen, G. J. Frost, E. Y. Hsie, M. K. Trainer, A. Richter, J. P. Burrows, S. E. Peckham, and G. A. Grell
2006. Satellite-observed US power plant NO_x emission reductions and their impact on air quality. Geophysical Research Letters, 33(22):L22812.

Kleinman, L. I., P. H. Daum, D. Imre, Y. N. Lee, L. J. Nunnermacker, S. R. Springston, J. Weinstein-Lloyd, and J. Rudolph
2002. Ozone production rate and hydrocarbon reactivity in 5 urban areas: A cause of high ozone concentration in Houston. Geophysical Research Letters, 29(10):1467.

Kleinman, L. I., P. H. Daum, J. H. Lee, Y. N. Lee, L. J. Nunnermacker, S. R. Springston, L. Newman, J. WeinsteinLloyd, and S. Sillman
1997. Dependence of ozone production on NO and hydrocarbons in the troposphere. Geophysical Research Letters, 24(18):2299–2302.

Knote, C., A. Hodzic, J. L. Jimenez, R. Volkamer, J. J. Orlando, S. Baidar, J. Brioude, J. Fast, D. R. Genter, A. H. Goldstein, P. L. Hayes, W. B. Knigton, H. Oetjen, A. Setyan, H. Stark, R. Thalman, J. Tyndall, R. A. Washenfelder, E. Waxman, and Q. Zhang
2014. Simulation of semi-explicit mechanisms of SOA formation from glyoxal in aerosol in a 3-D model. Atmospheric Chemistry and Physics, 14:6213–6239.

Konovalov, I. B., M. Beekmann, J. P. Burrows, and A. Richter
2008. Satellite measurement based estimates of decadal changes in European nitrogen oxides emissions. Atmospheric Chemistry and Physics, 8(10):2623–2641.

Kritten, L., A. Butz, M. Dorf, T. Deutschmann, S. Kuehl, C. Prados-Roman, J. Pukite, A. Rozanov, R. Schofield, and K. Pfeilsticker
2010. Time dependent profile retrieval of uv/vis absorbing radicals from balloon-borne limb measurements - a case study on NO_2 and O_3. Atmospheric Measurement Techniques, 3(4):933–946.

Kroll, J. H., N. L. Ng, S. M. Murphy, V. Varutbangkul, R. C. Flagan, and J. H. Seinfeld
2005. Chamber studies of secondary organic aerosol growth by reactive uptake of simple carbonyl compounds. Journal of Geophysical Research-Atmospheres, 110(D23):D23207.

Langford, A. O., J. Brioude, O. R. Cooper, C. J. Senff, R. J. Alvarez II, R. M. Hardesty, B. J. Johnson, and S. J. Oltmans
2012. Stratospheric influence on surface ozone in the Los Angeles area during late spring and early summer of 2010. Journal of Geophysical Research-Atmospheres, 117:D00V06.

Langford, A. O., C. J. Senff, R. J. Alvarez II, R. M. Banta, and R. M. Hardesty
2010. Long-range transport of ozone from the Los Angeles basin: A case study. Geophysical Research Letters, 37:L06807.

Langford, A. O., C. J. Senff, R. J. Alvarez II, R. M. Banta, R. M. Hardesty, D. D. Parrish, and T. B. Ryerson
2011. Comparison between the TOPAZ airborne ozone lidar and in situ measurements during TexAQS 2006. Journal of Atmospheric and Oceanic Technology, 28(10):1243–1257.

Lebron, F.
1975. Comparison of weekend-weekday ozone and hydrocarbon concentrations in Baltimore-Washington metropolitan area. Atmospheric Environment, 9(9):861–863.

Lee, M., B. G. Heikes, D. J. Jacob, G. Sachse, and B. Anderson
1997. Hydrogen peroxide, organic hydroperoxide, and formaldehyde as primary pollutants from biomass burning. Journal of Geophysical Research-Atmospheres, 102(D1):1301–1309.

Levelt, P. F., G. H. J. Van den Oord, M. R. Dobber, A. Malkki, H. Visser, J. de Vries, P. Stammes, J. O. V. Lundell, and H. Saari
2006. The Ozone Monitoring Instrument. IEEE Transactions on Geoscience and Remote Sensing, 44(5):1093–1101.

Liggio, J., S. M. Li, and R. McLaren
2005a. Heterogeneous reactions of glyoxal on particulate matter: Identification of acetals and sulfate esters. Environmental Science & Technology, 39(6):1532–1541.

Liggio, J., S. M. Li, and R. McLaren
2005b. Reactive uptake of glyoxal by particulate matter. Journal of Geophysical Research-Atmospheres, 110(D10):D10304.

Lin, X., M. Trainer, and S. C. Liu
1988. On the nonlinearity of the tropospheric ozone production. Journal of Geophysical Research-Atmospheres, 93(D12):15879–15888.

Liu, S. C., M. Trainer, F. C. Fehsenfeld, D. D. Parrish, E. J. Williams, D. W. Fahey, G. Hubler, and P. C. Murphy
1987. Ozone production in the rural troposphere and the implications for regional and global ozone distributions. Journal of Geophysical Research-Atmospheres, 92(D4):4191–4207.

Marr, L. C. and R. A. Harley
2002a. Modeling the effect of weekday-weekend differences in motor vehicle emissions on photochemical air pollution in central California. Environmental Science & Technology, 36(19):4099–4106.

Marr, L. C. and R. A. Harley
2002b. Spectral analysis of weekday-weekend differences in ambient ozone, nitrogen oxide, and non-methane hydrocarbon time series in California. Atmospheric Environment, 36(14):2327–2335.

McDonald, B. C., T. R. Dallmann, E. W. Martin, and R. A. Harley
2012. Long-term trends in nitrogen oxide emissions from motor vehicles at national, state, and air basin scales. Journal of Geophysical Research-Atmospheres, 117:D00V18.

McElroy, C. T.
1988. Stratospheric nitrogen-dioxide concentrations as determined from limb brightness measurements made on june 17, 1983. Journal of Geophysical Research-Atmospheres, 93(D6):7075–7083.

Melamed, M. L., A. O. Langford, J. S. Daniel, R. W. Portmann, H. L. Miller, C. S. Eubank, R. Schofield, J. Holloway, and S. Solomon
2008. Sulfur dioxide emission flux measurements from point sources using airborne near ultraviolet spectroscopy during the New England Air Quality Study 2004. Journal of Geophysical Research-Atmospheres, 113(D2):D02305.

Melamed, M. L., S. Solomon, J. S. Daniel, A. O. Langford, R. W. Portmann, T. B. Ryerson, D. K. J. Nicks, , and S. A. McKeen
2003. Measuring reactive nitrogen emissions from point sources using visible spectroscopy from aircraft. Journal of Environmental Monitoring, 5:29–34.

Meller, R. and G. Moortgat
2000. Temperature dependence of the absorption cross sections of formaldehyde between 223 and 323 K in the wavelength range 225-375 nm. Journal of Geophysical Research-Atmospheres, 105(D6):7089–7101.

Mellqvist, J., J. Samuelsson, J. Johansson, C. Rivera, B. Lefer, S. Alvarez, and J. Jolly
2010. Measurements of industrial emissions of alkenes in Texas using the solar occultation flux method. Journal of Geophysical Research-Atmospheres, 115:D00F17.

Merlaud, A., M. De Maziere, C. Hermans, and A. Cornet
2012. Equations for solar tracking. Sensors, 12(4):4074–4090.

Merlaud, A., M. Van Roozendael, N. Theys, C. Fayt, C. Hermans, B. Quennehen, A. Schwarzenboeck, G. Ancellet, M. Pommier, J. Pelon, J. Burkhart, A. Stohl, and M. De Maziere
2011. Airborne DOAS measurements in Arctic: vertical distributions of aerosol extinction coefficient and NO_2 concentration. Atmospheric Chemistry and Physics, 11(17):9219–9236.

Millstein, D. E. and R. A. Harley
2010. Effects of retrofitting emission control systems on in-use heavy diesel vehicles. Environmental Science & Technology, 44(13):5042–5048.

Monks, P. S., C. Granier, S. Fuzzi, A. Stohl, M. L. Williams, H. Akimoto, M. Amann, A. Baklanov, U. Baltensperger, I. Bey, N. Blake, R. S. Blake, K. Carslaw, O. R. Cooper, F. Dentener, D. Fowler, E. Fragkou, G. J. Frost, S. Generoso, P. Ginoux, V. Grewe, A. Guenther, H. C. Hansson, S. Henne, J. Hjorth, A. Hofzumahaus, H. Huntrieser, I. S. A. Isaksen, M. E. Jenkin, J. Kaiser, M. Kanakidou, Z. Klimont, M. Kulmala, P. Laj, M. G. Lawrence, J. D. Lee, C. Liousse, M. Maione, G. McFiggans, A. Metzger, A. Mieville, N. Moussiopoulos, J. J. Orlando, C. D. O'Dowd, P. I. Palmer, D. D. Parrish, A. Petzold, U. Platt, U. Poeschl, A. S. H. Prevot, C. E. Reeves, S. Reimann, Y. Rudich, K. Sellegri, R. Steinbrecher, D. Simpson, H. ten Brink, J. Theloke, G. R. van der Werf, R. Vautard, V. Vestreng, C. Vlachokostas, and R. von Glasow
2009. Atmospheric composition change - global and regional air quality. Atmospheric Environment, 43(33):5268–5350.

Myriokefalitakis, S., M. Vrekoussis, K. Tsigaridis, F. Wittrock, A. Richter, C. Bruehl, R. Volkamer, J. P. Burrows, and M. Kanakidou
2008. The influence of natural and anthropogenic secondary sources on the glyoxal global distribution. Atmospheric Chemistry and Physics, 8(16):4965–4981.

Neuman, J. A., M. Trainer, K. C. Aikin, W. M. Angevine, J. Brioude, S. S. Brown, J. A. de Gouw, W. P. Dube, J. H. Flynn, M. Graus, J. S. Holloway, B. L. Lefer, P. Nedelec, J. B. Nowak, D. D. Parrish, I. B. Pollack, J. M. Roberts, T. B. Ryerson, H. Smit, V. Thouret, and N. L. Wagner
2012. Observations of ozone transport from the free troposphere to the Los Angeles basin. Journal of Geophysical Research-Atmospheres, 117:D00V09.

Notholt, J., I. Beninga, and O. Schrems
1995. Ship-borne FTIR measurements of atmospheric trace gases on a south (33-degrees-S) to north (53-degrees-N) Atlantic traverse. Applied Spectroscopy, 49(10):1525–1527.

Notholt, J., G. C. Toon, C. P. Rinsland, N. S. Pougatchev, N. B. Jones, B. J. Connor, R. Weller, M. Gautrois, and O. Schrems
2000. Latitudinal variations of trace gas concentrations in the free troposphere measured by solar absorption spectroscopy during a ship cruise. Journal of Geophysical Research-Atmospheres, 105(D1):1337–1349.

Oetjen, H., S. Baidar, N. A. Krotkov, L. N. Lamsal, M. Lechner, and R. Volkamer
2013. Airborne MAX-DOAS measurements over California: Testing the NASA OMI tropospheric NO_2 product. Journal of Geophysical Research-Atmospheres, 118:7400–7413.

Parrish, D. and W. Stockwell
2015. Urbanization and air pollution: Then and now. Eos, 96.

Parrish, D. D., K. S. Law, J. Staehelin, R. Derwent, O. R. Cooper, H. Tanimoto, A. Volz-Thomas, S. Gilge, H. . Scheel, M. Steinbacher, and E. Chan
2012a. Long-term changes in lower tropospheric baseline ozone concentrations at northern mid-latitudes. Atmospheric Chemistry and Physics, 12(23):11485–11504.

Parrish, D. D., T. B. Ryerson, J. Mellqvist, J. Johansson, A. Fried, D. Richter, J. G. Walega, R. A. Washenfelder, J. A. de Gouw, J. Peischl, K. C. Aikin, S. A. McKeen, G. J. Frost, F. C. Fehsenfeld, and S. C. Herndon
2012b. Primary and secondary sources of formaldehyde in urban atmospheres: Houston Texas region. Atmospheric Chemistry and Physics, 12(7):3273–3288.

Pearson, G., F. Davies, and C. Collier
2009. An analysis of the performance of the UFAM pulsed doppler lidar for observing the boundary layer. Journal of Atmospheric and Oceanic Technology, 26(2):240–250.

Petritoli, A., F. Ravegnani, G. Giovanelli, D. Bortoli, U. Bonafe, I. Kostadinov, and A. Oulanovsky
2002. Off-axis measurements of atmospheric trace gases by use of an airborne ultraviolet-visible spectrometer. Applied Optics, 41(27):5593–5599.

Platt, U. and J. Stutz
2008. Differential Optical Absorption Spectroscopy: Principles and Applications. Heidelberg: Springer Verlag.

Pollack, I. B., T. B. Ryerson, M. Trainer, J. A. Neuman, J. M. Roberts, and D. D. Parrish
2013. Trends in ozone, its precursors, and related secondary oxidation products in Los Angeles, California: A synthesis of measurements from 1960 to 2010. Journal of Geophysical Research-Atmospheres, 118:5893–5911.

Pollack, I. B., T. B. Ryerson, M. Trainer, D. D. Parrish, A. E. Andrews, E. L. Atlas, D. R. Blake, S. S. Brown, R. Commane, B. C. Daube, J. A. de Gouw, W. P. Dube, J. Flynn, G. J. Frost, J. B. Gilman, N. Grossberg, J. S. Holloway, J. Kofler, E. A. Kort, W. C. Kuster, P. M. Lang, B. Lefer, R. A. Lueb, J. A. Neuman, J. B. Nowak, P. C. Novelli, J. Peischl, A. E. Perring, J. M. Roberts, G. Santoni, J. P. Schwarz, J. R. Spackman, N. L. Wagner, C. Warneke, R. A. Washenfelder, S. C. Wofsy, and B. Xiang
2012. Airborne and ground-based observations of a weekend effect in ozone, precursors, and oxidation products in the California South Coast Air Basin. Journal of Geophysical Research-Atmospheres, 117:D00V05.

Pope, C. A., I., M. Ezzati, and D. W. Dockery
2009. Fine-particulate air pollution and life expectancy in the United States. New England Journal of Medicine, 360(4):376–386.

Prados-Roman, C., A. Butz, T. Deutschmann, M. Dorf, L. Kritten, A. Minikin, U. Platt, H. Schlager, H. Sihler, N. Theys, M. Van Roozendael, T. Wagner, and K. Pfeilsticker
2011. Airborne DOAS limb measurements of tropospheric trace gas profiles: case studies on the profile retrieval of O_4 and BrO. Atmospheric Measurement Techniques, 4(6):1241–1260.

Pusede, S. E. and R. C. Cohen
2012. On the observed response of ozone to NO_x and VOC reactivity reductions in San Joaquin valley California 1995-present. Atmospheric Chemistry and Physics, 12(18):8323–8339.

Pusede, S. E., D. R. Gentner, P. J. Wooldridge, E. C. Browne, A. W. Rollins, K.-E. Min, A. R. Russell, J. Thomas, L. Zhang, W. H. Brune, S. B. Henry, J. P. DiGangi, F. N. Keutsch, S. A. Harrold, J. A. Thornton, M. R. Beaver, J. M. St. Clair, P. O. Wennberg, J. Sanders, X. Ren, T. C. VandenBoer, M. Z. Markovic, A. Guha, R. Weber, A. H. Goldstein, and R. C. Cohen
2014. On the temperature dependence of organic reactivity, nitrogen oxides, ozone production, and the impact of emission controls in San Joaquin valley, California. Atmospheric Chemistry and Physics, 14(7):3373–3395.

Ren, X. R., H. Harder, M. Martinez, R. L. Lesher, A. Oliger, T. Shirley, J. Adams, J. B. Simpas, and W. H. Brune
2003. HO_x concentrations and OH reactivity observations in New York City during PMTACS-NY2001. Atmospheric Environment, 37(26):3627–3637.

Richter, A., M. Begoin, A. Hilboll, and J. P. Burrows
2011. An improved NO_2 retrieval for the GOME-2 satellite instrument. Atmospheric Measurement Techniques, 4(6):1147–1159.

Richter, A., J. P. Burrows, H. Nuss, C. Granier, and U. Niemeier
2005. Increase in tropospheric nitrogen dioxide over China observed from space. Nature, 437(7055):129–132.

Rodgers, C. D.
2000. Inverse Methods for Atmospheric Sounding: Theory and Practice. Singapore: World Scientific.

Roscoe, H. K. and J. G. T. Hill
2002. Vertical resolution of oversampled limb-sounding measurements from satellites and aircraft. Journal of Quantitative Spectroscopy & Radiative Transfer, 72(3):237–248.

Rothman, L., D. Jacquemart, A. Barbe, D. Benner, M. Birk, L. Brown, M. Carleer, C. Chackerian, K. Chance, L. Coudert, V. Dana, V. Devi, J. Flaud, R. Gamache, A. Goldman, J. Hartmann, K. Jucks, A. Maki, J. Mandin, S. Massie, J. Orphal, A. Perrin, C. Rinsland, M. Smith, J. Tennyson, R. Tolchenov, R. Toth, J. Vander Auwera, P. Varanasi, and G. Wagner
2005. The HITRAN 2004 molecular spectroscopic database. Journal of Quantitative Spectroscopy & Radiative Transfer, 96(2):139–204.

Rothman, L. S., I. E. Gordon, Y. Babikov, A. Barbe, D. C. Benner, P. F. Bernath, M. Birk, L. Bizzocchi, V. Boudon, L. R. Brown, A. Campargue, K. Chance, E. A. Cohen, L. H. Coudert, V. M. Devi, B. J. Drouin, A. Fayt, J. . Flaud, R. R. Gamache, J. J. Harrison, J. . Hartmann, C. Hill, J. T. Hodges, D. Jacquemart, A. Jolly, J. Lamouroux, R. J. Le Roy, G. Li, D. A. Long, O. M. Lyulin, C. J. Mackie, S. T. Massie, S. Mikhailenko, H. S. P. Mueller, O. V. Naumenko, A. V. Nikitin, J. Orphal, V. Perevalov, A. Perrin, E. R. Polovtseva, C. Richard, M. A. H. Smith, E. Starikova, K. Sung, S. Tashkun, J. Tennyson, G. C. Toon, V. G. Tyuterev, and G. Wagner
2013. The HITRAN 2012 molecular spectroscopic database. Journal of Quantitative Spectroscopy & Radiative Transfer, 130:4–50.

Russell, A. R., L. C. Valin, E. J. Bucsela, M. O. Wenig, and R. C. Cohen
2010. Space-based constraints on spatial and temporal patterns of NO_x emissions in California, 2005-2008. Environmental Science & Technology, 44(9):3608–3615.

Russell, A. R., L. C. Valin, and R. C. Cohen
2012. Trends in OMI NO_2 observations over the United States: effects of emission control technology and the economic recession. Atmospheric Chemistry and Physics, 12(24):12197–12209.

Ryerson, T. B., A. E. Andrews, W. M. Angevine, T. S. Bates, C. A. Brock, B. Cairns, R. C. Cohen, O. R. Cooper, J. A. de Gouw, F. C. Fehsenfeld, R. A. Ferrare, M. L. Fischer, R. C. Flagan, A. H. Goldstein, J. W. Hair, R. M. Hardesty, C. A. Hostetler, J. L. Jimenez, A. O. Langford, E. McCauley, S. A. McKeen, L. T. Molina, A. Nenes, S. J. Oltmans, D. D. Parrish, J. R. Pederson, R. B. Pierce, K. Prather, P. K. Quinn, J. H. Seinfeld, C. J. Senff, A. Sorooshian, J. Stutz, J. D. Surratt, M. Trainer, R. Volkamer, E. J. Williams, and S. C. Wofsy
2013. The 2010 California research at the nexus of air quality and climate change (CalNex) field study. Journal of Geophysical Research-Atmospheres, 118(11):5830–5866.

Schiller, C., A. Wahner, U. Platt, H. P. Dorn, J. Callies, and D. H. Ehhalt
1990. Near uv atmospheric absorption-measurements of column abundances during airborne Arctic stratospheric expedition, January - February 1989, 2. OClO observations. Geophysical Research Letters, 17(4):501–504.

Schofield, R., B. J. Connor, K. Kreher, P. V. Johnston, and C. D. Rodgers
2004. The retrieval of profile and chemical information from ground-based uv-visible spectroscopic measurements. Journal of Quantitative Spectroscopy & Radiative Transfer, 86(2):115–131.

Seinfeld, J. H. and S. N. Pandis
2006. Atmospheric Chemisty and Physics: from air pollution to climate change, 2 edition. Hoboken, New Jersey: Wiley-Interscience.

Senff, C. J., R. J. Alvarez II, R. M. Hardesty, R. M. Banta, and A. O. Langford
2010. Airborne lidar measurements of ozone flux downwind of Houston and Dallas. Journal of Geophysical Research-Atmospheres, 115:D20307.

Shaiganfar, R., S. Beirle, M. Sharma, A. Chauhan, R. P. Singh, and T. Wagner
2011. Estimation of NO_x emissions from Delhi using car MAX-DOAS observations and comparison with OMI satellite data. Atmospheric Chemistry and Physics, 11(21):10871–10887.

Sheehy, P. M., R. Volkamer, L. T. Molina, and M. J. Molina
2010. Oxidative capacity of the Mexico City atmosphere - part 2: A RO_x radical cycling perspective. Atmospheric Chemistry and Physics, 10(14):6993–7008.

Sillman, S.
1999. The relation between ozone, NO_x and hydrocarbons in urban and polluted rural environments. Atmospheric Environment, 33(12):1821–1845.

Sinreich, R., S. Coburn, B. Dix, and R. Volkamer
2010. Ship-based detection of glyoxal over the remote tropical Pacific Ocean. Atmospheric Chemistry and Physics, 10(23):11359–11371.

Steck, T.
2002. Methods for determining regularization for atmospheric retrieval problems. Applied Optics, 41(9):1788–1797.

Stedman, D. H.
2004. Photochemical ozone formation, simplified. Environmental Chemistry, 1(2):65–66.

Thalman, R. and R. Volkamer
2013. Temperature dependent absorption cross-sections of O_2-O_2 collision pairs between 340 and 630 nm and at atmospherically relevant pressure. Physical Chemistry Chemical Physics, 15(37):15371–15381.

The Royal Society
2008. Ground-level ozone in the 21st century: future trends, impacts and policy implications. London: The Royal Society.

Thomson, J., P. L. Hayes, J. L. Jimenez, K. Adachi, X. Zhang, J. Liu, R. J. Weber, and R. R. Buseck
2012. Aerosol optical properties at Pasadena, CA during CalNex 2010. Atmospheric Environment, 55:190–200.

Trainic, M., A. A. Riziq, A. Lavi, J. M. Flores, and Y. Rudich
2011. The optical, physical and chemical properties of the products of glyoxal uptake on ammonium sulfate seed aerosols. Atmospheric Chemistry and Physics, 11(18):9697–9707.

U.S. Environmental Protection Agency
2012. U.S. Environmental Protection Agency: National Ambient Air Quality Standard (NAAQS). `http://www.epa.gov/air/criteria.html` (accessed: September 9, 2013).

U.S. Environmental Protection Agency
2015. Classifications of 8-hr ozone (2008) nonattainment areas. `http://www.epa.gov/airquality/greenbook/hnc.html` (accessed: April 15, 2015).

van der A, R. J., H. J. Eskes, K. F. Boersma, T. P. C. van Noije, M. Van Roozendael, I. De Smedt, D. H. M. U. Peters, and E. W. Meijer
2008. Trends, seasonal variability and dominant NO_x source derived from a ten year record of NO_2 measured from space. Journal of Geophysical Research-Atmospheres, 113(D4):D04302.

Vandaele, A., C. Hermans, P. Simon, M. Carleer, R. Colin, S. Fally, M. Merienne, A. Jenouvrier, and B. Coquart
1998. Measurements of the NO_2 absorption cross-section from 42 000 cm^{-1} to 10 000 cm^{-1} (238-1000 nm) at 220 K and 294 K. Journal of Quantitative Spectroscopy & Radiative Transfer, 59(3-5):171–184.

Volkamer, R., S. Coburn, B. Dix, and R. Sinreich
2009a. MAX-DOAS observations from ground, ship, and research aircraft: maximizing signal-to-noise to measure 'weak' absorbers. Proc. SPIE, 7462:746203–746203–9.

Volkamer, R., F. S. Martini, L. T. Molina, D. Salcedo, J. L. Jimenez, and M. J. Molina
2007. A missing sink for gas-phase glyoxal in Mexico City: Formation of secondary organic aerosol. Geophysical Research Letters, 34(19):L19807.

Volkamer, R., P. Sheehy, L. T. Molina, and M. J. Molina
2010. Oxidative capacity of the Mexico City atmosphere - part 1: A radical source perspective. Atmospheric Chemistry and Physics, 10(14):6969–6991.

Volkamer, R., P. Spietz, J. Burrows, and U. Platt
2005. High-resolution absorption cross-section of glyoxal in the uv-vis and IR spectral ranges. Journal of Photochemistry and Photobiology A-Chemistry, 172(1):35–46.

Volkamer, R., P. J. Ziemann, and M. J. Molina
2009b. Secondary organic aerosol formation from acetylene (C_2H_2): seed effect on SOA yields due to organic photochemistry in the aerosol aqueous phase. Atmospheric Chemistry and Physics, 9(6):1907–1928.

Vrekoussis, M., F. Wittrock, A. Richter, and J. P. Burrows
2009. Temporal and spatial variability of glyoxal as observed from space. Atmospheric Chemistry and Physics, 9(13):4485–4504.

Vrekoussis, M., F. Wittrock, A. Richter, and J. P. Burrows
2010. GOME-2 observations of oxygenated VOCs: what can we learn from the ratio glyoxal to formaldehyde on a global scale? Atmospheric Chemistry and Physics, 10(21):10145–10160.

Wagner, T., J. P. Burrows, T. Deutschmann, B. Dix, C. von Friedeburg, U. Friess, F. Hendrick, K. . Heue, H. Irie, H. Iwabuchi, Y. Kanaya, J. Keller, C. A. McLinden, H. Oetjen, E. Palazzi, A. Petritoli, U. Platt, O. Postylyakov, J. Pukite, A. Richter, M. van Roozendael, A. Rozanov, V. Rozanov, R. Sinreich, S. Sanghavi, and F. Wittrock
2007. Comparison of box-air-mass-factors and radiances for multiple-axis differential optical absorption spectroscopy (MAX-DOAS) geometries calculated from different uv/visible radiative transfer models. Atmospheric Chemistry and Physics, 7(7):1809–1833.

Wagner, T., T. Deutschmann, and U. Platt
2009. Determination of aerosol properties from MAX-DOAS observations of the Ring effect. Atmospheric Measurement Techniques, 2(2):495–512.

Wagner, T., B. Dix, C. von Friedeburg, U. Friess, S. Sanghavi, R. Sinreich, and U. Platt
2004. MAX-DOAS O_4 measurements: A new technique to derive information on atmospheric aerosols - principles and information content. Journal of Geophysical Research-Atmospheres, 109(D22):D22205.

Wagner, T., C. von Friedeburg, M. Wenig, C. Otten, and U. Platt
2002. UV-visible observations of atmospheric O_4 absorptions using direct moonlight and zenith-scattered sunlight for clear-sky and cloudy sky conditions. Journal of Geophysical Research-Atmospheres, 107(D20):4424.

Wahner, A., J. Callies, H. P. Dorn, U. Platt, and C. Schiller
1990a. Near uv atmospheric absorption-measurements of column abundances during airborne Arctic stratospheric expedition, January - February 1989, 1. Technique and NO_2 observations. Geophysical Research Letters, 17(4):497–500.

Wahner, A., J. Callies, H. P. Dorn, U. Platt, and C. Schiller
1990b. Near uv atmospheric absorption-measurements of column abundances during airborne Arctic stratospheric expedition, January - February 1989, 3. BrO observations. Geophysical Research Letters, 17(4):517–520.

Wang, P., A. Richter, M. Bruns, J. Burrows, R. Scheele, W. Junkermann, K. Heue, T. Wagner, U. Platt, and I. Pundt
2006. Airborne multi-axis DOAS measurements of tropospheric SO_2 plumes in the Po-valley, Italy. Atmospheric Chemistry and Physics, 6:329–338.

Wang, P., A. Richter, M. Bruns, V. Rozanov, J. Burrows, K. Heue, T. Wagner, I. Pundt, and U. Platt
2005. Measurements of tropospheric NO_2 with an airborne multi-axis DOAS instrument. Atmospheric Chemistry and Physics, 5:337–343.

Wang, S., B. Zhou, Z. Wang, S. Yang, N. Hao, P. Valks, T. Trautmann, and L. Chen
2012. Remote sensing of NO_2 emission from the central urban area of Shanghai (China) using the mobile DOAS technique. Journal of Geophysical Research-Atmospheres, 117:D13305.

Warneke, C., J. A. de Gouw, P. M. Edwards, J. S. Holloway, J. B. Gilman, W. C. Kuster, M. Graus, E. Atlas, D. Blake, D. R. Gentner, A. H. Goldstein, R. A. Harley, S. Alvarez, B. Rappenglueck, M. Trainer, and D. D. Parrish
2013. Photochemical aging of volatile organic compounds in the Los Angeles basin: Weekday-weekend effect. Journal of Geophysical Research-Atmospheres, 118(10):5018–5028.

Warneke, C., J. A. de Gouw, J. S. Holloway, J. Peischl, T. B. Ryerson, E. Atlas, D. Blake, M. Trainer, and D. D. Parrish
2012. Multiyear trends in volatile organic compounds in Los Angeles, California: Five decades of decreasing emissions. Journal of Geophysical Research-Atmospheres, 117:D00V17.

Washenfelder, R. A., C. J. Young, S. S. Brown, W. M. Angevine, E. L. Atlas, D. R. Blake, D. M. Bon, M. J. Cubison, J. A. de Gouw, S. Dusanter, J. Flynn, J. B. Gilman, M. Graus, S. Griffith, N. Grossberg, P. L. Hayes, J. L. Jimenez, W. C. Kuster, B. L. Lefer, I. B. Pollack, T. B. Ryerson, H. Stark, P. S. Stevens, and M. K. Trainer
2011. The glyoxal budget and its contribution to organic aerosol for Los Angeles, California, during CalNex 2010. Journal of Geophysical Research-Atmospheres, 116:D00V02.

Waxman, E. M., K. Dzepina, B. Ervens, J. Lee-Taylor, B. Aumont, J. L. Jimenez, S. Madronich, and R. Volkamer
2013. Secondary organic aerosol formation from semi- and intermediate-volatility organic compounds and glyoxal: Relevance of O/C as a tracer for aqueous multiphase chemistry. Geophysical Research Letters, 40(5):978–982.

Weidner, F., H. Bosch, H. Bovensmann, J. P. Burrows, A. Butz, C. Camy-Peyret, M. Dorf, K. Gerilowski, W. Gurlit, U. Platt, C. von Friedeburg, T. Wagner, and K. Pfeilsticker
2005. Balloon-borne limb profiling of uv/vis skylight radiances, O_3, NO_2, and BrO: technical set-up and validation of the method. Atmospheric Chemistry and Physics, 5:1409–1422.

Wittrock, F., H. Oetjen, A. Richter, S. Fietkau, T. Medeke, A. Rozanov, and J. Burrows
2004. MAX-DOAS measurements of atmospheric trace gases in Ny-Alesund - radiative transfer studies and their application. Atmospheric Chemistry and Physics, 4:955–966.

Wolff, G. T., D. F. Kahlbaum, and J. M. Heuss
2013. The vanishing ozone weekday/weekend effect. Journal of the Air & Waste Management Association, 63(3):292–299.

World Health Organisation
2002. World Health Organisation report: Reducing Risks, Promoting Healthy Life. http://www.who.int/whr/2002/en/ (accessed: April 15, 2015).

World Health Organisation
2011. World Health Organisation report: Air Quality and Health. http://www.who.int/mediacentre/factsheets/fs313/en/ (accessed: September 9, 2013).

Yarwood, G., J. Grant, B. Koo, and A. M. Dunker
2008. Modeling weekday to weekend changes in emissions and ozone in the Los Angeles basin for 1997 and 2010. Atmospheric Environment, 42(16):3765–3779.

Yarwood, G., T. E. Stoeckenius, J. G. Heiken, and A. M. Dunker
2003. Modeling weekday/weekend Los Angeles region for 1997. Journal of the Air & Waste Management Association, 53(7):864–875.

Zaveri, R. A., W. J. Shaw, D. J. Cziczo, B. Schmid, R. A. Ferrare, M. L. Alexander, M. Alexandrov, R. J. Alvarez, W. P. Arnott, D. B. Atkinson, S. Baidar, R. M. Banta, J. C. Barnard, J. Beranek, L. K. Berg, F. Brechtel, W. A. Brewer, J. F. Cahill, B. Cairns, C. D. Cappa, D. Chand, S. China, J. M. Comstock, M. K. Dubey, R. C. Easter, M. H. Erickson, J. D. Fast, C. Floerchinger, B. A. Flowers, E. Fortner, J. S. Gaffney, M. K. Gilles, K. Gorkowski, W. I. Gustafson, M. Gyawali, J. Hair, R. M. Hardesty, J. W. Harworth, S. Herndon, N. Hiranuma, C. Hostetler, J. M. Hubbe, J. T. Jayne, H. Jeong, B. T. Jobson, E. I. Kassianov, L. I. Kleinman, C. Kluzek, B. Knighton, K. R. Kolesar, C. Kuang, A. Kubatova, A. O. Langford, A. Laskin, N. Laulainen, R. D. Marchbanks, C. Mazzoleni, F. Mei, R. C. Moffet, D. Nelson, M. D. Obland, H. Oetjen, T. B. Onasch, I. Ortega, M. Ottaviani, M. Pekour, K. A. Prather, J. G. Radney, R. R. Rogers, S. P. Sandberg, A. Sedlacek, C. J. Senff, G. Senum, A. Setyan, J. E. Shilling, M. Shrivastava, C. Song, S. R. Springston, R. Subramanian, K. Suski, J. Tomlinson, R. Volkamer, H. W. Wallace, J. Wang, A. M. Weickmann, D. R. Worsnop, X. . Yu, A. Zelenyuk, and Q. Zhang
2012. Overview of the 2010 Carbonaceous Aerosols and Radiative Effects Study (CARES). Atmospheric Chemistry and Physics, 12(16):7647–7687.

Zieger, P., E. Weingartner, J. Henzing, M. Moerman, G. de Leeuw, J. Mikkila, M. Ehn, T. Petaja, K. Clemer, M. van Roozendael, S. Yilmaz, U. Friess, H. Irie, T. Wagner, R. Shaiganfar, S. Beirle, A. Apituley, K. Wilson, and U. Baltensperger
2011. Comparison of ambient aerosol extinction coefficients obtained from in-situ, MAX-DOAS and lidar measurements at Cabauw. Atmospheric Chemistry and Physics, 11(6):2603–2624.

Appendix A

Supplementary Materials for Chapter 2-7

This Appendix section contains supporting information from Chapter 2-7.

A.1 Chapter 2: AMAX-DOAS

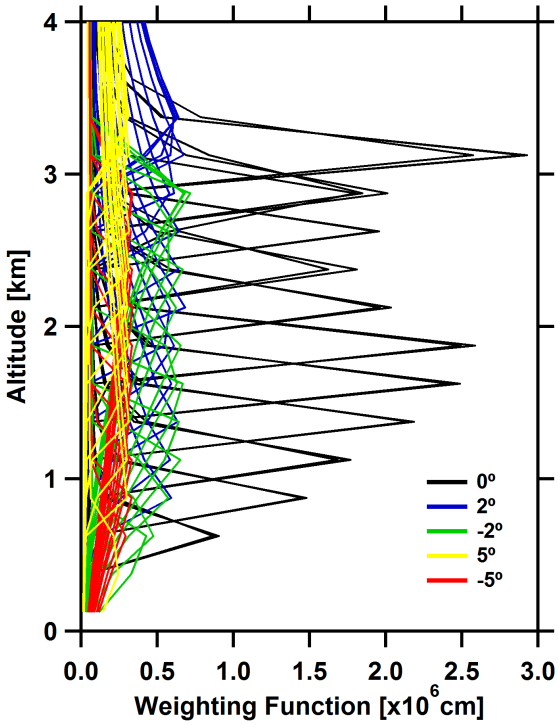

Figure A.1: Weighting function calculated at 455 nm using McArtim for CHOCHO vertical profile retrievals for RF# 46 on 16 July 2010.

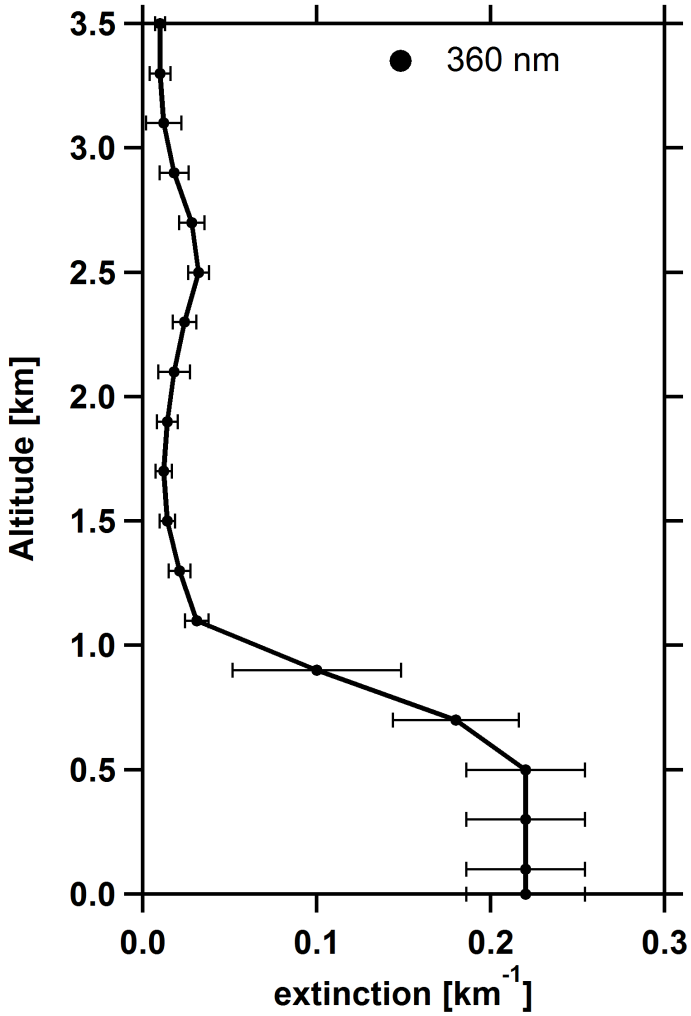

Figure A.2: Aerosol extinction coefficient profile retrieved at 360 nm using O_4 dSCD measurements at 360 nm for the above mentioned flight.

A.2 Chapter 3: HCHO and CHOCHO Vertical Columns

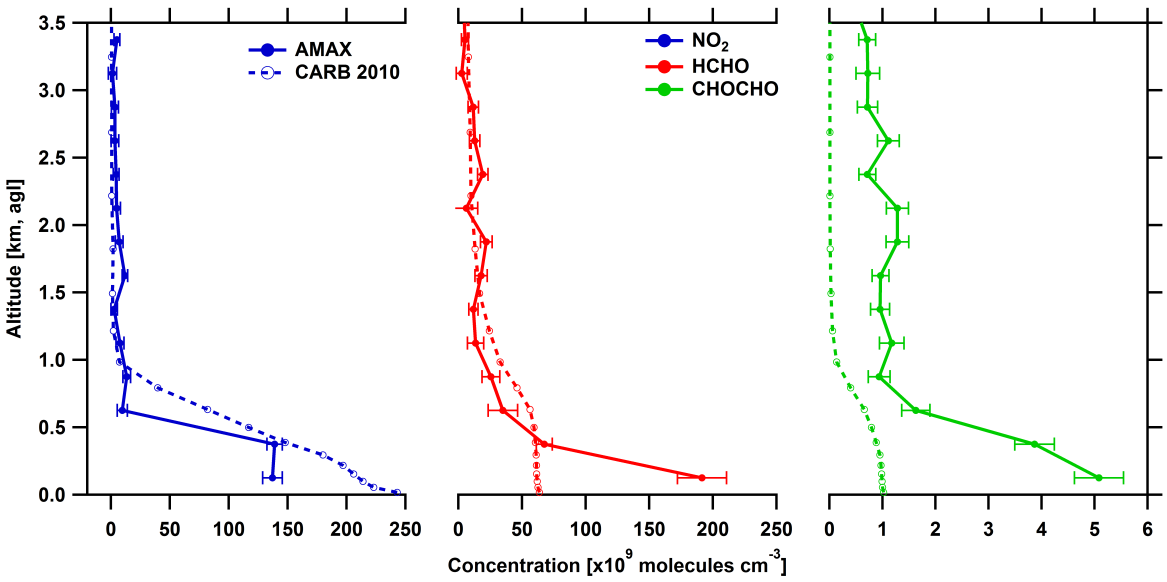

Figure A.3: Vertical profiles of NO_2 (blue), HCHO (red) and CHOCHO (green) retrieved from CU AMAX-DOAS measurements (solid) and modeled by CMAQ model using CARB 2010 emission inventory (dotted, open circle) on July 16, 2010 at Santa Monica, CA.

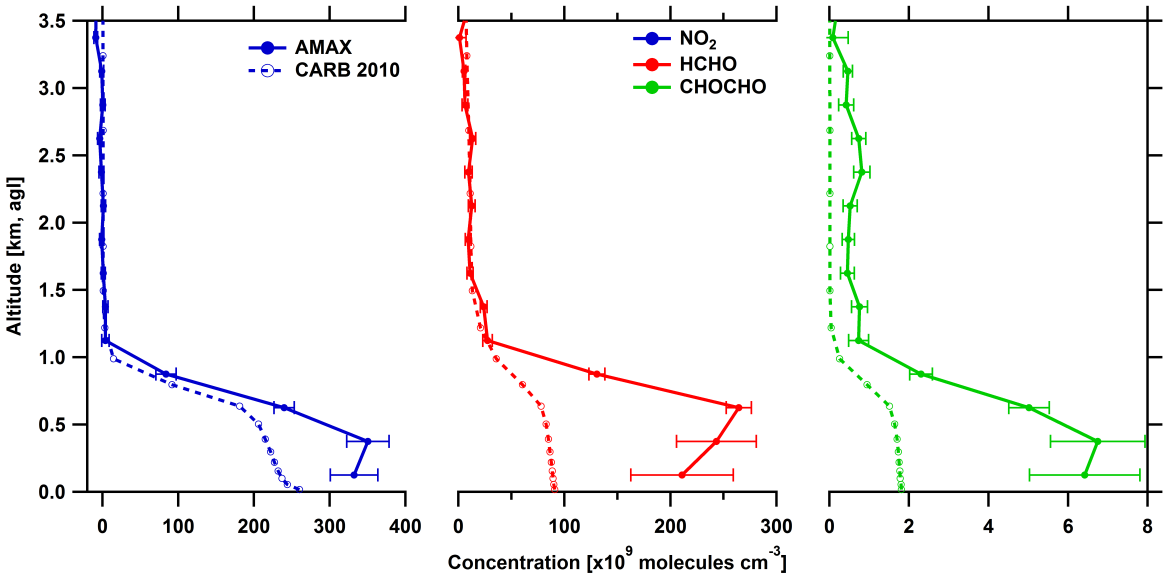

Figure A.4: Vertical profiles of NO_2 (blue), HCHO (red) and CHOCHO (green) retrieved from CU AMAX-DOAS measurements (solid) and modeled by CMAQ model using CARB 2010 emission inventory (dotted, open circle) on July 16, 2010 at Brackett, CA.

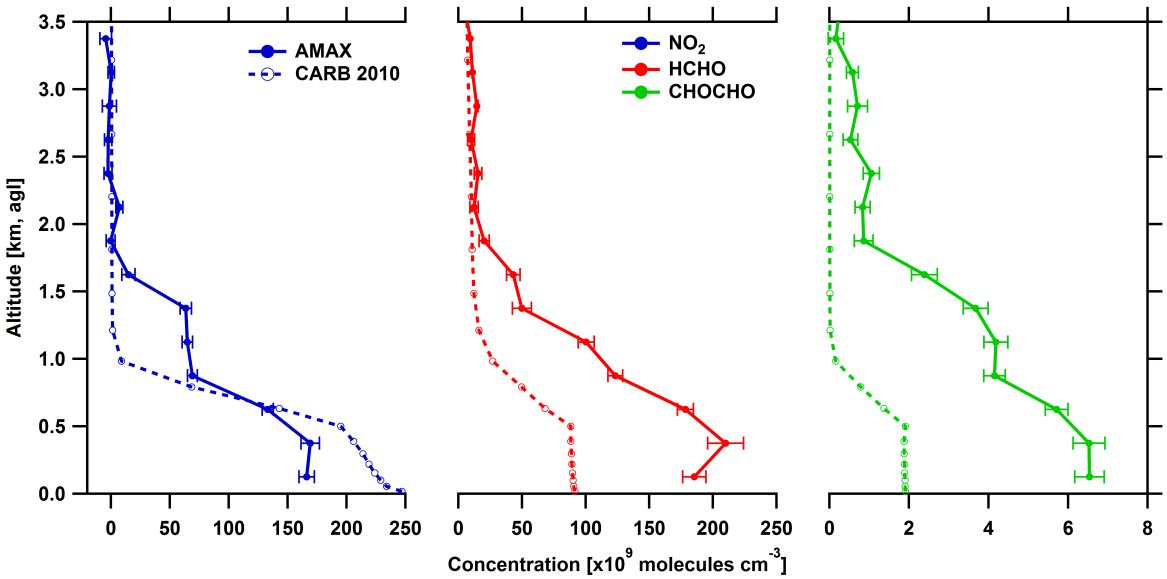

Figure A.5: Vertical profiles of NO_2 (blue), HCHO (red) and CHOCHO (green) retrieved from CU AMAX-DOAS measurements (solid) and modeled by CMAQ model using CARB 2010 emission inventory (dotted, open circle) on July 16, 2010 at Ontario, CA.

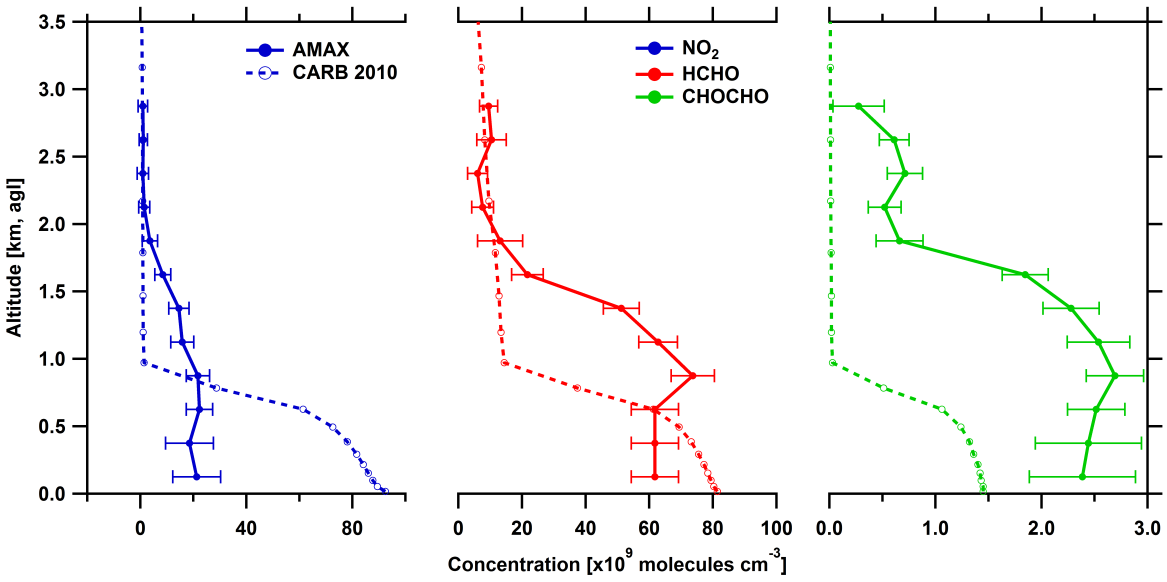

Figure A.6: Vertical profiles of NO_2 (blue), HCHO (red) and CHOCHO (green) retrieved from CU AMAX-DOAS measurements (solid) and modeled by CMAQ model using CARB 2010 emission inventory (dotted, open circle) on July 16, 2010 at Banning, CA.

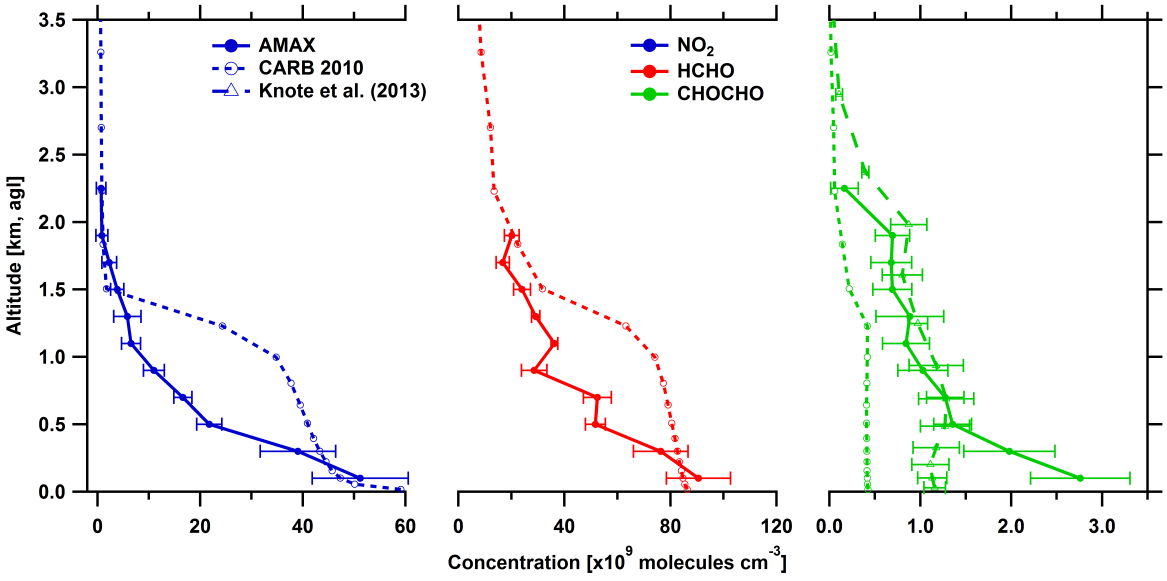

Figure A.7: Vertical profiles of NO_2 (blue), HCHO (red) and CHOCHO (green) retrieved from CU AMAX-DOAS measurements (solid) and modeled by CMAQ model using CARB 2010 emission inventory (dotted, open circle) on June 15, 2010 at Bakersfield, CA. The green dashed line with open triangle is the CHOCHO profile from Knote et al. (2014).

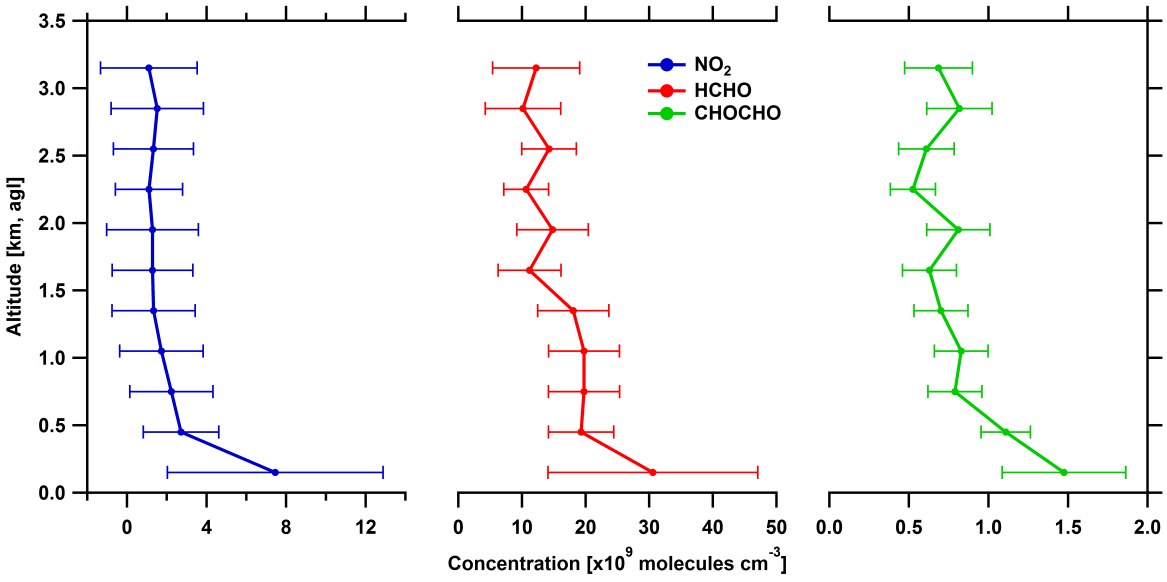

Figure A.8: Vertical profiles of NO_2 (blue), HCHO (red) and CHOCHO (green) retrieved from CU AMAX-DOAS measurements on July 19, 2010 at Page, AZ.

A.3 Chapter 5: Weekend O_3 Effect

A.3.1 Trend in NO_2 and O_3

Figures A.9 and A.10 show time series of three year mean NO_2 and O_3 concentrations measured at the downtown Los Angeles and San Bernardino monitoring stations. These two sites are representative of sites in the western and eastern part of the SCAB, respectively. The data have been segregated by ambient maximum temperature conditions (hot; 34-45 °C and moderate; 25-33 °C) and weekday (WD; Thursday and Friday) and weekend (WE; Saturday and Sunday). Only Thursday and Friday were considered for calculating the mean weekday value to keep it consistent with the analysis presented in the main text. The daily mean NO_2, and O_3 and maximum temperature were calculated between 12:00 and 16:00 PST.

NO_2 for both downtown Los Angeles and San Bernardino has significantly decreased from 1996 to 2014. Both sites show reduction on weekends attributed to lower emissions from diesel trucks on WE. NO_2 at downtown Los Angeles also shows a temperature dependence, with higher NO_2 being observed during hot conditions (34-45 °C) compared to moderate conditions (25-33 °C). Recently, there is a contrasting trend in NO_2 between the two sites. The decreasing trend in NO_2 seems to have leveled in the last few years in San Bernardino while NO_2 is starting to decrease again after 2010 in downtown Los Angeles.

O_3 on the WE during hot conditions has been decreasing steadily at both sites. In contrast, the O_3 decrease during hot WD conditions is much slower with San Bernardino even showing an increasing trend during the economic recession. This contrasting trend in the WD and WE resulted in a large decrease in P_{WEO3} observed at most of the locations in the SCAB during the recession. O_3 at both sites shows a significant temperature dependence, with higher O_3 being observed during hot conditions. This is very likely due to the temperature dependence of VOCR. The effect of temperature is similar to NO_x reduction on weekends. Hence, to avoid potential bias due to this temperature dependence of O_3, we constrained our analysis for P_{WEO3} by temperature. However, the overall conclusions reached did not depend on the choice of the temperature interval used.

A.3.2 Distribution of WE to WD difference in O_3 concentrations

Example distribution of difference in mean WE to WD O_3 concentration for downtown Los Angeles and San Bernardino for the four year periods 2003-2006 and 2011-2014 are shown in Fig. A.11 and A.12. At Los Angeles where P_{WEO3} change from 2003-2006 to 2011-2014 was very small and not very robust, no shift in the distribution of difference in WE to WD O_3 is observed but only a tightening of the distribution in recent years. At San Bernardino, the decrease in P_{WEO3} in recent years is accompanied by the shift in difference in WE to WD O_3 towards smaller values. A similar shift towards lower differences are observed for other sites in the eastern part of the SCAB (not shown). The overall shift in the distribution in difference in WE to WD O_3 towards not only smaller values but also negative values show that there is increasingly more weekends with lower O_3 compared to weekdays. This shift in atmospheric state is not visible when statistical parameters such as mean O_3 is compared between weekdays and weekends but is captured in our analysis of P_{WEO3}. The P_{WEO3} is essentially the sum of the probabilities to the right of 0 in Fig. A.11 and A.12 except for the points that fall within the 3 ppb equal O_3 threshold. The relatively large width of the distribution makes it unlikely that the P_{WEO3} calculations are sensitive to the choice of this equal O_3 threshold, as was confirmed by our sensitivity studies (see Fig. A.14).

A.3.3 Sensitivity Studies

To determine the robustness of the calculated P_{WEO3}, sensitivity studies were performed for the following parameters: (i) only considering Sunday as the weekend day, (ii) changing the equal O_3 threshold value from 3 ppb by ± 1 ppb, (iii) changing the O_3 threshold value from 70 ppb to 60 and 80 ppb, (iv) changing the temperature range to 25-45 °C, (v) using temperature from Upland surface monitoring station in the middle of the basin as opposed to San Bernardino, (vi) changing the time period for daily mean O_3 calculation from 12:00-16:00 PST to 11:00-17:00 PST, and (vii) changing the parameter from mean O_3 to maximum O_3. The results from the base case are shown in Chapter 5 Fig. 5.2 and results from the sensitivity studies shown here follow the same template.

The temperature condition (34-45 °C), which was employed to reduce uncertainty due to the temperature dependence of VOCR, removed the largest number of data points, i.e., removing 51% and 68% of the data points for the four year periods 2003-2006 and 2011-2014, respectively. Further, the O_3 threshold of 70 ppb removed about 1% and 24% of the data for San Bernardino and downtown Los Angeles, respectively. When the temperature condition was expanded to 25-45 °C, only 4% of the data were removed for the most recent four year period. However, the number of data points not meeting the O_3 threshold increased to 5% and 88% respectively for San Bernardino and downtown Los Angeles. The effect of NO_2 was fairly small mostly removing data points when NO_2 measurements were not available. The other conditions deal with the statistical treatment of data, rather than filtering of data.

Results from the sensitivity studies showed that P_{WEO3} was very robust and does not depend upon the choice of parameters. All results show the same decreasing trend, with a larger decrease in the eastern part of the basin. Changes in P_{WEO3} were within 5-10% in the eastern part of the basin. The largest sensitivity was observed for increasing the temperature range to 25-45°C. Only the downtown Los Angeles showed some sensitivity to the choice of parameter, with P_{WEO3} decreasing instead of increasing for 60 ppb as the O_3 threshold and maximum O_3 parameters. However, these decreases were small and P_{WEO3} remain high in downtown Los Angeles. Excluding Saturday as the weekend only had the effect of worsening the statistics but did not change the overall trend in P_{WEO3} and is shown in Fig. A.13. Selected results from the sensitivity studies are shown in Fig. A.13-A.19. The results from the base case shown in Fig. 5.2 (Chapter 5) are included in each figure as grey lines.

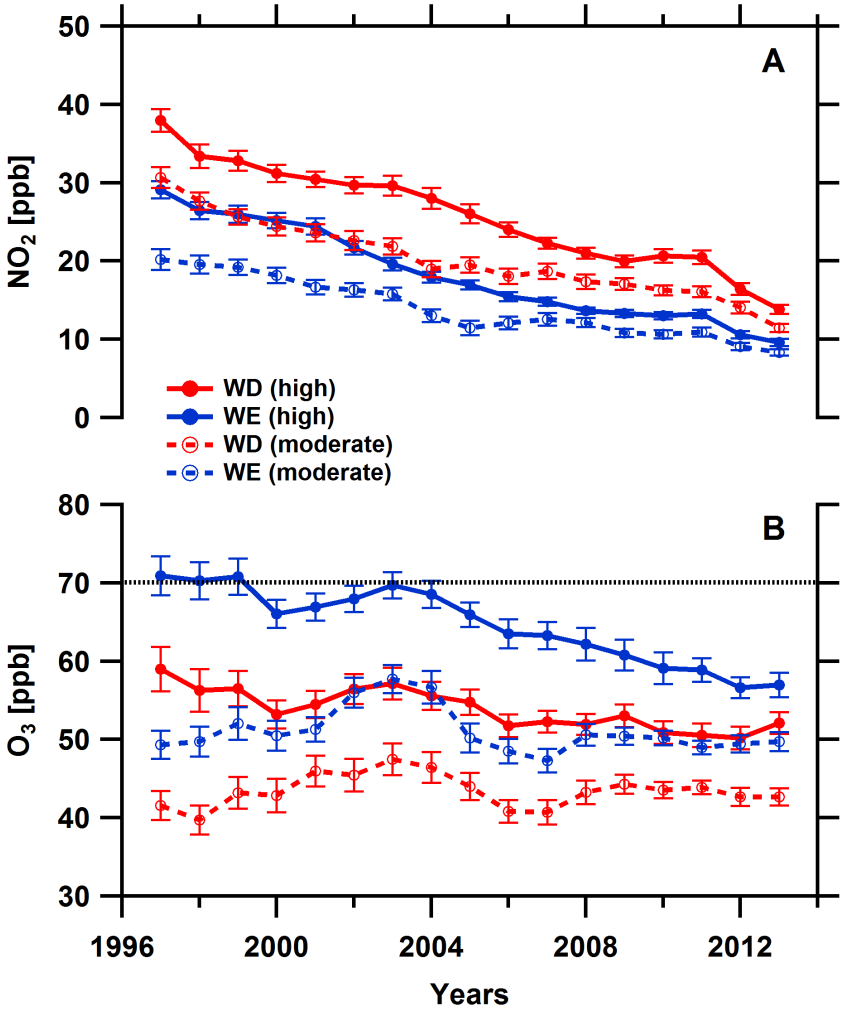

Figure A.9: Time series of three year mean (12:00-16:00 PST) (A) NO_2 and (B) O_3 concentrations measured at downtown Los Angeles for weekdays (Thursday and Friday, red lines) and weekends (Saturday and Sunday, blue lines) at hot (34-45 °C, solid lines) and moderate (25-33 °C, dashed lines) temperature conditions from 1996-2014. The error bars represent standard error of the mean. The black dashed line shows the O_3 threshold value used in the analysis.

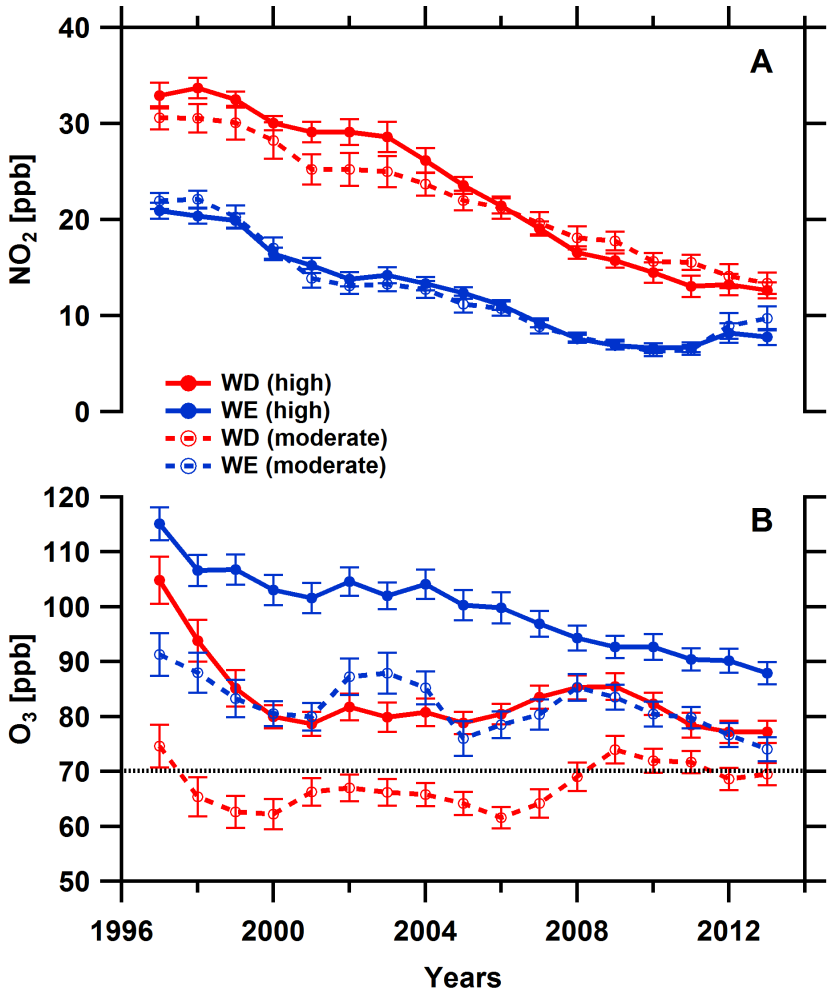

Figure A.10: Same as Fig. A.9 for San Bernardino monitoring site.

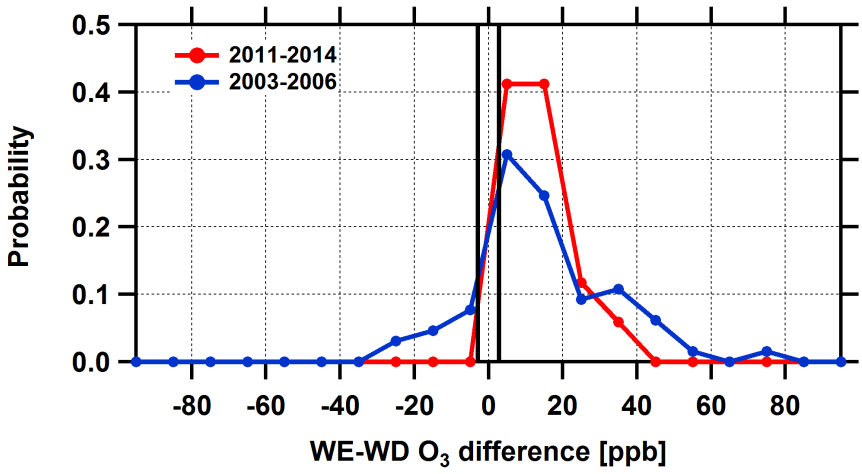

Figure A.11: Distribution of difference in mean weekend to weekday O_3 at downtown Los Angeles site for the four year periods (i) 2003-2006 (blue) and (ii) 2011-2014 (red). The black solid lines show the equal O_3 threshold used in the analysis.

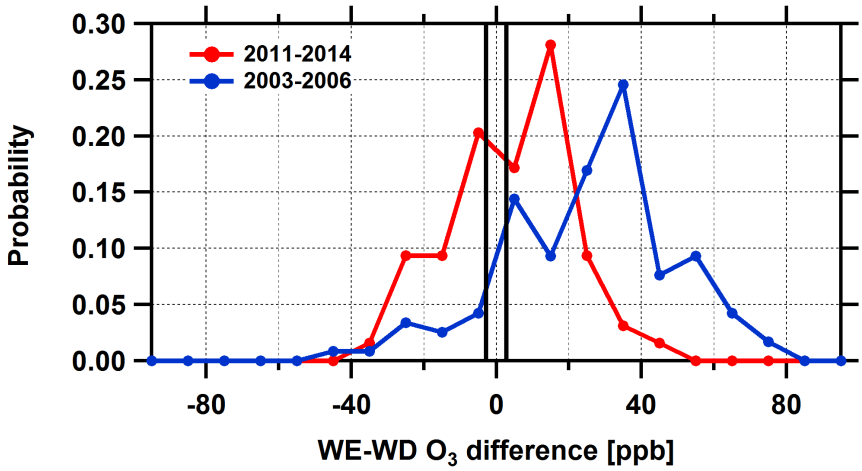

Figure A.12: Same as Fig. A.11 for San Bernardino monitoring site.

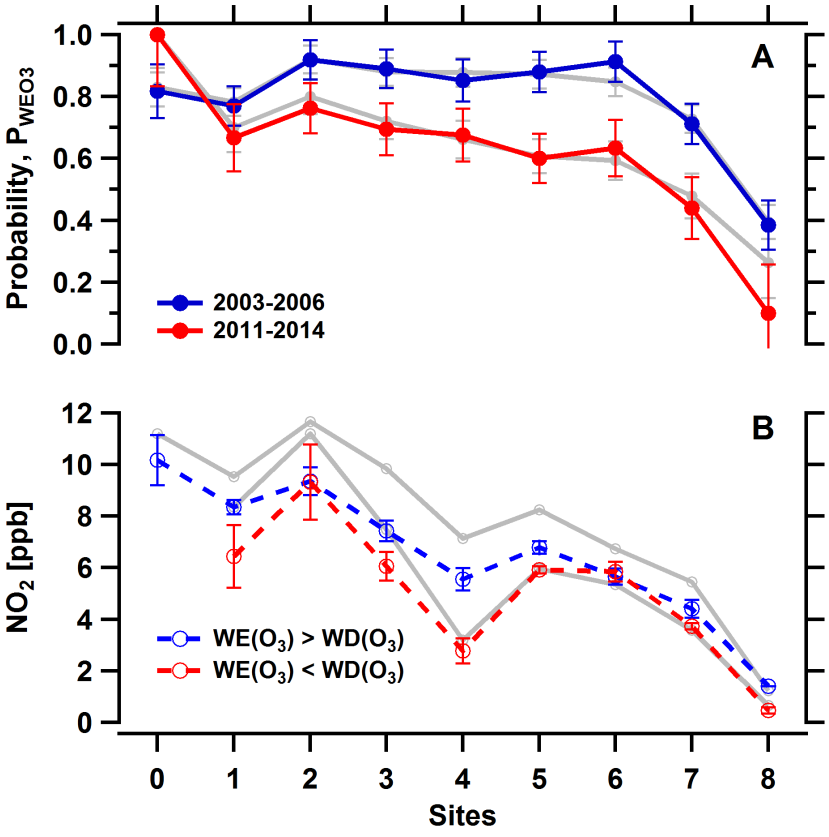

Figure A.13: Sensitivity study for the weekend day. Four year probability of weekend O_3 effect occurrences (P_{WEO3}) and mean NO_2 values at different sites in the SCAB when only Sunday is considered as the weekend day. A) Four year P_{WEO3} for 2003-2006 (blue) and 2011-2014 (red). The error bars represent uncertainty in counting statistics. B) Mean weekend NO_2 when weekend O_3 is higher than weekday (blue) and weekend O_3 is lower than weekday (red) for the year 2011-2014. The error bars represent standard error of the mean. The grey lines in the background show the base case scenario shown in Fig. 5.2 (Chapter 5).The name of sites are as follows: 0) Los Angeles, 1) Pasadena, 2) Azusa, 3) Pomona, 4) Upland, 5) Fontana, 6) San Bernardino, 7) Riverside and 8) Banning.

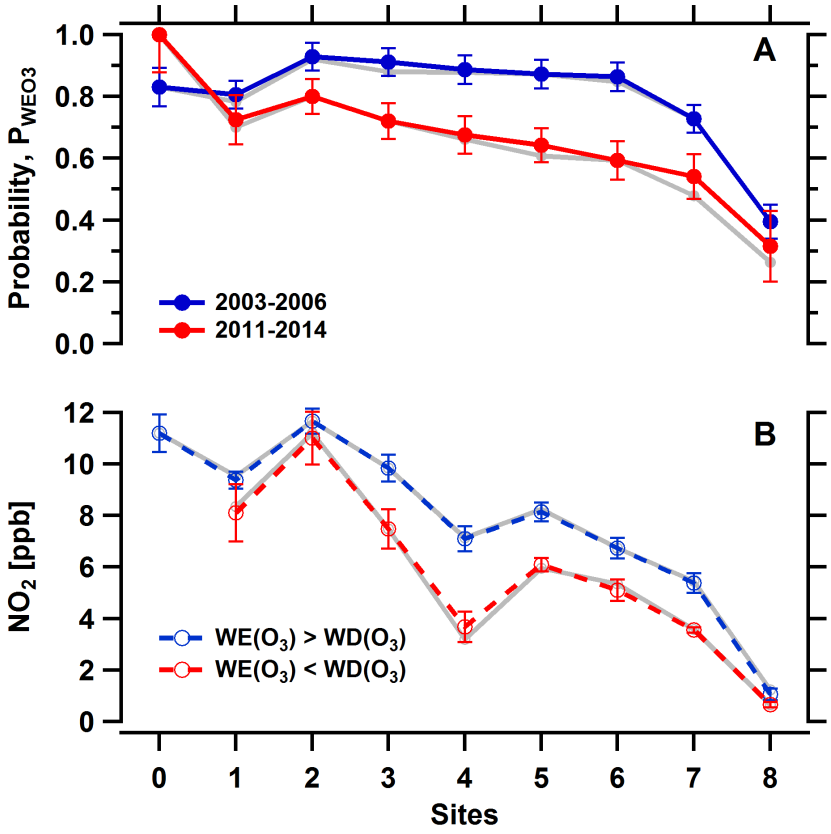

Figure A.14: Sensitivity study for the equal O_3 threshold. Same as Fig. A.13 using equal O_3 threshold of 2 ppb instead of 3 ppb. The grey lines in the background show the base case scenario shown in Fig. 5.2 (Chapter 5).

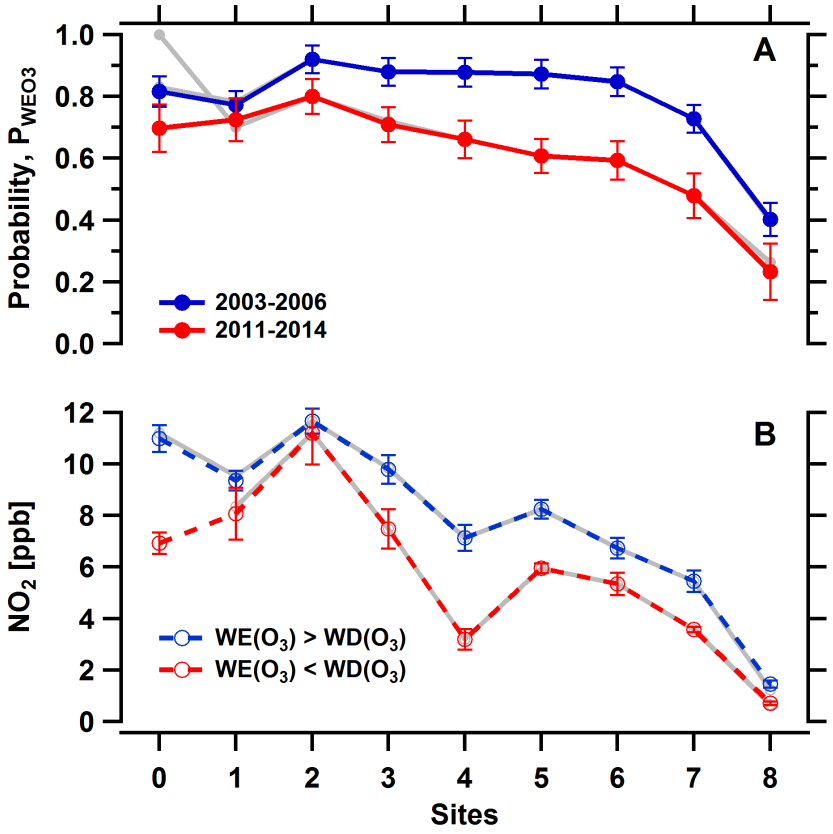

Figure A.15: Sensitivity study for the O_3 threshold. Same as Fig. A.13 using O_3 threshold of 60 ppb instead of 70 ppb. The grey lines in the background show the base case scenario shown in Fig. 5.2 (Chapter 5).

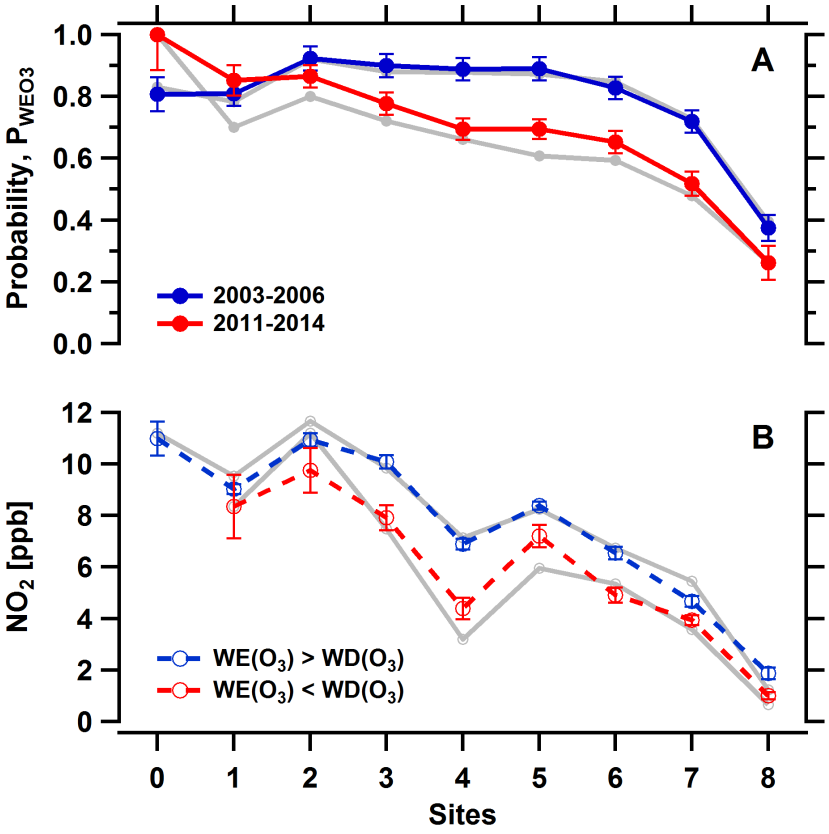

Figure A.16: Sensitivity Study for the temperature range. Same as Fig. A.13 using the temperature range 25-45 °C. The grey lines in the background show the base case scenario shown in Fig. 5.2 (Chapter 5).

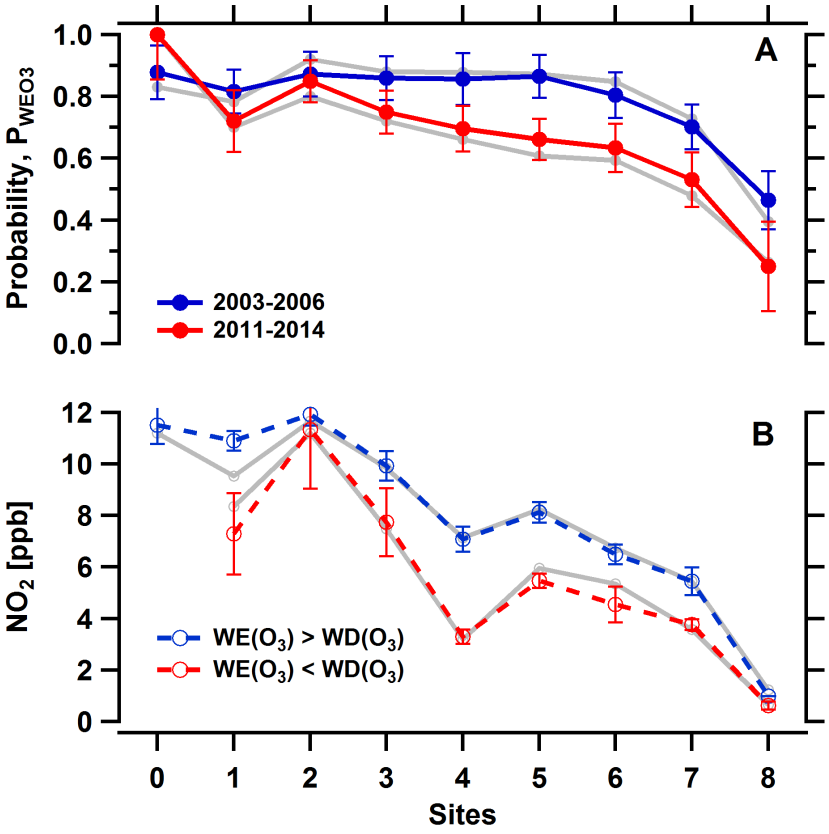

Figure A.17: Sensitivity study for the location of temperature data. Same as Fig. A.13 using temperature data from Upland monitoring site. The grey lines in the background show the base case scenario shown in Fig. 5.2 (Chapter 5).

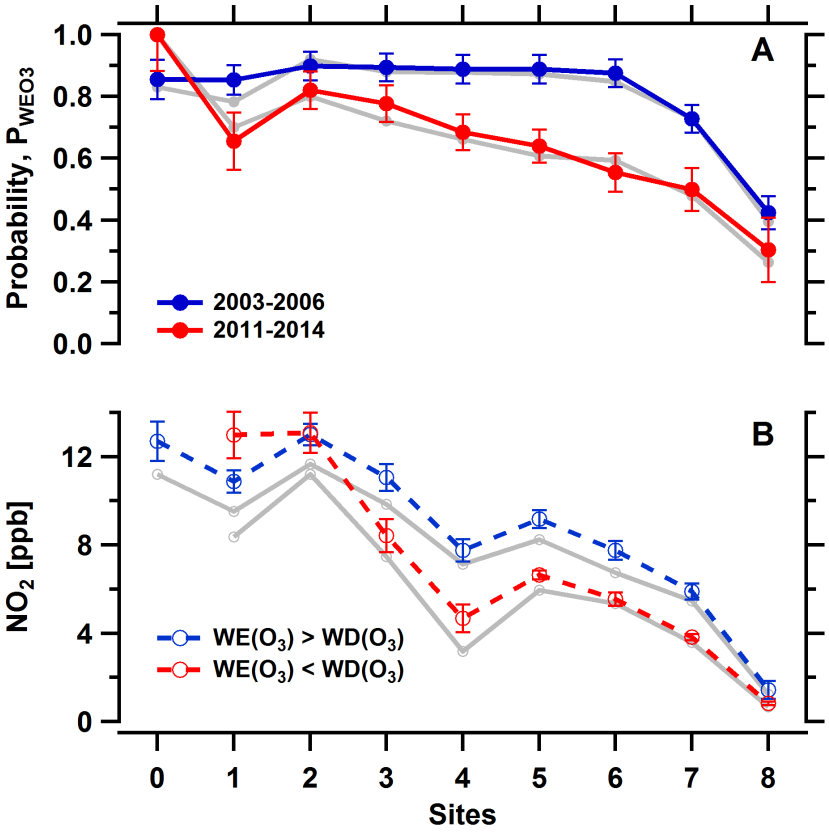

Figure A.18: Sensitivity study for changing the averaging time period. Same as Fig. A.13 using averaging period from 11:00-17:00 PST. The grey lines in the background show the base case scenario shown in Fig. 5.2 (Chapter 5).

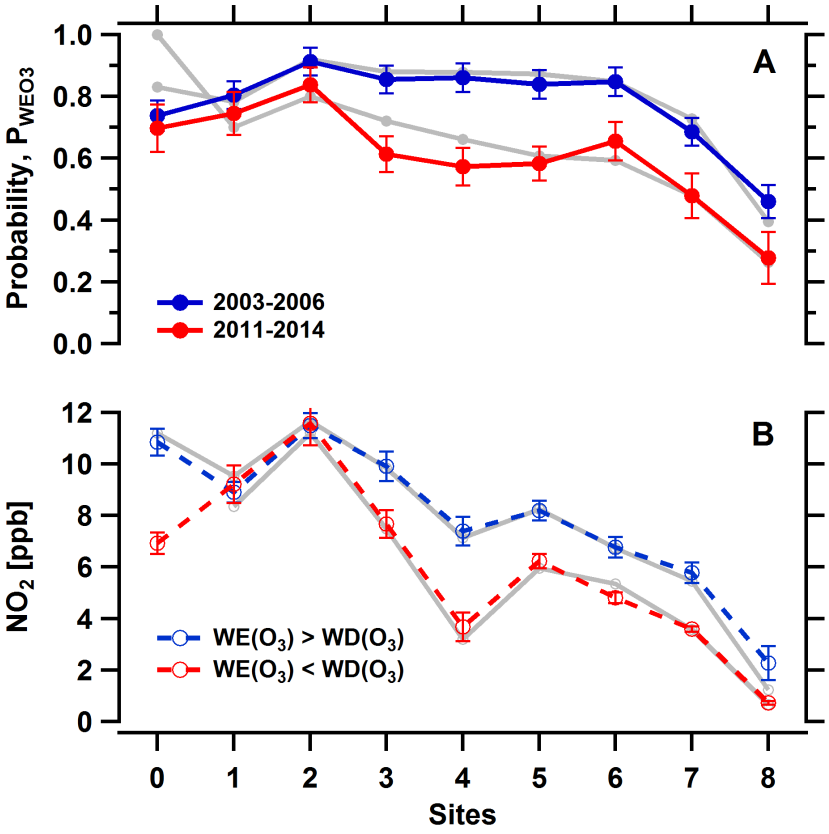

Figure A.19: Sensitivity study for the statistical parameter. Same as Fig. A.13 using maximum O_3 instead of mean O_3 for comparison. The grey lines in the background show the base case scenario shown in Fig. 5.2 (Chapter 5).

A.4 Chapter 6: Sand Signature

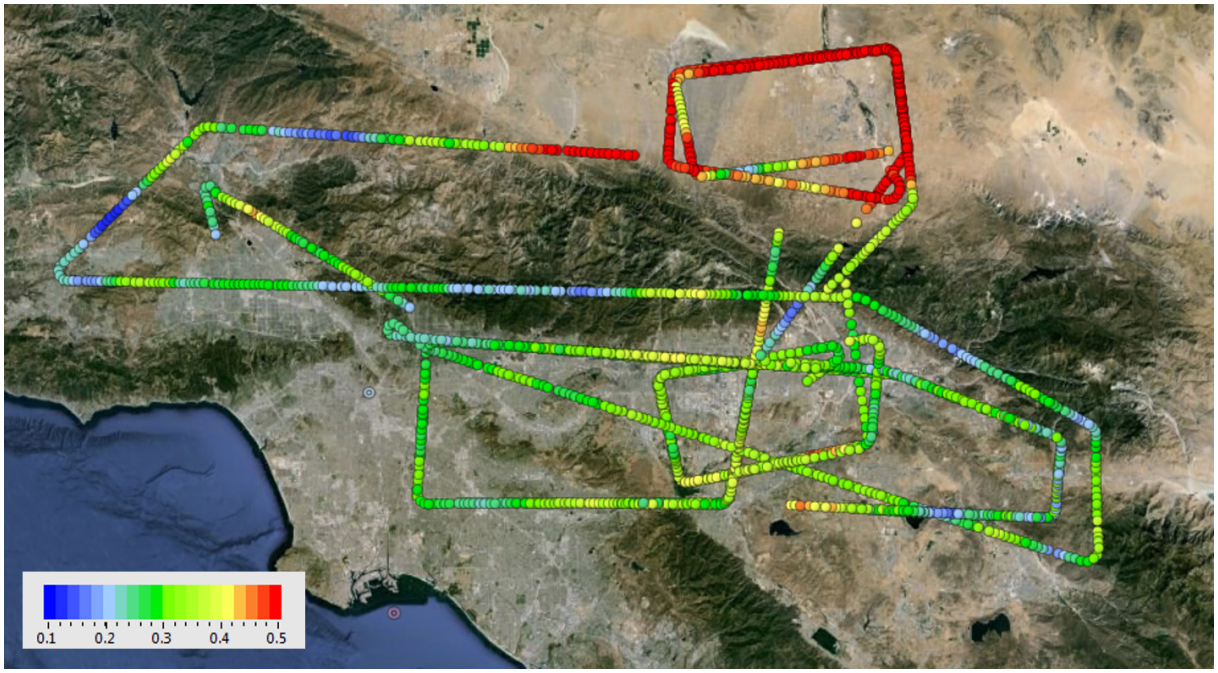

Figure A.20: Map of sand fit coefficients for three flights inside the SCAB.

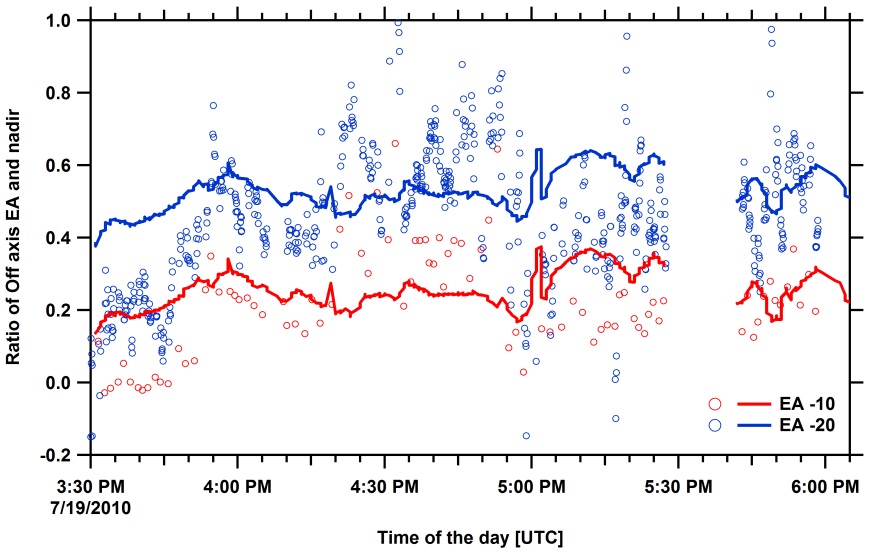

Figure A.21: Time series of ratio of sand signal measured at EAs -10° (red open circles) and -20° (blue open circles) relative to EA -90° during the research flight on July 19, 2010. Also shown are fraction of ground scattered photons observed at EAs -10° (red line) and -20° (blue line) relative to EA -90° based on RTM calculations.

Figure A.22: Map of surface albedo from the research flight on July 19, 2010 over the desert in Nevada and Arizona.

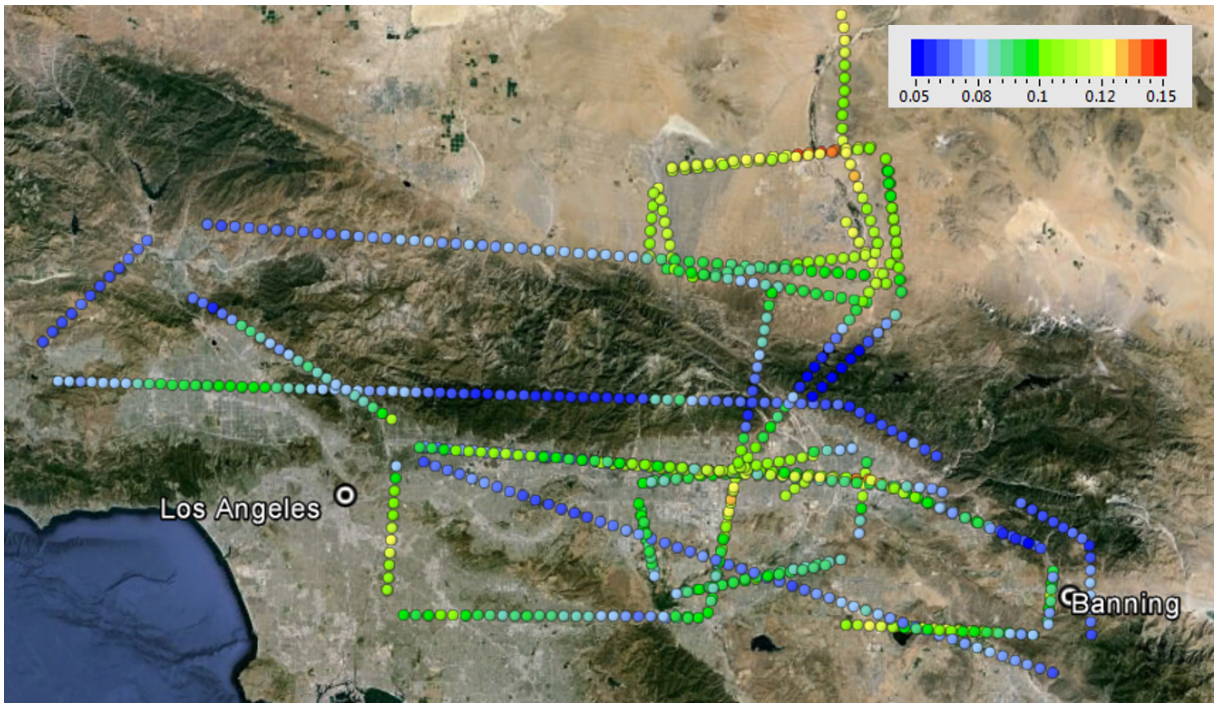

Figure A.23: Map of surface albedo from three research flights inside the SCAB.

A.5 Chapter 7: Solar Tracker

A.5.1 Note on the coordinate system

Because we inherited the MMQ coordinate system used for the AMAX-DOAS and solar position (elevation and azimuth) calculation from the 2-D-MAX-DOAS for the Solar Tracker we decided to define a single right hand coordinate system for all calculations required for the solar tracker and then convert them back to respective coordinate system to move the motors. For all mirror calculations we use a right hand coordinate system where X is defined as East, Y is defined as North and Z is Up. In this coordinate system, positive heading is from East to North in counter clock wise direction, positive pitch is defined as nose down and positive roll is defined as left side up.

MMQ coordinate system: Right hand coordinate system where X is defined as East, Y is defined as South and Z is Down. In this coordinate system, positive heading is from north to east in clockwise direction with North being zero, positive pitch is defined as nose up and positive roll is defined as left side up.

MMQ heading is converted to the Solar Tracker right hand coordinate system as described above by rotating 180 degrees around x-axis and redefining heading as Heading = 90 - MMQ heading. This makes MMQ x = x but MMQ y = -y. Since roll is around x, roll does not change. However pitch is around y and hence it is negated.

A.5.2 Corrections for pitch, roll and heading

Calculations for the position of the Sun in the sky at a given time and location is very well documented. Reference algorithm is readily available in various programming languages such as C and Matlab. The challenge with the mobile system is to account for the attitude of the platform in real-time and determine the position of the Sun in the sky with respect to platform orientation. Bertleff (2014) used a fish-eye camera with a FOV covering the entire horizon to locate the sun from a research vessel. Merlaud et al. (2012) showed how Euler angles can be used to correct for

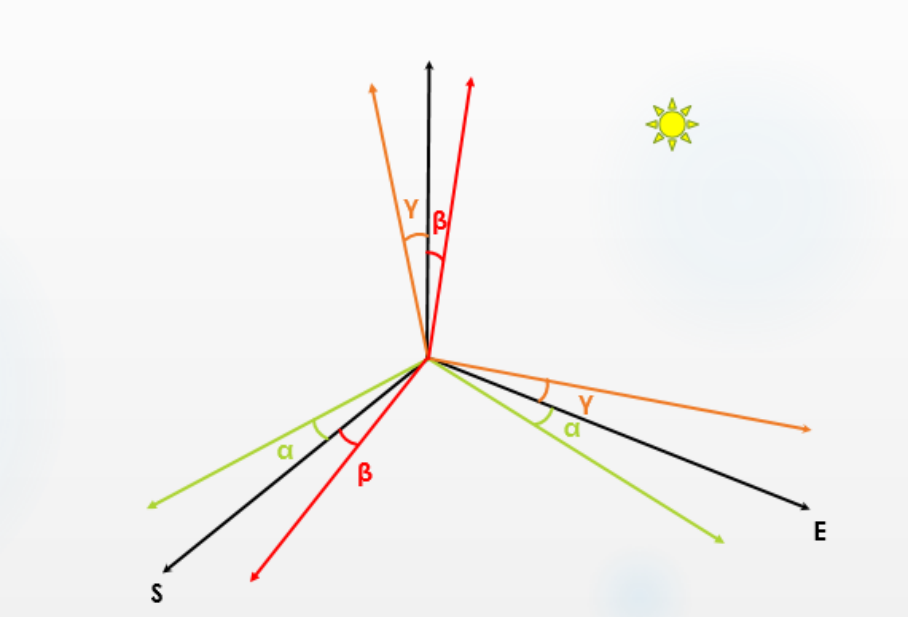

Figure A.24: Graphical representation of pitch (β), roll (γ) and heading (α) of the platform relative to a fixed geographical coordinate system.

misalignment between the tracker baseplate and solar azimuthal coordinate system in a stationary setup. The heading (α), pitch (β), and roll (γ) of the vehicle can be considered as the Euler angles and can be accounted as consecutive rotations around the three orthogonal axes. For a right handed co-ordinate system rotating in counter clockwise direction, the transformation of the coordinates due to the Euler angles is given by the product of three rotational matrices $R_x(\gamma)$, $R_y(\beta)$, and $R_z(\alpha)$ along the three axes, $M_{attitude}$.

$$M_{attitude} = \begin{bmatrix} 1 & 0 & 0 \\ 0 & cos\,\gamma & sin\,\gamma \\ 0 & -sin\,\gamma & cos\,\gamma \end{bmatrix} \times \begin{bmatrix} cos\,\beta & 0 & -sin\,\beta \\ 0 & 1 & 0 \\ sin\,\beta & 0 & cos\,\beta \end{bmatrix} \times \begin{bmatrix} cos\,\alpha & sin\,\alpha & 0 \\ -sin\,\alpha & cos\,\alpha & 0 \\ 0 & 0 & 1 \end{bmatrix} \tag{A.1}$$

The Sun position in the sky in the in the solar spherical coordinates system (alt, az) can be converted into Cartesian coordinate system and is given by Eq.A.2

$$\begin{bmatrix} x_0 \\ y_0 \\ z_0 \end{bmatrix} = \begin{bmatrix} cos\,(alt_0) \cdot cos\,(az_0) \\ cos\,(alt_0) \cdot sin\,(az_0) \\ sin\,(alt_0) \end{bmatrix} \tag{A.2}$$

The direction of the sun in the vehicular frame is then given by the unit vector (x_v, y_v, z_v) and can be calculated as product of $M_{attitude}$ and the solar position in fixed Cartesian coordinates given by Eq.A.2

$$\begin{bmatrix} x_v \\ y_v \\ z_v \end{bmatrix} = M_{attitude} \times \begin{bmatrix} x_0 \\ y_0 \\ z_0 \end{bmatrix} \tag{A.3}$$

We can easily convert the new Cartesian coordinate system to altitude (alt_v) and azimuth (az_v) angles relative to the vehicle orientation.

$$\begin{aligned} \rho_v &= \sqrt{x_v^2 + y_v^2} \\ alt_v &= atan_2(z_v, \rho_v) \\ az_v &= atan_2(y_v, x_v) \end{aligned} \tag{A.4}$$

We implemented this coordinate transformation using the pitch, roll and heading as Euler angles to determine the solar position in the sky relative to the local vehicular real time position while mobile.

A.5.3 Corrections based on camera pixel offset data

Mirrors with any orientation can be represented using rotations. The matrix method uses well defined coordinate transformations which use simple matrix multiplications. The effect of rotation of a mirror M, or system of mirrors that has equivalent matrix M is

$$M_r = R \times M \times R^T \tag{A.5}$$

where M_r is the new matrix and R is the rotation matrix give below

$$X\ rotation, R_x = \begin{bmatrix} 1 & 0 & 0 \\ 0 & cos\,\alpha & -sin\,\alpha \\ 0 & sin\,\alpha & cos\,\alpha \end{bmatrix}$$

$$Y\ rotation, R_y = \begin{bmatrix} cos\,\beta & 0 & sin\,\beta \\ 0 & 1 & 0 \\ -sin\,\beta & 0 & cos\,\beta \end{bmatrix}$$

$$Z\ rotation, R_z = \begin{bmatrix} cos\,\gamma & -sin\,\gamma & 0 \\ sin\,\gamma & cos\,\gamma & 0 \\ 0 & 0 & 1 \end{bmatrix}$$

The two mirror in our tracker system can be defined as y mirrors rotated by -45° and is given by

$$M_R = R(-45^\circ) \times M_y \times R(45^\circ) \tag{A.6}$$

where

$$M_y = \begin{bmatrix} 1 & 0 & 0 \\ 0 & -1 & 0 \\ 0 & 0 & 1 \end{bmatrix} \tag{A.7}$$

Then,

$$M_R = \begin{bmatrix} 1 & 0 & 0 \\ 0 & 0 & 1 \\ 0 & 1 & 0 \end{bmatrix} \tag{A.8}$$

For our tracker at a solar azimuth angle and zenith angle of θ_1 and θ_2, the optical system inside the two mirrors can be derived as rotation of elevation mirror followed by rotation of azimuth mirror. This is given by the matrix, $M_{tracker}$:

$$M_{tracker} = R_z(\theta_1) \times R_y(\theta_2) \times M_R \times R_y(-\theta_2) \times M_R \times R_z(-\theta_1) \tag{A.9}$$

This transformation matrix can be used to convert the pixel offset data from the camera to angular movements of the elevation and azimuth mirrors of the tracker to correct for misalignment. The pixel offset data (δx, δy) represents 2 coordinates of the beam vector. The third, δz, is the distance from the aperture plate to the elevation mirror. For the current setup we use z =10000. The product of matrix $M_{tracker}$ and this vector gives the new corrected solar position in Cartesian coordinate system as given by

$$\begin{bmatrix} x_s \\ y_s \\ z_s \end{bmatrix} = M_{tracker} \times \begin{bmatrix} \delta x \\ \delta y \\ \delta z \end{bmatrix} \tag{A.10}$$

The calculated position (x_s, y_s, z_s) in Cartesian coordinate system is then converted to the spherical coordinates by using Eq. A.4 and gives the new motor angles. We use the current azimuth and elevation motor position for solar azimuth and zenith angle in the calculations so that the corrections for the Euler angles are already incorporated and motor movements are in the local tracker coordinate system.

A.5.4 How to operate the tracker

Steps for operating the solar tracker are as follows:

(1) Open the newest LabVIEW program folder and double click on the project.

(2) Open the control program and the solar tracker RT program and run both the programs.

(3) Start the PC104 and run the MCRT program.

(4) Select the Manual option and enter the current pitch, roll and heading information.

(5) Reset both motors.

(6) On the Solar Tracker RT, select the Auto circle/ellipse option and set circle/ellipse to 100.

(7) Turn on the Auto Stabilize button on the MCRT.

(8) If the sun is not in the FOV of the camera, adjust the heading, pitch and roll appropriately. This is only required if the current heading, pitch and roll information is not available.

(9) Adjust the threshold on the Solar Tracker RT to appropriate value to get correct size (radius) for the solar disk (∼70 pixels) and aperture (∼40 pixels).

(10) Adjust the X and Y controls for small and large circle centers appropriately to get it in the center of the aperture if needed.

(11) Once you have the solar tracker tracking the sun, check the freeze small circle/ellipse button.

(12) Select the MMQ option if you are going to be driving.

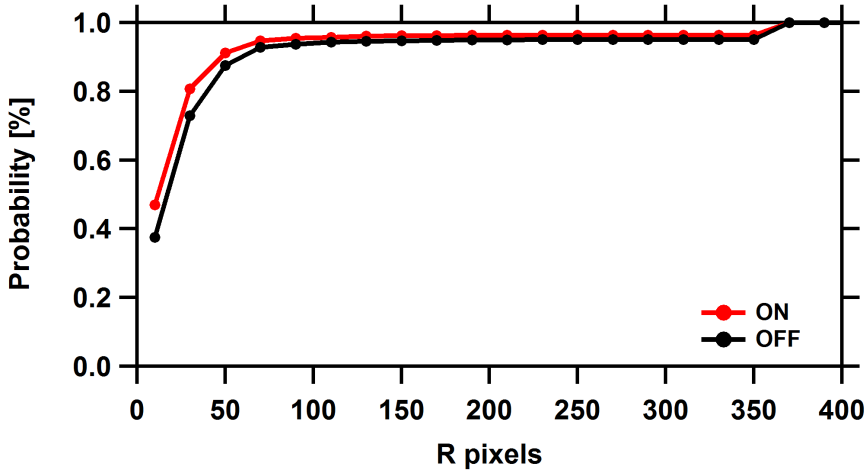

Figure A.25: Cumulative distribution of pixel offset between the center of the solar disk and the aperture for (A) when correction for real time pitch and roll was applied (red) and (B) correction was not applied (black). An improvement of up to 25% was observed when the correction based on real time pitch and roll was applied.

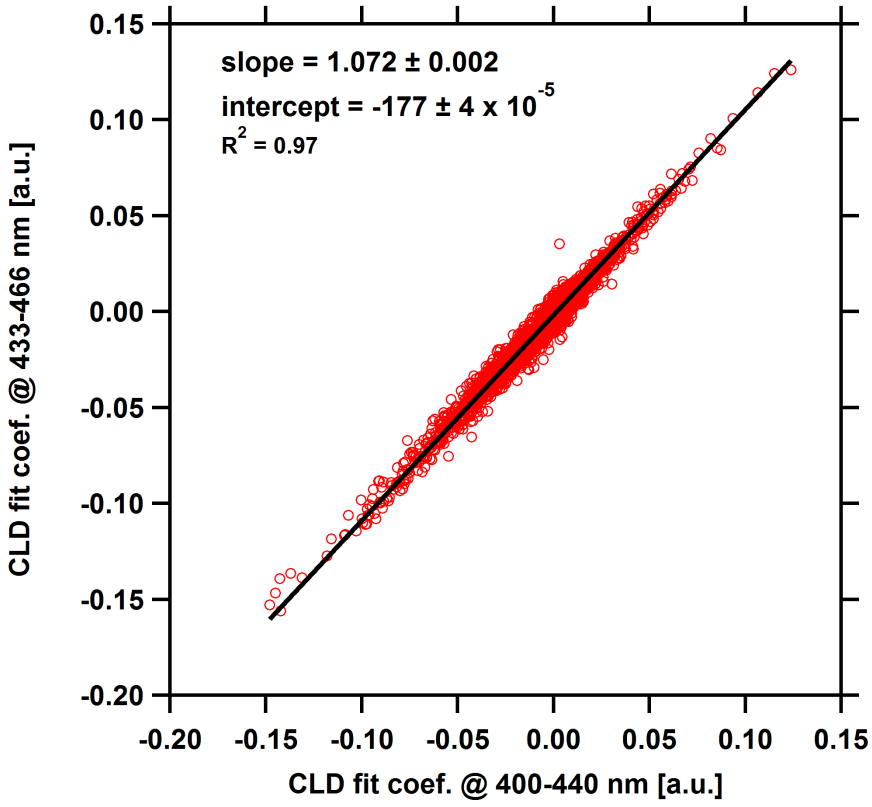

Figure A.26: Correlation of CLD fit coefficients retrieved at 400-440 nm and 433-466 nm DOAS fit windows.

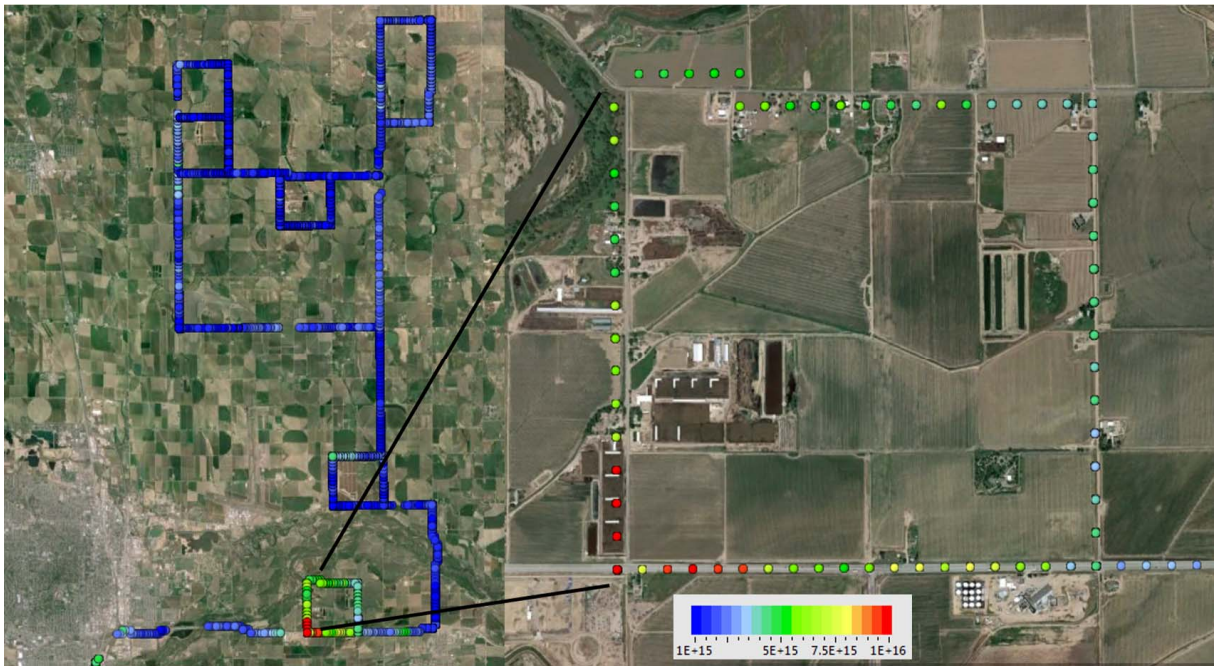

Figure A.27: Map of NO_2 vertical column measured during the RD#10 on August 12, 2014 around various farms near Greeley, CO. The right panel shows the zoomed map around a beef farm.

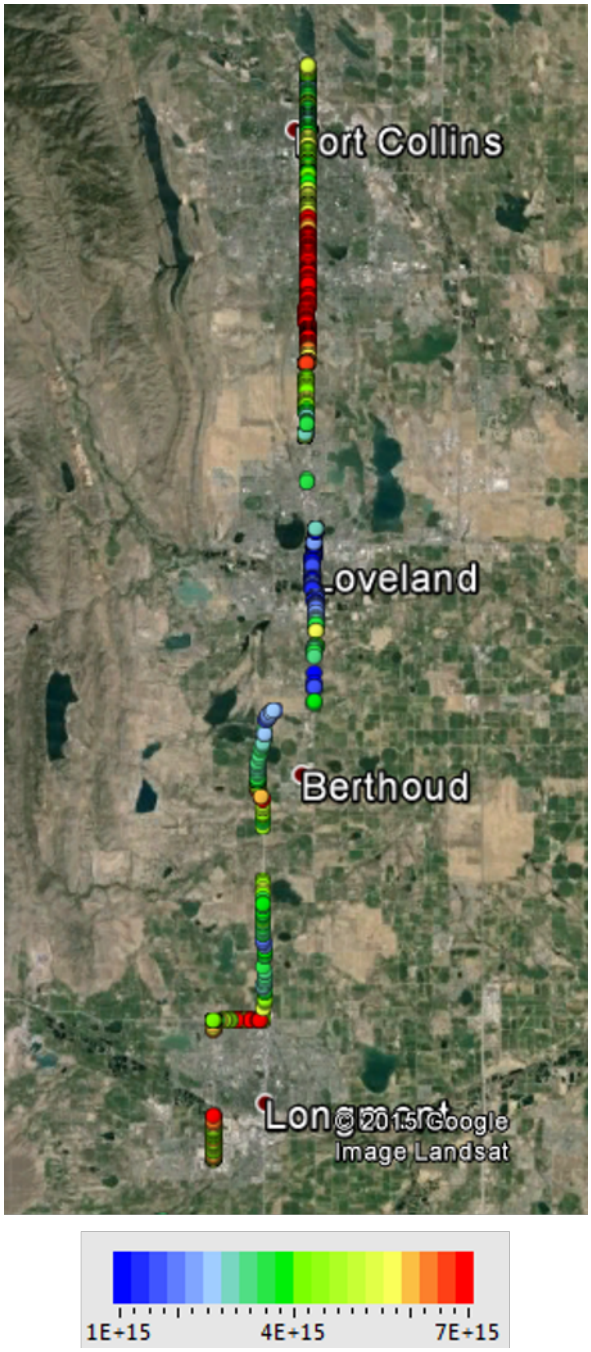

Figure A.28: Map of NO_2 vertical column measured during the RD#14 on August 18, 2014 in Northern Colorado used for Fig. 7.14.

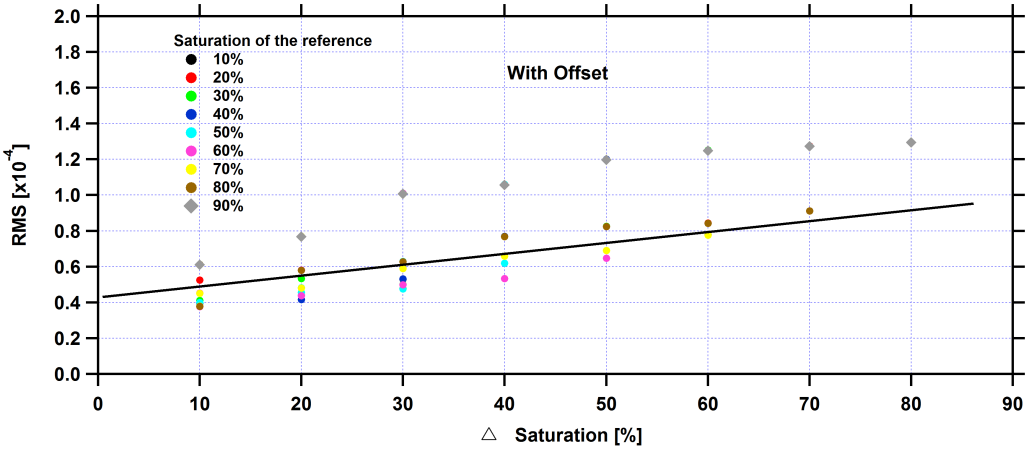

Figure A.29: Correlation plot for RMS and detector saturation difference between measured spectrum and reference spectrum to test for non linearity of the CCD detector at 440 nm.

Table A.1: Overview of research drives during FRAPPE 2014 with description of the drives and comments.

RD #	Drive date	Description	Comments
1	07/21/2014	Sampling at Magnum CAFO	
2	07/28/2014	Urban emission around Denver	
3	08/01/2014	Urban emission around Denver	Aborted due to MAX-DOAS motor issue shortly after start
4	08/02/2014	Urban emission around Denver	
5	08/04/2014	Regional outflow from CAFO and sampling at Magnum CAFO	Aborted due to weather conditions after reaching Longmont
6	08/06/2014	Regional outflow	
7	08/08/2014	Regional within Boulder County	
8	08/09/2014	Regional outflow	Similar to RD06
9	08/11/2014	Regional	
10	08/12/2014	Various farms around Greeley	Coordinated with NOAA, Aerodyne and other mobile labs
11	08/13/2014	Various farms around Greeley	Coordinated with NOAA, Aerodyne and other mobile labs
12	08/15/2014	Regional within Boulder County	Aborted due to motor issues and weather at mid-point
13	08/16/2014	Overflight, BAO tower	Start from Denver
14	08/18/2014	Early morning mountain upslope flow	
15	08/18/2014	Late evening mountain upslope flow	Testing for changes made to FTIR
16	09/03/2014	Urban emission around Denver	

Table A.2: Performance of solar tracker for research drives during FRAPPE 2014.

Research Drive #	Speed (ms^{-1}) avg ± sdev	Number of points	X-precision (◦)	Y-precision (◦)	Overall precision (◦)
1	49 ± 42	54846	0.052	0.065	0.083
2	72 ± 18	86891	0.064	0.078	0.101
3	64 ± 27	11716	0.064	0.108	0.125
4	66 ± 22	173387	0.066	0.097	0.117
5	44 ± 31	26187	0.058	0.067	0.088
6	63 ± 28	244409	0.049	0.070	0.085
7	43 ± 17	68712	0.050	0.054	0.073
8	54 ± 20	85880	0.048	0.046	0.066
9	52 ± 26	71446	0.048	0.064	0.080
10	34 ± 29	259773	0.043	0.058	0.073
11	39 ± 28	258715	0.035	0.039	0.052
12	41 ± 18	44842	0.042	0.054	0.069
13	44 ± 21	210113	0.050	0.070	0.086
14	54 ± 21	131198	0.043	0.039	0.059
15	61 ± 26	7955	0.076	0.083	0.112
16	72 ± 21	105815	0.064	0.080	0.102